

Fundamentals of Diffraction-Based Residual Stress and Texture Analysis of Laser Powder Bed Fused Inconel 718



vorgelegt von:

M.Sc.

Jakob Schröder

kumulative Dissertation

zur Erlangung des akademischen Grades

“Doktoringenieur”

(Dr.-Ing.)

in der Wissenschaftsdisziplin “Experimentalphysik”

eingereicht an der

Mathematisch-Naturwissenschaftlichen Fakultät

Institut für Physik und Astronomie

der Universität Potsdam

und

der Bundesanstalt für Materialforschung und -prüfung

Ort und Tag der Disputation: Potsdam, 14.11.2023

This work is protected by copyright and/or related rights. You are free to use this work in any way that is permitted by the copyright and related rights legislation that applies to your use. For other uses you need to obtain permission from the rights-holder(s).

<https://rightsstatements.org/page/InC/1.0/?language=en>

Hauptbetreuer: Prof. Dr. Giovanni Bruno
Erstgutachter *Universität Potsdam*
Bundesanstalt für Materialforschung und -prüfung

Betreuer: Prof. Dr. Winfried Petry
Zweitgutachter *Technische Universität München*

Drittgutachter: Prof. Dr. Thomas Niendorf
Universität Kassel

Mentoren: Dr. Alexander Evans
Bundesanstalt für Materialforschung und -prüfung

Dr. Michael Hofmann
Technische Universität München

Published online on the
Publication Server of the University of Potsdam:
<https://doi.org/10.25932/publishup-62197>
<https://nbn-resolving.org/urn:nbn:de:kobv:517-opus4-621972>

Additive manufacturing (AM) processes enable the production of metal structures with exceptional design freedom, of which laser powder bed fusion (PBF-LB) is one of the most common. In this process, a laser melts a bed of loose feedstock powder particles layer-by-layer to build a structure with the desired geometry. During fabrication, the repeated melting and rapid, directional solidification create large temperature gradients that generate large thermal stress. This thermal stress can itself lead to cracking or delamination during fabrication. More often, large residual stresses remain in the final part as a footprint of the thermal stress. This residual stress can cause premature distortion or even failure of the part in service. Hence, knowledge of the residual stress field is critical for both process optimization and structural integrity.

Diffraction-based techniques allow the non-destructive characterization of the residual stress fields. However, such methods require a good knowledge of the material of interest, as certain assumptions must be made to accurately determine residual stress. First, the measured lattice plane spacings must be converted to lattice strains with the knowledge of a strain-free material state. Second, the measured lattice strains must be related to the macroscopic stress using Hooke's law, which requires knowledge of the stiffness of the material. Since most crystal structures exhibit anisotropic material behavior, the elastic behavior is specific to each lattice plane of the single crystal. Thus, the use of individual lattice planes in monochromatic diffraction residual stress analysis requires knowledge of the lattice plane-specific elastic properties. In addition, knowledge of the microstructure of the material is required for a reliable assessment of residual stress.

This work presents a toolbox for reliable diffraction-based residual stress analysis. This is presented for a nickel-based superalloy produced by PBF-LB. First, this work reviews the existing literature in the field of residual stress analysis of laser-based AM using diffraction-based techniques. Second, the elastic and plastic anisotropy of the nickel-based superalloy Inconel 718 produced by PBF-LB is studied using *in situ* energy dispersive synchrotron X-ray and neutron diffraction techniques. These experiments are complemented by *ex situ* material characterization techniques. These methods establish the relationship between the microstructure and texture of the material and its elastic and plastic anisotropy. Finally, surface, sub-surface, and bulk residual stress are determined using a texture-based approach. Uncertainties of different methods for obtaining stress-free reference values are discussed.

The tensile behavior in the as-built condition is shown to be controlled by texture and cellular sub-grain structure, while in the heat-treated condition the precipitation of strengthening phases and grain morphology dictate the behavior. In fact, the results of this thesis show that the diffraction elastic constants depend on the underlying microstructure, including texture and grain morphology. For columnar microstructures in both as-built and heat-treated conditions, the diffraction elastic constants are best described by the Reuss iso-stress model. Furthermore, the low accumulation of intergranular strains during deformation demonstrates the robustness of using the 311 reflection for the diffraction-based residual stress analysis with columnar textured microstructures. The differences between texture-based and quasi-isotropic approaches for the residual stress analysis are shown to be insignificant in the observed case. However, the analysis of the sub-surface residual stress distributions show, that different scanning strategies result in a change in the orientation of the residual stress tensor. Furthermore, the location of the critical sub-surface tensile residual stress is related to the surface roughness and the microstructure. Finally, recommendations are given for the diffraction-based determination and evaluation of residual stress in textured additively manufactured alloys.

Kurzfassung

Additive Fertigungsverfahren (AM) ermöglichen die Herstellung von Metallstrukturen mit außergewöhnlicher Gestaltungsfreiheit, wobei das pulverbettbasierte Laserstrahlschmelzen (PBF-LB) eines der gängigsten dieser Verfahren darstellt. In diesem Verfahren schmilzt ein Laser ein Pulverbett schichtweise auf, um ein Bauteil mit der gewünschten Geometrie zu erzeugen. Während der Fertigung kommt es aufgrund des wiederholten Aufschmelzens und der schnellen, gerichteten Erstarrung zu hohen Temperaturgradienten, die hohe thermische Spannungen erzeugen. Einerseits können diese thermischen Spannungen während des Fertigungsprozesses zur Rissbildung oder zur Ablösung des Bauteils führen. Häufiger jedoch verbleiben große Eigenspannungen im gefertigten Bauteil als Folge der thermischen Spannungen. Diese Eigenspannungen begünstigen die Verzerrung der Bauteile und können sogar ihr vorzeitiges Versagen im Betrieb verursachen. Daher ist die Kenntnis der Eigenspannungsverteilung im Bauteil sowohl für die Prozessoptimierung als auch die strukturelle Integrität bedeutend.

Beugungsbasierte Verfahren ermöglichen die zerstörungsfreie Bestimmung des Eigenspannungsfeldes. Diese Verfahren erfordern jedoch eine vorhergehende Kenntnis der Materialeigenschaften, da gewisse Annahmen getroffen werden müssen, um die Eigenspannungen genau bestimmen zu können. Zunächst müssen aus den gemessenen Abständen der Gitterebenen Gitterdehnungen berechnet werden, wozu der dehnungsfreie Referenzzustand bekannt sein muss. Weiterhin müssen die Gitterdehnungen über das Hookesche Gesetz, unter Bezugnahme der elastischen Eigenschaften, in Spannungen überführt werden. Da die meisten Kristallstrukturen durch ein anisotropes Verhalten gekennzeichnet sind, ist ihr elastisches Verhalten für jede Gitterebene spezifisch. Deshalb bedarf es bei der Nutzung monochromatischer Strahlung zur beugungsbasierten Eigenspannungsbestimmung der Kenntnis der gitterebenspezifischen elastischen Eigenschaften. Zusätzlich ist das Wissen über die Mikrostruktur des Materials unabdingbar für eine zuverlässige Bestimmung der Eigenspannungen.

Die vorliegende Arbeit präsentiert eine Reihe von Bedingungen, die für eine zuverlässige beugungsbasierte Eigenspannungsanalyse notwendig sind. Dies wird exemplarisch an einer mittels PBF-LB gefertigten Nickelbasis Superlegierung gezeigt. Einleitend wird ein Überblick der Literatur im Bereich der beugungsbasierten Eigenspannungsanalyse mit Bezug zur additiven Fertigung gegeben. Anschließend wird die elastische und plastische Anisotropie der mittels PBF-LB gefertigten Nickelbasis Superlegierung Inconel 718 durch *in situ* energiedispersive Synchrotron Röntgen- und Neutronenbeugung charakterisiert. Diese Methoden werden durch *ex situ* Untersuchungsverfahren ergänzt. So wird die Beziehung zwischen der Mikrostruktur und der Textur zur elastischen und plastischen Anisotropie hergestellt. Abschließend werden die Oberflächen-, oberflächennahen-, sowie Volumeneigenspannungen in einem texturbasierten Ansatz bestimmt. Dabei werden Unsicherheiten verschiedener Methoden zur Bestimmung der spannungsfreien Referenz diskutiert.

Das mechanische Verhalten unter Zugbelastung des as-built Zustandes ist dabei durch die Textur und die zelluläre Substruktur bedingt, während es im wärmebehandelten Zustand vom Ausscheidungszustand und der geänderten Kornmorphologie bestimmt wird. Die Ergebnisse dieser Arbeit zeigen, dass die diffraktionselastischen Konstanten von der zugrundeliegenden Mikrostruktur abhängen. Für die kolumnaren Mikrostrukturen, egal ob im as-built oder wärmebehandeltem Zustand, werden die diffraktionselastischen Konstanten am besten durch die Reuss Annahme homogener Spannung beschrieben. Darüber hinaus zeigt die geringe Akkumulation intergranularer Dehnung des 311 Reflexes seine Robustheit für die

Kurzfassung

beugungsbasierte Eigenspannungsanalyse. Im vorhandenen Fall ist der Unterschied zwischen texturbasierten und quasiisotropen Ansätzen zur Eigenspannungsanalyse unbedeutend. Oberflächennahe Eigenspannungsanalysen zeigen jedoch, dass verschiedene Scanstrategien zu einer Änderung in der Ausrichtung des Eigenspannungstensors führen. Weiterhin zeigt die Lage der kritischen oberflächennahen Zugeigenspannungen eine Abhängigkeit zur Oberflächenrauheit und dem Gefüge. Abschließend werden Empfehlungen zur beugungsbasierten Ermittlung und Bewertung von Eigenspannungen in texturierten additiv gefertigten Legierungen gegeben.

Acknowledgements

When I started studying materials science in 2014, I never thought that I would ever write the acknowledgements section of my dissertation. In this regard, I must thank the Bundesanstalt für Materialforschung und -prüfung for this opportunity. I would like to especially thank my supervisors Prof. Dr. Giovanni Bruno and Dr. Alexander Evans, who have paved the way for this project. I am also very grateful for their endless support in the form of scientific discussions and reviews of my work. Overall, the open-minded and interdisciplinary atmosphere in division 8.5 has helped my scientific ideas to flourish, and I would like to thank each member of 8.5 for their support. Especially the (scientific) discussions with my office partner Thanos and during the countless coffee breaks with Tatiana and Itziar have to be mentioned. I would also like to thank Tobi, Alex, Shahab, Maximilian, Bruno, and Keerthana for their help and support. On the organizational side, Bianca and Bernd have been a huge help in overcoming obstacles and have been a huge time saver on many occasions. In addition, I am grateful for the fruitful collaborations and discussions with Gunther Mohr, Juan Simón Muzás (9.6), Arne Kromm (9.4), Luis Avila (5.2), and Romeo Saliwan-Neumann (5.1).

From our partner institution, the research reactor FRM II in Munich, I would like to thank Dr. Michael Hofmann for his role as mentor and Prof. Dr. Winfried Petry for his role as second supervisor of this project. Although not a single experiment could be carried out as originally planned, they were of great help in finding alternative solutions without compromise. Special thanks also go to Dr. Weimin Gan, Dr. Michael Hofmann, Dr. Alexander Heldmann, and Dr. Markus Hölzel for performing the *in situ* tensile test at DESY. For the sample preparation, I would like to thank my uncle, Dirk Steinhagen, for his extraordinary expertise and his help at short notice and my aunt Andrea Steinhagen for the food supply during the long day. Thanks to the international collaboration a significant part of the experiments required for this work could be carried out at neutron and synchrotron facilities around the world. I would like to specifically thank all the beamline scientists at DESY's P61A beamline (Dr. Guilherme Abreu Faria, Sebastian Degener, Dr. Gleb Dovzhenko), at SINQ's POLDI beamline (Dr. Efthymios Polatidis, Dr. Jan Čapek), at ANSTO's KOWARI (Dr. Vladimir Luzin), and at BESSY II's EDDI beamline (Dr. Manuela Klaus, Prof. Dr. Christoph Genzel) for their dedicated efforts in the preparation, the execution, and the data analysis of the experiments. Furthermore, I want to acknowledge Dr. Daniel Apel for his support in data analysis and Dr. Matthias Meixner for performing surface X-ray diffraction measurements.

I want to express my gratitude to Dr. Judith Schneider for her guidance in the early stages of the project, especially during the first publication process I went through. I benefited greatly from her experience with both nickel-based superalloys and additive manufacturing processes.

Thanks also to Prof. Dr. Thomas Niendorf, who didn't hesitate to take on the role of the third examiner of this work.

I also want to express my gratitude to my parents and my entire family, as they have been a huge emotional anchor throughout my life. I do not take it for granted that my parents have made this educational path possible for me and supported me in all my decisions. Last but not least, I must thank my better half for her immense emotional and substantive support. The visualizations in this dissertation benefited immensely from her neutral point of view during several iterations.

If you have made it to the end of this page and feel forgotten, rest assured: You were a significant help, just one that slipped through my residual stress-filled memory.

Overview of Publications and Related Works

Publications in peer-reviewed journals as first author:

- **J. Schröder**, T. Mishurova, T. Fritsch, I. Serrano-Munoz, A. Evans, M. Sprengel, M. Klaus, C. Genzel, J. Schneider, and Giovanni Bruno. “*On the influence of heat treatment on microstructure and mechanical behavior of laser powder bed fused Inconel 718*”. *Materials Science and Engineering: A*, Vol. 805, 2021, 140555.
DOI: 10.1016/j.msea.2020.140555

My contribution: *EBSD data analysis (100 %)*
Ex situ and in situ tensile test data analysis (80 %)
Conceptualization (70 %)
Formal analysis (75 %)
Visualization (100 %)
Writing, editing, and reviewing the original draft (85 %)

- **J. Schröder**, A. Evans, T. Mishurova, A. Ulbricht, M. Sprengel, I. Serrano-Munoz, T. Fritsch, A. Kromm, T. Kannengießer, G. Bruno. “*Diffraction-Based Residual Stress Characterization in Laser Additive Manufacturing of Metals*”. *Metals* **2021**, 11(11), 1830.
DOI: 10.3390/met11111830

My contribution: *Conceptualization (85 %)*
Methodology (70 %)
Validation (65 %)
Investigation (literature review) (100 %)
Writing, editing, and reviewing original draft (80 %)
Visualization (100 %)

- **J. Schröder**, A. Evans, E. Polatidis, J. Čapek, G. Mohr, I. Serrano-Munoz, and G. Bruno. “*Understanding the impact of texture on the micromechanical anisotropy of laser powder bed fused Inconel 718*”. *Journal of Materials Science* **57**, 15036-15058 (2022).
DOI: 10.1007/s10853-022-07499-9

My contribution: *Conceptualization (85 %)*
Data curation (90 %)
Formal analysis (70 %)
Investigation (50 %)
Methodology (70 %)
Supervision (80 %)
Writing, editing, and reviewing original draft (90 %)

Overview of Publications and Related Works

- **J. Schröder**, A. Evans, V. Luzin, G. Abreu Faria, S. Degener, E. Polatidis, J. Čapek, A. Kromm, G. Dovzhenko, and G. Bruno. “*Texture-based residual stress analysis of laser powder bed fused Inconel 718 parts*”. Minor revisions resubmitted to Journal of Applied Crystallography (2023)

My contribution: *EBSD data analysis (100 %)*
Conceptualization (80 %)
Performing diffraction measurements (75 %)
Visualization (100 %)
Writing, editing, and reviewing original draft (90 %)

Presentations, Posters, and other Publications:

- **J. Schröder**, T. Mishurova, T. Fritsch, I. Serrano-Munoz, A. Evans, M. Sprengel, M. Klaus, C. Genzel, J. Schneider, and Giovanni Bruno. “*On the influence of heat treatment on microstructure and mechanical behavior of laser powder bed fused Inconel 718*”. EUROMAT 2021 (European Congress and Exhibition on Advanced Materials and Processes). September 14th, 2021. Online presentation.

My contribution: *Preparing and giving presentation (100 %)*

- **J. Schröder**, T. Mishurova, T. Fritsch, I. Serrano-Munoz, A. Evans, M. Sprengel, M. Klaus, C. Genzel, J. Schneider, and Giovanni Bruno. “*The heat treatment of L-PBF Inconel 718: A manifold problem*”. EURO Superalloys 2022. September 19th, 2022. Oral Poster contribution (Bamberg, Germany).

My contribution: *Preparing and giving poster presentation (100 %)*

- **J. Schröder**, A. Evans, E. Polatidis, J. Čapek, G. Mohr, I. Serrano-Munoz, and G. Bruno. “*Texture Dependent Micromechanical Anisotropy of Laser Powder Bed Fused Inconel 718*”. ICAM 2022 (International Conference on Additive Manufacturing). October 31st, 2022. Presentation (Orlando, U.S.A).

My contribution: *Preparing and giving presentation (100 %)*

- **J. Schröder**, A. Evans, E. Polatidis, J. Čapek, G. Mohr, I. Serrano-Munoz, A. Kromm, V. Luzin, and G. Bruno. “*Fundamentals of diffraction-based residual stress and texture analysis of laser powder bed fused Inconel 718*”. FRM II User Meeting 2022. December 08th, 2022. Presentation (Munich, Germany).

My contribution: *Preparing and giving presentation (100 %)*

- C.-H. Yu, Maximilian Sprengel, **J. Schröder**, I. Serrano-Munoz, G. Mohr, A. Evans, A. Kromm, R. L. Peng, T. Kannengießer, G. Bruno, and J. Moverare. “*Distribution of subsurface residual stress as a function of wall thickness in stainless steel 316L LPBF structures*”. The 11th International Conference on Residual Stress. March 29th, 2022. Conference publication & poster contribution (Nancy, France).

My contribution: *Performing residual stress measurements (30 %)*
Visualization of the residual stress data (20 %)

List of Abbreviations

Abbreviation	Explanation
Al	Aluminum
Al ₂ O ₃	Aluminum Oxide
AM	Additive Manufacturing
AMS	Aerospace Material Specifications
ASTM	American Society for Testing and Materials
BD	Building Direction
BSE	Backscattered Electrons
DA	Direct Age
DECs	Diffraction Elastic Constants
DED	Direct Energy Deposition
DIN	Deutsches Institut für Normung
DMLS	Direct Metal Laser Sintering
EBSD	Electron Backscatter Diffraction
EDS	Energy Dispersive Spectroscopy
ED-XRD	Energy Dispersive X-Ray Diffraction
FCC	Face Centered Cubic
FHT	Full Heat Treatment
HCP	Hexagonal Close Packed
HIP	Hot Isostatic Pressing
HOMO	Homogenization
HP	Hall-Petch
ILT	Interlayer Time
IS	Internal Stress
ISO	International Standardization Organization
LMD	Laser Metal Deposition
L-PBF / LPBF / PBF-LB*	Laser Powder Bed Fusion
*Terminology changed over time. To be understood as synonyms within this work	
m.r.d.	Multiples of a Random Distribution
MC	Metallic Carbide

List of Abbreviations

Abbreviation	Explanation
Mo	Molybdenum
Nb	Niobium
NbC	Niobium Carbide
ND	Neutron Diffraction
Ni	Nickel
PH	Precipitation Hardening
PM	Powder Metallurgy
Q	Rapid Quench
RP	Raw Powder
RS	Residual Stress
SAE	Society of Automotive Engineers
SC	Slow Cooling
SCEC	Single-crystal elastic Constants
SEM	Scanning Electron Microscope
SH	Strain Hardening
SLS	Selective Laser Sintering
SP	Sample Filings
SR	Stress relief
SSS	Solid Solution Strengthening
ST	Solutionizing
TGM	Temperature-Gradient-Mechanism
Ti	Titanium
TOF	Time-of-Flight
TTT	Time-Temperature-Transformation
UTS	Ultimate Tensile Strength
XRD	X-Ray Diffraction
YS	Yield Strength

Nomenclature

Symbol	Unit	Description
A	%	Elongation to Failure
A^Z	[]	Zener Anisotropy Ratio
A^L	[]	Universal Anisotropy Ratio
b	nm	Magnitude of Burger's Vector
d	μm	Average Grain Diameter
d_0^{hkl}	\AA	Stress-Free Reference Lattice Spacing of Reflection hkl
D_{50}	μm	Particle Diameter Class of 50%
d^{hkl} or d_{hkl}	\AA	Lattice Spacing of Reflection hkl
E^{hkl}	GPa	Young's modulus of reflection hkl
E_{laser}	W mm^{-3}	Volumetric Energy Density
E^{M}	GPa	Macroscopic Young's modulus
G	GPa	Shear Modulus
h	mm	Hatch Spacing
I	cts.	Observed Diffraction Intensity
M	[]	Taylor Factor
n	[]	Work Hardening Rate
P	W	Laser Power
\vec{q}	[]	Diffraction Vector
q	[]	Contraction Ratio
Q	\AA^{-1}	Absolute Value of Diffraction Vector
t	mm	Layer Thickness
v	mm s^{-1}	Laser Speed or Scanning Velocity

Nomenclature

Greek Symbols		
Symbol	Unit	Description
γ		Face Centered Cubic Supersaturated Solid Solution
γ'		$\text{Ni}_3(\text{Al, Ti})$ $L1_2$ Cubic Crystal Structure
γ''		Ni_3Nb $D0_{22}$ Metastable Tetragonal Crystal Structure
ρ		Dislocation Density
δ		Ni_3Nb $D0_a$ Stable Orthorhombic Crystal Structure
σ_{YS}	MPa	0.2% Yield Strength
σ_{UTS}	MPa	Ultimate Tensile Strength
σ_{T}	MPa	True Stress
ϵ_{T}	[-]	True Strain
ϵ^{hkl}	[-]	Lattice Strain of Reflection hkl
θ	[°]	Diffraction Angle
σ_0	MPa	Friction Stress
φ	[°]	Azimuthal Angle
χ	[°]	Tilt Angle
Ψ	[°]	Polar Angle
η	[°]	Sample Rotation Around Diffraction Vector
τ	μm	Information Depth
τ_0	μm	Information Depth at $\Psi = 0^\circ$
Γ_{hkl}	[-]	Anisotropy Factor

Table of Contents

Abstract		III
Kurzfassung		IV
Acknowledgements		VI
Overview of Publications and Related Works		VII
List of Abbreviations		IX
Nomenclature		XI
Table of Contents		XIII
I	Introduction	1
	1 Additive Manufacturing: Opportunities and Challenges	1
	2 Laser Powder Bed Fusion of Nickel-Based Superalloys	2
	3 Process Parameter Overview	4
	4 Residual Stress Formation	5
	5 Microstructure & Texture Development	6
	6 Mechanical Performance	7
	7 Diffraction-Based Determination of Residual Stress	8
II	Aims of this Work	9
III	Publications	11
P1	Diffraction-Based Residual Stress Characterization in Laser Additive Manufacturing	11
	0 Preface	11
	1 Introduction	12
	2 Laser-Based AM Processes	14
	2.1 Laser Powder Bed Fusion	14
	2.2 Laser Metal Deposition	14
	3 Definition of Residual Stress	15
	4 Residual Stress with Respect to Laser-Based AM	16
	4.1 Origin of Residual Stress	16
	4.2 Distribution of Residual Stress	17
	5 Determination of Residual Stress with Diffraction-Based Methods	17
	5.1 General Aspects of Diffraction-Based Methods	18
	5.2 X-ray Diffraction	19
	5.2.1 The Monochromatic Case for Surface Analysis	19
	5.2.2 The Energy Dispersive Case	20
	5.3 Neutron Diffraction	21
	5.3.1 The Monochromatic Method	22

Table of Contents

	5.3.2 The Time-of-Flight Method	23
6	Peculiarities of Diffraction-Based Methods in the Case of AM	23
	6.1 Strain-Free Lattice Spacing (d_0^{hkl})	23
	6.1.1 Use of Raw Powder	24
	6.1.2 Use of Mechanical Filings	25
	6.1.3 Use of Macroscopically Relaxed Samples	25
	6.1.4 Stress and Moment Balance	26
	6.2 Principal Stress Directions	27
	6.3 Diffraction Elastic Constants	28
	6.3.1 The Anisotropy of Single Crystals	29
	6.3.2 Grain Interaction Models for the Calculation of DECs	30
	6.3.3 Experimental Determination of DECs	30
	6.4 Choice of the Appropriate Lattice Planes	33
7	Summary & Outlook	37
8	References	38
P2	On the influence of heat treatment on microstructure and Mechanical behavior of Laser Powder Bed fused Inconel 718	47
0	Preface	47
1	Background	48
2	Experimental procedure	50
	2.1 Sample fabrication	50
	2.2 Heat treatment schedule	50
	2.3 Ex-situ mechanical testing	50
	2.4 In-situ mechanical testing	51
	2.5 Metallographic preparation	51
	2.6 Phase analysis	51
	2.7 X-ray computed tomography	51
3	Results	51
	3.1 Phase analysis	51
	3.2 Microstructure	51
	3.3 Porosity content	52
	3.4 Ex-situ tensile testing	52
	3.5 In-situ tensile testing	53
4	Discussion	55
	4.1 Macro mechanical behavior	55
	4.1.1 Porosity and surface roughness	55
	4.1.2 Hall-Petch relationship	56
	4.1.3 Strain hardening	56

Table of Contents

	4.1.4	Precipitations	57
	4.1.5	Texture influence	57
	4.2	Micro-mechanical properties	58
	4.2.1	Lattice strain evolution	58
	4.2.2	Splitting of diffraction peaks	58
	4.2.3	Diffraction elastic constants	58
5		Conclusions	59
6		Appendix	60
7		References	60
P3		Understanding the impact of texture on the micromechanical anisotropy of laser powder bed fused Inconel 718	63
0		Preface	63
1		Introduction	65
2		Materials and methods	66
	2.1	Sample fabrication	66
	2.2	Microstructural analysis	67
	2.3	X-ray diffraction	68
	2.4	<i>Ex situ</i> mechanical testing	68
	2.5	<i>In situ</i> mechanical testing	68
3		Results	69
	3.1	Microstructure and texture	69
	3.2	X-ray diffraction	70
	3.3	<i>Ex situ</i> tensile testing	72
	3.4	<i>In situ</i> tensile testing	72
	3.4.1	Diffraction peaks	73
	3.4.2	Lattice strain evolution during deformation	73
	3.4.3	Lattice micro residual strain accumulation	74
4		Discussion	75
	4.1	Microstructure and texture	75
	4.2	Precipitation of primary and secondary phases	75
	4.3	Macromechanical behavior	76
	4.3	Micromechanical behavior	77
	4.3.1	Elastic behavior	77
	4.3.2	Plastic behavior	78
	4.3.3	Accumulation of residual strain	78
	4.4	Origin of the diffraction peak asymmetry	79
	4.4.1	Role of cell walls on deformation mechanisms	79
5		Conclusions	81

Table of Contents

6	References	82
S	Supplementary Information	87
M4	Texture-based residual stress analysis of laser powder bed fused Inconel 718 prisms	93
0	Preface	93
1	Introduction	94
2	Material and methods	95
2.1	Sample manufacturing	95
2.2	Microstructural analysis	96
2.2.1	Electron backscattered diffraction (EBSD)	96
2.2.2	Neutron diffraction texture measurements	96
2.3	Texture-based residual stress analysis	96
2.3.1	Laboratory X-ray diffraction	96
2.3.2	Electrolytic layer removal	97
2.3.3	Synchrotron X-ray diffraction	97
2.3.4	Time-of-flight neutron diffraction	97
2.3.5	Monochromatic neutron diffraction stress analysis	98
3	Results	98
3.1	Microstructure & texture	98
3.2	Stress factors	99
3.3	X-ray diffraction: surface and sub-surface residual stress	99
3.3.1	Prior to removal from the baseplate	99
3.3.2	Post removal from the baseplate	99
3.3.3	Determination of sub-surface principal stress	100
3.3.4	Layer removal	101
3.4	Neutron diffraction: Bulk residual stress	101
3.4.1	The stress-free reference d_0^{311}	101
3.4.2	Stress mapping	102
4	Discussion	103
4.1	Influence of preferred grain orientation	103
4.2	The scanning strategy determines the residual stress distribution	104
4.3	Residual stress redistribution upon removal from baseplate	104
4.4	On the choice of the stress-free reference	104
4.5	Trough thickness stress distribution	105
5	Conclusions	106
6	Appendix	107
7	References	107
S	Supplementary information	109

Table of Contents

IV	Discussion	112
1	Deformation Behavior	112
1.1	Macroscopic Behavior	112
1.2	Microscopic Behavior	113
2	Towards a Reliable Assessment of Residual Stress	114
2.1	Selection of a Suitable Lattice Plane	114
2.2	Stress-Free Reference	115
2.3	Diffraction Elastic Constants	115
2.4	Unique Aspects of RS Distribution	117
V	Summary & Outlook	120
1	Summary	120
2	Outlook	122
VI	Appendix	124
A	Determination of Single-Crystal Elastic Constants From Diffraction Experiments	124
VII	References	130

1 Additive Manufacturing: Opportunities and Challenges

The general term additive manufacturing (also referred to as 3D-printing) covers processes that can realize complex component geometries by layer wise production in a single manufacturing step [1]. Additive manufacturing technologies first emerged in the 1970s, but only were taken into serious consideration in the industrial context within the last decade [2]. These manufacturing processes are capable to handle different materials such as polymers, ceramics, and metals [3]. Even further, composites of these materials can be realized (see e.g. [4]). However, as physical properties (e.g. melting point, thermal conductivity) of materials differ, tailored processes are required for their production. Thus, various processes have been developed since the first emergence of additive manufacturing. In regard to additive manufacturing of metallic alloys, such methods are first differentiated by their underlying manufacturing approach; in general, techniques which involve melting of feedstock materials such as powder-bed based, or direct energy deposition techniques are distinguished. More specifically, further subcategories are defined by the used energy source, which can be for instance a laser beam, an electron beam, or a wire-arc. Moreover, each of these processes require specific manufacturing environments (e.g. inert atmosphere, shielding gas, or pre-heating).

In this work, the emphasis lies on one of the most common additive manufacturing processes: the laser powder bed fusion process. In such process, a laser selectively melts powder layer-wise to build up a part [5]. This is realized by feeding powder layers of specific thickness from a feedstock to the build platform [5]. The whole system is contained in inert gas atmosphere (typically argon) to prevent oxidation during production [5]. Furthermore, a continuous inert gas flow is maintained over the powder-bed to limit the redeposition of by-products (i.e. spatter) on the powder bed and the laser attenuation induced by such by-products in the laser path [5, 6].

Alike all other additive manufacturing techniques laser powder bed fusion benefits from the previously mentioned geometrical freedom in design. Although such process enables the production of almost dense (i.e. with low amount of porosity) and dimensionally accurate parts, it suffers from the inherent part's surface roughness [7]. In that regard, recent developments of the technique improved the surface quality of the builds [7]. Although subtractive techniques can still provide much better surface finishes, they suffer from larger material waste. The build envelope (i.e. the volume of the build chamber) governs a further constraint as it limits the build volume. Therefore, the manufacturing must take place in small batches, which is inefficient for largescale production.

Besides these hindrances, the inherent localized melting and solidification of the process pose serious challenges to the process. Inevitable large internal stress (i.e., thermal stress) builds up during part manufacturing [8]. In some occasions this internal stress might lead to failure by cracking or delamination during processing [8]. In the best cases, residual stress remains as a footprint of the internal stress after production [8]. This residual stress may result in undesired distortion upon part removal from baseplate or premature in-service part failure [8, 9]. Therefore, it is crucial from both manufacturing and "lifing" perspective to characterize the residual stress distribution in the as-built structures or components. Another consequence of the localized melting and directional solidification is the typical formation of columnar grains featured by crystallographic texture [10]. All these factors may require sophisticated post processing treatments (e.g. heat treatments), if they are not accounted for in part design. These peculiarities not only

I Introduction

complicate the design of the processing routes, but also pose metrological challenges for the characterization of residual stress by means of diffraction-based techniques [11]. Such aspects are introduced on the following pages in regard of the microstructure, texture, and mechanical performance.

2 Laser Powder Bed Fusion of Nickel-Based Superalloys

Subject of this study is the nickel-based superalloy Inconel 718. In general, such alloy family is used in harsh temperature environments in oil and gas, aviation, or aerospace industry, especially in turbine engine applications [12]. All these sectors have in common the fact that materials must withstand extreme temperature conditions while experiencing mechanical load in-service [12]. The limited geometrical freedom in the design of parts produced by conventional methods impedes the direct incorporation of inner cooling channels or weight-saving constructions. Therefore, sophisticated post-manufacturing machining is inevitable for parts manufactured by conventional processes. In that regard, additive manufacturing techniques such as laser powder bed fusion become handy: the immense geometrical freedom offers flexibility in the design and could solve the some of the problems mentioned above. However, laser powder bed fusion relies on the weldability of the metallic material to process a component.

In essence, the propensity of nickel-based alloys to form intermetallic precipitates limits their weldability. In this regard, the Al and Ti content classifies the weldability of such alloy class, as those favor the precipitation of intermetallic $Ni_3(Al, Ti)$ precipitates [12]. In simple words, the faster precipitation kinetics are in alloys containing more Ti and Al, the more susceptible the alloy is to hot cracking during welding [12]. As a result, an alloy is considered non-weldable if the Al + Ti content exceeds 4 wt.% [13]. A more generalized approach considers the content of the solid solution stabilizers Cr and Co alongside the Al + Ti content for the classification of the weldability [14]. Figure 1 summarizes the weldability of most common nickel-based superalloys. Although Inconel 718, a Ni-Cr-Fe based alloy, with additions of Al, Ti, Mo, and Nb forms so-called intermetallic γ' and γ'' precipitates upon aging, it remains readily weldable, while achieving excellent mechanical properties [15, 16].

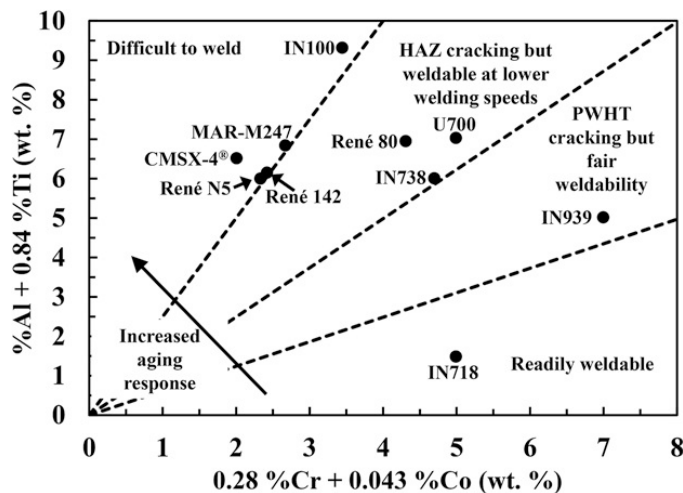


Figure 1: Modified weldability assessment chart after considering the effects of the content of γ -phase stabilizers Cr and Co vs. the γ' -phase stabilizers Al and Ti for different nickel-based alloys. With an increasing aging response (i.e., increasing Al + Ti content and simultaneously decreasing Cr + Co content), the weldability decreases. Representation after [14]. Figure reproduced from [17] with permission from John Wiley and Sons.

I Introduction

On the one hand, the sluggish precipitation kinetics of the main strengthening tetragonal γ'' (Ni_3Nb , D0_{22} crystal structure) benefits the weldability [15]. The mechanical performance further increases thanks to the low amounts of γ' precipitates ($\text{Ni}_3(\text{Al}, \text{Ti})$, ordered cubic, L1_2) [18]. On the other hand, the coarsening, and the transformation of the desired metastable γ'' precipitates to undesired δ (orthorhombic, D0_a crystal structure) beyond 650-700 °C precludes the application of Inconel 718 at higher temperatures [18]. The necessity to add minor elements to produce high-performance nickel-based superalloys governs another critical aspect, as they are essential for grain boundary “pinning” [19]. For example, a low content of hafnium contributes to grain refinement, retards grain growth, and promotes the formation of MC carbides [20]. However, the addition of such minor elements (e.g., boron) is known to negatively affect the weldability of Inconel 718: their presence alters the liquid wettability on grain boundaries, lowers the solidification range, and they segregate at grain boundaries [21]. Hence, the manufacturability of nickel-based superalloys, as presented in Figure 2, depends on both their propensity to form $\text{Ni}_3(\text{Al}, \text{Ti})$ precipitates and the containment of minor elements. In fact, the minor elements tend to have extremely detrimental effects on the manufacturability of nickel-based alloys by means of laser powder bed fusion, as they significantly increase the tendency of solidification cracking [22]. In contrast, higher γ' -containing alloys are manufacturable, as long the content of minor elements remains on a low level [22].

The selection of Inconel 718 for this study is, therefore, driven by its excellent manufacturability by means of laser powder bed fusion. In addition, open literature provides many studies regarding residual stress analysis of laser powder bed fusion by means of diffraction-based techniques. Nevertheless, additive manufacturing poses serious metrological challenges to the diffraction-based residual stress determination [11]. This work aims to identify and fill these existing challenges for the nickel-based superalloy Inconel 718 produced by laser powder bed fusion.

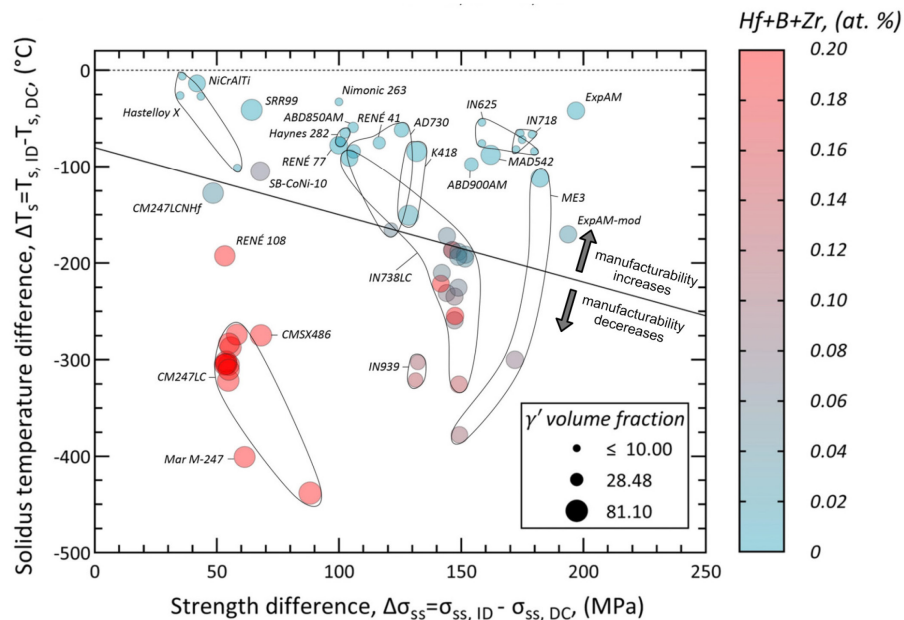


Figure 2: The manufacturability of common nickel-based superalloys by means of laser powder bed fusion, classified according to their susceptibility to cracking. This susceptibility is expressed as the thermal resistance (y-axis) as a function of the deformation resistance (x-axis). The size of the marks indicates the volume fraction γ' from thermodynamic calculations at 800 °C. In addition, the marks are colored by the included sum of Hf + B + Zr, according to the color bar shown. Ni-based alloys resistant to cracking during laser powder bed fusion appear at high deformation and thermal resistances, respectively. Adapted from [22] under the open access CC-BY 4.0 license (<https://creativecommons.org/licenses/by/4.0/>).

I Introduction

3 Process Parameter Overview

The process parameters are of paramount importance for both, the build quality, and the residual stress formation [23]. Therefore, a considerable amount of literature related to PBF-LB has focused on optimizing the different process parameters by studying their influence on microstructure, texture, and defect formation [23]. In laser powder bed fusion systems, more than a hundred parameters are empirically derived to produce dense parts with acceptable material properties [24]. The general parameter sets developed for each material are designed to satisfy as many priorities and build geometries as possible [24]. Thus, significant opportunities remain in optimizing process parameters with respect to specific geometries and applications [24]. In this context, the main process parameters considered are the *laser power*, the *layer thickness*, the *hatch distance*, the *laser scanning velocity*, and the *scanning strategy*. A short description of these main process parameters is given in the following (Figure 3a):

1. *Laser power*: The main parameter controlling the energy transfer from the PBF-LB system into the powder-bed [23]. The photons are absorbed by the powder-bed and are converted into heat that dissipates through conduction [24]. In that context, the material only melts if the energy introduced is higher than the dissipated energy [24].
2. *Layer thickness*: Defines the height of each successively added powder layer. [23]
3. *Hatch distance*: The space between adjacent paths of the laser beam, which determines the overlap of neighboring tracks. [23]
4. *Laser scanning velocity*: Describes the speed at which the beam travels through the surface of the powder bed. [23]
5. *Scanning strategy*: Defines the path of the laser through the surface of the powder bed within the layer and the related rotation between layers (i.e. the inter layer rotation). [23]

In general, a range of these key process parameters allows the production of fully dense parts [24]. Within this window, further optimization of the process parameters allows the microstructure and texture to be tailored to specific requirements. For example, the scanning strategy provides an elegant tool to control the crystallographic texture of the manufactured part in relation to its geometry [23]. Some of the possible scanning strategies are shown in Figure 3b and c. It should be noted that other process parameters, such as *baseplate preheating* and *interlayer time*, affect the residual stress formation because they influence thermal gradients. The latter parameter describes the time interval between subsequent energy inputs to a single volume element from layer to layer [25].

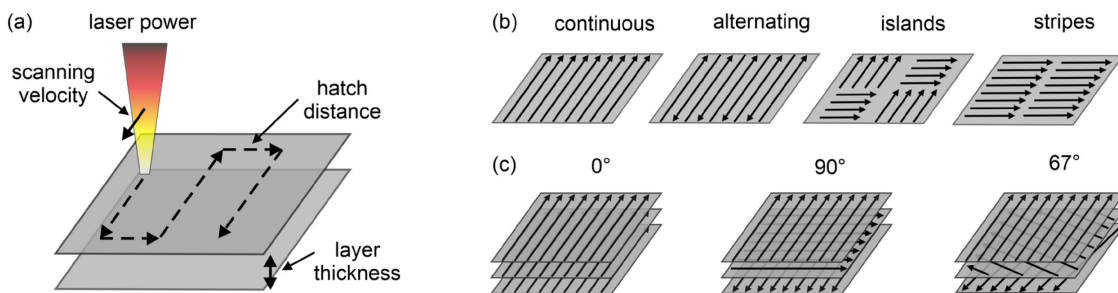


Figure 3: Main process parameters adapted from [24] under the open access CC-BY 4.0 license (<https://creativecommons.org/licenses/by/4.0/>) (a) and various possible scanning strategies (b). Examples of some inter layer rotations for a continuous scanning strategy are shown in (c).

4 Residual Stress Formation

As a general term, residual stress is defined as a stress present in a part without the application of external loads, moments, or thermal gradients [26]. As usual, residual stress is classified into three different kinds: those referred to as type I, balancing over larger distances (part level), type II, varying over a few grains (grain level), and type III only acting within a grain at atomic scale [27]. For engineering applications, the type I residual stress is the main concern [9]. Often, this type of residual stress results in significant part deformations [9]. In laser powder bed fusion, two separate mechanism account for the formation of type I residual stress:

1. The Temperature-Gradient-Mechanism

The temperature-gradient-mechanism, with respect to additive manufacturing, was first mentioned by Kruth et al. [8] in 2004. The rapid, local heating of the uppermost layer by the laser beam in conjunction with the rather slow cooling results in a steep temperature gradient. In that regard, the underlying material restricts the expansion of the heated top layer. In consequence, the top layer is subjected to plastic compression upon surpassing the material's yield limit. In absence of a mechanical constraint, the part would experience a bending opposite to the laser beam (Figure 4a). Upon cooling of the plastically compressed upper layers shrink and a bending angle towards the laser beam is introduced (Figure 4b). [8, 9]

2. The Thermal Contraction Upon Cooling

While the temperature-gradient-mechanism controls the thermal stress evolution during manufacturing, the thermal contraction upon part cooling conditions the residual stress distribution in the final part [28]. As the underlying layer inhibits the free contraction of the added top layer, the development of tensile stress is the consequence in the top layer. Compressive stress in the material below balances the tensile stresses at the surface. [8, 9]

Due to the layer wise nature of the laser powder bed fusion process, these two mechanisms repeat in cycles. Indeed, the main heat dissipation must appear through the substrate plate, whereas the thermal history becomes decisive for the development of the residual stress field [29]. Therefore, the residual stress after manufacturing is linked to the process parameters (e.g. laser power, scanning strategy) and the building height in an inherent manner [9].

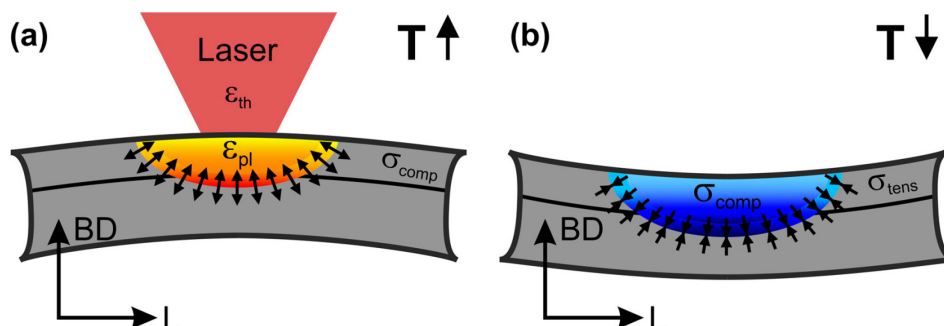


Figure 4: The formation of residual stress during the laser powder bed fusion process. (a) The temperature gradient mechanism acting upon heating, and (b) upon cooling. Reproduced from [30] under the open access CC-BY 4.0 license (<https://creativecommons.org/licenses/by/4.0/>).

I Introduction

5 Microstructure & Texture Development

Besides the residual stress formation, the large temperature gradients during production lead to the formation of characteristic microstructures and textures: In fact, the large temperature gradients may induce the epitaxial (i.e. columnar) grain growth in such parts. On a smaller length scale, one observes cellular solidification based on local segregation [31, 32] (or precipitation). In the context of laser powder bed fusion of Inconel 718, the local segregation of Nb on the one hand corroborates the formation of γ'' during manufacturing (Figure 5a) [33]. On the other hand, the local segregation of Nb also increases the formation risk of undesired δ or Laves phases (see [31, 32]). Further, the various options in process parameter control impede the generalization of the propensity to precipitate phases during manufacturing.

The FCC crystals (i.e. the γ -phase in Inconel 718) have the propensity to grow in their $\langle 100 \rangle$ directions aligned with the direction of largest heat flow [34]. Therefore, the local orientation and size of cells depends on the heat flow direction [32]. The latter relates to the process parameters, such as the scanning strategy or the laser beam parameters. For example, by the introduction of a 90° interlayer rotation (i.e. relative rotation of the alternating scan vectors between successive layers), the texture changes from $[110]$ -type along the build direction to $[100]$ -type (Figure 5b and c). As the laser beam parameters (e.g. laser power) control the melt pool shape, such parameter set also contributes to local changes in the heat flow [35]. Therefore, the process parameter control allows to tailor the grain morphology and the crystallographic texture (see [35]). Even further, the microstructure and crystallographic texture determine the mechanical performance of the component [36]. The next paragraph expands on this link between microstructure and texture to the mechanical performance.

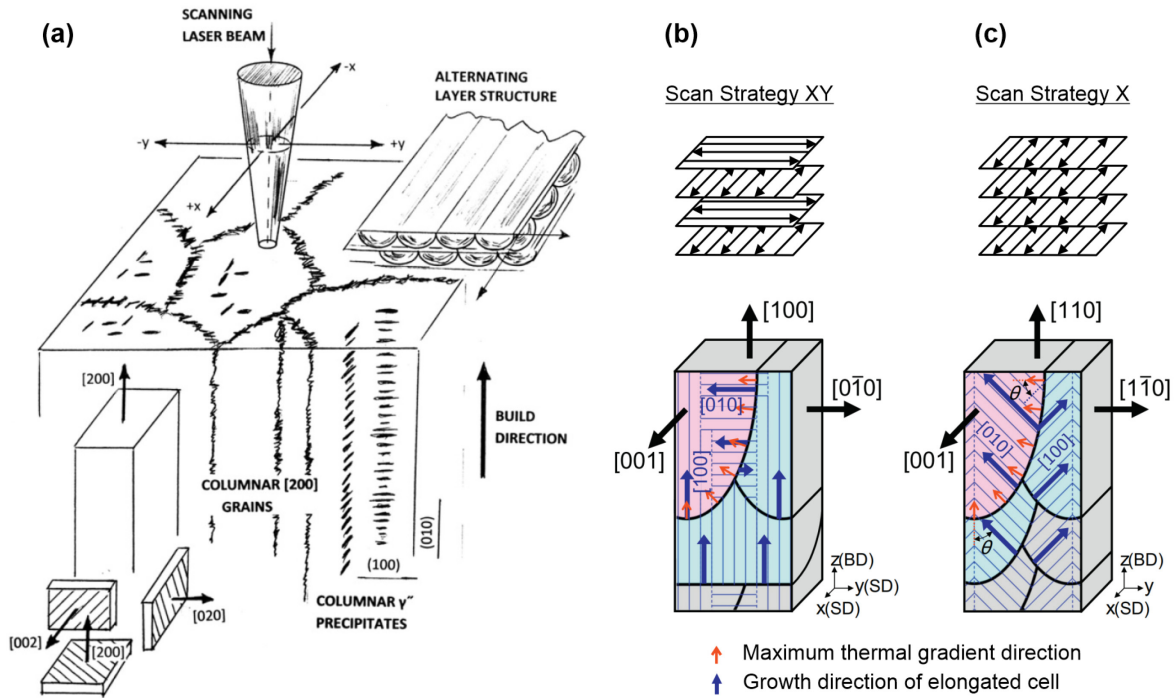


Figure 5: Schematic views illustrating the directional solidification-induced columnar grains (reprinted from [33] with permission from Elsevier) (a). Schematics of the mechanism for the texture evolution for (b) Scan Strategy XY and (c) Scan Strategy X (adapted from [37] under the open access CC-BY 4.0 license (<https://creativecommons.org/licenses/by/4.0/>)).

6 Mechanical Performance

The influence of the as-built microstructure on the mechanical performance are manifold and depend on the manufacturing parameters. In fact, the direct correlation of the microstructure and texture with the mechanical behavior derives from the single crystal properties: Each crystal structure is on the one hand characterized by so-called single-crystal elastic constants, which quantify their elastic stiffness [38]. On the other hand, slip or twinning events realize plastic deformation (Figure 6a). While slip refers to sliding of a certain crystal plane along a specific direction, twinning is characterized by local uniform shearing of a certain region of a crystal [36]. Slip can be quantified by the Schmid's law [39], which states that when the resolved shear stress acting along the slip direction on the slip plane reaches a critical value (i.e. the critical resolved shear stress τ_c) slip occurs (Figure 6b). It becomes evident that in a polycrystalline aggregate the microstructure and texture (i.e. the arrangement of single crystals) define the deformation behavior [36].

In as-built (i.e. non heat treated) laser powder bed fused Inconel 718, the columnar grain structure, accompanied by crystallographic texture, often results in an anisotropy of the mechanical properties [31, 40, 41]. However, for the optimization of the mechanical performance of Inconel 718 precipitation heat treatments are required [18]. The thermal history of the laser powder bed fusion process significantly deviates from conventional processes (e.g. casting). In fact, besides the precipitation of the desired γ'' and γ' phases one necessity is the previous homogenization of the material to avoid local precipitation from the segregated regions [42]. Such homogenization treatments need to be conducted above the solvus temperature of undesired precipitates, i.e. at temperatures close to the melting point [42, 43]. Therefore, these heat treatments often affect the microstructure by grain growth and/or recrystallization [43]. Thus, there is a demand for tailored heat treatments. Although many studies have assessed the macroscopic mechanical behavior induced by various heat treatment schemes, the micromechanical aspects are not explored. Since the micromechanical behavior of a polycrystalline aggregate reflects the single crystal properties, they are of utmost importance for the design of structural components.

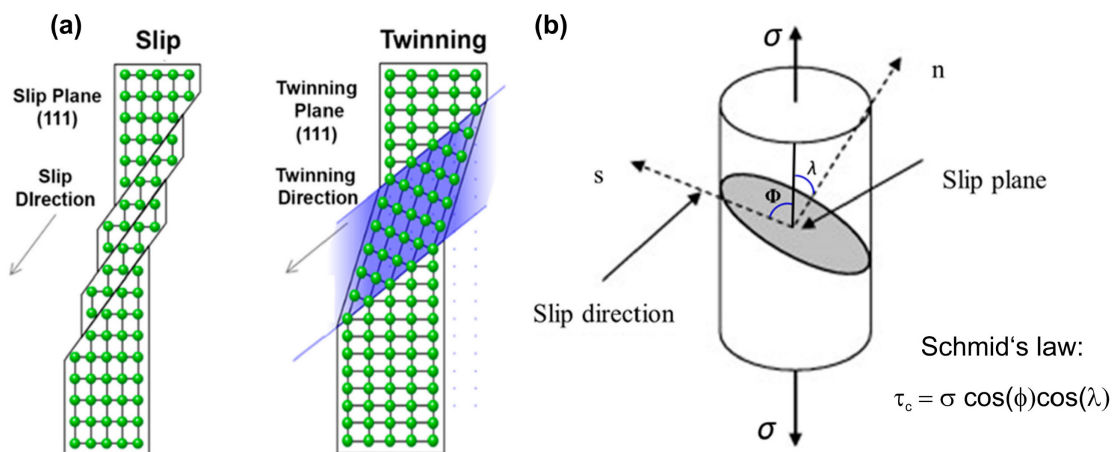


Figure 6: (a) Slip and twinning events in a face-centered cubic crystal. (b) Graphical representation of Schmid's law where n is the normal vector to the slip plane and s is the slip direction. Adapted from [44] under the open access CC-BY 4.0 license (<https://creativecommons.org/licenses/by/4.0/>).

I Introduction

7 Diffraction-Based Determination of Residual Stress

Diffraction-based methods enable the non-destructive characterization of the residual stress distribution within parts. These methods rely on the constructive interference of radiation with crystal structures, which is described by Bragg's law [45]. In essence, such methods are characterized by translation of microscopic lattice strains to macroscopic residual stress [26]. The overarching challenges in the diffraction-based residual stress can be defined as follows (see Figure 7):

1. *Bragg's law*: In case of monochromatic radiation, prior to measurements a suitable lattice plane needs to be first selected. When type I residual stress is of interest, such lattice plane should exhibit a low propensity to accumulate type II strain, as the latter would influence the micro strain [46]. In addition, the selected lattice plane should be insensitive towards crystallographic texture [46].
2. *Conversion to microscopic strain*: In most cases the knowledge of an accurate strain-free lattice spacing is compulsory. However, under certain conditions (i.e. biaxial stress state) a precise knowledge is not required and tabulated values of the material are sufficient. In most cases, only the stressed specimen is available, which requires separate sophisticated measurements to determine such. [47]
3. *Single-crystal properties*: For the reliable determination of residual stress, the knowledge of the single-crystal elastic properties is decisive. Hooke's law connects the measured lattice strain with macroscopic stress by knowledge of the stiffness of the material [26]. Therefore, especially in anisotropic crystals, where the stiffness of different lattice planes vastly deviates within the crystal, the use of macroscopic values leads to errors in the determined residual stress values.
4. *Diffraction elastic constants*: Finally, as measurements on polycrystalline specimens are concerned, the knowledge of the grain structure (i.e. how the single crystals are assembled) is needed. These constants, depend in the quasi-isotropic approach only on the anisotropy of the single crystal, but not on the measurement direction [26]. In presence of crystallographic texture (i.e. the crystals are not randomly oriented within the measurement volume) they become dependent on the measurement direction [26]. The diffraction elastic constants can be either inferred from grain-interaction models considering the single-crystal elastic properties, or directly measured for the specimen of interest [26].

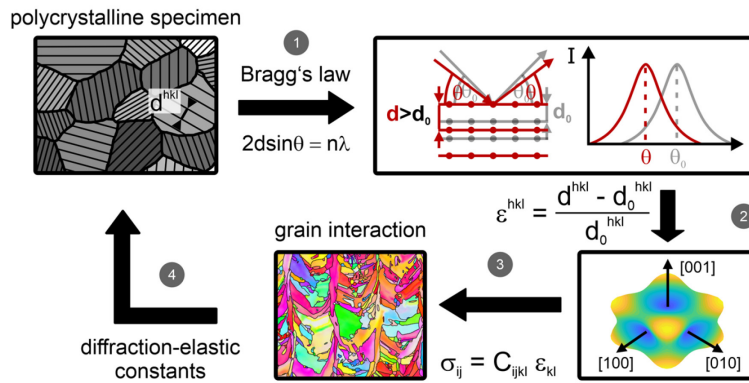


Figure 7: Schematic representation of the challenges in the domain of diffraction-based characterization of residual stress. Representation of the single-crystal anisotropy was done based on the MATLAB script reported by Nordmann et al. [48].

II Aims of the Work

Inconel 718 is one of the most studied materials within the realm of laser powder bed fusion. Despite this, several aspects regarding the fundamental understanding of the influence of the microstructure and texture on the deformation mechanics of laser powder bed fused Inconel 718 are lacking. With view on the diffraction-based analysis of residual stress such knowledge is, however, of paramount importance for material reliability.

Therefore, based on the general challenges in the domain of diffraction-based residual stress analysis, the four general aims of this work can be defined as follows:

The *first aim* is to clearly identify existing gaps and challenges in regard to diffraction-based residual stress analysis of additively manufactured materials within the open literature. The scope is not limited to the laser powder bed fusion process but is opened to laser-based additive manufacturing technologies in general.

The *second aim* of this work is to understand the deformation behavior of both, heat treated and as-built laser powder bed fused Inconel 718. The impact of microstructural and textural changes on the deformation mechanics are of interest. Regarding as-built material, the influence of the texture and the cellular solidification sub-structure presents peculiar features. However, heat treatments are designed to change such structures and herein their influence on the deformation mechanics is crucial.

The *third aim* is to comprehend how the multiscale microstructure of as-built laser powder bed fused Inconel 718 affects the diffraction-based determination of type I residual stress. In particular, the reliable determination of the strain-free reference and the diffraction elastic constants are investigated. As key requirements for residual stress analysis by diffraction methods, they influence the accuracy of their determination.

The *fourth aim* is to accurately determine residual stress in laser powder bed fused Inconel 718 by means of diffraction. The approach should consider the consequences of microstructural and textural effects on the elastic anisotropy. In addition, the effect of changes in scanning strategy on the residual stress distribution within the specimen is to be characterized.

To fulfill these objectives, different diffraction-based methods are employed to characterize surface, sub-surface, and bulk residual stress within laser powder bed fused Inconel 718 parts. On the one hand, *in situ* diffraction techniques under mechanical load allow the characterization of the deformation behavior on the micro scale. On the other hand, electron backscatter diffraction allows the assessment of both, the spatial grain morphology, and the crystallographic texture *ex situ*.

Diffraction-Based Residual Stress Characterization in Laser Additive Manufacturing of Metals

P1

J. SCHRÖDER, A. EVANS, T. MISHUROVA, A. ULBRICHT, M. SPRENGEL,
I. SERRANO-MUNOZ, T. FRITSCH, A. KROMM, T. KANNENGIEßER, G. BRUNO

13th November 2021

Metals **2021**, 11(11), 1830

DOI: 10.3390/met11111830

0 Preface

The following article reviews common diffraction-based methods for non-destructive determination of residual stress in laser-based additive manufactured materials and components. This publication reviews the literature on the topic of diffraction-based residual stress analysis in laser-based additive manufacturing. Special emphasis lies on the challenges presented by the peculiar microstructure and texture of common metallic alloys produced by such processes. In fact, the literature review identifies the metrological challenges when determining residual stress by means of diffraction-based methods. In addition, the article gives recommendations for the conduction of residual stress analysis in case of additively manufactured alloys.

With that in mind, the article serves as a guideline to identify research topics to tackle within this work.




Reprinted under the open access CC BY 4.0 license

<https://creativecommons.org/licenses/by/4.0/>



Review

Diffraction-Based Residual Stress Characterization in Laser Additive Manufacturing of Metals

Jakob Schröder ^{1,*}, Alexander Evans ¹, Tatiana Mishurova ¹ , Alexander Ulbricht ¹, Maximilian Sprengel ¹ , Itziar Serrano-Munoz ¹, Tobias Fritsch ¹ , Arne Kromm ¹ , Thomas Kannengiesser ^{1,2} and Giovanni Bruno ^{1,3,*} 

- ¹ Bundesanstalt für Materialforschung und -Prüfung (BAM), Unter den Eichen 87, 12205 Berlin, Germany; Alexander.Evans@bam.de (A.E.); Tatiana.Mishurova@bam.de (T.M.); Alexander.Ulbricht@bam.de (A.U.); Maximilian.Sprengel@bam.de (M.S.); Itziar.Serrano-Munoz@bam.de (I.S.-M.); Tobias.Fritsch@bam.de (T.F.); Arne.Kromm@bam.de (A.K.); Thomas.Kannengiesser@bam.de (T.K.)
- ² Institut für Werkstoff- und Fügetechnik, Otto-von-Guericke-Universität Magdeburg, Universitätsplatz 2, 39106 Magdeburg, Germany
- ³ Institut für Physik und Astronomie, Universität Potsdam, Karl-Liebknecht-Str. 24-25, 14476 Potsdam, Germany
- * Correspondence: Jakob.Schroeder@bam.de (J.S.); Giovanni.Bruno@bam.de (G.B.); Tel.: +49-30-8104-3667 (J.S.); +49-30-8104-1850 (G.B.)

Abstract: Laser-based additive manufacturing methods allow the production of complex metal structures within a single manufacturing step. However, the localized heat input and the layer-wise manufacturing manner give rise to large thermal gradients. Therefore, large internal stress (IS) during the process (and consequently residual stress (RS) at the end of production) is generated within the parts. This IS or RS can either lead to distortion or cracking during fabrication or in-service part failure, respectively. With this in view, the knowledge on the magnitude and spatial distribution of RS is important to develop strategies for its mitigation. Specifically, diffraction-based methods allow the spatial resolved determination of RS in a non-destructive fashion. In this review, common diffraction-based methods to determine RS in laser-based additive manufactured parts are presented. In fact, the unique microstructures and textures associated to laser-based additive manufacturing processes pose metrological challenges. Based on the literature review, it is recommended to (a) use mechanically relaxed samples measured in several orientations as appropriate strain-free lattice spacing, instead of powder, (b) consider that an appropriate grain-interaction model to calculate diffraction-elastic constants is both material- and texture-dependent and may differ from the conventionally manufactured variant. Further metrological challenges are critically reviewed and future demands in this research field are discussed.

Keywords: laser-based additive manufacturing; residual stress analysis; X-ray and neutron diffraction; diffraction-elastic constants; strain-free lattice spacing



Citation: Schröder, J.; Evans, A.; Mishurova, T.; Ulbricht, A.; Sprengel, M.; Serrano-Munoz, I.; Fritsch, T.; Kromm, A.; Kannengiesser, T.; Bruno, G. Diffraction-Based Residual Stress Characterization in Laser Additive Manufacturing of Metals. *Metals* **2021**, *11*, 1830. <https://doi.org/10.3390/met11111830>

Academic Editor: Matteo Benedetti

Received: 25 October 2021

Accepted: 9 November 2021

Published: 13 November 2021

Publisher's Note: MDPI stays neutral with regard to jurisdictional claims in published maps and institutional affiliations.



Copyright: © 2021 by the authors. Licensee MDPI, Basel, Switzerland. This article is an open access article distributed under the terms and conditions of the Creative Commons Attribution (CC BY) license (<https://creativecommons.org/licenses/by/4.0/>).

1. Introduction

In recent years additive manufacturing (AM) has evolved from a technology for rapid prototyping to a mature production process used in several industries from aerospace to medical applications [1]. In essence, an energy source incrementally manufactures a part in a layer-by-layer process from a wire or powder feedstock [2]. AM processes allow the fabrication of complex structures, which cannot be produced via conventional manufacturing methods [3,4]. This freedom of design enables improvements in component performance and weight reduction of parts [4,5]. In addition, the rapid solidification rates and tailored heat treatment schedules can improve certain material properties, leading to further performance and efficiency gains [6–9]. However, process-related internal stress (IS) may lead to the formation of cracks or delamination [10–13]. IS may severely reduce the applicability of the process to manufacture materials more prone to this type of in-process damage. Moreover, very often IS locks large residual stress (RS) in the parts after production [14].

Therefore, certain materials, which are less susceptible to IS and to related defect formation, are generally preferred to date for the production with laser-based AM methods. These include engineering materials such as stainless steels, titanium-, aluminum-, and nickel-based alloys. In fact, alloys such as 316L, Ti6Al4V, AlSi10Mg, as well as Inconel 625 and 718 are widely used in laser-based AM. It is extremely difficult to monitor IS during production, especially in such complex AM-based processes. Therefore, extensive research has been dedicated to the topics of RS (i.e., the final footprint of IS). The RS determination and mitigation for those alloys are the subjects of this review.

The subjects have a further relevance: In recent years efforts have also been made to extend the laser-based AM production to materials more prone to IS and RS related defects, such as Nickel alloys Inconel 939 [15,16], Inconel 738 [17–20], or martensitic steels [21–23]. In these cases, the control and knowledge of the RS state gains an even greater importance. In fact, investigations have shown that even optimized process parameters (e.g., hatch spacing, laser power, scan speed or scan strategy) can result in high RS magnitudes [24,25]. In general, a careful selection of the process parameters allows the reduction of the RS level and thus increases the overall mechanical performance [26].

Several destructive and non-destructive techniques are available to determine the RS within a material. Due to their non-destructive nature diffraction methods are, naturally, the most widespread for the characterization of RS. The complete stress state within the bulk (by means of neutrons), the subsurface (by means of synchrotron X-rays) and surface (using Lab X-ray) can be characterized.

To allow the precise determination of RS using diffraction-based methods, knowledge about the microstructure, the texture and the processing conditions is required. First, a strain-free lattice spacing (d_0^{hkl}) must be found as a reference to permit the calculation of the strain [27]. The situation is akin to weldments, in which a chemical gradient appears across the weld line, provoking a variation of d_0^{hkl} [27–30]: chemical gradients due to solute-concentration variation are present in AM alloys [31]. This poses a new challenge for the determination of strain and subsequently stress. Secondly, the anisotropic nature of most single crystals requires material specific constants to enable the precise determination of RS by diffraction-based strain measurements [32–34]. The so-called diffraction-elastic constants (DECs) are not only dependent on the alloy, but also rely on the underlying microstructure and texture. In fact, the RS determination by diffraction methods is facilitated if a non-textured polycrystal with relatively small equiaxed grains is measured: in such a case the so-called quasi-isotropic approximation can be used [32,34]. In practice, this assumption is often invalid, as the microstructure can strongly deviate from equiaxed. However, the crystallographic texture and morphology strongly depend on the processing conditions. Rolled or hot-extruded materials, for example, typically exhibit a strong crystallographic texture, which may cause an anisotropic behavior [35,36]. Methods to deal with such process-related peculiar microstructures have been developed in the past for established manufacturing methods [27]. The columnar microstructures, which develop during laser-based AM, typically exhibit a strong crystallographic texture in conjunction with an inhomogeneous grain size along the build direction [37]. Therefore, well established models to determine the DECs in conventional products may fail to predict correct values for AM alloys [38–40].

While detailed reviews on the process parameter dependence and process-specific strategies of RS mitigation can be found in the literature [14,41–44], an extensive review on the methodology of diffraction-based methods with respect to laser-based AM processes is absent.

A first assessment of the critical aspects to account for in the domain of RS determination of AM was provided by Mishurova et al. [45]. Building on this, the present paper showcases an in-depth critical review of the literature in the domain of experimental characterization of RS in laser-based powder AM via non-destructive diffraction methods: An overview of practices and related challenges in diffraction-based RS determination for laser-based AM will be given. Especially, the appropriate choice of the DECs and d_0^{hkl} is

paramount to provide accurate absolute RS levels [33,45]. Furthermore, it is indispensable to take the principal stress directions into account, which are for AM materials not necessarily governed by the geometry but instead by the building strategy and, consequently, by the microstructure anisotropy [46]. We will show that significant method development work is still necessary to reliably determine RS by diffraction methods in AM parts.

2. Laser-Based AM Processes

The first laser-based AM process, namely selective laser sintering (SLS), was first developed in 1979, although it took until the 1990's until metal materials were manufacturable [47]. In this process a laser compacts loose powder in a layer-by-layer process to form a green body using a binding polymer [47]. A following infiltration fills the porosity to improve the overall mechanical performance [48]. The development of laser sources allowed EOS (Electro Optical Systems GmbH, Krailing, Germany) to develop a variant of SLS, which no longer needed a binding polymer, as the peripheral region of the powder particles was meltable [47]. The resulted parts were porous but had reasonable mechanical properties [49]. Further development in laser technology finally allowed the manufacturer to fully melt the powder bed [47]. The laser powder bed fusion (LPBF) and laser metal deposition (LMD) processes were then developed. These processes will be introduced in the next paragraphs and are the focus of this review, owing to their propensity to generate high residual stresses. These also are the leading metal AM processes for both new part production and repair engineering [50,51]. Therefore, they have high technological and environmental importance.

2.1. LPBF (Laser Powder Bed Fusion)

The usage of increasingly powerful lasers has increased the ability to fully melt the metallic powder [47]. This advance has gradually enabled the production of nearly fully dense (>99.9%) parts, if the process parameters are optimized, with mechanical properties comparable to those of conventionally produced metals [52,53]. Figure 1a illustrates the LPBF process. In a chamber flooded with a protective gas (typically Argon, to prevent oxidation during production), a recoater delivers powder from a reservoir to the build platform. A laser then melts predefined areas within the powder layer. The reservoir and build platform move accordingly to the part design and the steps are repeated in a layer-wise manner until the final part is produced.

The most relevant parameters for process optimization are laser power, scanning speed, layer thickness, hatching distance and, ultimately, the scanning strategy [54,55]. To reduce the temperature gradient during manufacturing, thereby reducing RS and distortions, preheating the baseplate is a typical approach [56]. Nowadays, preheating temperatures up to 1000 °C are realized [57]. The so-called inter layer time, which defines the time passed between deposition of subsequent layers can help to reduce microstructural gradients due to heat accumulation in the part [58]. Not only the process parameters but also the feedstock powder significantly influence the quality of the part. Typically, spherical particles with a size between 10–60 µm are ideal in terms of processability [59]. A comprehensive review on powders for LPBF can be found elsewhere [59]. When the process parameters are carefully controlled, parts with superior properties compared to SLS and direct metal laser sintering (DMLS) are manufacturable [52]. Due to the high heat input and high cooling rates, IS play a major role in those parts, which can lead to distortions and cracking, and remain locked in the part as RS [10,60].

2.2. LMD (Laser Metal Deposition)

While in the processes of SLS, DMLS and LPBF a first applied powder layer is selectively melted for part manufacture, during LMD a powder or wire feedstock, is directly fed into the laser beam focus [61]. In a powder-based process a carrier gas drags the powder from the feeder to the nozzle into the melt pool [62]. A second gas is used to prevent oxidation, whereby different gases are available as carrier and shielding [62,63].

Depending on the application different type of nozzles are available; they can influence the efficiency of the process [64,65]. The laser beam then fully melts the feedstock material, and the part is created in an incremental manner (Figure 1b). One of the main advantages of the LMD process is that in contrast to other processes the excess material is minimized, even though material loss can still be a problem due to overspray of the nozzle [65]. In addition, the deposition rates are higher during LMD, but the overall part quality typically suffers compared to LPBF [66]. The most relevant process parameters for process optimization are powder or wire feed rate, laser power, gas flow and scanning velocity [67]. In the LMD process layer thicknesses and particle sizes are commonly larger as compared to the LPBF process.

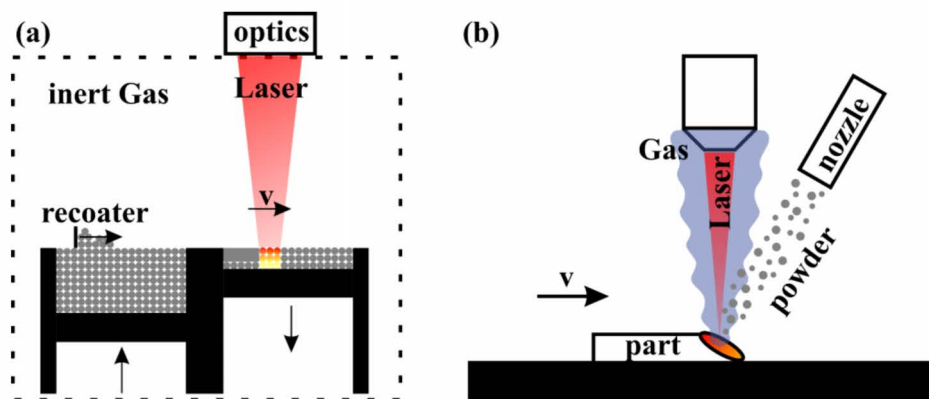


Figure 1. Simplified schematic images of the different laser-based additive manufacturing processes of (a) laser-powder bed fusion (adapted from [68]) and (b) powder-based laser metal deposition with a lateral injection nozzle (adapted from [69]).

3. Definition of Residual Stress

Residual stress (RS) is stress that exist in a manufactured part without the application of external loads, moments, or thermal gradients [34]. It is very unlikely for manufactured parts to be completely free of RS [70]. Figure 2 visualizes the different types of RS as defined in literature. Depending on the length scale over which the RS self-equilibrate, they can be categorized as the following [71]:

- Type I stresses (σ^I) equilibrate over large distances (comparable to the size of the part). This type of RS can be caused e.g., by temperature gradients, machining, and other treatments at the component scale. They depend on the material and its history, as well as on the component geometry.
- Type II or intergranular stresses (σ^{II}) vary over the grain scale and balance over a few grains. They strongly depend on the microstructure, and on the materials history, but weakly on the part geometry. Type II stress is very common in composites and crystallographically anisotropic materials
- Type III stresses (σ^{III}) vary over the atomic scale. Typically, this type is caused by defects of the crystal lattice (e.g., dislocations). They are balanced within each grain and depend on both the microstructure and the materials history.

While the failure of materials can depend on local features, and therefore on Type II and III stresses, in engineering applications usually Type I stress dominates. Indeed, a major contributor to RS in AM polycrystalline parts is Type I RS caused by localized heating, melting, and rapid solidification during the manufacturing process [60].

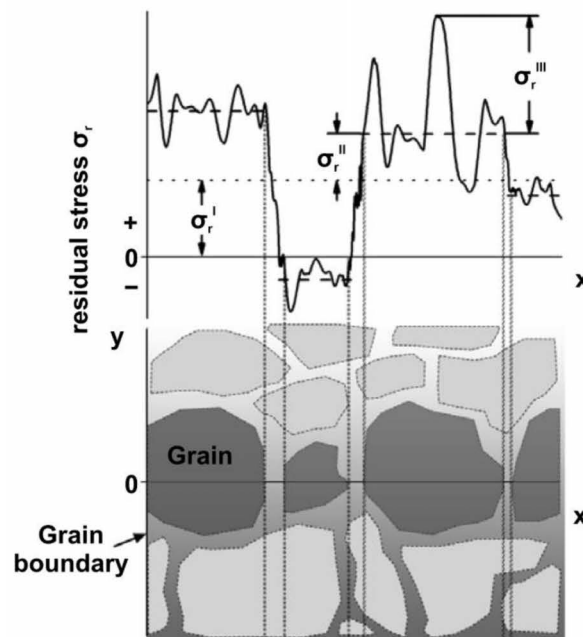


Figure 2. Schematic representation of the different types of RS within a polycrystalline material where σ^I , σ^{II} , σ^{III} denote the type I, II and II stresses respectively. Adapted from [72].

4. Residual Stress with Respect to Laser-Based AM

4.1. Origin of Residual Stress

Previous studies showed that RS in AM parts is primarily caused by the thermal gradients in conjunction with the solidification shrinkage that arise due to continuous re-heating, re-melting, and cooling of previously solidified layers [60,73,74]. The local and rapid heating of the upper layer by the laser beam, combined with slow heat conduction (Figure 3a), consequently leads to a steep temperature gradient within the material [60]. However, the already solidified layers restrict the expansion of the uppermost layer, thus leading to the formation of elastic compressive strains [60]. These strains eventually become plastic upon reaching the local temperature dependent yield strength [60]. Therefore, without the presence of mechanical constraints, such plastic strains (ϵ_{pl}) would lead to bending as indicated in Figure 3a [60]. During cooling, the shrinkage (ϵ_{th}) of the plastically compressed upper layers leads to an inversion of the bending [60]. The aforementioned is accompanied by the formation of tensile RS in the locally plastically deformed region, balanced by surrounding compression (Figure 3b) [60]. Finally, solidification shrinkage of the molten layer superimposes on the solid-state mechanisms, which leads to tensile RS at the upper most surface balanced by subjacent compression [60]. Extending this phenomenon over multiple layers leads to large thermal gradients particularly along the building direction. Thus, large RS may appear in the final part. The RS itself is influenced by many manufacturing parameters, e.g., the number and the thickness of the layers [60], the geometry, the scanning strategy [38,75–77], and the laser energy density [13]. Optimization of these parameters can significantly reduce RS but also needs to be balanced against the impact on defects and microstructure. The current approach is to optimize some scanning parameters and the scanning strategy, since they highly affect thermal gradients [78]. An alternative approach is the use of stress relieving heat treatments to reduce the magnitude and subsequent impact of RS [41]. These heat treatments must also be balanced against manufacturing cost considerations and both the desired microstructure and the consequent mechanical properties of the alloys.

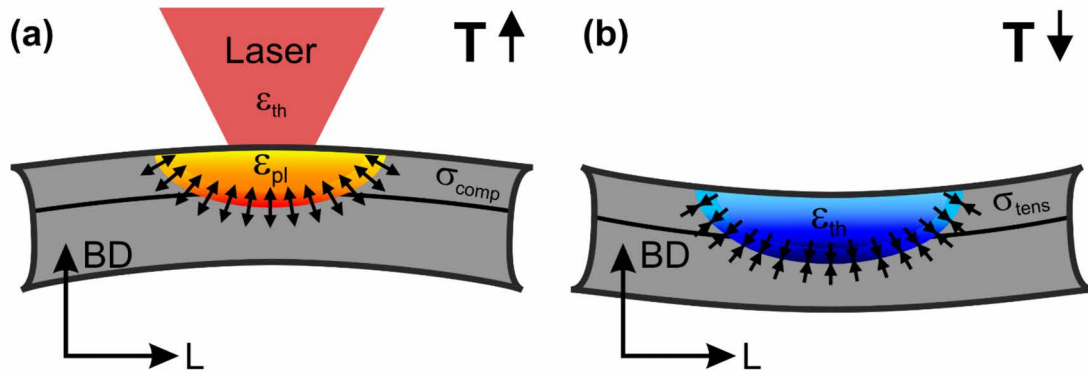


Figure 3. Schematic images showing the effect of the heat input on the stress state during (a) heating and (b) cooling in LPBF manufacturing (adapted from [60]).

4.2. Distribution of Residual Stress

An exemplary RS distribution for LPBF of 316L is shown in Figure 4, acquired on 24 mm × 46 mm × 21 mm prisms at middle height [79]. Measurements conducted by X-ray diffraction reveal the presence of high magnitude tensile RS at the surfaces [79]. Bulk neutron diffraction measurements show that stresses invert to compressive RS at an approximate distance of 6 mm from the surfaces, balancing the tensile RS [79]. In fact, it is typical that tensile stresses develop at the surfaces which are balanced by compressive stresses in the bulk [12,60,74,75,79–91]. As mentioned before, the magnitude and distribution of the RS locked in the part is dependent on the manufacturing parameters. However, the general aspects remain unchanged irrespective of the alloy being produced. To characterize the complete stress distribution within a sample, different measurement methods may be required [79]. The methods and the associated challenges to determine the RS from diffraction-based methods in the domain of laser-based AM will be introduced in the following paragraphs.

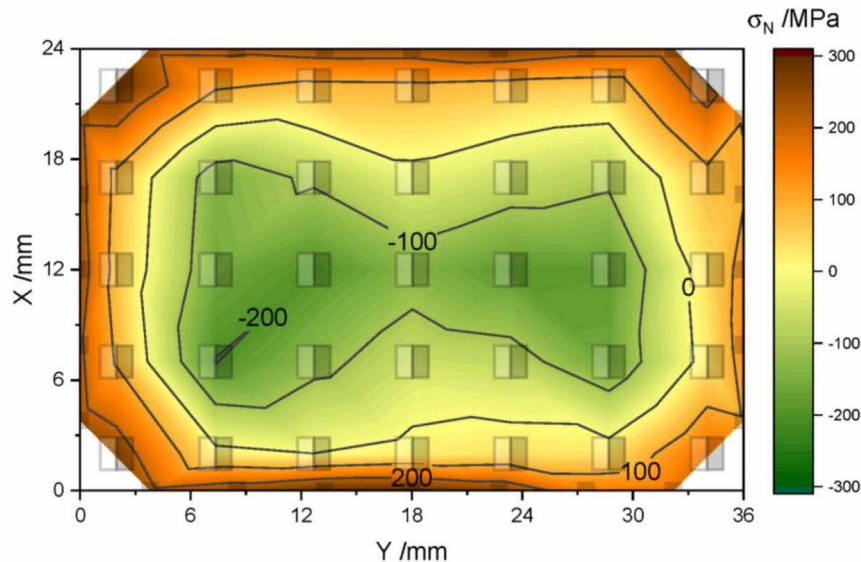


Figure 4. Example of a stress distribution along the build direction (σ_N) in LPBF of 316L prisms measured by ND (bulk) and lab X-ray (surface). Reproduced from [79].

5. Determination of Residual Stresses with Diffraction-Based Methods

The determination of RS can be categorized into destructive (e.g., hole drilling, crack compliance method, hardness testing, etc.) and non-destructive methods (e.g., Bridge curvature method, diffraction, etc.) [92]. However, this paper will solely focus on the

methodology of non-destructive diffraction-based methods for RS analysis used for laser-based AM. Therefore, in the following paragraphs the most relevant diffraction techniques will be introduced. Diffraction techniques are well established non-destructive method to evaluate RS in both academia and industry. Determining elastic strains by measuring the variation of lattice spacing provides a powerful method to identify RS at the surface (X-ray diffraction, XRD), at the subsurface (synchrotron energy dispersive diffraction, ED-XRD), as well as in the bulk (synchrotron or neutron diffraction, ND) [13,74,82,83].

5.1. General Aspects of Diffraction-Based Methods

The Bragg equation [93] (Equation (1)) describes the condition for constructive interference of spherical waves emitted by an ordered arrangement of atoms (in lattice planes with distance d^{hkl}), induced by an impinging planar wave of wavelength λ with its order of diffraction n . This law provides the basis for the determination of RS with diffraction-based methods, as the lattice (quantified by the interplanar distance d^{hkl}) can be used as a strain gauge. Consequently, once a material is under the effect of RS the d^{hkl} are altered. Since the beam size in XRD, SXRD or ND measurements is finite, the measured diffraction peak contains a superposition of type I and type II RS within the sampling volume [71]. In all diffraction measurements, the total strain of the lattice is expressed by a shift of the respective diffraction peak (Equation (1)). For the monochromatic case, with a defined wavelength λ , and a known strain-free lattice spacing (d_0^{hkl}), a peak shift to lower scattering angles represents a tensile strain, while a shift to larger scattering angles a compressive one. Type III stresses will mostly contribute to the broadening of the peak or changes in the peak shape [32].

$$2d^{hkl} \sin\theta = n\lambda \quad (1)$$

The strain is then calculated as

$$\left\{ \varepsilon^{hkl} \right\} = \left\{ \frac{d^{hkl} - d_0^{hkl}}{d_0^{hkl}} \right\} \quad (2)$$

However, to link the determined lattice strains in the laboratory coordinate systems to macroscopic stresses in the sample coordinate systems a few more considerations are necessary. A short description of the fundamentals of RS determination with diffraction-based method is, therefore, presented in the following. For a more detailed description on RS analysis by diffraction-based methods, the reader is referred to the literature [32–34,71,94].

In the general case, RS is derived from lattice strains of a particular set of lattice planes. The measured values are $d_{\varphi\psi}^{hkl}$, i.e., interplanar distances at different sample orientations (φ, ψ) . For the RS determination, the strains are calculated as in Equation (2) and successively converted to **elastic** stresses via Hooke's law. This yields the general equation for RS determination in the Voigt notation (Equation (3)). Equation (3) connects the elastic lattice strain $\left\{ \varepsilon_{\varphi\psi}^{hkl} \right\}$ (in all directions (φ, ψ)) with the components of the stress tensor in the sample coordinate system by using a transformation matrix (Figure 5). The stress (denoted by $\langle \sigma^S \rangle$) is averaged over all crystallites contained in the gauge volume. The values $\frac{1}{2}S_2^{hkl}$ (Equation (4a)) and S_1^{hkl} (Equation (4b)) represent the diffraction elastic constants (DECs), which in general depend on the measurement direction in the crystal system. These constants take the elastic anisotropy of the single crystal into account and are discussed in detail later. However, for quasi-isotropic (poly)-crystals they are independent of the sample coordinate system. The DECs serve as proportionality constants, which connect the measured $d_{\varphi\psi}^{hkl}$ to a macroscopic RS for the different lattice planes. A further unknown parameter is d_0^{hkl} , which represents the reference value for the determination of the strain. Different strategies are available to determine the d_0^{hkl} , which will be examined later.

$$\begin{aligned} \left\{ \varepsilon_{\varphi\psi}^{hkl} \right\} &= \left\{ \frac{d^{hkl}}{d_{\varphi\psi}} - d_0^{hkl} \right\} \\ &= \frac{1}{2} S_2^{hkl} \left[\sin^2\psi \left(\langle \sigma_{11}^S \rangle \cos^2\varphi + \langle \sigma_{22}^S \rangle \sin^2\varphi + \langle \sigma_{12}^S \rangle \sin 2\varphi - \langle \sigma_{33}^S \rangle \right) + \langle \sigma_{33}^S \rangle \right. \\ &\quad \left. + 2\sin 2\psi \left(\langle \sigma_{13}^S \rangle \cos\varphi + \langle \sigma_{23}^S \rangle \sin\varphi \right) \right] + S_1^{hkl} \left(\langle \sigma_{11}^S \rangle + \langle \sigma_{22}^S \rangle + \langle \sigma_{33}^S \rangle \right) \end{aligned} \quad (3)$$

$$\frac{1}{2} S_2^{hkl} = \frac{1 + \nu^{hkl}}{E^{hkl}} \quad (4a)$$

$$S_1^{hkl} = \frac{-\nu^{hkl}}{E^{hkl}} \quad (4b)$$

Equation (3) represents the most general case, where all stress components are present. If simplifying assumptions can be made, such as the absence of shear stress components (i.e., the fact that the sample coordinate system coincides with the principal stress system), plane stress or plane strain states, or that a particular component vanishes, the equation would simplify. Some cases are developed in more detail below. The same would happen if we can apply simplifications on the DECs, as for instance assume that the material is isotropic.

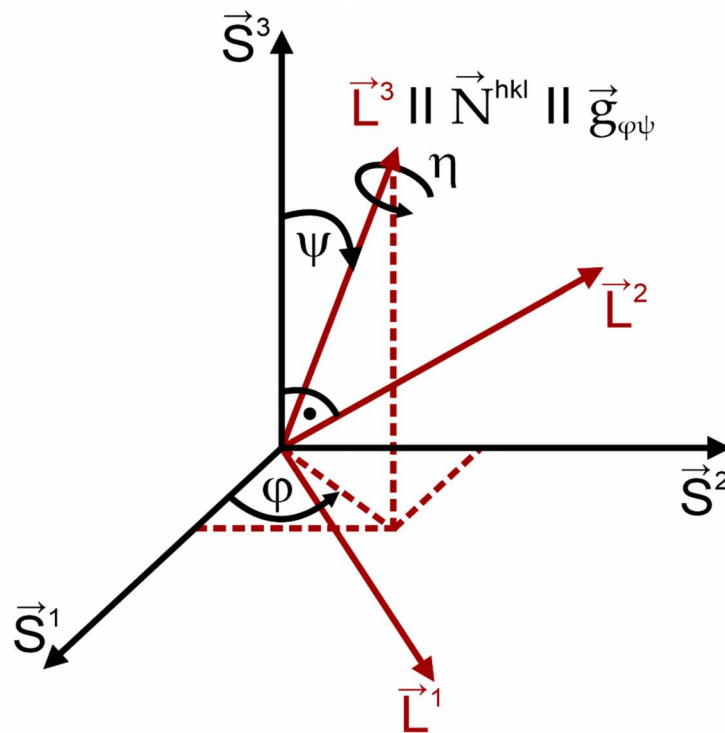


Figure 5. Orientation of the laboratory coordinate system (L) with respect to the sample coordinate system (S), and the associated angles φ and ψ . η denotes the rotation angle around the measurement direction (adapted from [32]).

5.2. X-ray Diffraction

5.2.1. The Monochromatic Case for Surface Analysis

The use of monochromatic X-ray sources for the determination of RS is widely spread. The penetration depth is in the order of a few μm . The general equation for RS determination (Equation (3)) can thus be simplified: The stress components normal to the measurement plane 12 [$\sigma_{i3} = 0$ ($i = 1, 2, 3$)] can be considered zero (Equation (5)).

$$\varepsilon_{\varphi\psi}^{hkl} = \frac{1}{2} S_2 \sigma_{\varphi} \sin^2\psi + S_1 (\sigma_{11} + \sigma_{22}) \text{ with } \sigma_{\varphi} = \sigma_{11} \cos^2\varphi + \sigma_{22} \sin^2\varphi + \sigma_{12} \sin 2\varphi \quad (5)$$

As laboratory setups mostly use monochromatic X-rays sources, an appropriate lattice plane representing the bulk material must be chosen. A guideline for this can be found in DIN EN 15305 [95], but will be discussed more in detail in Section 6.4. The main approach used in laboratory X-ray devices is the $\sin^2\psi$ method in which the lattice spacing is measured under variation of the ψ angle under a (usually) fixed φ angle (Figure 5). Equation (5) can be considered a linear equation of the form $\varepsilon(\sin^2\psi) = a \cdot \sin^2\psi + b$. The straight line has a slope of $a = \frac{1}{2} S_2 \sigma_\varphi$ and intersects the $\varepsilon(\sin^2\psi)$ axis at $b = S_1(\sigma_{11} + \sigma_{22})$. From the linear regression of the respective $\varepsilon(\sin^2\psi)$ —distribution the RS can be determined in the direction φ (Figure 6). In an ideal case, where an elastically isotropic or non-textured material in a homogeneous stress state is sampled, the obtained $\varepsilon(\sin^2\psi)$ is truly linear [32]. Even though these requirements are often not fulfilled, the errors are typically of small order and can thus be neglected [32]. However, for strongly textured materials (e.g., rolled, additively manufactured) the deviations can be severe. In the case of present shear stresses (e.g., σ_{13} and σ_{23}) an ellipsoid is observable (different $\varepsilon(\sin^2\psi)$ for $\pm\psi$) rather than a linear distribution. By the subtraction of the respective $-\psi$ and $+\psi$ distributions a linear equation is obtained. Finally, from its slope the shear stress component in the direction φ can be determined. Although normal stress components can also be determined within the information depth of the radiation this requires the precise knowledge of d_0^{hkl} , which is not needed for the determination of shear stresses [32]. Due to the relatively low penetration of lab X-rays into metallic materials, the surface roughness of additively manufactured material impacts the determined stress values [96].

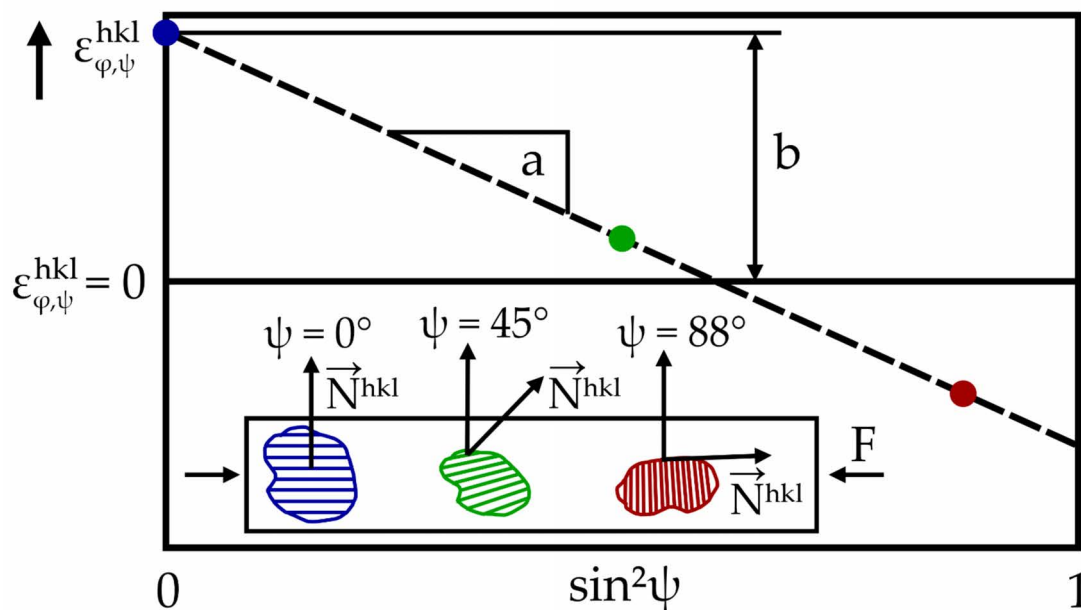


Figure 6. Simplified $\varepsilon(\sin^2\psi)$ distribution assuming an elastically isotropic or non-textured material in a homogeneous compression stress state (adapted from [32]).

5.2.2. The Energy Dispersive Case

In addition to the monochromatic (angular dispersive) XRD technique, it is also possible to use polychromatic radiation (white beam) for RS determination. An energy dispersive detector detects the respective energies of the diffracted X-rays at a fixed diffraction angle θ . In such manner the entire diffraction spectrum of the respective material can be obtained for each measurement direction (φ, ψ) [32]. Due to the wide energy range used,

the information retrieved arises from different depths of the specimen [97]. The information depth of the respective energy can be calculated using the following equation [97]:

$$\tau_{\eta} = \frac{\sin^2\theta - \sin^2\psi + \cos^2\theta\sin^2\psi\sin^2\eta}{2 u(E^{hkl})\sin\theta\cos\psi} \quad (6)$$

The information depth is a function of the sample rotation around the diffraction vector η , the diffraction angle θ , the tilt angle ψ and the energy dependent linear absorption coefficient $u(E^{hkl})$. The latter is material dependent. τ_{η} defines the depth below the surface from which 63% of the total diffracted intensity comes from [98].

The Energy of each respective reflection can be directly transferred to the lattice plane spacing by rewriting the Braggs law in terms of photon Energy E^{hkl} [99]:

$$d^{hkl}(\text{\AA}) = \frac{h \cdot C}{2\sin\theta} \cdot \frac{1}{E^{hkl}} \approx \frac{6.199}{\sin\theta} \cdot \frac{1}{E^{hkl}} \quad (7)$$

In Equation (7) h is the Planck constant and c the speed of light. The $\sin^2\psi$ method is also applicable for the energy dispersive case. The $\varepsilon(\sin^2\psi)$ distributions are simply calculated using Equation (7) together with the strain definition (see Equation (2)). The same simplifications (as for lab X-ray) apply whenever measuring in reflection mode or a biaxial stress state can otherwise be justified. In fact, the plane stress assumption might only hold for lower energy ranges with a low penetration depth. This complicates the RS analysis of higher energy reflections, as the triaxial approach could be more suitable. The acquisition of the entire diffraction spectrum allows the stress analysis for each lattice plane observed. Therefore, a depth resolved stress analysis (near surface) is possible up to the maximum information depth (according to Equation (6)). With respect to laser-based AM, authors have extracted RS depth profiles by using the combination of different reflections (under the assumption of vanishing stress component normal to the surface) [38,96]. In addition, a full pattern refinement to obtain an average d^{hkl} can be conducted (e.g., Rietveld refinement) [100]. Recently, Hollmann et al. [101] proposed methods for near surface measurements of materials with cubic symmetry and nearly single crystalline texture (e.g., additively manufactured).

Due to the high energies available in synchrotron facilities even measurements in transmission are possible both in angular (monochromatic) and energy dispersive (polychromatic) modes, depending on the material measured and the sample thickness [32]. In these cases, depending on the geometry, the out-of-plane stress cannot be neglected and hence the triaxial stress analysis approach is required. However, the ability to perform triaxial RS measurements is hampered by the use of elongated lozenge-shaped sampling volume, typical in high energy diffraction measurements (because of the required small diffraction angle [32]). On the one hand, the method therefore allows a very high spatial resolution (in the order of 10–100 μm) in the two in-plane directions, but on the other hand the spatial resolution becomes poor (several millimeters) in the out-of-plane direction. Despite this limitation, energy dispersive techniques are well suited for thick wall geometries, whereby the stress state is closer to the plane strain condition and limit gradients exist though the thickness. Moreover, significant work is reported on the use of transmission set-up for the determination of DECs through in situ tensile testing. This topic is addressed in Section 6.3.3.

5.3. Neutron Diffraction

As neutrons have a high penetration depth in most materials, fully 3D stress states can be probed. The gain in generality of the approach must be paid at a price: the strong dependence of the RS analysis on the reference interplanar spacing, d_0^{hkl} . Additional complications arise when d_0^{hkl} differs over the analyzed region due to chemical gradients over the specimen. These points are discussed in detail in Section 6.1. There are two neutron diffraction methods to determine RS: the monochromatic and the time-of-flight

(TOF) method. The TOF method uses a polychromatic beam and rests on the detection of many diffraction peaks. Thus, the method leverages on the fact that the velocity of the neutrons is inversely proportional to its wavelength. In the monochromatic case, the instrument operates with a fixed wavelength, and most commonly only one peak at a time can be detected. The two methods will be introduced briefly below. For a more detailed description the reader is referred to the literature [94].

5.3.1. The Monochromatic Method

In scattering, a neutron may be described by its wave vector k , of magnitude $2\pi/\lambda$ directed along its velocity part [94]. Due to the wave nature of matter, the de Broglie wavelength of the neutron (λ) is directly linked to the momentum (p) of the respective particle [94]:

$$p = m_n v = \frac{hk}{2\pi} = hk \quad (8)$$

This allows the calculation of an associated wavelength in dependence of the neutron velocity v and mass m_n with the Planck's constant h . In the monochromatic case, neutrons with a given wavelength are used to study the lattice strain within the material [102]. The wavelength of the neutrons is usually selected using a single crystal monochromator from a broader neutron wavelength spectrum [102]. Typically, the wavelength is chosen so that a diffraction angle of around $2\theta \sim 90^\circ$ is used. The condition $2\theta \sim 90^\circ$ allows the definition of a nearly cubic sampling (gauge) volume. Thereby, probing the same region upon any sample rotation. The diffracted signal is usually then detected on a position sensitive detector or a scanning point detector [94]. An example of a typical diffraction peak obtained is shown in Figure 7, which are typically fitted using a symmetric function (e.g., Gaussian).

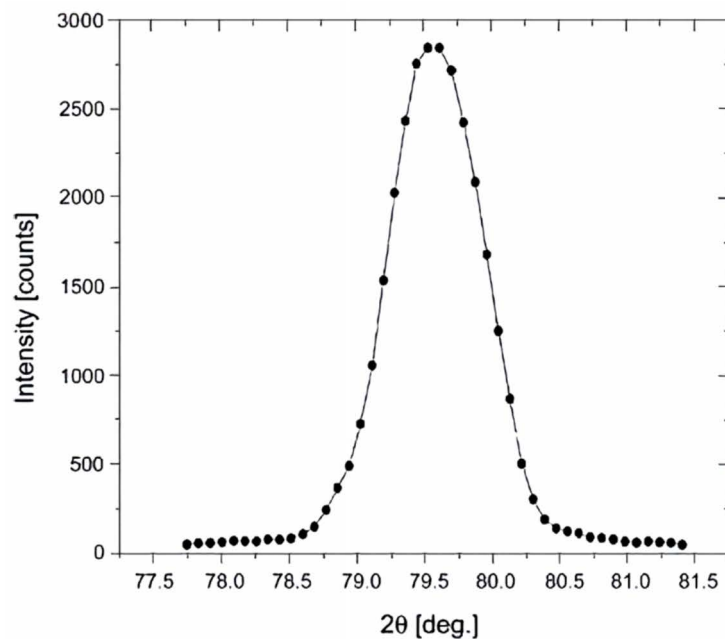


Figure 7. Neutron peak profile. Reproduced from [102] with permission from Elsevier.

The change of diffraction angle with respect to a reference value yields variations of the lattice strain and can be expressed in the angular form as [102]:

$$\epsilon^{hkl} = \frac{\Delta d^{hkl}}{d^{hkl}} = -\Delta\theta^{hkl} \cot\theta^{hkl} \quad (9)$$

Similar to the angular dispersive X-ray methods (see Section 5.2.1), an appropriate lattice-plane must be chosen, which represent the bulk behavior the best. For the stress analysis the same relations remain valid. However, the isotropic form of the Hooke’s law typically is applied along three orthogonal principal strain components [94] (see Equation (14)). The consequences for the related assumptions with respect to principal directions are discussed in Section 6.2.

5.3.2. The Time-of-Flight Method

The neutron diffraction (ND) time-of-flight method is the equivalent to polychromatic diffraction in the X-ray case. From the neutron travel time between source and detector, the associated wavelength can be calculated (Equation (10)) [94].

$$\lambda = \frac{ht}{m_n L} \tag{10}$$

As detectors are placed at $2\theta \sim 90^\circ$, using Bragg’s law (Equation (1)) one can directly determine d^{hkl} from the wavelength at which peaks appear in the diffraction spectrum (for a known crystal structure). A typical ND diffraction spectrum is shown in Figure 8. In contrast, to steady state sources (monochromatic), the time-pulsed source instruments (time-of-flight) typically cause an asymmetry due to the moderation process: More complicated fitting functions are typically necessary [94]. Using the TOF methods an average d can be obtained by a full pattern refinement, but also single peak fits are performable [102].

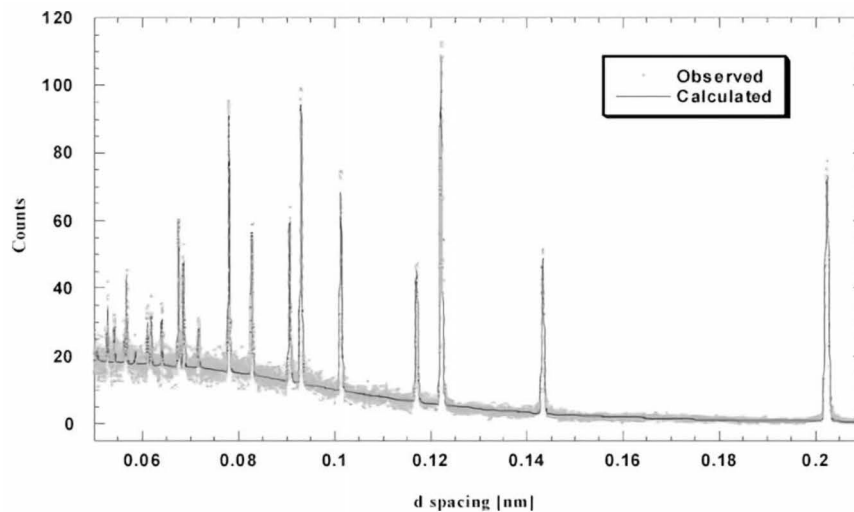


Figure 8. Time-of-flight pattern. Reproduced from [102] with permission from Elsevier.

6. Peculiarities of Diffraction-Based Methods in the Case of AM

6.1. Strain-Free Lattice Spacing (d_0^{hkl})

To precisely determine RS in parts using diffraction-based techniques, the knowledge of a d_0^{hkl} as a reference is essential (see Equation (2)). A comprehensive description of the methods to obtain a d_0^{hkl} value is given by Withers et al. [27]. In the case of laboratory X-ray diffraction measurements ($\sin^2\psi$), where out-of-plane stresses can be considered to equal zero ($\sigma_{i3} = 0$), a prior knowledge of d_0^{hkl} is not required, as it can even be calculated by the combination of several measurements [32]. In addition, the method is relatively insensitive to an inaccuracy in d_0^{hkl} up to 10^{-3} nm [32].

For example, one could measure d^{hkl} vs. $\sin^2\psi$ for the directions ($\varphi = 90^\circ, \psi$) and ($\varphi = 0, \psi$) and then determine their average value:

$$\frac{d^{hkl}(\varphi = 90^\circ, \psi) + d^{hkl}(\varphi = 0^\circ, \psi)}{2} = (\sigma_{11} + \sigma_{22})d_0^{hkl} \left[2S_1^{hkl} + \frac{1}{2}S_2^{hkl}\sin^2\psi \right] + d_0^{hkl} \tag{11}$$

The right term equals to d_0^{hkl} , when (isotropic, no steep gradient, $\bar{\sigma}_{22} \neq \bar{\sigma}_{11}$) [34]:

$$\sin^2\psi = \sin^2\psi^* = \frac{-S_1^{hkl}}{\frac{1}{2}S_2^{hkl}} \left(1 + \frac{\bar{\sigma}_{22}}{\bar{\sigma}_{11}} \right) \quad (12)$$

Consequently, the d_0^{hkl} can be defined as (e.g., for $\bar{\sigma}_{11} = \bar{\sigma}_{22}$):

$$d_0^{hkl} = \frac{d^{hkl}(\varphi = 0^\circ, \psi^*) + d^{hkl}(\varphi = 90^\circ, \psi^*)}{2} \text{ with } \sin^2\psi^* = \frac{-2S_1^{hkl}}{\frac{1}{2}S_2^{hkl}} \quad (13)$$

Therefore, in this particular case, the bare elastic constants define the strain-free direction ψ^* , and the half average of $d^{hkl}(\varphi = 90^\circ, \psi)$ and $d^{hkl}(\varphi = 0^\circ, \psi)$ at the position $\sin^2\psi^*$ provides the d_0^{hkl} (at the location where the $\sin^2\psi$ scan was carried out). A more detailed description and examples for other stress states to derive a d_0^{hkl} are given in [34].

Although this method leads to a simplified experimental determination of d_0^{hkl} it still bears the problem of DEC values (Equation (12)). As the determination of d_0^{hkl} by this method is dependent upon knowledge of DEC values (Equation (12)), the reliability of the DEC values must be high to determine a correct value for d_0^{hkl} . The determination of the DEC values is a separate topic and will be examined later.

While the method is sensitive to intergranular and interphase stresses [27], a relative comparison of d_0^{hkl} near the surface is often still possible. Thiede et al. [82] used this method to determine d_0^{hkl} variations across the surface of LPBF manufactured Inconel 718 prisms (assuming $\bar{\sigma}_{11} = \bar{\sigma}_{22}$) (Figure 9a). A small normal stress component σ_n was observed, which was reported to correlate with the scanning strategy. The $\sin^2\psi$ method has also been used by other researchers to determine d_0^{hkl} in LPBF Ti6Al4V [83,96]. As an alternative, Pant et al. [81] used the d^{hkl} value measured at $\psi = 0^\circ$ as d_0^{hkl} for calculating RS values.

For the cases in which the out-of-plane stress cannot be considered to equal zero ($\sigma_{i3} \neq 0$) the precise knowledge of d_0^{hkl} remains indispensable. An independent determination of d_0^{hkl} can be made by means of the following strategies:

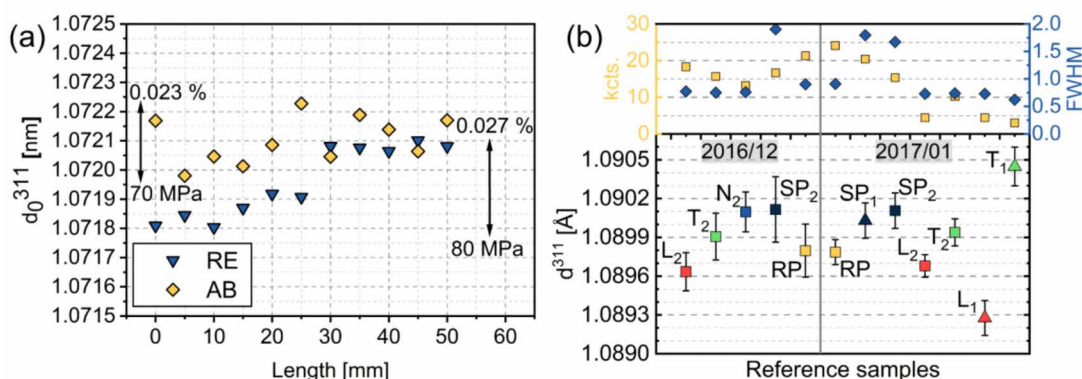


Figure 9. d_0^{311} values extracted from d^{311} versus $\sin^2\psi$ plots (a) and from raw powder (RP), filings (SP) and cuboids (L, T, N) (b). Data taken from [82].

6.1.1. Use of Raw Powder

In the case of AM there is also the possibility to obtain d_0^{hkl} by measurements on raw powder. This is a method, which does not require a twin specimen and is non-destructive by nature. However, the thermal history of the raw powder, and consequently the local chemical composition and microstructure, may differ significantly from that of the printed part [103]. The macro- and micro-scale differences in chemistry can significantly alter the lattice parameters of the material [104–106]. As Thiede et al. [82] have concluded, a shift due to different local chemical segregation prevented the use of it as a reference (Figure 9b). Similar findings were made by Kolbus et al. [103] and more recently Serrano-Munoz et al. [107].

While there may be examples of low alloyed or commercially pure materials, where the use of the raw powder may be applicable due to the lower amount of segregation, using raw manufacturing powder as d_0^{hkl} is generally not recommended in the domain of AM [45].

6.1.2. Use of Mechanical Filings

Mechanical filings from either the specimen itself or taken from a twin specimen can be used. This approach would capture the effect of the thermal cycles on the local chemical segregation and has the advantage that in a powder the macroscopic RS is fully relieved [27]. However, the filing process tends to induce plastic deformation within the powder, leading to strong diffraction peak broadening associated with microscopic stresses (Type III and possibly Type II [103]). In addition, filings certainly contain different intergranular strain than the component, so that they cannot be considered fully stress-free [27].

It was recently shown that using the d_0^{hkl} reference value of mechanical filings, a compressive stress was found for all measured points, which contradicts the stress balance condition [107]. This mismatch was attributed to the high accumulation of plastic strain in the as-filed condition, and in fact the FWHM vastly reduced upon heat treatment (indicating a significant plastic recovery). Even if some circumstances lead to the conclusion that the filings from the material are the most suitable d_0^{hkl} [82], the applicability of mechanical filings as d_0^{hkl} shall be limited to exceptional cases and rarely be considered an appropriate approach in the general case of AM.

6.1.3. Use of Macroscopically Relaxed Samples (Cubes/Combs/Arrays)

In neutron diffraction, it is common to determine the d_0^{hkl} with small cubes (or combs) cut from a sister sample. These cubes are assumed to be free of macroscopic stress. Although they appropriately represent the (possible) variation of chemical composition of the specimen, other problems must be considered: The cubes could retain intergranular stresses and are vulnerable to geometrical effects if poorly positioned on the sample manipulator [27]. Thiede et al. [82] measured small 5 mm × 5 mm × 5.5 mm cubes extracted from sister samples of LPBF Inconel 718. However, they found a significant dependence of the d^{hkl} value on the measurement direction (Figure 9b). This suggests that the cubes were not fully macroscopically stress free and thus could not yield a reliable d_0^{hkl} [82]. Nevertheless, a similar d^{hkl} dependence on the measurement direction was found by Ulbricht et al. [79] for LPBF manufactured stainless steel 316L, this time using 3 mm × 3 mm × 3 mm coupons.

To obtain a representative d_0^{hkl} they averaged the values over all measured directions (which correspond to the main geometrical directions). Kolbus et al. [103] attributed the different d_0^{hkl} in different directions of reassembled DMLS Inconel 718 cubes (2.5 mm × 2.5 mm × 2.5 mm and 5 mm × 5 mm × 5 mm) to anisotropic micro stress between the fcc matrix and the precipitation phases. They applied an average obtained from measurements on reference cubes extracted from different positions but did not average over different strain directions. Regardless of the direction being measured, Pant et al. [81] found that the average value of the measured d_0^{hkl} on the LPBF manufactured Inconel 718 array (cut by wire electric discharge machining) was position independent. The average value, however, showed to not provide sufficient accuracy concerning the stress balance condition in the cross sections [81]. Other approaches based on relaxing macroscopic stresses by cutting or extracting small geometries from sister samples were conducted by several researchers [31,85,91,108–112]. Although some inconsistencies in defining a representative d_0^{hkl} from measurements on macroscopically stress-free samples have been reported, approaches to determine d_0^{hkl} using coupons (or small pieces of the printed part) are widespread; to date, this approach is considered the best to produce a reliable measured d_0^{hkl} .

6.1.4. Stress and Moment Balance

Another method to determine a d_0^{hkl} is based on the continuum mechanics-based requirements that force and moment must balance across selected cross sections or over the whole specimen [27]. Therefore, by mapping the d^{hkl} in the required sample region the reference d_0^{hkl} can be iteratively found by imposing stress and moment balance, even starting from a nominal value [27]. However, great care must be taken to prove the applicability of the method: the experimental data must cover the whole cross section and it must be ensured that a global d_0^{hkl} is appropriate (i.e., the method would not work if d_0^{hkl} varies across the sample) [27]. Serrano-Munoz et al. [107] applied this method to obtain a d_0^{hkl} for different cross sections of LPBF manufactured Inconel 718 prisms. The method produced a similar d_0^{hkl} , indicating no dependence on the scanning strategy and the cross section being analyzed (i.e., there is no spatial variation of d_0^{hkl} along the length of the sample). Therefore, an average value was used for the d_0^{hkl} in the RS calculation [107], which applicability was later shown [80].

In fact, Kolbus et al. [103] proposed the method of stress balance as a possibility to check the measured d_0^{hkl} , as also indicated by Withers et al. [27]. To cross-check the values measured on mechanically relaxed samples, Pant et al. [81] used the stress balance approach and found a significant difference. Such discrepancy was attributed to microstructural variations: the average d_0^{hkl} value obtained by stress balance was used for the final RS calculations. Stress balance is often applied as an alternative approach to obtain a d_0^{hkl} without additional experimental effort [86,113]. However, in order to check the applicability of the hypotheses mentioned above, one should always compare the results (stress fields, d_0^{hkl}) obtained by using the stress balance condition with those obtained using experimental methods [27,80,103].

Indeed, the applicability of the stress balance approach for AM materials, which possibly exhibit 2D or 3D chemical variations due to the differential cooling rates, still requires further experimentation to test the robustness of the approach. Although this method would aid to make the RS determination by diffraction fully non-destructive, great care must be taken to avoid large errors in the RS values. In fact, Wang et al. [31] showed a LMD manufactured Inconel 625 wall displayed local variations of d_0^{hkl} due to the chemical and microstructural heterogeneity of the builds (Figure 10). This fact impeded the applicability of the stress balance condition.

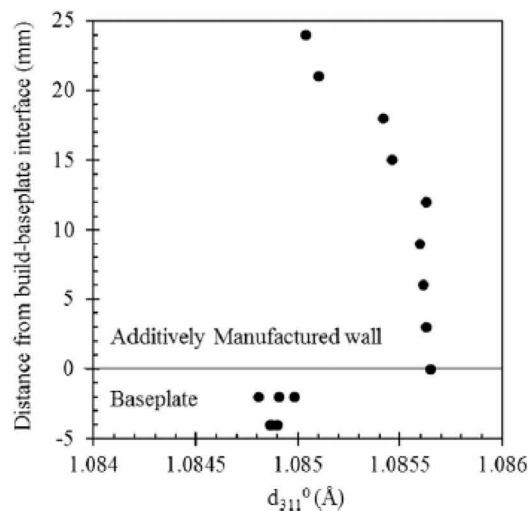


Figure 10. Reference d_0^{311} as a function of distance from the build-baseplate interface measured by neutron diffraction in the 40 s dwell time stress-free reference samples without heat treatment. Reproduced from [31] with permission from Elsevier.

The following table (Table 1) summarizes available methods to obtain d_0^{hkl} . It also reports the references in which each method was applied (in the case of laser-based AM parts).

Table 1. Overview of the different methods to obtain a d_0^{hkl} in the domain of laser-based AM.

Method	Advantages	Disadvantages	References
Cubes/ matchsticks	<ul style="list-style-type: none"> Can capture spatial variations when taken from several regions Represent thermal history Contain same chemical segregation if taken from representative twin 	<ul style="list-style-type: none"> Need a sister sample Require precise sample alignment Contain possible type I and II stresses Display possible anisotropy of d_0^{hkl} depending on direction Are destructive for twin or actual specimen 	[79,82,103, 109,110,112]
Comb/arrays	<ul style="list-style-type: none"> Can capture spatial variations Are easier to align (relative to cubes) Are easier to extract with respect to cubes taken from distinct positions 	Same as Cubes/matchsticks and: <ul style="list-style-type: none"> Are time consuming to measure Require twin or destruction of specimen 	[31,46,80,81, 91,111]
Stress balance	<ul style="list-style-type: none"> Does not need twin sample Is fully non-destructive 	<ul style="list-style-type: none"> Cannot capture spatial variations of d_0^{hkl} Only works with a high density of measurement points over a cross section Needs to be experimentally verified 	[80,81,86,103, 107,113]
Feedstock powder	<ul style="list-style-type: none"> Is easily obtained for powder-based AM 	<ul style="list-style-type: none"> Does not represent the thermal history of the AM process Has different segregation from the AM part 	[82,103,107]
Powder filings	<ul style="list-style-type: none"> Represent thermal history of the sample 	<ul style="list-style-type: none"> Are plastically deformed Need a twin specimen (or partially destroy the specimen) Can yield spatially resolved d_0^{hkl} only if extracted from distinct locations 	[82,107]
$\text{Sin}^2\psi$	<ul style="list-style-type: none"> Is fully non-destructive 	<ul style="list-style-type: none"> Can only be applied for plane stress states Relies on the DECs 	[38,82]

6.2. Principal Stress Directions

A simplification of Equation (3) with the hypothesis of isotropic elastic constants (i.e., with the use of E , Young's modulus, and ν Poisson's ratio) would read for normal stress and strain components ($ii = xx, yy, zz$ in cartesian coordinates) [94]:

$$\sigma_{ii} = \frac{E^{hkl}}{(1 + \nu^{hkl})} \left[\varepsilon_{ii} + \frac{\nu^{hkl}}{(1 - 2\nu^{hkl})} (\varepsilon_{xx} + \varepsilon_{yy} + \varepsilon_{zz}) \right] \quad (14)$$

For isotropic materials, Equation (14) is valid also in presence of shear stress [114]. However, without the knowledge about the principal stress directions, such a determination would not necessarily capture the maximum stress values. A common assumption to reduce the experimental effort is, that the principal stress directions coincide with the sample geometrical axes (e.g., see [82,83,103,110,115]). If the principal stress directions are known, Equation (14) can be used to calculate the principal stress components. This would reduce the number of measurements needed down to 3, if d_0^{hkl} is known. In the general case, where the principal stress axes are not known particular attention (and effort) needs to be dedicated to this aspect. In AM parts, the determination of the principal stress directions goes through the knowledge of the manufacturing process and of its impact on the principal stress directions.

Although several process parameters largely influence the magnitude of the RS, such as layer thickness, scanning speed, beam power, and vector length, the major influencing

parameter on the stress distribution (and principal axes) is the relative orientation of the scanning pattern to the corresponding geometry [107].

Investigations about the principal stress direction in AM-Material started on simple geometries such as prisms [108]. Six strain directions were used for the calculation of the principal stress direction, which was not found to coincide with the sample geometrical ones. In contrast, complex structures were investigated by Fritsch et al. [116] using ND. It was shown, that for LPBF manufactured IN 625 lattice structures measurements along 6 independent strain directions are not sufficient to determine the principal stress directions and magnitudes. The authors found that at least seven independent directions are required to experimentally determine the direction of principal stress and even 8 directions are needed if the correct RS magnitude needs to be determined. In that case the calculated directions become insensitive to the choice of the measurement directions. Furthermore, it was proven that the RS tensor ellipsoid axes align well with the orientation of the struts within the lattice structure. [116].

Gloaguen et al. [46] showed, for example, that when assuming the principal stresses along the geometrical specimen axes for LPBF manufactured Ti6Al4V, the RS is affected by significant errors. This can be attributed to the fact that the principal stress axes deviate from the sample axes. This observation was made even though a simple bidirectional scanning strategy along the geometry with a 90° interlayer rotation was applied.

In fact, Vrancken [117] found for LPBF manufactured Ti6Al4V produced by a comparable scanning strategy, that the principal stress directions coincide with the direction of the scanning tracks. In other studies researchers found the principal stress directions to align with the sample geometrical axes [76,82], if the scanning strategy is more complicated (e.g., rotation between subsequent layers etc.).

These results emphasize that an increasing part complexity requires advanced measurement techniques and strategies to reach the desired precision for a reliable assessment of RS states. Again, given the complexity of laser-based additive manufacturing processes, the general assumption that the principal stress directions are governed by the sample geometry must be used carefully [46]. Therefore, for the alignment of the specimen in the laboratory coordinate system it is recommended not to make any assumption about the principal direction of stress and measure at least eight independent directions at all locations.

6.3. Diffraction-Elastic Constants (DECs)

To obtain stress values, the DECs act as proportionality constants to link the measured microscopic (i.e., lattice) strains to macroscopic stresses (see Equation (3)). Their precise knowledge is important, because the magnitude of the resulting RS depends on the values of the DECs (see Equation (3)). RS are thus highly vulnerable to errors if reliable values of the DEC are not used.

Two methods are available to obtain the DECs: They can be calculated from the single crystal elastic constants (SCEC) using different theoretical schemes (for instance a grain interaction model for the polycrystalline aggregate). This method is to be preferred if the SCECs are reliably known (note that much work needs still to be made for AM materials). The presence of a strong crystallographic texture in conjunction with crystal anisotropy can hamper the determination of the DECs by theoretical calculations, as one must properly take the texture into account. Alternatively, one can directly determine them in an in situ deformation test during diffraction. In this case, the microscopic response is monitored during a macroscopic deformation, and the proportionality constant between applied stress and lattice strain is the plane-specific Young's modulus E^{hkl} . A guideline for this is given in DIN EN 15305 [95]. The latter method, however, is connected to a relatively high experimental effort.

6.3.1. The Anisotropy of Single Crystals

The anisotropy of the single crystal can be expressed by the differences of the different elements of the compliance tensor. For cubic materials Zener [118] proposed the following coefficient, written in the Voigt notation, to calculate the anisotropy of the single crystal:

$$A^Z = \frac{2 \cdot C_{44}}{C_{11} - C_{12}} \tag{15}$$

In this definition, full isotropy is expressed by a value of $A^Z = 1$. Any deviation from $A^Z = 1$ signifies a certain degree of crystal anisotropy. However, as the Zener ratio only remains valid in the cubic case, researchers were motivated to formulate a more general anisotropy index, which would be valid for an arbitrary crystal structure. Such an index (A^U) was derived by Rangathan and Ostoja-Starzewski [119]. It is based on the fractional difference between the upper (Voigt) and lower (Reuss) bounds on the bulk (κ^V , κ^R) and shear (μ^V , μ^R) moduli. The values can be determined by the following equation (Equation (16)).

$$A^U = \frac{\kappa^V}{\kappa^R} + 5 \frac{\mu^V}{\mu^R} - 6 \tag{16}$$

The main advantage of this formulation is its applicability to any type of crystal symmetry. However, it remains a relative measure of anisotropy. In fact, it has not been proven, that a crystal with twice an A^U also is twice as anisotropic. Therefore, Kube [120] provided an alternative definition, the anisotropy index A^L (Equation (17)), whereby the value of $A^L = 0$ expresses isotropy.

$$A^L(C^V, C^R) = \sqrt{\left[\ln\left(\frac{\kappa^V}{\kappa^R}\right) \right]^2 + 5 \left[\ln\left(\frac{\mu^V}{\mu^R}\right) \right]^2} \tag{17}$$

There are also different approaches such as the Ledbetter and Migliori ratio [121] or the method proposed by Chung and Buessem [122]. However, we will use A^L in the following to compare the single crystal anisotropy of the commonly materials used in laser-based AM. One last important remark must be made: the applicability of all DEC calculation schemes heavily rests on the availability of reliable SCEC. A compiled list with the single crystal elastic constants (SCEC) of important alloys for laser based additive manufacturing is given in Table 2. The significant difference in the elastic anisotropy of the different single crystals is evident. The data shown are mainly inferred from measurements on conventionally produced polycrystalline materials or represent measurements on the respective single crystals. Data directly related to additively manufactured materials are still lacking. This may have an impact on the determination of the DECs and of RS. This is because the calculation of DECs is made under the assumption, that tabulated SCECs are still suitable for additively manufactured materials. Nevertheless, some authors have already tackled the problem of the determination of SCEC from experimental data on textured polycrystalline alloys [123].

Table 2. Single crystal elastic constants (SCEC) of several engineering alloys in GPa, with their dimensionless calculated Zener (A^Z) and universal (A^L) anisotropy ratios. For the calculation of A^L the Matlab script provided by Kube [120] was used.

Material	Crystal Structure	C_{11}	C_{12}	C_{44}	C_{33}	C_{13}	Ref.	A^Z	A^L [$\cdot 10^{-2}$]
Aluminium	FCC	108.2	61.3	28.5	-	-	[124]	1.2	2.04
		107.9	60.4	28.6	-	-	[125]	1.2	1.85
		106.8	60.7	28.2	-	-	[126]	1.2	2.18
		112.4	66.3	27.7	-	-	[127]	1.2	1.81
		108.2	62.2	28.4	-	-	[128]	1.2	2.38
		105.6	63.9	28.5	-	-	[129]	1.4	5.22
		107.3	60.9	28.3	-	-	[130]	1.2	2.12
Average		108.1	62.2	28.3	-	-	-	1.2	2.35
Ti6Al4V	HCP	150	83	42	137	53	[123]	-	5.67

Table 2. Cont.

Material	Crystal Structure	C_{11}	C_{12}	C_{44}	C_{33}	C_{13}	Ref.	A^Z	A^L [$\cdot 10^{-2}$]
Inconel 625	FCC	243.3	156.7	117.8	-	-	[131]	2.7	51.88
		240.9	140.5	105.7	-	-	[132]	2.1	29.17
Inconel 718	FCC	259.6	179	109.6	-	-	[133]	2.7	51.85
		231.2	145.1	117.2	-	-	[134]	2.7	51.95
		Average	243.9	154.9	110.8	-	-	-	2.5
316L	FCC	191.2	117.9	138.6	-	-	[135]	3.8	89.33
		215.9	144.6	128.9	-	-	[136]	3.6	83.72
		198	125	122	-	-	[137]	3.3	71.38
Average		204.4	131.8	128.8	-	-	-	3.6	81.41

6.3.2. Grain Interaction Models for the Calculation of DECs

Several models have been developed to calculate DECs from SCEC. The first model developed by Voigt [138] (Figure 11a) assumes that adjacent grains undergo the same strain during deformation. However, this assumption violates the equilibrium of forces at the interfaces. On the other hand, Reuss [139] later proposed a model where the equilibrium of forces is fulfilled as a homogenous stress state is assumed (Figure 11b). This leads to the problem, that the different crystals undergo different strains, which would not satisfy the compatibility conditions [114]. To solve these problems Kröner developed a model based on Eshelby's theory [140], which fulfills the interface and the compatibility conditions (Figure 11c). Such scheme considers a spherical particle of arbitrary anisotropy embedded in an isotropic material. With the assumption of spherical particles and isotropic matrix, Kröner derived a closed (analytical) solution to the problem [141]. If the surrounding matrix is not texture free (e.g., as in the case of AM materials), numerical approaches must be considered [141]. In general, the Voigt model is the least applicable, as it results in elastic properties, such as E^{hkl} , that are independent on the plane $\{hkl\}$. This does not apply for most crystals. In contrast, the Kröner model has been shown to well match to experimentally determined values in an excellent manner for non-textured microstructures [142–144]. Interestingly, if a strong texture is present, as it has been observed in certain cases (including AM materials), the Reuss model displays better agreement with experimental data [32]. In fact, for columnar structures (the case of AM microstructures) the assumption that each crystal undergoes the same stress could be a good approximation.

From the discussion above, it is clear that for the application of each model, the microstructure and texture present in the material must be considered to determine appropriate values for the DECs. Indeed, many modifications and developments of the three schemes mentioned above have been made over the past years, to encompass the microstructure in the calculation of DECs. Initially, Dölle and Hauk [145] introduced the so-called stress factors to account for the texture using the crystallographic orientation distribution function (ODF). Several authors (e.g., Slim et al. [146], Brakman et al. [147], Welzel et al. [148–150], Gnäupel-Herold et al. [151]) proposed alternative approaches to embed the ODF in the determination of the DECS. More recently Mishurova et al. [40] have shown, that the use of Wu's tensor [152] is equivalent to using Kröner's approach. In addition, they showcased the applicability of the procedure to LPBF Ti6Al4V. They concluded that, since hexagonal polycrystals possess transverse isotropy and LPBF Ti6Al4V had a fiber texture, the calculated DECs (using the best-fit isotropy assumption) reasonably agreed with experimentally determined values.

6.3.3. Experimental Determination of Diffraction Elastic Constants

The main method for the experimental determination of DECs are in situ mechanical tests, i.e., during high-energy X-ray or neutron diffraction experiments. The response of each lattice plane is monitored as a function of applied stress. It is important to mention that this approach rests on the hypothesis that a statistically significant ensemble of grains with the normal to the planes $\{hkl\}$ is oriented along the load axis. From these datasets, the

DECs for each monitored plane then can be derived (see Table 3). For LPBF Ti6Al4V and IN718 a comparison of the model prediction with experimentally obtained values is given in Figure 12.

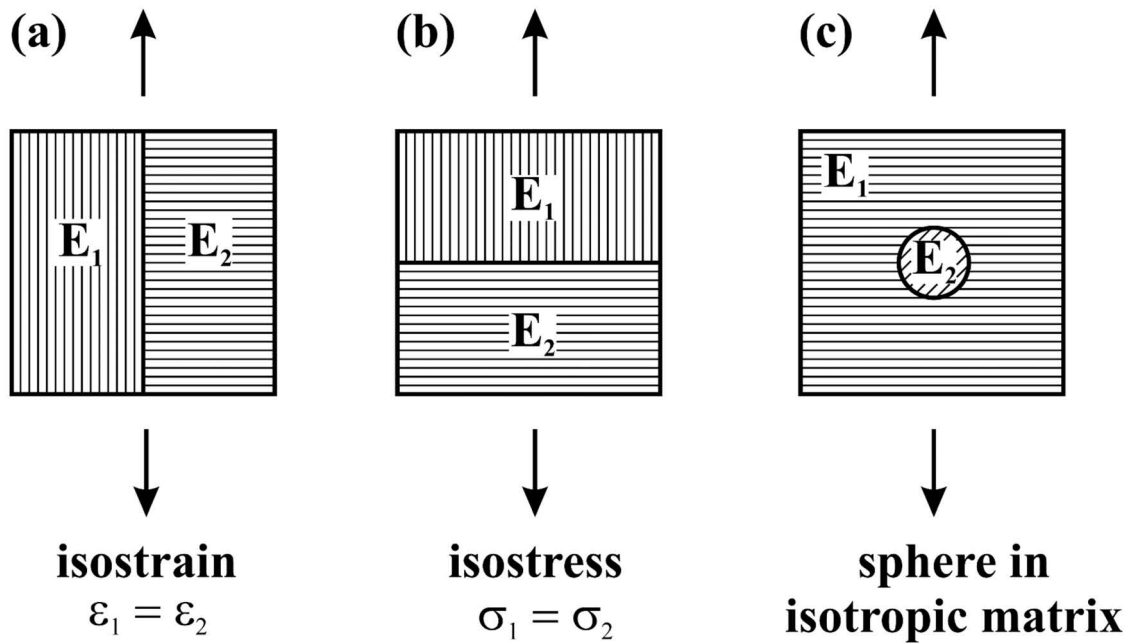


Figure 11. Overview of different model approaches for the calculation of the diffraction elastic constants. (a) Voigt model [138] (b) Reuss model [139] (c) Eshelby–Kröner model [141].

Table 3. Experimentally determined diffraction elastic constants by the means of diffraction methods. The plane-specific elastic moduli (E^{hkl}) are given in GPa.

Material	Process	Condition	E^{200}	E^{311}	E^{420}	E^{220}	E^{331}	E^{111}	Ref.	
AlSi10Mg	LPBF	As built tension	66	68	-	71	-	73	[153]	
IN625	LMD	As built compression	123	156	169	210	219	278	[131]	
IN718	LPBF	FHT * tension	194	196	231	-	230	-	[39]	
IN718	LPBF	DA ** tension	152	173	173	199	227	197	[39]	
316L	LPBF	As built tension	139	180	-	219	-	246	[154]	
Ti6Al4V	LPBF			$E^{10\bar{1}0}$	$E^{10\bar{1}1}$	$E^{11\bar{2}2}$	E^{0002}	$E^{10\bar{1}2}$	$E^{10\bar{1}3}$	
		As built tension		110	106	117	-	107	117	
		HT-730 tension		106	116	126	134	128	125	[155]
		HT-900 tension		111	114	113	132	118	127	
			$E^{21\bar{3}0}$	$E^{11\bar{2}0}$	$E^{10\bar{1}1}$	$E^{11\bar{2}2}$	$E^{20\bar{2}3}$	$E^{10\bar{1}2}$	$E^{10\bar{1}3}$	
As built tension		108	110	115	115	116	120	125		
As built compression		-	115	-	117	123	125	126	[156]	

* FHT (°C/h/MPa): 1066/1.5 + 1150/3/105 + 982/1 + 720/8 + 620/10, ** DA (°C/h): 1066/1.5 + 720/8.

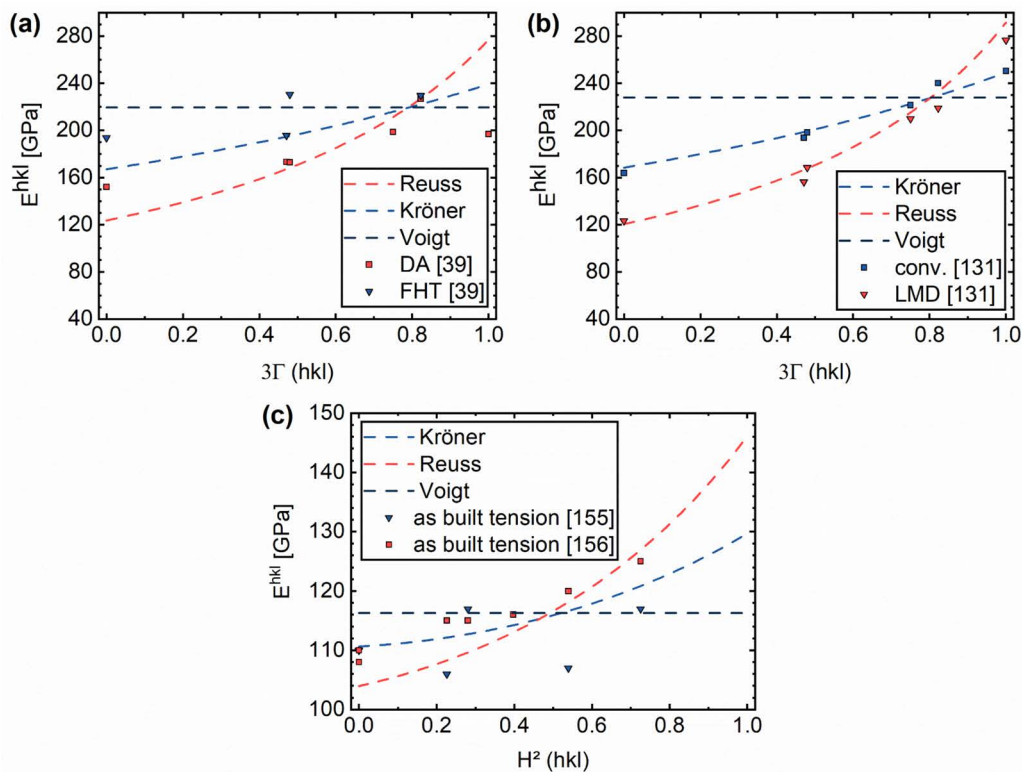


Figure 12. Comparison of the model predictions of Reuss, Voigt and Kröner for Ni-based alloys Inconel 718 (a), Inconel 625 (b) [39] and Ti6Al4V [155,156] (c).

For the alloys 316L and AlSi10Mg such a comparative figure is not necessary, since the model prediction of Kröner nearly perfectly matches the experimental values of the elastic moduli [153,154]. This is different for additively manufactured Ti6Al4V, Inconel 718 and Inconel 625. For a recrystallized and, thus, untextured microstructure (FHT) the Kröner model best matches the experimental values (Figure 12a) [39]. When, on the contrary, the columnar as-built microstructure (exhibiting relatively strong crystallographic texture) was retained, the model prediction of Reuss best fit the experimental data for Inconel 718 and 625 (Figure 12a,b) [39,131]. The AM Ti6Al4V alloy seems to deviate from this behavior: Mishurova et al. [156] showed, that for low H^2 (prismatic planes) the model predictions by Kröner agreed better with experimental data than other schemes (Figure 12c). In contrast, for higher H^2 (basal planes) the model prediction of Reuss better matched with the data [156]. This can be explained by the transverse isotropy of the single crystal elastic tensor, exhibiting an isotropic behavior in the basal directions but a strong anisotropy along its c-axis. It has been shown that when considering the transversal isotropy in the material model a reasonable agreement between model and experimental data can be obtained [40]. In presence of crystallographic texture, materials with a higher anisotropy factor (Table 2) tend to be better described by the predictions of the Reuss model than by those of Kröner's scheme. The exception to this trend is given by the alloy 316, for which the model approach of Kröner yields a good prediction of the polycrystal behavior, although the single crystal itself is highly anisotropic [154]. Such an agreement can be explained by the rather weak crystallographic texture along the loading direction in conjunction with the relatively small grain size [154].

As Mishurova et al. [45,156] argue, it is mandatory to report the DECs used to obtain stress values if one wants to compare own data with literature. Severe differences in the RS magnitude are the consequence if different model predictions considered for the determination of DEC. This was shown by Serrano-Munoz et al. [38] for LPBF manufactured Inconel 718: Applying the Kröner model led to a spiky stress depth profile. Stress values

of 1200 MPa were reached, which far exceed the yield strength of the non-heat-treated material (630–800 MPa). Much more realistic stress values (up to 870 MPa) were obtained by applying the Reuss model to the experimental data. Also, the spikes of the stress depth profile were smoothed. This indicates the ability of the Reuss model to reasonably describe the intergranular behavior of LPBF Inconel 718 [157]. This was also supported by the findings of Pant et al. [81], who found stresses up to 1000 MPa in their study of as built LPBF manufactured Inconel 718. They used DEC values measured for conventionally manufactured Inconel 718 and nearly equal to the Kröner model calculations [158].

Currently, a lack of consistency is observable in the open literature, as summarized in Table 4. It is to remark that, so far, DEC values of additively manufactured microstructures have been mainly determined for loading along the building direction. The micromechanical behavior of the microstructure perpendicular to the build direction is, to the best of the authors' knowledge, not yet reported.

Table 4. Origins of applied diffraction elastic constants used for stress calculation in additively manufactured specimens.

Origin of DEC	References
Not given	[75,76,85,88,109,113,159–163]
unknown origin	[10,103,110,164]
Experimental values (conventional)	[81,86,165,166]
Reuss Model	[38,107,167]
Eshelby–Kröner Model	[13,26,74,79,82,83,96,108,112,168–170]
Voigt–Reuss–Hill	[171]
Experimental values (AM)	[31,115]

To summarize, in order to reliably calculate the DEC values the proper SCECs of the material and both the microstructure and texture of the specimen should be considered. The crystal and macroscopic anisotropy provide guidance for the choice of the model to consider.

One last remark must be made: To obtain the plane specific Poisson ratio (ν^{hkl}) one would have to track the same set of grains during the deformation in both, the transverse and axial direction (i.e., along the tensile axis) [156]. However, this is practically impossible. In the case of nearly texture-free conventionally manufactured materials with small grain size the calculation of the ν^{hkl} using measurements in two perpendicular sample direction is a good approximation, as the gauge volume contains a sufficient amount of randomly oriented crystals. This approximation, in contrast, cannot be made for strongly textured AM materials. In this case, the use of suitable model schemes is recommended.

6.4. Choice of the Appropriate Lattice Planes

In the angular dispersive (monochromatic) case, one uses specific grains with specific lattice orientations as strain monitors [172]. It is assumed that the statistical ensemble is representative of the material. However, because of their particular elastic and plastic response, these grains are not necessarily representative of the overall stress state [172]. Consequently, the choice of a suitable reflection, whose grains represent the macroscopic RS in a body, is of utter importance [172,173]. Thereby, three main aspects need to be addressed:

- Insensitivity to intergranular stress accumulation (material dependent)
- Crystal symmetry
- Texture of the material

Whenever a sample is under stresses, a superposition of macroscopic (Type I) and intergranular stress (Type II) occurs [172]. If our goal is to determine the macroscopic stress state, a lattice plane, which exhibits a low tendency to accumulate intergranular stresses during deformation should be chosen. This tendency can be tested during in-situ loading experiments. Increasing non-linearity of the lattice plane response to a macroscopic load is an indication for the intergranular strain accumulation [174,175]. In fact, if the lattice strain

vs. applied stress curve is non-linear residual strain is retained upon unloading. Such residual strain increases with increasing macroscopic plastic deformation.

The accumulation of intergranular stresses is critically dependent on the elastic and plastic anisotropy of the material [175]. In general, it is advisable to choose the lattice planes with the lowest Miller indices possible, as a high multiplicity of the lattice plane helps to reduce the required measurement time.

Besides these general considerations, one should take the underlying texture into account [176]. For example, for a (cubic) material with a strong cube texture, one should use the 200 reflection in spite of its typically high sensitivity to intergranular strains [172]. In fact, the 200 reflection represents most of the grains in such particular case [172]. For conventionally manufactured materials a general guideline on the selection of an appropriate lattice plane is given in ISO-21432 [177]. However, for AM the situation might be different, as strong textures typically prevail.

Very little studies on the topic of the accumulation of intergranular strains in laser-based AM materials are available in the open literature. Table 5 shows the lattice planes typically considered for RS analysis of different laser-based AM materials and outlines their suitability compared to their conventionally manufactured counterparts. In the case of fcc materials the 311 reflection is almost exclusively used [26,74,82,83,103,108]. However, it has been shown by Choo et al. [178] for LPBF 316L that the {311} oriented grains accumulate more intergranular strain than the {111} and {220} grains, which is in contrast to conventional rolled 316L [179]. In fact, considering the $\langle 220 \rangle$ texture along the building direction [178], the 220 reflection is more easily detected than others, and yields less data scatter. Likewise, Wang et al. [180] observed a strong nonlinear micromechanical response during initial loading of LPBF manufactured 316L, which has been attributed to anisotropic residual strains within the as-built samples. Consequently, the hierarchical heterogeneous microstructures of AM 316L may give rise to significant differences in the buildup of intergranular stresses and should be accounted for.

For hexagonally closed packed (hcp) materials the pyramidal planes {102} and {103} are considered to exhibit low intergranular stress (for conventionally processed materials) [181,182]. However, Cho et al. [183] showed for conventionally manufactured α -Ti-834 that the first eight diffraction peaks (i.e., those with the lowest Miller indices) accumulate significant intergranular strains. In fact, studies on the topic of intergranular strain accumulation are absent for additively manufactured hcp materials. Although Zhang et al. [155] showed that a high dislocation density is present within the α' Phase of as-built LPBF Ti6Al4V, the micromechanical response show anomalies to conventional Ti6Al4V: sometimes it remains linear well beyond the early stages of loading, sometimes it shows footprints of twinning [184,185]. Thus, the question of the accumulation of intergranular strains is yet far from fully elucidated in AM hcp materials.

In general, more research needs to be dedicated to the topic of intergranular stresses within the domain of laser-based AM materials. One must carefully evaluate whether the requirements are fulfilled for a certain lattice plane to represent the bulk behavior. The approach of using the full pattern refinement of the lattice parameter minimizes (actually, averages) the possible contributions of high intergranular stress to the determined macroscopic type I RS.

Table 5. Material dependent selection of Lattice planes for RS determination in laser-based AM.

Material	AM	Conventional	Conclusion
Inconel 718 (fcc)	<ul style="list-style-type: none"> • DA: <200> texture along BD max. 3 m.r.d (corresponds to loading direction) [39] • 311 only slightly non-linear upon loading [39] • As built: 311 remains linear upon loading (<220> textured along BD) [186] • Heat-treated: 311 shows increased non-linearity (untextured) [186] • 311, 111 linear upon loading in as built condition, with increased non-linearity of (311) in heat-treated condition (possibly γ shedding load to δ) [187] 	<ul style="list-style-type: none"> • Low texture (max. 1.5 m.r.d) [143] • 311, 111 remain linear upon loading [143] • 220 displays non-linearity at larger strains [143] • 222 and 311 accumulate low intergranular strain [143] 	<ul style="list-style-type: none"> • Heat-treatments affect the micromechanical behavior upon loading • 311 appears suitable for as built samples • Texture up to 3 m.r.d has little influence on the choice of the lattice plane
	<ul style="list-style-type: none"> • <220> texture along BD (<200> perpendicular which corresponds to LD max. 4 m.r.d) [154] • 311: remains linear upon loading in the loading direction [154] • 200, 111, 220 display increased non-linearity upon loading [154] • <110> texture along BD (max. 2.8 m.r.d) 311, 200 accumulates significant intergranular strain; 220, 111 accumulate low intergranular strain [178] • Nearly untextured (≈ 1 m.r.d) lower magnitude of total intergranular strain accumulated [178] 	<ul style="list-style-type: none"> • Weak cube texture (max. 2 m.r.d) [179] • 311 slightly non-linear at larger strains [179] • 311, 111 accumulate low residual strain [179] 	<ul style="list-style-type: none"> • 311 accumulates significant intergranular strain, but remains linear upon loading • 220 lowest intergranular strain accumulation and representative for the bulk (along BD; dependent on processing conditions)
304 (fcc)	<ul style="list-style-type: none"> • Austenite <200> textured perpendicular to BD (max. 3 m.r.d corresponds to loading direction) [188] • 311: Slight increase in non-linearity upon loading [188] • Different behavior in compression/tension for 200, 111, 220 [188] • 200 carries load shed from 220 and 111 [188] 	<ul style="list-style-type: none"> • Low texture (max. 1 m.r.d) [188] • 311: linear behavior [188] • No difference in compression/tension [188] • 200 carries load shed from 220 and 111 [188] 	<ul style="list-style-type: none"> → Comparison to full pattern fit required to draw a general conclusion → Texture must be taken into consideration

Table 5. Cont.

Material	AM	Conventional	Conclusion
AlSiMg10 (fcc)	<ul style="list-style-type: none"> • Texture with max. 3.4 m.r.d [153] • Interphase and intergranular strains between Al matrix and Si particles [153] • Strong non-linearity in plastic region for every reflection [153] • <100> texture along BD with max. 4.5 m.r.d [189] • Al phase accumulates significant residual strains for 220 < 111 < 311 < 200 (parallel to loading direction) [189] • Si phase accumulates significant residual strains for 111 and 311 [189] • Rietveld refinement reasonably agrees with the trend for both Al and Si 311 [189] 	-	<ul style="list-style-type: none"> • Significant residual strains accumulate in 311 • Still 311 displays best agreement with average obtained by Rietveld refinement (represents bulk behavior) • 220 accumulates least residual strain
Ti6Al4V (hcp)	<ul style="list-style-type: none"> • <002> texture along BD (max. 6 m.r.d) in as built specimen [155] • Increased non-linearity for 100, 101, 102 at higher deformations in as built condition [155] • <002> texture along BD [184] • Early deviation from linearity for 002 and 110 (elastic region) [184] • 102 and 103 start to deviate at higher strains [184] • Strong non-linearity for every reflection upon compressive loading for different build orientations (horizontal, 45°, vertical) [185] • Strong twinning formation in vertically build specimen (driven by initial texture) [185] 	<p>Unidirectionally rolled plate (UD) (loading along rolling direction (RD)) [181]:</p> <ul style="list-style-type: none"> • <002> texture along transverse direction (max. 3.8 m.r.d) • 103, 002 accumulate lowest residual strain • Largest in 101, 201 • Cross rolled plate [181]: • <002> texture along RD (max. 3.5 m.r.d) • 103, 002 accumulate lowest residual strain • Largest in 101, 201 • Bar vs. UD plate [182]: • UD: Strong texture up to max. 6 m.r.d • Bar: texture up to max. 2 m.r.d • Low accumulation of residual lattice strains for 102 and 002 in both cases • Larger accumulation of residual lattice strains for 100 and 110 in UD due to stronger texture 	<ul style="list-style-type: none"> • Comparable texture intensity of AM and conventional • Still significant change of micromechanical behavior between additively manufactured and conventional Ti6Al4V • Full pattern fit recommended • For AM materials (along BD) 002 may represent the bulk behavior the best <p>→ Question not resolved: Studies on accumulation of residual strains required</p>

7. Summary & Outlook

Additive manufacturing (AM) methods allow the fabrication of complex structures within a single manufacturing step. Still the heterogeneity of the process often leads to mechanically anisotropic, columnar, and textured microstructures. While one of the biggest challenges in AM is to develop mitigation strategies for the large residual stress that inevitably appears after production, the precise determination of such residual stress remains challenging. Diffraction-based methods provide a powerful tool to non-destructively determine the residual stress. However, the peculiar microstructures of AM materials pose challenges for the characterization of residual stress. Therefore, assumptions and measurement conditions must be chosen with great care:

- First, one must evaluate if the assumption of a biaxial stress state can be justified (e.g., surface measurements with $\sin^2\psi$ method) or a triaxial stress state must be considered. In the latter case, neutron diffraction should be preferred to other techniques and precise knowledge about the strain-free lattice spacing (d_0^{hkl}) is required. To obtain such a reference, measurements on mechanically relaxed samples are recommended. The stress balance method is recommended as a validation method. If the requirements for the correct application of stress balance conditions (no spatial variation of composition with large number of points) are known to be fulfilled, the stress balance method can be used to obtain a global d_0^{hkl} . Still, the strategy to determine d_0^{hkl} needs to be tailored for each case.
- Secondly, the principal stress directions should be known in advance if one wants to determine the maximum stress values. For conventional processes such as forging or rolling these are often known (they coincide with the main geometrical sample axes). In the case of AM, the complexity of the process conditions hinders the prior knowledge of the principal stress directions. Although research indicates the principal directions to be determined by the scanning strategy (i.e., the main stress axes follow the scanning vector) it is recommended to run experimental checks. Ideally the full stress tensor should be characterized.
- Thirdly, the microstructure and texture of the sample should be well characterized. Texture is one of the driving factors for the determination of the diffraction elastic constants (DECs). Furthermore, the DECs are material-dependent, dictated by the single crystal properties. Therefore, choosing the appropriate modeling scheme for the calculation of DECs from single crystal elastic constants is challenging. At best the DECs should be experimentally determined. If that is not possible, it is indispensable to take the microstructure and the texture into account in the selection of the grain-interaction model.
- Lastly, an appropriate lattice plane must be chosen in the case of a monochromatic measurement technique (Laboratory XRD or steady state Neutron sources), as stresses are derived from one single lattice plane. Such plane should be insensitive to accumulation of intergranular strain and possess a high multiplicity, to represent the macroscopic behavior of the sample.

The amount of research dedicated to the methodology of diffraction-based methods in the domain of AM is increasing but still limited. In particular, the understanding of the influence of the microstructure and texture on the DECs should be addressed for all metal AM processes. This would aid to provide a general strategy to determine the DECs for an additively manufactured material. Further research is needed to develop a uniform strategy to determine an appropriate d_0^{hkl} ; this would increase the comparability of results. It is also worthwhile to dedicate research to gain a better understanding of intergranular stress accumulation for the hierarchical structures occurring in laser-based AM.

Author Contributions: Conceptualization, J.S., A.E. and M.S.; methodology, J.S. and A.K.; validation, J.S., T.M. and I.S.-M.; formal analysis, T.M.; investigation, J.S. and A.U.; resources, G.B.; writing—original draft preparation, J.S., A.E. and A.U.; writing—review and editing, J.S., A.E., T.M., A.U., M.S., I.S.-M., T.F., A.K., T.K. and G.B.; visualization, J.S., A.K. and T.F.; supervision, A.E., G.B. and T.K.; project administration, G.B. and T.K. All authors have read and agreed to the published version of the manuscript.

Funding: This research received no external funding.

Institutional Review Board Statement: Not applicable.

Informed Consent Statement: Not applicable.

Data Availability Statement: Not applicable.

Acknowledgments: The authors kindly acknowledge the fruitful scientific discussions on the topic with Michael Hofmann (TU Munich), Winfried Petry (TU Munich), Christoph Genzel (HZB, Berlin), and Manuela Klaus (HZB, Berlin). This work was supported by the internal BAM focus area materials project AGIL “Microstructure development in additively manufactured metallic components: from powder to mechanical failure” and the internally funded project MIT1-2019-45.

Conflicts of Interest: The authors declare no conflict of interest.

References

- Appleyard, D. Powering up on powder technology. *Met. Powder Rep.* **2015**, *70*, 285–289. [[CrossRef](#)]
- Emmelmann, C.; Kranz, J.; Herzog, D.; Wycisk, E. Laser Additive Manufacturing of Metals. *Biol. Med. Phys. Biomed.* **2013**, 143–191. [[CrossRef](#)]
- Kranz, J.; Herzog, D.; Emmelmann, C. Design guidelines for laser additive manufacturing of lightweight structures in TiAl6V4. *J. Laser Appl.* **2015**, *27*, S14001. [[CrossRef](#)]
- Khorasani, M.; Ghasemi, A.; Rolfe, B.; Gibson, I. Additive manufacturing a powerful tool for the aerospace industry. *Rapid Prototyp. J.* **2021**, ahead-of-Print. [[CrossRef](#)]
- Herzog, D.; Seyda, V.; Wycisk, E.; Emmelmann, C. Additive manufacturing of metals. *Acta Mater.* **2016**, *117*, 371–392. [[CrossRef](#)]
- Gallmeyer, T.G.; Moorthy, S.; Kappes, B.B.; Mills, M.J.; Amin-Ahmadi, B.; Stebner, A.P. Knowledge of process-structure-property relationships to engineer better heat treatments for laser powder bed fusion additive manufactured Inconel 718. *Addit. Manuf.* **2020**, *31*, 100977. [[CrossRef](#)]
- Voisin, T.; Forien, J.B.; Perron, A.; Aubry, S.; Bertin, N.; Samanta, A.; Baker, A.; Wang, Y.M. New insights on cellular structures strengthening mechanisms and thermal stability of an austenitic stainless steel fabricated by laser powder-bed-fusion. *Acta Mater.* **2021**, *203*, 116476. [[CrossRef](#)]
- Pröbstle, M.; Neumeier, S.; Hopfenmuller, J.; Freund, L.P.; Niendorf, T.; Schwarze, D.; Goken, M. Superior creep strength of a nickel-based superalloy produced by selective laser melting. *Mater. Sci. Eng. A* **2016**, *674*, 299–307. [[CrossRef](#)]
- Vrancken, B.; Thijs, L.; Kruth, J.P.; Van Humbeeck, J. Heat treatment of Ti6Al4V produced by Selective Laser Melting: Microstructure and mechanical properties. *J. Alloy. Compd.* **2012**, *541*, 177–185. [[CrossRef](#)]
- Yadroitsev, I.; Yadroitsava, I. Evaluation of residual stress in stainless steel 316L and Ti6Al4V samples produced by selective laser melting. *Virtual. Phys. Prototyp.* **2015**, *10*, 67–76. [[CrossRef](#)]
- Kruth, J.P.; Froyen, L.; Van Vaerenbergh, J.; Mercelis, P.; Rombouts, M.; Lauwers, B. Selective laser melting of iron-based powder. *J. Mater. Process. Technol.* **2004**, *149*, 616–622. [[CrossRef](#)]
- Mukherjee, T.; Zhang, W.; DebRoy, T. An improved prediction of residual stresses and distortion in additive manufacturing. *Comput. Mater. Sci.* **2017**, *126*, 360–372. [[CrossRef](#)]
- Mishurova, T.; Cabeza, S.; Artzt, K.; Haubrich, J.; Klaus, M.; Genzel, C.; Requena, G.; Bruno, G. An Assessment of Subsurface Residual Stress Analysis in SLM Ti-6Al-4V. *Materials* **2017**, *10*, 348. [[CrossRef](#)]
- Carpenter, K.; Tabei, A. On Residual Stress Development, Prevention, and Compensation in Metal Additive Manufacturing. *Materials* **2020**, *13*, 255. [[CrossRef](#)]
- Marchese, G.; Parizia, S.; Saboori, A.; Manfredi, D.; Lombardi, M.; Fino, P.; Ugues, D.; Biamino, S. The Influence of the Process Parameters on the Densification and Microstructure Development of Laser Powder Bed Fused Inconel 939. *Metals* **2020**, *10*, 882. [[CrossRef](#)]
- Kanagarajah, P.; Brenne, F.; Niendorf, T.; Maier, H.J. Inconel 939 processed by selective laser melting: Effect of microstructure and temperature on the mechanical properties under static and cyclic loading. *Mater. Sci. Eng. A* **2013**, *588*, 188–195. [[CrossRef](#)]
- Zhang, X.Q.; Chen, H.B.; Xu, L.M.; Xu, J.J.; Ren, X.K.; Chen, X.Q. Cracking mechanism and susceptibility of laser melting deposited Inconel 738 superalloy. *Mater. Des.* **2019**, *183*, 108105. [[CrossRef](#)]
- Muñiz-Lerma, J.A.; Tian, Y.; Wang, X.; Gauvin, R.; Brochu, M. Microstructure evolution of Inconel 738 fabricated by pulsed laser powder bed fusion. *Prog. Addit. Manuf.* **2019**, *4*, 97–107. [[CrossRef](#)]
- Ramakrishnan, A.; Dinda, G.P. Direct laser metal deposition of Inconel 738. *Mater. Sci. Eng. A* **2019**, *740*, 1–13. [[CrossRef](#)]

20. Sotov, A.V.; Agapovichev, A.V.; Smelov, V.G.; Kokareva, V.V.; Dmitrieva, M.O.; Melnikov, A.A.; Golanov, S.P.; Anurov, Y.M. Investigation of the IN-738 superalloy microstructure and mechanical properties for the manufacturing of gas turbine engine nozzle guide vane by selective laser melting. *Int. J. Adv. Manuf. Tech.* **2020**, *107*, 2525–2535. [[CrossRef](#)]
21. Seede, R.; Shoukr, D.; Zhang, B.; Whitt, A.; Gibbons, S.; Flater, P.; Elwany, A.; Arroyave, R.; Karaman, I. An ultra-high strength martensitic steel fabricated using selective laser melting additive manufacturing: Densification, microstructure, and mechanical properties. *Acta Mater.* **2020**, *186*, 199–214. [[CrossRef](#)]
22. Boes, J.; Rottger, A.; Theisen, W.; Cui, C.; Uhlenwinkel, V.; Schulz, A.; Zoch, H.W.; Stern, F.; Tenkamp, J.; Walther, F. Gas atomization and laser additive manufacturing of nitrogen-alloyed martensitic stainless steel. *Addit. Manuf.* **2020**, *34*, 101379. [[CrossRef](#)]
23. Saeidi, K.; Zapata, D.L.; Lofaj, F.; Kvetkova, L.; Olsen, J.; Shen, Z.J.; Akhtar, F. Ultra-high strength martensitic 420 stainless steel with high ductility. *Addit. Manuf.* **2019**, *29*, 100803. [[CrossRef](#)]
24. Lu, Y.; Wu, S.; Gan, Y.; Huang, T.; Yang, C.; Junjie, L.; Lin, J. Study on the microstructure, mechanical property and residual stress of SLM Inconel-718 alloy manufactured by differing island scanning strategy. *Opt. Laser Technol.* **2015**, *75*, 197–206. [[CrossRef](#)]
25. Valdez, M.; Kozuch, C.; Faierson, E.J.; Jasiuk, I. Induced porosity in Super Alloy 718 through the laser additive manufacturing process: Microstructure and mechanical properties. *J. Alloys Compd.* **2017**, *725*, 757–764. [[CrossRef](#)]
26. Nadammal, N.; Mishurova, T.; Fritsch, T.; Serrano-Munoz, I.; Kromm, A.; Haberland, C.; Portella, P.D.; Bruno, G. Critical role of scan strategies on the development of microstructure, texture, and residual stresses during laser powder bed fusion additive manufacturing. *Addit. Manuf.* **2021**, *38*, 101792. [[CrossRef](#)]
27. Withers, P.J.; Preuss, M.; Steuwer, A.; Pang, J.W.L. Methods for obtaining the strain-free lattice parameter when using diffraction to determine residual stress. *J. Appl. Crystallogr.* **2007**, *40*, 891–904. [[CrossRef](#)]
28. Dixneit, J.; Kromm, A.; Boin, M.; Wimpory, R.C.; Kannengiesser, T.; Gibmeier, J.; Schroepfer, D. Residual stresses of LTT welds in large-scale components. *Weld. World* **2017**, *61*, 1089–1097. [[CrossRef](#)]
29. Kromm, A. Evaluation of weld filler alloying concepts for residual stress engineering by means of Neutron and X-ray diffraction. *Adv. Mater. Res.* **2014**, *996*, 469–474. [[CrossRef](#)]
30. Altenkirch, J.; Gibmeier, J.; Kromm, A.; Kannengiesser, T.; Nitschke-Pagel, T.; Hofmann, M. In situ study of structural integrity of low transformation temperature (LTT)-welds. *Mater. Sci. Eng. A* **2011**, *528*, 5566–5575. [[CrossRef](#)]
31. Wang, Z.; Denlinger, E.; Michaleris, P.; Stoica, A.D.; Ma, D.; Beese, A.M. Residual stress mapping in Inconel 625 fabricated through additive manufacturing: Method for neutron diffraction measurements to validate thermomechanical model predictions. *Mater. Des.* **2017**, *113*, 169–177. [[CrossRef](#)]
32. Spieß, L.; Teichert, G.; Schwarzer, R.; Behnken, H.; Genzel, C. *Moderne Röntgenbeugung*, 2nd ed.; Vieweg+Teubner Verlag: Wiesbaden, Germany, 2009. [[CrossRef](#)]
33. Noyan, I.C.; Cohen, J.B. *Residual Stress: Measurement by Diffraction and Interpretation*; Springer: New York, NY, USA, 1987; p. x. 276p.
34. Hauk, V.; Behnken, H. *Structural and Residual Stress Analysis by Nondestructive Methods: Evaluation, Application, Assessment*; Elsevier: Amsterdam, The Netherlands, 1997; p. xiv. 640p.
35. Ye, T.; Li, L.X.; Liu, X.; Liu, W.H.; Guo, P.C.; Tang, X. Anisotropic deformation behavior of as-extruded 6063-T4 alloy under dynamic impact loading. *Mater. Sci. Eng. A* **2016**, *666*, 149–155. [[CrossRef](#)]
36. You, Z.; Fu, H.; Qu, S.; Bao, W.; Lu, L. Revisiting anisotropy in the tensile and fracture behavior of cold-rolled 316L stainless steel with heterogeneous nano-lamellar structures. *Nano Mater. Sci.* **2020**, *2*, 72–79. [[CrossRef](#)]
37. Charmi, A.; Falkenberg, R.; Avila, L.; Mohr, G.; Sommer, K.; Ulbricht, A.; Sprengel, M.; Neumann, R.S.; Skrotzki, B.; Evans, A. Mechanical anisotropy of additively manufactured stainless steel 316L: An experimental and numerical study. *Mater. Sci. Eng. A* **2021**, *799*, 140154. [[CrossRef](#)]
38. Serrano-Munoz, I.; Fritsch, T.; Mishurova, T.; Trofimov, A.; Apel, D.; Ulbricht, A.; Kromm, A.; Hesse, R.; Evans, A.; Bruno, G. On the interplay of microstructure and residual stress in LPBF IN718. *J. Mater. Sci.* **2021**, *56*, 5845–5867. [[CrossRef](#)]
39. Schröder, J.; Mishurova, T.; Fritsch, T.; Serrano-Munoz, I.; Evans, A.; Sprengel, M.; Klaus, M.; Genzel, C.; Schneider, J.; Bruno, G. On the influence of heat treatment on microstructure and mechanical behavior of laser powder bed fused Inconel 718. *Mater. Sci. Eng. A* **2021**, *805*, 140555. [[CrossRef](#)]
40. Mishurova, T.; Bruno, G.; Evsevlev, S.; Sevostianov, I. Determination of macroscopic stress from diffraction experiments: A critical discussion. *J. Appl. Phys.* **2020**, *128*, 025103. [[CrossRef](#)]
41. Bartlett, J.L.; Li, X. An overview of residual stresses in metal powder bed fusion. *Addit. Manuf.* **2019**, *27*, 131–149. [[CrossRef](#)]
42. DebRoy, T.; Wei, H.L.; Zuback, J.S.; Mukherjee, T.; Elmer, J.W.; Milewski, J.O.; Beese, A.M.; Wilson-Heid, A.; De, A.; Zhang, W. Additive manufacturing of metallic components—Process, structure and properties. *Prog. Mater. Sci.* **2018**, *92*, 112–224. [[CrossRef](#)]
43. Acevedo, R.B.O.; Kantarowska, K.; Santos, E.C.; Fredel, M.C. Residual stress measurement techniques for Ti6Al4V parts fabricated using selective laser melting: State of the art review. *Rapid Prototyp. J.* **2020**. [[CrossRef](#)]
44. Fang, Z.C.; Wu, Z.L.; Huang, C.G.; Wu, C.W. Review on residual stress in selective laser melting additive manufacturing of alloy parts. *Opt. Laser Technol.* **2020**, *129*, 106283. [[CrossRef](#)]
45. Mishurova, T.; Serrano-Munoz, I.; Fritsch, T.; Ulbricht, A.; Sprengel, M.; Evans, A.; Kromm, A.; Madia, M.; Bruno, G. A Critical Discussion on the Diffraction-Based Experimental Determination of Residual Stress in AM Parts. In *Structural Integrity of Additive Manufactured Materials and Parts*; Shamsaei, N., Seifi, M., Eds.; ASTM International: West Conshohocken, PA, USA, 2020; pp. 122–138. [[CrossRef](#)]

46. Glogaen, D.; Girault, B.; Courant, B.; Dubos, P.A.; Moya, M.J.; Edy, F.; Kornmeier, J.R. Study of Residual Stresses in Additively Manufactured Ti-6Al-4V by Neutron Diffraction Measurements. *Metall. Mater. Trans. A* **2020**, *51*, 951–961. [[CrossRef](#)]
47. Vayre, B.; Vignat, F.; Villeneuve, F. Metallic additive manufacturing: State-of-the-art review and prospects. *Mech. Ind.* **2012**, *13*, 89–96. [[CrossRef](#)]
48. Kumar, S.; Kruth, J.P. Effect of bronze infiltration into laser sintered metallic parts. *Mater. Des.* **2007**, *28*, 400–407. [[CrossRef](#)]
49. Kruth, J.P.; Vandenbroucke, B.; Van Vaerenbergh, J.; Mercelis, P. Benchmarking of different SLS/SLM processes as rapid manufacturing techniques. In Proceedings of the International Conference Polymers & Moulds Innovations PMI, Gent, Belgium, 20–24 April 2005.
50. Saboori, A.; Aversa, A.; Marchese, G.; Biamino, S.; Lombardi, M.; Fino, P. Application of Directed Energy Deposition-Based Additive Manufacturing in Repair. *Appl. Sci.* **2019**, *9*, 3316. [[CrossRef](#)]
51. Onuike, B.; Bandyopadhyay, A. Additive manufacturing in repair: Influence of processing parameters on properties of Inconel 718. *Mater. Lett.* **2019**, *252*, 256–259. [[CrossRef](#)]
52. Kruth, J.P.; Mercelis, P.; Van Vaerenbergh, J.; Froyen, L.; Rombouts, M. Binding mechanisms in selective laser sintering and selective laser melting. *Rapid Prototyp. J.* **2005**, *11*, 26–36. [[CrossRef](#)]
53. Poprawe, R.; Loosen, P.; Hoffmann, H.-D. The future of high power laser techniques. In *XVI International Symposium on Gas Flow, Chemical Lasers, and High-Power Lasers, Pts 1 and 2*; International Society for Optics and Photonics: Bellingham, WA, USA, 2007; Volume 6346, p. 34602. [[CrossRef](#)]
54. Aboulkhair, N.T.; Everitt, N.M.; Ashcroft, I.; Tuck, C. Reducing porosity in AlSi10Mg parts processed by selective laser melting. *Addit. Manuf.* **2014**, *1–4*, 77–86. [[CrossRef](#)]
55. Oliveira, J.P.; LaLonde, A.D.; Ma, J. Processing parameters in laser powder bed fusion metal additive manufacturing. *Mater. Des.* **2020**, *193*, 108762. [[CrossRef](#)]
56. Buchbinder, D.; Meiners, W.; Pirch, N.; Wissenbach, K.; Schrage, J. Investigation on reducing distortion by preheating during manufacture of aluminum components using selective laser melting. *J. Laser Appl.* **2014**, *26*, 012004. [[CrossRef](#)]
57. von Müller, A.; Schlick, G.; Neu, R.; Anstatt, C.; Klimkait, T.; Lee, J.; Pascher, B.; Schmitt, M.; Seidel, C. Additive manufacturing of pure tungsten by means of selective laser beam melting with substrate preheating temperatures up to 1000 degrees C. *Nucl. Mater. Energy.* **2019**, *19*, 184–188. [[CrossRef](#)]
58. Mohr, G.; Altenburg, S.J.; Hilgenberg, K. Effects of inter layer time and build height on resulting properties of 316L stainless steel processed by laser powder bed fusion. *Addit. Manuf.* **2020**, *32*, 101080. [[CrossRef](#)]
59. Vock, S.; Klöden, B.; Kirchner, A.; Weißgräber, T.; Kieback, B. Powders for powder bed fusion: A review. *Prog. Addit. Manuf.* **2019**, *4*, 383–397. [[CrossRef](#)]
60. Mercelis, P.; Kruth, J.P. Residual stresses in selective laser sintering and selective laser melting. *Rapid Prototyp. J.* **2006**, *12*, 254–265. [[CrossRef](#)]
61. Gu, D.D.; Meiners, W.; Wissenbach, K.; Poprawe, R. Laser additive manufacturing of metallic components: Materials, processes and mechanisms. *Int. Mater. Rev.* **2012**, *57*, 133–164. [[CrossRef](#)]
62. Ruiz, J.E.; Cortina, M.; Arrizubieta, J.I.; Lamikiz, A. Study of the Influence of Shielding Gases on Laser Metal Deposition of Inconel 718 Superalloy. *Materials* **2018**, *11*, 1388. [[CrossRef](#)]
63. Cortina, M.; Arrizubieta, J.I.; Ruiz, J.E.; Lamikiz, A.; Ukar, E. Design and manufacturing of a protective nozzle for highly reactive materials processing via Laser Material Deposition. *Procedia CIRP* **2018**, *68*, 387–392. [[CrossRef](#)]
64. Arrizubieta, J.I.; Ruiz, J.E.; Martinez, S.; Ukar, E.; Lamikiz, A. Intelligent nozzle design for the Laser Metal Deposition process in the Industry 4.0. *Procedia Manuf.* **2017**, *13*, 1237–1244. [[CrossRef](#)]
65. Bernhard, R.; Neef, P.; Eismann, T.; Wiche, H.; Hoff, C.; Hermsdorf, J.; Kaieler, S.; Wesling, V. Additive manufacturing of LMD nozzles for multi-material processing. *Procedia CIRP* **2020**, *94*, 336–340. [[CrossRef](#)]
66. Gruber, S.; Grunert, C.; Riede, M.; Lopez, E.; Marquardt, A.; Brueckner, F.; Leyens, C. Comparison of dimensional accuracy and tolerances of powder bed based and nozzle based additive manufacturing processes. *J. Laser Appl.* **2020**, *32*, 032016. [[CrossRef](#)]
67. Mahamood, R.M. Processing Parameters in Laser Metal Deposition Process. In *Laser Metal Deposition Process of Metals, Alloys, and Composite Materials. Engineering Materials and Processes*, 1st ed.; Springer: Cham, Switzerland, 2018. [[CrossRef](#)]
68. Frazier, W.E. Metal Additive Manufacturing: A Review. *J. Mater. Eng. Perform.* **2014**, *23*, 1917–1928. [[CrossRef](#)]
69. Gibson, I.; Rosen, D.; Stucker, B. Directed Energy Deposition Processes. In *Additive Manufacturing Technologies: 3D Printing, Rapid Prototyping, and Direct Digital Manufacturing*; Springer: New York, NY, USA, 2015; pp. 245–268. [[CrossRef](#)]
70. Withers, P.J.; Bhadeshia, H.K.D.H. Overview—Residual stress part 2—Nature and origins. *Mater. Sci. Technol.* **2001**, *17*, 366–375. [[CrossRef](#)]
71. Withers, P.J.; Bhadeshia, H.K.D.H. Overview—Residual stress part 1—Measurement techniques. *Mater. Sci. Technol.* **2001**, *17*, 355–365. [[CrossRef](#)]
72. Mo, F.J.; Sun, G.G.; Li, J.; Zhang, C.S.; Wang, H.; Chen, Y.; Liu, Z.; Yang, Z.K.; Li, H.J.; Yang, Z.L.; et al. Recent Progress of Residual Stress Distribution and Structural Evolution in Materials and Components by Neutron Diffraction Measurement at RSND. *Quantum Beam Sci.* **2018**, *2*, 15. [[CrossRef](#)]
73. Patterson, A.E.; Messimer, S.L.; Farrington, P.A. Overhanging Features and the SLM/DMLS Residual Stresses Problem: Review and Future Research Need. *Technologies* **2017**, *5*, 15. [[CrossRef](#)]

74. Nadammal, N.; Cabeza, S.; Mishurova, T.; Thiede, T.; Kromm, A.; Seyfert, C.; Farahbod, L.; Haberland, C.; Schneider, J.A.; Portella, P.D.; et al. Effect of hatch length on the development of microstructure, texture and residual stresses in selective laser melted superalloy Inconel 718. *Mater. Des.* **2017**, *134*, 139–150. [\[CrossRef\]](#)
75. Wu, A.S.; Brown, D.W.; Kumar, M.; Gallegos, G.F.; King, W.E. An Experimental Investigation into Additive Manufacturing-Induced Residual Stresses in 316L Stainless Steel. *Metall. Mater. Trans. A* **2014**, *45*, 6260–6270. [\[CrossRef\]](#)
76. Bagg, S.D.; Sochalski-Kolbus, L.M.; Bunn, J.R. The Effect of Laser Scan Strategy on Distortion and Residual Stresses of Arches Made With Selective Laser Melting. In Proceedings of the American Society for Precision Engineering (ASPE), Raleigh, NC, USA, 27–30 June 2016.
77. Schmidt, M.; Merklein, M.; Bourell, D.; Dimitrov, D.; Hausotte, T.; Wegener, K.; Overmeyer, L.; Vollertsen, F.; Levy, G.N. Laser based additive manufacturing in industry and academia. *CIRP Ann.-Manuf. Technol.* **2017**, *66*, 561–583. [\[CrossRef\]](#)
78. Vastola, G.; Zhang, G.; Pei, Q.X.; Zhang, Y.W. Controlling of residual stress in additive manufacturing of Ti6Al4V by finite element modeling. *Addit. Manuf.* **2016**, *12*, 231–239. [\[CrossRef\]](#)
79. Ulbricht, A.; Altenburg, S.J.; Sprengel, M.; Sommer, K.; Mohr, G.; Fritsch, T.; Mishurova, T.; Serrano-Munoz, I.; Evans, A.; Hofmann, M.; et al. Separation of the Formation Mechanisms of Residual Stresses in LPBF 316L. *Metals* **2020**, *10*, 1234. [\[CrossRef\]](#)
80. Serrano-Munoz, I.; Evans, A.; Mishurova, T.; Sprengel, M.; Pirling, T.; Kromm, A.; Bruno, G. The Importance of Subsurface Residual Stress in Laser Powder Bed Fusion IN718. *Adv. Eng. Mater.* **2021**, 2100895. [\[CrossRef\]](#)
81. Pant, P.; Proper, S.; Luzin, V.; Sjoström, S.; Simonsson, K.; Moverare, J.; Hosseini, S.; Pacheco, V.; Peng, R.L. Mapping of residual stresses in as-built Inconel 718 fabricated by laser powder bed fusion: A neutron diffraction study of build orientation influence on residual stresses. *Addit. Manuf.* **2020**, *36*, 101501. [\[CrossRef\]](#)
82. Thiede, T.; Cabeza, S.; Mishurova, T.; Nadammal, N.; Kromm, A.; Bode, J.; Haberland, C.; Bruno, G. Residual stress in selective laser melted Inconel 718: Influence of the removal from base plate and deposition hatch length. *Mater. Perform. Charact.* **2018**, *7*, 717–735. [\[CrossRef\]](#)
83. Mishurova, T.; Cabeza, S.; Thiede, T.; Nadammal, N.; Kromm, A.; Klaus, M.; Genzel, C.; Haberland, C.; Bruno, G. The influence of the support structure on residual stress and distortion in SLM Inconel 718 parts. *Metall. Mater. Trans. A* **2018**, *49*, 3038–3046. [\[CrossRef\]](#)
84. Casavola, C.; Campanelli, S.L.; Pappalettere, C. Preliminary investigation on distribution of residual stress generated by the selective laser melting process. *J. Strain Anal. Eng. Des.* **2009**, *44*, 93–104. [\[CrossRef\]](#)
85. Zaeh, M.F.; Branner, G. Investigations on residual stresses and deformations in selective laser melting. *Prod. Eng.* **2010**, *4*, 35–45. [\[CrossRef\]](#)
86. Moat, R.J.; Pinkerton, A.J.; Li, L.; Withers, P.J.; Preuss, M. Residual stresses in laser direct metal deposited Waspaloy. *Mater. Sci. Eng. A* **2011**, *528*, 2288–2298. [\[CrossRef\]](#)
87. Kruth, J.-P.; Deckers, J.; Yasa, E.; Wauthlé, R. Assessing and comparing influencing factors of residual stresses in selective laser melting using a novel analysis method. *Proc. Inst. Mech. Eng. Part B J. Eng. Manuf.* **2012**, *226*, 980–991. [\[CrossRef\]](#)
88. Liu, Y.; Yang, Y.; Wang, D. A study on the residual stress during selective laser melting (SLM) of metallic powder. *Int. J. Adv. Manuf. Technol.* **2016**, *87*, 647–656. [\[CrossRef\]](#)
89. Cheng, B.; Shrestha, S.; Chou, K.V. Stress and deformation evaluations of scanning strategy effect in selective laser melting. *Addit. Manuf.* **2016**, *12*, 240–251. [\[CrossRef\]](#)
90. Attallah, M.M.; Jennings, R.; Wang, X.; Carter, L.N. Additive manufacturing of Ni-based superalloys: The outstanding issues. *MRS Bull.* **2016**, *41*, 758–764. [\[CrossRef\]](#)
91. Ghasri-Khouzani, M.; Peng, H.; Rogge, R.; Attardo, R.; Ostiguy, P.; Neidig, J.; Billo, R.; Hoelzle, D.; Shankar, M.R. Experimental measurement of residual stress and distortion in additively manufactured stainless steel components with various dimensions. *Mater. Sci. Eng. A* **2017**, *707*, 689–700. [\[CrossRef\]](#)
92. Lu, J.; Society for Experimental Mechanics (U.S.). *Handbook of Measurement of Residual Stresses*; Fairmont Press: Lilburn, GA, USA; Prentice Hall PTR: Upper Saddle River, NJ, USA, 1996; p. xv. 238p.
93. Bragg, W.H.; Bragg, W.L. The reflection of X-rays by crystals. *Proc. R. Soc. Lond. A* **1913**, *88*, 428–438. [\[CrossRef\]](#)
94. Hutchings, M.T.; Withers, P.J.; Holden, T.M.; Lorentzen, T. *Introduction to the Characterization of Residual Stress by Neutron Diffraction*; CRC Press Taylor & Francis Group: Boca Raton, FL, USA, 2005. [\[CrossRef\]](#)
95. DIN-EN-15305. *Non-Destructive Testing—Test Method for Residual Stress Analysis by X-ray Diffraction*; German Institute for Standardization: Berlin, Germany, 2019. [\[CrossRef\]](#)
96. Mishurova, T.; Artzt, K.; Haubrich, J.; Requena, G.; Bruno, G. Exploring the Correlation between Subsurface Residual Stresses and Manufacturing Parameters in Laser Powder Bed Fused Ti-6Al-4V. *Metals* **2019**, *9*, 261. [\[CrossRef\]](#)
97. Genzel, C. Formalism for the Evaluation of Strongly Nonlinear Surface Stress-Fields by X-Ray-Diffraction Performed in the Scattering Vector Mode. *Phys. Status Solidi A* **1994**, *146*, 629–637. [\[CrossRef\]](#)
98. Genzel, C.; Denks, I.A.; Gibmeler, J.; Klaus, M.; Wagener, G. The materials science synchrotron beamline EDDI for energy-dispersive diffraction analysis. *Nucl. Instrum. Meth. A* **2007**, *578*, 23–33. [\[CrossRef\]](#)
99. Giessen, B.C.; Gordon, G.E. X-ray Diffraction—New High-Speed Technique Based on X-ray Spectrography. *Science* **1968**, *159*, 973–975. [\[CrossRef\]](#)
100. Apel, D.; Klaus, M.; Genzel, M.; Genzel, C. Rietveld-based energy-dispersive residual stress evaluation: Analysis of complex stress fields $\sigma_{ij}(z)$. *J. Appl. Crystallogr.* **2014**, *47*, 511–526. [\[CrossRef\]](#)

101. Hollmann, A.; Meixner, M.; Klaus, M.; Genzel, C. Concepts for nondestructive and depth-resolved X-ray residual stress analysis in the near-surface region of nearly single crystalline materials with mosaic structure. *J. Appl. Crystallogr.* **2021**, *54*, 22–31. [[CrossRef](#)]
102. Webster, G.A.; Wimpory, R.C. Non-destructive measurement of residual stress by neutron diffraction. *J. Mater. Process. Technol.* **2001**, *117*, 395–399. [[CrossRef](#)]
103. Kolbus, L.; Payzant, E.; Cornwell, P.; Watkins, T.; Babu, S.; Dehoff, R.; Lorenz, M.; Ovchinnikova, O.; Duty, C. Comparison of Residual Stresses in Inconel 718 Simple Parts Made by Electron Beam Melting and Direct Laser Metal Sintering. *Metall. Mater. Trans. A* **2015**, *46*, 1419–1432. [[CrossRef](#)]
104. Liu, W.C.; Yao, M.; Chen, Z.L.; Wang, S.G. Niobium segregation in Inconel 718. *J. Mater. Sci.* **1999**, *34*, 2583–2586. [[CrossRef](#)]
105. Bobbio, L.D.; Bocklund, B.; Otis, R.; Borgonia, J.P.; Dillon, R.P.; Shapiro, A.A.; McEnerney, B.; Liu, Z.K.; Beese, A.M. Characterization of a functionally graded material of Ti-6Al-4V to 304L stainless steel with an intermediate V section. *J. Alloys Compd.* **2018**, *742*, 1031–1036. [[CrossRef](#)]
106. Carroll, B.E.; Otis, R.A.; Borgonia, J.P.; Suh, J.O.; Dillon, R.P.; Shapiro, A.A.; Hofmann, D.C.; Liu, Z.K.; Beese, A.M. Functionally graded material of 304L stainless steel and inconel 625 fabricated by directed energy deposition: Characterization and thermodynamic modeling. *Acta Mater.* **2016**, *108*, 46–54. [[CrossRef](#)]
107. Serrano-Munoz, I.; Ulbricht, A.; Fritsch, T.; Mishurova, T.; Kromm, A.; Hofmann, M.; Wimpory, R.C.; Evans, A.; Bruno, G. Scanning Manufacturing Parameters Determining the Residual Stress State in LPBF IN718 Small Parts. *Adv. Eng. Mater.* **2021**, *23*, 2100158. [[CrossRef](#)]
108. Bayerlein, F.; Bodensteiner, F.; Zeller, C.; Hofmann, M.; Zaeh, M.F. Transient development of residual stresses in laser beam melting—A neutron diffraction study. *Addit. Manuf.* **2018**, *24*, 587–594. [[CrossRef](#)]
109. Syed, A.K.; Ahmad, B.; Guo, H.; Machry, T.; Eatock, D.; Meyer, J.; Fitzpatrick, M.E.; Zhang, X. An experimental study of residual stress and direction-dependence of fatigue crack growth behaviour in as-built and stress-relieved selective-laser-melted Ti6Al4V. *Mater. Sci. Eng. A* **2019**, *755*, 246–257. [[CrossRef](#)]
110. Brown, D.W.; Bernardin, J.D.; Carpenter, J.S.; Clausen, B.; Spornjak, D.; Thompson, J.M. Neutron diffraction measurements of residual stress in additively manufactured stainless steel. *Mater. Sci. Eng. A* **2016**, *678*, 291–298. [[CrossRef](#)]
111. Woo, W.; Kim, D.-K.; Kingston, E.J.; Luzin, V.; Salvemini, F.; Hill, M.R. Effect of interlayers and scanning strategies on through-thickness residual stress distributions in additive manufactured ferritic-austenitic steel structure. *Mater. Sci. Eng. A* **2019**, *744*, 618–629. [[CrossRef](#)]
112. Pratt, P.; Felicelli, S.D.; Wang, L.; Hubbard, C.R. Residual Stress Measurement of Laser-Engineered Net Shaping AISI 410 Thin Plates Using Neutron Diffraction. *Metall. Mater. Trans. A* **2008**, *39*, 3155–3163. [[CrossRef](#)]
113. Cottam, R.; Wang, J.; Luzin, V. Characterization of microstructure and residual stress in a 3D H13 tool steel component produced by additive manufacturing. *J. Mater. Res.* **2014**, *29*, 1978–1986. [[CrossRef](#)]
114. Hosford, W.F. *Mechanical Behavior of Materials*; Cambridge University Press: Cambridge, UK; New York, NY, USA, 2005; p. xx. 425p.
115. An, K.; Yuan, L.; Dial, L.; Spinelli, I.; Stoica, A.D.; Gao, Y. Neutron residual stress measurement and numerical modeling in a curved thin-walled structure by laser powder bed fusion additive manufacturing. *Mater. Des.* **2017**, *135*, 122–132. [[CrossRef](#)]
116. Fritsch, T.; Sprengel, M.; Evans, A.; Farahbod-Sternahl, L.; Saliwan-Neumann, R.; Hofmann, M.; Bruno, G. On the determination of residual stresses in additively manufactured lattice structures. *J. Appl. Crystallogr.* **2021**, *54*, 228–236. [[CrossRef](#)] [[PubMed](#)]
117. Vrancken, B. *Study of Residual Stresses in Selective Laser Melting*; KU Leuven: Leuven, Belgium, 2016.
118. Zener, C.M. *Elasticity and Anelasticity of Metals*; University of Chicago Press: Chicago, IL, USA, 1948; p. x. 170p.
119. Ranganathan, S.I.; Ostojic-Starzewski, M. Universal elastic anisotropy index. *Phys. Rev. Lett.* **2008**, *101*, 055504. [[CrossRef](#)]
120. Kube, C.M. Elastic anisotropy of crystals. *AIP Adv.* **2016**, *6*, 095209. [[CrossRef](#)]
121. Ledbetter, H.; Migliori, A. A general elastic-anisotropy measure. *J. Appl. Phys.* **2006**, *100*, 063516. [[CrossRef](#)]
122. Chung, D.H.; Buessem, W.R. Elastic Anisotropy of Crystals. *J. Appl. Phys.* **1967**, *38*, 2010–2012. [[CrossRef](#)]
123. Heldmann, A.; Hoelzel, M.; Hofmann, M.; Gan, W.M.; Schmahl, W.W.; Griesshaber, E.; Hansen, T.; Schell, N.; Petry, W. Diffraction-based determination of single-crystal elastic constants of polycrystalline titanium alloys. *J. Appl. Crystallogr.* **2019**, *52*, 1144–1156. [[CrossRef](#)]
124. Dieter, G.E. *Mechanical Metallurgy*, 3rd ed.; McGraw-Hill: New York, NY, USA, 1986; p. xxiii. 751p.
125. Tallon, J.L.; Wolfenden, A. Temperature-Dependence of the Elastic-Constants of Aluminum. *J. Phys. Chem. Solids* **1979**, *40*, 831–837. [[CrossRef](#)]
126. Kamm, G.N.; Alers, G.A. Low-Temperature Elastic Moduli of Aluminum. *J. Appl. Phys.* **1964**, *35*, 327–330. [[CrossRef](#)]
127. Sutton, P.M. The Variation of the Elastic Constants of Crystalline Aluminum with Temperature between 63-Degrees-K and 773-Degrees-K. *Phys. Rev.* **1953**, *91*, 816–821. [[CrossRef](#)]
128. Goens, E. The main resilience constants of monocrystal of copper, gold and lead. *Phys. Z.* **1936**, *37*, 321–326.
129. Lazarus, D. The Variation of the Adiabatic Elastic Constants of Kcl, Nacl, CuZn, Cu, and Al with Pressure to 10,000 Bars. *Phys. Rev.* **1949**, *76*, 545–553. [[CrossRef](#)]
130. Schmunk, R.E.; Smith, C.S. Pressure Derivatives of the Elastic Constants of Aluminum and Magnesium. *J. Phys. Chem. Solids* **1959**, *9*, 100–112. [[CrossRef](#)]
131. Wang, Z.; Stoica, A.D.; Ma, D.; Beese, A.M. Diffraction and single-crystal elastic constants of Inconel 625 at room and elevated temperatures determined by neutron diffraction. *Mater. Sci. Eng. A* **2016**, *674*, 406–412. [[CrossRef](#)]

132. Haldipur, P.; Margetan, F.J.; Thompson, R.B. Estimation of single-crystal elastic constants from ultrasonic measurements on polycrystalline specimens. *AIP* **2004**, *700*, 1061–1068. [[CrossRef](#)]
133. Martin, G.; Ochoa, N.; Sai, K.; Herve-Luanco, E.; Cailletaud, G. A multiscale model for the elastoviscoplastic behavior of Directionally Solidified alloys: Application to FE structural computations. *Int. J. Solids Struct.* **2014**, *51*, 1175–1187. [[CrossRef](#)]
134. Jothi, S.; Merzlikin, S.V.; Croft, T.N.; Andersson, J.; Brown, S.G.R. An investigation of micro-mechanisms in hydrogen induced cracking in nickel-based superalloy 718. *J. Alloys Compd.* **2016**, *664*, 664–681. [[CrossRef](#)]
135. Kikuchi, M. Elastic Anisotropy and Its Temperature Dependence of Single-Crystals and Polycrystal of 18-12 Type Stainless-Steel. *Trans. Jpn. Inst. Met.* **1971**, *12*, 417–421. [[CrossRef](#)]
136. Bradfield, G. Comparison of Elastic Anisotropy of 2 Austenitic Steels. *J. Iron Steel Inst.* **1964**, *202*, 616.
137. Mangalick, M.C.; Fiore, N.F. Orientation Dependence of Dislocation Damping and Elastic Constants in Fe-18cr-Ni Single Crystals. *Trans. Metall. Soc. AIME* **1968**, *242*, 2363.
138. Voigt, W. Ueber die Beziehung zwischen den beiden Elasticitätsconstanten isotroper Körper. *Ann. Phys.* **1889**, *274*, 573–587. [[CrossRef](#)]
139. Reuss, A. Account of the liquid limit of mixed crystals on the basis of the plasticity condition for single crystal. *Z. Angew. Math. Mech.* **1929**, *9*, 49–58. [[CrossRef](#)]
140. Eshelby, J.D. The Determination of the Elastic Field of an Ellipsoidal Inclusion, and Related Problems. *Proc. R. Soc. Lond. Ser. A-Math. Phys. Sci.* **1957**, *241*, 376–396. [[CrossRef](#)]
141. Kröner, E. Berechnung Der Elastischen Konstanten Des Vielkristalls Aus Den Konstanten Des Einkristalls. *Z. Fur Phys.* **1958**, *151*, 504–518. [[CrossRef](#)]
142. Holden, T.M.; Holt, R.A.; Clarke, A.P. Intergranular strains in Inconel-600 and the impact on interpreting stress fields in heat steam-generator tubing. *Mater. Sci. Eng. A* **1998**, *246*, 180–198. [[CrossRef](#)]
143. Wagner, J.N.; Hofmann, M.; Wimpory, R.; Krempaszy, C.; Stockinger, M. Microstructure and temperature dependence of intergranular strains on diffractometric macroscopic residual stress analysis. *Mater. Sci. Eng. A* **2014**, *618*, 271–279. [[CrossRef](#)]
144. Daymond, M.R.; Bouchard, P.J. Elastoplastic deformation of 316 stainless steel under tensile loading at elevated temperatures. *Metall. Mater. Trans. A-Phys. Metall. Mater. Sci.* **2006**, *37*, 1863–1873. [[CrossRef](#)]
145. Dölle, H.; Hauk, V. Influence of Mechanical Anisotropy of Polycrystal (Texture) Upon Stress Evaluation by Means of X-rays. *Z. Fur Met.* **1978**, *69*, 410–417.
146. Slim, M.F.; Alhoussein, A.; Zgheib, E.; Francois, M. Determination of single-crystal elasticity constants of the beta phase in a multiphase tungsten thin film using impulse excitation technique, X-ray diffraction and micro-mechanical modeling. *Acta Mater.* **2019**, *175*, 348–360. [[CrossRef](#)]
147. Brakman, C.M. Diffraction Elastic-Constants of Textured Cubic Materials—The Voigt Model Case. *Philos. Mag. A-Phys. Condens. Matter Struct. Defects Mech. Prop.* **1987**, *55*, 39–58. [[CrossRef](#)]
148. Welzel, U.; Mittemeijer, E.J. Diffraction stress analysis of macroscopically elastically anisotropic specimens: On the concepts of diffraction elastic constants and stress factors. *J. Appl. Phys.* **2003**, *93*, 9001–9011. [[CrossRef](#)]
149. Welzel, U.; Ligot, J.; Lamparter, P.; Vermeulen, A.C.; Mittemeijer, E.J. Stress analysis of polycrystalline thin films and surface regions by X-ray diffraction. *J. Appl. Crystallogr.* **2005**, *38*, 1–29. [[CrossRef](#)]
150. Welzel, U.; Freour, S.; Kumar, A.; Mittemeijer, E.J. Diffraction stress analysis using direction dependent grain-interaction models. *Mater. Sci. Forum* **2005**, *490–491*, 7–12. [[CrossRef](#)]
151. Gnäupel-Herold, T.; Creuziger, A.A.; Iadicola, M. A model for calculating diffraction elastic constants. *J. Appl. Crystallogr.* **2012**, *45*, 197–206. [[CrossRef](#)]
152. Wu, T.T. The effect of inclusion shape on the elastic moduli of a two-phase material. *Int. J. Solids Struct.* **1966**, *2*, 1–8. [[CrossRef](#)]
153. Zhang, X.X.; Lutz, A.; Andrä, H.; Lahres, M.; Gan, W.M.; Maawad, E.; Emmelmann, C. Evolution of microscopic strains, stresses, and dislocation density during in-situ tensile loading of additively manufactured AlSi10Mg. *Int. J. Plast.* **2021**, *139*, 102946. [[CrossRef](#)]
154. Chen, W.; Voisin, T.; Zhang, Y.; Florien, J.B.; Spadaccini, C.M.; McDowell, D.L.; Zhu, T.; Wang, Y.M. Microscale residual stresses in additively manufactured stainless steel. *Nat. Commun.* **2019**, *10*, 4338. [[CrossRef](#)]
155. Zhang, D.C.; Wang, L.Y.; Zhang, H.; Maldar, A.; Zhu, G.M.; Chen, W.; Park, J.S.; Wang, J.; Zeng, X.Q. Effect of heat treatment on the tensile behavior of selective laser melted Ti-6Al-4V by in situ X-ray characterization. *Acta Mater.* **2020**, *189*, 93–104. [[CrossRef](#)]
156. Mishurova, T.; Artzt, K.; Haubrich, J.; Evsevlev, S.; Evans, A.; Meixner, M.; Munoz, I.S.; Sevostianov, I.; Requena, G.; Bruno, G. Connecting Diffraction-Based Strain with Macroscopic Stresses in Laser Powder Bed Fused Ti-6Al-4V. *Metall. Mater. Trans. A* **2020**, *51*, 3194–3204. [[CrossRef](#)]
157. Klaus, M.; Genzel, C. Reassessment of evaluation methods for the analysis of near-surface residual stress fields using energy-dispersive diffraction. *J. Appl. Crystallogr.* **2019**, *52*, 94–105. [[CrossRef](#)]
158. Aba-Perea, P.E.; Pirling, T.; Withers, P.J.; Kelleher, J.; Kabra, S.; Preuss, M. Determination of the high temperature elastic properties and diffraction elastic constants of Ni-base superalloys. *Mater. Des.* **2016**, *89*, 856–863. [[CrossRef](#)]
159. Song, J.; Wu, W.; Zhang, L.; He, B.; Lu, L.; Ni, X.; Long, Q.; Zhu, G. Role of scanning strategy on residual stress distribution in Ti-6Al-4V alloy prepared by selective laser melting. *Optik* **2018**, *170*, 342–352. [[CrossRef](#)]
160. Anderson, L.S.; Venter, A.M.; Vrancken, B.; Marais, D.; van Humbeeck, J.; Becker, T.H. Investigating the Residual Stress Distribution in Selective Laser Melting Produced Ti-6Al-4V using Neutron Diffraction. *Mater. Res. Proc.* **2018**, *4*, 73–78. [[CrossRef](#)]

161. Wang, L.; Felicelli, S.D.; Pratt, P. Residual stresses in LENS-deposited AISI 410 stainless steel plates. *Mater. Sci. Eng. A* **2008**, *496*, 234–241. [[CrossRef](#)]
162. Lesyk, D.A.; Martinez, S.; Mordyuk, B.N.; Dzhemelinskyi, V.V.; Lamikiz, A.; Prokopenko, G.I. Post-processing of the Inconel 718 alloy parts fabricated by selective laser melting: Effects of mechanical surface treatments on surface topography, porosity, hardness and residual stress. *Surf. Coat. Tech.* **2020**, *381*, 125136. [[CrossRef](#)]
163. Li, L.; Pan, T.; Zhang, X.C.; Chen, Y.T.; Cui, W.Y.; Yan, L.; Liou, F. Deformations and stresses prediction of cantilever structures fabricated by selective laser melting process. *Rapid Prototyp. J.* **2021**, *27*, 453–464. [[CrossRef](#)]
164. van Zyl, I.; Yadroitsava, I.; Yadroitsev, I. Residual Stress in Ti6Al4v Objects Produced by Direct Metal Laser Sintering. *S. Afr. J. Ind. Eng.* **2016**, *27*, 134–141. [[CrossRef](#)]
165. Shah, K.; Haq, I.U.; Shah, S.A.; Khan, F.U.; Khan, M.T.; Khan, S. Experimental Study of Direct Laser Deposition of Ti-6Al-4V and Inconel 718 by Using Pulsed Parameters. *Sci. World J.* **2014**, *2014*, 841549. [[CrossRef](#)]
166. Levkulich, N.C.; Semiatin, S.L.; Gockel, J.E.; Middendorf, J.R.; DeWald, A.T.; Klingbeil, N.W. The effect of process parameters on residual stress evolution and distortion in the laser powder bed fusion of Ti-6Al-4V. *Addit. Manuf.* **2019**, *28*, 475–484. [[CrossRef](#)]
167. Serrano-Munoz, I.; Mishurova, T.; Thiede, T.; Sprengel, M.; Kromm, A.; Nadammal, N.; Nolze, G.; Saliwan-Neumann, R.; Evans, A.; Bruno, G. The residual stress in as-built Laser Powder Bed Fusion IN718 alloy as a consequence of the scanning strategy induced microstructure. *Sci. Rep.* **2020**, *10*, 14645. [[CrossRef](#)]
168. Mishurova, T.; Artzt, K.; Haubrich, J.; Requena, G.; Bruno, G. New aspects about the search for the most relevant parameters optimizing SLM materials. *Addit. Manuf.* **2019**, *25*, 325–334. [[CrossRef](#)]
169. Rangaswamy, P.; Griffith, M.L.; Prime, M.B.; Holden, T.M.; Rogge, R.B.; Edwards, J.M.; Sebring, R.J. Residual stresses in LENS[®] components using neutron diffraction and contour method. *Mater. Sci. Eng. A* **2005**, *399*, 72–83. [[CrossRef](#)]
170. Rangaswamy, P.; Holden, T.M.; Rogge, R.B.; Griffith, M.L. Residual stresses in components formed by the laserengineered net shaping (LENS[®]) process. *J. Strain Anal. Eng. Des.* **2003**, *38*, 519–527. [[CrossRef](#)]
171. Vrancken, B.; Wauthle, R.; Kruth, J.-P.; Humbeeck, J. Study of the influence of material properties on residual stress in selective laser melting. In Proceedings of the 24th International SFF Symposium: An Additive Manufacturing Conference, Austin, TX, USA, 12–14 August 2013; pp. 393–407.
172. Clausen, B.; Leffers, T.; Lorentzen, T. On the proper selection of reflections for the measurement of bulk residual stresses by diffraction methods. *Acta Mater.* **2003**, *51*, 6181–6188. [[CrossRef](#)]
173. Daymond, M.R.; Bourke, M.A.M.; VonDreele, R.B.; Clausen, B.; Lorentzen, T. Use of Rietveld refinement for elastic macrostrain determination and for evaluation of plastic strain history from diffraction spectra. *J. Appl. Phys.* **1997**, *82*, 1554–1562. [[CrossRef](#)]
174. Dye, D.; Stone, H.J.; Reed, R.C. Intergranular and interphase microstresses. *Curr. Opin. Solid State Mater. Sci.* **2001**, *5*, 31–37. [[CrossRef](#)]
175. Clausen, B.; Lorentzen, T.; Leffers, T. Self-consistent modelling of the plastic deformation of FCC polycrystals and its implications for diffraction measurements of internal stresses. *Acta Mater.* **1998**, *46*, 3087–3098. [[CrossRef](#)]
176. Daymond, M.R.; Tome, C.N.; Bourke, M.A.M. Measured and predicted intergranular strains in textured austenitic steel. *Acta Mater.* **2000**, *48*, 553–564. [[CrossRef](#)]
177. ISO-21432. *Non-Destructive Testing—Standard Test Method for Determining Residual Stresses by Neutron Diffraction*; International Organization for Standardization: Geneva, Switzerland, 2019. [[CrossRef](#)]
178. Choo, H.; Koehler, M.R.; White, L.P.; Ren, Y.; Morin, D.; Garlea, E. Influence of defect characteristics on tensile deformation of an additively manufactured stainless steel: Evolutions of texture and intergranular strain. *Mater. Sci. Eng. A* **2020**, *791*, 139637. [[CrossRef](#)]
179. Clausen, B.; Lorentzen, T.; Bourke, M.A.M.; Daymond, M.R. Lattice strain evolution during uniaxial tensile loading of stainless steel. *Mater. Sci. Eng. A* **1999**, *259*, 17–24. [[CrossRef](#)]
180. Wang, Y.M.; Voisin, T.; McKeown, J.T.; Ye, J.C.; Calta, N.P.; Li, Z.; Zeng, Z.; Zhang, Y.; Chen, W.; Roehling, T.T.; et al. Additively manufactured hierarchical stainless steels with high strength and ductility. *Nat. Mater.* **2018**, *17*, 63–71. [[CrossRef](#)]
181. Warwick, J.L.W.; Coakley, J.; Raghunathan, S.L.; Tailing, R.J.; Dye, D. Effect of texture on load partitioning in Ti-6Al-4V. *Acta Mater.* **2012**, *60*, 4117–4127. [[CrossRef](#)]
182. Stapleton, A.M.; Raghunathan, S.L.; Bantounas, I.; Stone, H.J.; Lindley, T.C.; Dye, D. Evolution of lattice strain in Ti-6Al-4V during tensile loading at room temperature. *Acta Mater.* **2008**, *56*, 6186–6196. [[CrossRef](#)]
183. Cho, J.R.; Dye, D.; Conlon, K.T.; Daymond, M.R.; Reed, R.C. Intergranular strain accumulation in a near-alpha titanium alloy during plastic deformation. *Acta Mater.* **2002**, *50*, 4847–4864. [[CrossRef](#)]
184. Voisin, T.; Calta, N.P.; Khairallah, S.A.; Forien, J.B.; Balogh, L.; Cunningham, R.W.; Rollett, A.D.; Wang, Y.M. Defects-dictated tensile properties of selective laser melted Ti-6Al-4V. *Mater. Des.* **2018**, *158*, 113–126. [[CrossRef](#)]
185. Vallejos, J.M.; Barriobero-Vila, P.; Gussone, J.; Haubrich, J.; Kelm, K.; Stark, A.; Schell, N.; Requena, G. In Situ High-Energy Synchrotron X-Ray Diffraction Reveals the Role of Texture on the Activation of Slip and Twinning during Deformation of Laser Powder Bed Fusion Ti-6Al-4V. *Adv. Eng. Mater.* **2021**, 2001556. [[CrossRef](#)]
186. Sangid, M.D.; Book, T.A.; Naragani, D.; Rotella, J.; Ravi, P.; Finch, A.; Kenesei, P.; Park, J.-S.; Sharma, H.; Almer, J.; et al. Role of heat treatment and build orientation in the microstructure sensitive deformation characteristics of IN718 produced via SLM additive manufacturing. *Addit. Manuf.* **2018**, *22*, 479–496. [[CrossRef](#)]

187. Capek, J.; Polatidis, E.; Knappek, M.; Lyphout, C.; Casati, N.; Pederson, R.; Strobl, M. The Effect of γ'' and δ Phase Precipitation on the Mechanical Properties of Inconel 718 Manufactured by Selective Laser Melting: An In Situ Neutron Diffraction and Acoustic Emission Study. *JOM* **2021**, *73*, 223–232. [[CrossRef](#)]
188. Brown, D.W.; Adams, D.P.; Balogh, L.; Carpenter, J.S.; Clausen, B.; King, G.; Reedlunn, B.; Palmer, T.A.; Maguire, M.C.; Vogel, S.C. In Situ Neutron Diffraction Study of the Influence of Microstructure on the Mechanical Response of Additively Manufactured 304L Stainless Steel. *Metall. Mater. Trans. A* **2017**, *48*, 6055–6069. [[CrossRef](#)]
189. Zhang, X.X.; Andra, H.; Harjo, S.; Gong, W.; Kawasaki, T.; Lutz, A.; Lahres, M. Quantifying internal strains, stresses, and dislocation density in additively manufactured AlSi10Mg during loading-unloading-reloading deformation. *Mater. Des.* **2021**, *198*, 109339. [[CrossRef](#)]

On the influence of heat treatment on microstructure and mechanical behavior of laser powder bed fused Inconel 718

P2

J. SCHRÖDER, T. MISHUROVA, T. FRITSCH, I. SERRANO-MUNOZ, A. EVANS,
M. SPRENGEL, M. KLAUS, C. GENZEL, J. SCHNEIDER, G. BRUNO

19th November 2020

Materials Science & Engineering A 805 (2021) 140555

DOI: 10.1016/j.msea.2020.140555

0 Preface

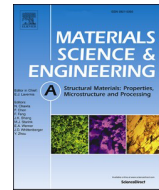
One of the key necessities for the characterization of residual stress by means of diffraction-based methods is governed by knowledge on the connection between the microstructure, the texture, and the mechanical properties. As such, the diffraction elastic constants represent the micromechanical behavior of the material of interest. Therefore, appropriate constants need to be used to convert diffraction measurements into macroscopic stress. Moreover, heat treatments are required to achieve the desired mechanical performances of laser powder bed fused Inconel 718. Those heat treatments may significantly change the microstructure and the crystallographic texture. In this article, two different heat treatments are applied to as-built PBF-LB/M/IN718 and the mechanical behavior is studied, both, on the macro and micro scale. It is shown how tailored heat treatments can change the microstructure and texture, whilst also affect which diffraction elastic constants represent the material behavior.

Reprinted from Materials Science & Engineering A, **805** (2021), Jakob Schröder, Tatiana Mishurova, Tobias Fritsch, Itziar Serrano-Munoz, Alexander Evans, Maximilian Sprengel, Manuela Klaus, Christoph Genzel, Judith Schneider, Giovanni Bruno, *On the influence of heat treatment on microstructure and mechanical behavior of laser powder bed fused Inconel 718*, 140555, Copyright (2020), with permission from Elsevier B.V.



Contents lists available at ScienceDirect

Materials Science & Engineering A

journal homepage: <http://www.elsevier.com/locate/msea>

On the influence of heat treatment on microstructure and mechanical behavior of laser powder bed fused Inconel 718

Jakob Schröder^{a,*}, Tatiana Mishurova^a, Tobias Fritsch^a, Itziar Serrano-Munoz^a,
Alexander Evans^a, Maximilian Sprengel^a, Manuela Klaus^b, Christoph Genzel^b,
Judith Schneider^c, Giovanni Bruno^{a,d}

^a Bundesanstalt für Materialforschung und -prüfung (BAM), Unter den Eichen 87, 12205, Berlin, Germany

^b Helmholtz-Zentrum Berlin für Materialien und Energie GmbH, Hahn-Meiner Platz 1, 14109, Berlin, Germany

^c Department of Mechanical and Aerospace Engineering, University of Alabama in Huntsville, Huntsville, 35899, USA

^d Universität Potsdam, Institut für Physik und Astronomie, Karl-Liebknecht-Str. 24-25, 14476, Potsdam, Germany

ARTICLE INFO

Keywords:

Electron microscopy
X-ray analysis
Inconel 718
Additive manufacturing (AM)
Mechanical behavior
Diffraction elastic constants (DECs)

ABSTRACT

A range of heat treatments have been developed for wrought Inconel 718 to obtain desired properties. For additively manufactured Inconel 718, the recently developed standard ASTM F3301 provides guidance for heat treatment of powder bed fusion specimens. Although this standard is based on standards developed for wrought Inconel 718, it does not include direct aging. Since direct aging reduces the number of processing steps, it can result in a post processing cost reduction if the desired properties are obtained. In this study, we characterized the microstructure and tensile behavior of Inconel 718 specimens produced by a laser powder bed fusion process. The specimens were heat treated according to two different routines after stress relieving: a full heat treatment versus a one-step direct aging process. Differences in the resulting texture and grain morphology were observed. The ex-situ stress-strain behavior was broadly similar. However, a slight increase in yield strength was observed for the direct aged specimen. In order to understand this behavior, investigations with in-situ synchrotron energy dispersive X-ray diffraction tensile testing revealed differences in the load partitioning among different crystal directions. Importantly, the elastic anisotropy expressed by the magnitude of the diffraction elastic constants showed a dependency on the microstructures.

1. Background

Additive manufacturing (AM) of age hardenable alloys with a significant number of alloying elements results in inhomogeneous microstructures with varying phase distributions and grain sizes [1]. Although AM processing offers significant increases in the freedom of design, the microstructures resulting from high thermal gradients and rapid cooling differ significantly from conventional methods such as wrought, cast or powder metallurgy [1].

One alloy of interest for laser powder bed fusion (L-PBF) processing is the Nickel Based (Ni-based) superalloy Inconel 718. Inconel 718 is a γ'/γ'' age hardenable alloy whose phases are summarized in Table 1 [2–7]. Various heat treatments which have been developed for Inconel 718 are summarized in Table 2. Similarities and differences are noted in the various heat treatment steps, which are dependent on the initial

microstructures formed during manufacturing [8–16].

In castings, a moderate cooling rate can promote the formation of Laves phases. The Laves phases are detrimental to mechanical properties since they deplete the matrix of Niobium (Nb), which is needed for subsequent aging. Therefore, castings use a series of heat treatments including homogenization (HOMO) to reduce elemental segregation and hot isostatic pressing (HIP), to minimize shrinkage voids. Due to the slow cooling (SC) common to HIP and HOMO processing, a subsequent solutionizing (ST) heat treatment is used with a rapid quench (Q) prior to a two-step aging for the formation of the γ'/γ'' strengthening precipitates. The ST/Q heat treatment solutionizes the matrix, although it also precipitates δ phase along the grain boundaries. Thus, the ST greatly influences the morphology of the resulting microstructure [18–21]. The γ'' phase precipitates mainly from the supersaturated solid solution in the range of 718 °C–760 °C, and the γ' phase in the lower temperature

* Corresponding author.

E-mail address: Jakob.Schroeder@bam.de (J. Schröder).

<https://doi.org/10.1016/j.msea.2020.140555>

Received 31 July 2020; Received in revised form 10 November 2020; Accepted 16 November 2020

Available online 19 November 2020

0921-5093/© 2020 Elsevier B.V. All rights reserved.

Table 1
Composition and structure of phases in Inconel 718 [2–7].

Phase	Crystal Structure	Chemical Formula	Nom. volume fraction (%)	Nb Content wt%	Occurrence
γ	FCC	Ni	balance		Matrix
γ'	FCC (L1 ₂)	Ni ₃ (Al,Ti, Nb)	<4	<4	Aging heat treatment
γ''	BCT (DO ₂₂)	Ni ₃ Nb	16	4	Aging heat treatment
δ	Ortho. (DO _a)	Ni ₃ (Nb,Ti)	5	6–8	Solidification, solutionizing and overaging of γ''
Carbide	Cubic	(Nb,Ti)C			Solidification
Laves	HCP (TCP)	(Fe) ₂ (Nb, Mo,Ti)		10–12	Solidification

Table 2
Summary of various heat treatments developed for Inconel 718 given as temperature in °C/time in hours.

Number	SR/SC	HIP/SC	HOMO/Q	ST/Q	Age 1	Age 2
Investment casting [8–10]		1163	1093	954	718/8	621/8
Powder metallurgy [11–13]		1180		980 to 1160	720/8	620/10
AM - ASTM F3301 [17]	1065/1.5	1120-1185/4	Per AMS 5662 or 5664			
Wrought - AMS 5662 [14]				954	718/8	621/10
Wrought - AMS 5663 [15]				941 to 1010	718 to 760/8	621 to 649/10
Wrought - AMS 5664 [16]				1038 to 1066	760/10	649/10

range of 621 °C–649 °C during a typical two-stage aging cycle [2, 22–24]. The γ'' phase precipitates appear as thin ellipsoidal discs which are coherent to the matrix with a cube-to-cube orientation as: $\{100\}_{\gamma'}$ // $\{100\}_{\gamma}$ and $100_{\gamma'} // 100_{\gamma}$ [3]. In contrast, the γ' precipitates, while also being generally coherent to the matrix, exhibit a spherical size of around 20 nm [25]. The effectiveness of the aging process is dependent on the Nb concentration in the γ matrix [2], in addition to the Al/Ti ratio [26].

For wrought Inconel 718, thermo-mechanical working precludes the need for HIP and HOMO processes. Table 2 includes the various standards developed for wrought 718. They differ in response to meeting varying mechanical behavior requirements. The primary variable in processing wrought material is the ST temperature, which in addition to forming a supersaturated matrix prior to the aging heat treatment, controls the morphology of the δ phase and resulting microstructure [18, 22,27–30]. Since re-precipitation of the δ phase is reported to be relatively stable at the lower ST temperatures of 950 °C and 975 °C over times ranging from 0.5 to 24 hours, only slight volume fraction differences with minor change in the mechanical properties are reported [18]. This is reflected in the various standards where AMS 5662 was developed for creep resistance [14], AMS 5663 for high tensile and fatigue strength [15] and AMS 5664 for optimum ductility, impact properties and low temperature toughness [16]. A direct age approach (DATM) was initially introduced by Krueger [31] for wrought alloys as a cost-efficient way to produce turbine discs which require resistance to creep. The solutionizing stage was eliminated since the DATM heat treatment is based on an initial forging operation at 1024 °C which is above the δ solvus temperature. Powder metallurgy (PM) techniques also use HIP to consolidate the powder in the solid state. As there is no solidification

segregation, the material is directly ST after HIPing [11–13]. More recent studies suggest that DA after HIP in PM processing is beneficial for optimization of the yield strength, stress rupture life and ductility [32]. In the study by Chang et al. [32], the DA heat treatment parameters included only the HIP prior to the one step aging. A higher temperature was used to promote the precipitation of γ'' , which is the main strengthening phase in Inconel 718 [32].

In contrast, the non-equilibrium nature of AM favors the formation of non-homogenous microstructures that are different from those of cast or wrought material [32–40]. The high cooling rates in AM processing of Ni-based superalloys are reported to form a strongly textured material; this processing favors one of the $\langle 100 \rangle$ directions of the crystal lattice to align with the direction of the largest heat flow [41]. Nevertheless, the AM processing parameters can be adjusted to influence the resulting texture and microstructure of AM materials [42]. Also note that homogenization treatments at temperatures above 1065 °C can induce recrystallization of the original grain structure. Thus, multi-modal grain size distributions are reported as the heat treatment temperatures increase over 1100 °C at times over 1 hour [19,43–45]. While the presence of residual stress is often cited as the mechanism driving recrystallization [44,45], other studies dispute this correlation [46,47].

Due to the high cooling rates, macrosegregation is usually inhibited. However, the high solidification front velocity favors the formation of cell-like substructures [39,40,48–50], where interdendritic microsegregation of alloying elements generally occurs at the cell walls [39, 40,48–51]. These cellular structures are observed to improve the yield strength of the material [25,52]. As previously mentioned, the formation of Laves phases in the interdendritic regions can be detrimental to mechanical properties [49]. Therefore, a concern with applying a stress relief (SR) used to remove residual stresses and avoid distortion, while homogenizing the microstructure at the same time [51] followed by DA, is the retention of the solidification Laves phases. Furthermore, recent studies on the time-temperature-transformation (TTT) of as-built Ni-based superalloys showed that microsegregations, especially in the interdendritic regions as they are enriched in Nb and Mo, shift the precipitation towards shorter times [53,54]. Specifically, for AM Inconel 718, Kumara et al. [54] showed, that the driving force for δ , γ'' and γ' precipitation is the highest in the interdendritic regions for the respective temperatures.

Since the HIP cycle, listed in Table 3, is in the temperature range of the Laves solvus and above the δ solvus, it could potentially dissolve the microsegregations. However, in a study by Deng et al., a heat treatment at a temperature as high as 1080 °C for 1 hour was used and Laves phases were reported to remain in the interdendritic regions [49]. In contrast, Tucho et al. reported nearly full solutionizing after heat treatment at 1100 °C for 1 hour, where only a few sub-grain boundaries were found to be enriched in Nb based phases [39]. Another characteristic of the as-built L-PBF microstructures is the high dislocation density within the interdendritic regions [35,39,51].

Furthermore, while HIP minimizes solidification voids in castings,

Table 3
Summary of the heat treatment parameters (temperature °C/time in hours).

Gauge section ID	SR/SC	HIP/SC	ST/Q	Age 1	Age 2	Ref.
DA (6 round mm)	1066/1.5	–	–	720/8	–	[43]
FHT (6 round mm)	1066/1.5	1163/3	954/1	720/8	620/10	[43]
DA (3 flat mm)	1066/1.5	–	–	720/8	–	This study
FHT (3 flat mm)	1066/1.5	1150/3	982/1	720/8	620/10	This study
DA (3 round mm)	1066/1.5	–	–	720/8	–	This study
FHT (3 round mm)	1066/1.5	1150/3	982/1	720/8	620/10	This study

the voids in AM can form from non-optimized process parameters or trapped gas in the starting powders or during deposition [47,55–58]. Thus, the effectiveness of the HIPing is dependent on the void formation mechanism. Studies have shown that although HIP reduces the void size in AM, voids have been observed to increase in size during subsequent heat treatments [59,60].

Due to the debate within the literature, various studies on the AM process have investigated the effectiveness of various treatments based on standard procedures developed for wrought and cast [33,43,49,61,62]. The recently developed standard, ASTM F3301, combines the best practices from casting with the various wrought standards for the application to AM Inconel 718. Addressing the residual stress state and internal porosity typical for as-built AM microstructures, the ASTM standard includes SR and HIP heat treatment stages to existing ASM standards for Inconel 718. As introduced above, while a large body of research has investigated the influence of heat treatment post-processing on the mechanical response of L-PBF Inconel 718 materials, few of them deal with the effect of grain structure and texture on the mechanical response. This is a relevant question in order to decide if it is more convenient to retain the usually textured as-built grain structure (e.g., by SR + DA) or to fully recrystallize it (e.g., by HIP).

In the present study we refer to a full heat treatment (FHT) as that in accordance with ASTM F3301. A comparison is made with the DA™ heat treatment, with the addition of a prior SR, which represents the lower boundary of heat treatment steps required for L-PBF Inconel 718. In our previous study, alongside several different heat treatment variants, the DA and FHT variants were also examined in terms of optical microscopy and monotonic room temperature tensile properties [43]. In order to provide a deeper insight into the tensile behaviors of different heat-treatments this follow up study thus aims to further increase the understanding on the microstructural evolution and the micro mechanical behavior. This will be achieved by the means of scanning electron microscopy and in-situ tensile testing during synchrotron X-ray diffraction, respectively.

2. Experimental procedure

2.1. Sample fabrication

Specimens used in this study were built in a M2 Cusing machine (Concept Laser GmbH, Lichtenfels, Germany) using Micro-Melt Inconel 718 AM powder from Carpenter Powder Products. The powder was spheroidized in an argon gas atomization process and sieved to obtain a 37 μm D₅₀ particle diameter. To prevent oxidation during L-PBF, a constant argon flow was maintained over the powder bed.

The build parameters utilized in this study were: 180 W laser power, 600 mm/s laser speed, 0.105 mm hatch spacing and 0.035 mm layer thickness. For the 3 mm specimens, the outer surface of the build had a nominal 0.06 mm thick two-pass contour layer where the laser speed was increased to 1600 mm/s. An alternating pattern of X and Y directions with a 90° interlayer rotation was used.

Three sets of specimens were printed, as illustrated in Fig. 1, with the tensile axis aligned with the Z build direction. First, 15 mm diameter cylinders with a height of 100 mm were built and stress relieved. After removal from the build plate, these cylinders underwent the two heat treatments prior to machining to 6 mm diameter ex-situ tensile test specimens. Fig. 1a shows the geometry from the ASTM standard E8 for the subscale specimen #3. It should be noted that no contouring was used for these specimens. For more details on these specimens the reader is referred to our previous work [43].

Furthermore, flat and round specimens with a nominal thickness of 3 mm were directly printed to the dimensions shown in Fig. 1b and c, respectively. To prevent distortion these specimens were built with a reduced contact area (tip) to the build plate. The flat specimens (Fig. 1b) were used for in-situ synchrotron X-ray diffraction studies under load. Their size was dictated by the characteristics of the synchrotron X-ray

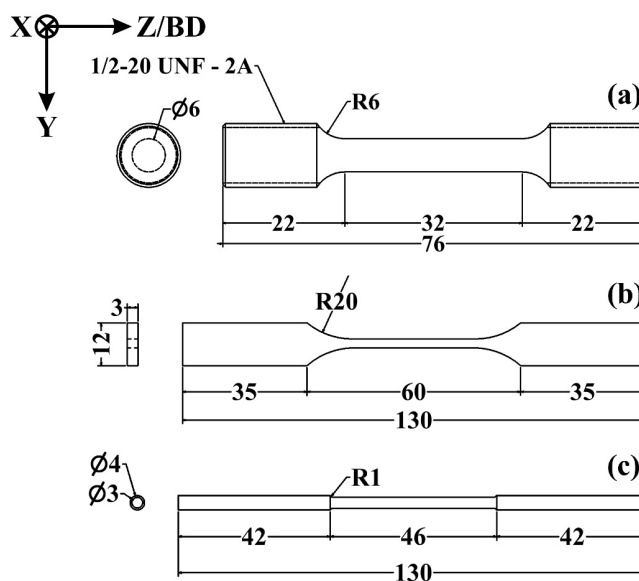


Fig. 1. (a) 6 mm diameter specimen geometry for standard ex-situ tension tests [43] according to the ASTM standard E8, (b) custom flat tension specimen geometry with a 3 × 3 mm cross section for in-situ studies and (c) round 3 mm diameter specimen geometry for porosity evaluation. All dimensions are nominal and given in mm.

beam to be able to penetrate through the specimen thickness and were therefore non-standard. Due to the 3 mm thickness of the specimen, it was not feasible to easily machine these to the final shape. Thus, the contour layer was retained in these specimens. The round specimens were only used for porosity evaluation (Fig. 1c) with X-ray Computed tomography.

2.2. Heat treatment schedule

All specimens were wrapped in stainless steel foil and heat treated in air atmosphere according to the steps listed in Table 3 in the sequence from left to right. In contrast, the HIPing was conducted in argon environment at a pressure of 105 ± 5 MPa. After a SR process, the heat treatment steps for the full heat treated (FHT) specimens [19,47] were based on a combination of SAE/AMS 5383 standard for investment castings [10] and SAE/AMS 5663 for [15] wrought alloys. The HIP treatment was based on reported best practices in casting and powder metallurgy processing [8–13]. The slight difference in the ST temperature was within the range of SAE/AMS 5663 (941–1010 °C).

2.3. Ex-situ mechanical testing

A total of six 6 mm diameter tensile specimens were machined for each heat treatment. Standard tension tests were conducted on an electro-mechanical Instron 8862 (Instron, Norwood, U.S.A) tester equipped with an MTS Bionix elite controller (MTS systems GmbH, Berlin, Germany). The tensile axis was aligned with the Z build direction. All tests were run in displacement control at a constant crosshead velocity of 1.3 mm/min per ASTM standard E8. Measurements of the yield (σ_{YS}) and ultimate (σ_{UTS}) stresses were based on loads obtained from an 89 kN load cell and measurements of each specimen dimensions. Strain measurements, to obtain percentage (%) elongation to failure (A), were obtained from a 25 mm extensometer calibrated to 50 % strain. For the calculation of the work hardening rate (n) the true stress (σ_T) vs true strain (ϵ_T) curves were derived and plotted on a log-log plot. From the slope the work hardening rate can be then determined (eqn. (1)). K is a material constant.

$$\sigma_T = K\varepsilon_T^n \quad (1)$$

2.4. In-situ mechanical testing

The in-situ tensile tests were performed on the EDDI beamline at the BESSY II synchrotron source at the Helmholtz Zentrum Berlin, Germany. Two 3 mm flat specimens (Fig. 1b) from each heat treatment were tested. The primary beam size was 1 mm × 1 mm. The lattice spacing of different lattice families {hkl} was monitored using energy dispersive X-ray diffraction (ED-XRD) over the range of 10 keV–150 keV, while the specimens were deformed in a 20 kN load rig (Walter + Bai AG, Löhningen, Switzerland). The crosshead displacement was used to calculate the macroscopic strain. The diffraction measurements were performed along the Z build direction to obtain the axial strain component. The diffraction peaks were fitted using a Pseudo-Voigt function within an in-house developed Mathematica (Wolfram Research, Champaign, U.S.A) code. The test was run in displacement control mode with 8 min holds to enable the diffraction data to be collected. The lattice strain ε^{hkl} was calculated from d^{hkl} values at every load step given in equation (2):

$$\varepsilon^{hkl} = \frac{d_{in}^{hkl} - d^{hkl}}{d_{in}^{hkl}} \quad (2)$$

Where d_{in}^{hkl} was the initial lattice spacing for crystallographic plane families {hkl} [63] at a pre-load of approximately 10 N. More detailed information about the experimental setup are given in Ref. [64].

2.5. Metallographic preparation

After testing, sections were extracted from the grip ends of the 6 mm and 3 mm tensile specimens for microstructural characterization. The extracted samples were further sectioned in two orientations, the Z build direction and the XY build plane. Samples from all tensile specimens were mounted in epoxy resin and metallographically prepared using standard practices with a final polish of 0.5 μm Al₂O₃. All samples were imaged using a XioVert.A1m Inverted Microscope (Zeiss, Oberkochen, Germany) for Reflected Light Techniques. As the 6 mm and 3 mm sections showed similarities, the images shown in this work refer to the 3 mm sections. To reveal the grain structure in the optical images, the samples were etched with waterless Kallings reagent. Additionally, scanning electron microscope (SEM) samples, were further polished using a colloidal SiO₂ suspension. A field emission LEO 1530VP (FEG) SEM device (Zeiss, Oberkochen, Germany) was used to obtain backscattered electron (BSE) images. The elemental information was obtained using an Oxford (Oxford Instruments, Abingdon, England) energy dispersive spectrometer (EDS), while Electron backscatter diffraction data (EBSD) were obtained using a Nano e⁻-Flash (Bruker, Billerica, U.S.A). For quantitative image analysis the open-source toolbox MTEX [65] within the software MATLAB (The MathWorks, Inc., Natick, U.S.A) was used. For the grain analysis the misorientation angle threshold was set to 5°. A pixel size of 4 μm was achieved. The calculation of the grain size was based on the equivalent spherical diameter of the grain area. Twin boundaries were excluded. The data were then weighted by the area fraction.

2.6. Phase analysis

The phase content was analyzed using a Seifert 3000 PTS X-ray diffractometer (XRD Eigenmann GmbH, Schnaittach, Germany) operated at 40 kV and 40 mA. Measurements were performed in the Z build direction. A Co Kα source was used. X-ray diffraction (XRD) data were acquired over the ranges 35°–55° and 50°–95° with a step scan of 0.02° and 1200 s measurement time per point. The detector was a multi-channel, semiconductor.

2.7. X-ray computed tomography

The void population was evaluated using X-ray computed tomography (XCT) imaging. XCT measurements were performed in the center of the gauge section over a length of 14 mm. A GE v|tome|x 300 kV CT scanner was used, equipped with a 0.5 mm Ag pre-filter. The tube current was set at 70 μA and the voltage at 140 kV. A voxel size of 7 μm was achieved. 1200 projections were acquired with an acquisition time of 4 s per projection. The pore detection tool implemented in the VGStudio Max 3.2 (Volume Graphics GmbH, Heidelberg, Germany) software was used for segmentation of the porosity. To reduce the probability of false segmentation, only voids with a minimum volume of 8 voxels were considered. This corresponds to the minimum equivalent diameter of around 17 μm.

3. Results

3.1. Phase analysis

Fig. 2 shows the bulk phase analysis for the DA and the FHT specimens. Fig. 2a shows a slower scan over a narrower range of 2-theta angles to investigate the presence of minor phases with detection of δ, NbC and Laves. A slight increase in intensity for the δ phase between the DA and FHT specimens is attributed to a slight increase in volume fraction. The NbC and Laves phases show similar intensities for the DA and the FHT specimens suggesting no change in volume fraction. A complementary wider 2-theta range scan in Fig. 2b shows the major peaks associated with the Ni matrix along with a smaller peak associated with the minor δ phase.

3.2. Microstructure

Optical microscopy images of the microstructure of the DA and FHT specimens are shown in Fig. 3. The primary differences are noted in the grain morphology for the XY (Fig. 3a, b) and Z plane (Fig. 3c and d). For the DA specimens columnar grains along the build direction are clearly visible (Fig. 3c) and a checkerboard structure is identifiable in the XY plane. In contrast, in the FHT specimens (Fig. 3b, d) the columnar structure and the checkerboard structure disappeared resulting in an equiaxed grain distribution featuring a large grain size distribution.

Details of the grain boundaries are shown in the backscattered SEM images for different magnifications (Fig. 4). Pointwise EDS analysis was used to determine elemental content of particles observed for correlation with the XRD phase indications. The low magnification image in Fig. 4a shows regions of coarse and fine grains along the columnar structure. Relatively clean grain boundaries, free of precipitation, are observed in the DA specimens in Fig. 4a, c, and e. Some isolated particles rich in Nb are observed; These could correspond to either NbC or globular δ phases.

In contrast, the grain boundaries of the FHT specimens in Fig. 4b, d and f, are decorated with fine acicular particles. These fine particles are assumed to be δ phase which precipitated during the ST/Q heat treatment. Here the acicular phase tends to primarily decorate the grain boundaries of the smaller grains. Also noted is the presence of globular Nb-rich particles that are assumed to correspond to NbC.

Dark spots are observed in Fig. 4c, d, e and f. However, it is impossible to distinguish here between voids and oxide inclusions. While oxides were not observed in the XRD analysis, Gruber et al. have reported the presence of small oxides in Electron Beam AM of Inconel 718 [66].

Additional EBSD imaging in the SEM was used to obtain images of the grain orientation of the specimens in the Z build direction. Orientation maps and their corresponding {100} pole figures are shown in Fig. 5a, c and b, d for the DA and FHT samples, respectively.

For the DA specimens, in Fig. 5a, coarse columnar grains are observed to be separated by fine-grained regions. In contrast, Fig. 5b for the FHT specimens shows equiaxed grains of varying sizes, most

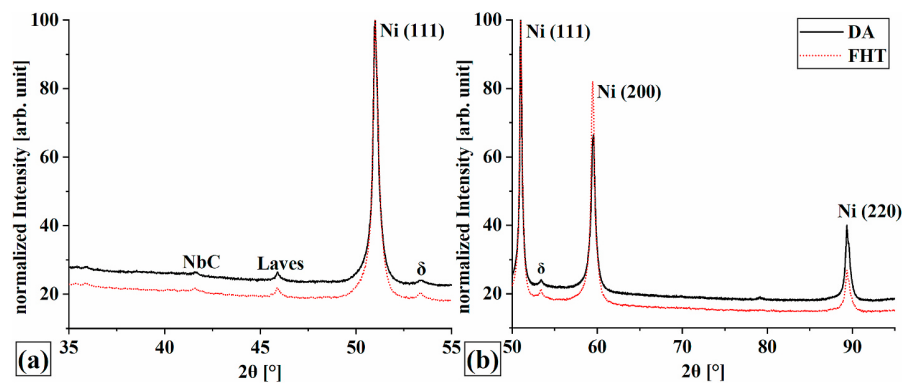


Fig. 2. XRD phase analysis for the scattering ranges of (a) 35–55° and (b) 50–95°.

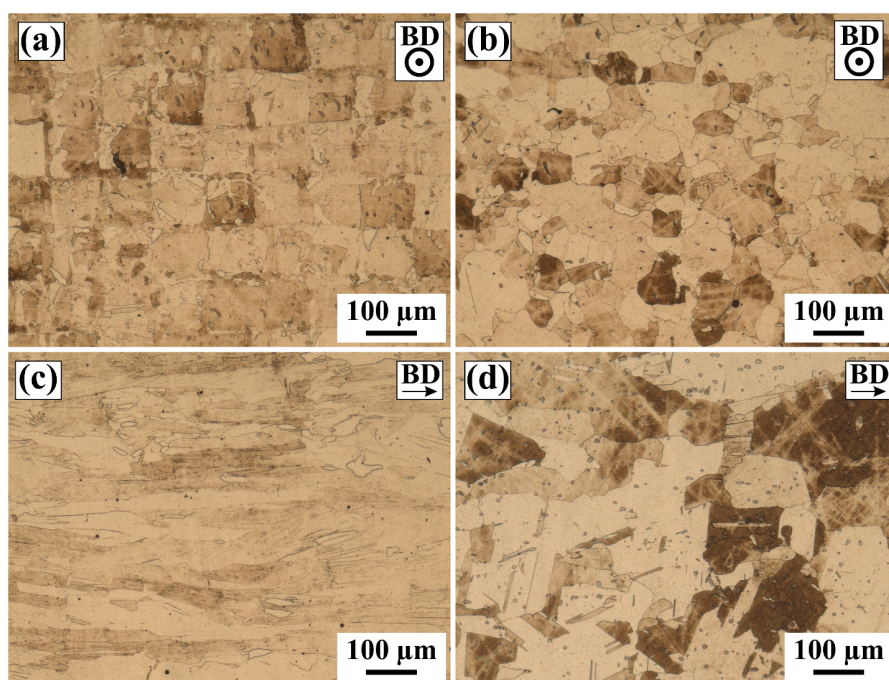


Fig. 3. Optical micrographs for DA (a, c) and FHT specimens (b, d) with respect to the building direction.

probably caused by recrystallization and/or subsequent grain growth. The columnar structures in the DA specimens gave rise to an uneven equiaxed grain distribution with smaller and larger grains in the FHT specimens. The grain size distributions obtained from the EBSD maps in Fig. 5a and b are shown in Fig. 5e and f. They correspond to an increase in the average grain size from $146 \pm 124 \mu\text{m}$ (7769 grains) to $467 \pm 297 \mu\text{m}$ (1740 grains) for the DA and FHT specimens, respectively.

The corresponding $\{100\}$ pole figures show the texture differences as a result of the heat treatment condition. Fig. 5a and c of the DA heat treatment show texture in the X direction of $\langle 110 \rangle$ and $\langle 111 \rangle$ character, with the $\langle 001 \rangle$ directions aligned in the Z build direction.

For the FHT treatment, as shown in Fig. 5d, the higher temperature of the HIPing led to a weaker texture compared to Fig. 5c. It must be noted that, within the sample volume for the EBSD characterization, fewer grains were sampled for the FHT as compared with the DA specimens. It is to be noted that, global texture measurements obtained from XRD agree with the EBSD analysis (see Appendix A 1).

3.3. Porosity content

Fig. 6 shows the porosity distribution obtained from XCT, as a projection through each sample along the 3 mm diameter gauge length. The porosity volume fraction was found to be 0.12 % for the DA specimens and 0.02 %, for the FHT specimens. HIP processing of the FHT specimen was effective in reducing the internal closed voids. The DA and FHT 3 mm round tensile specimens show similarity in the porosity near the outer surface, corresponding to the 60 μm thick contour layer. The correlation between the void distribution and contour scan is significant. Other works also report that the region between the core filling and contour hatches is enriched with pores [67,68]. A distinction of the different pore types has been made by Laquai et al. in Ni-base superalloys [69], and Ti6Al4V [70,71] by combining X-ray computed tomography and X-ray refraction techniques.

3.4. Ex-situ tensile testing

Fig. 7a shows representative engineering stress vs engineering strain data for the ex-situ 6 mm diameter specimens. The obtained values for

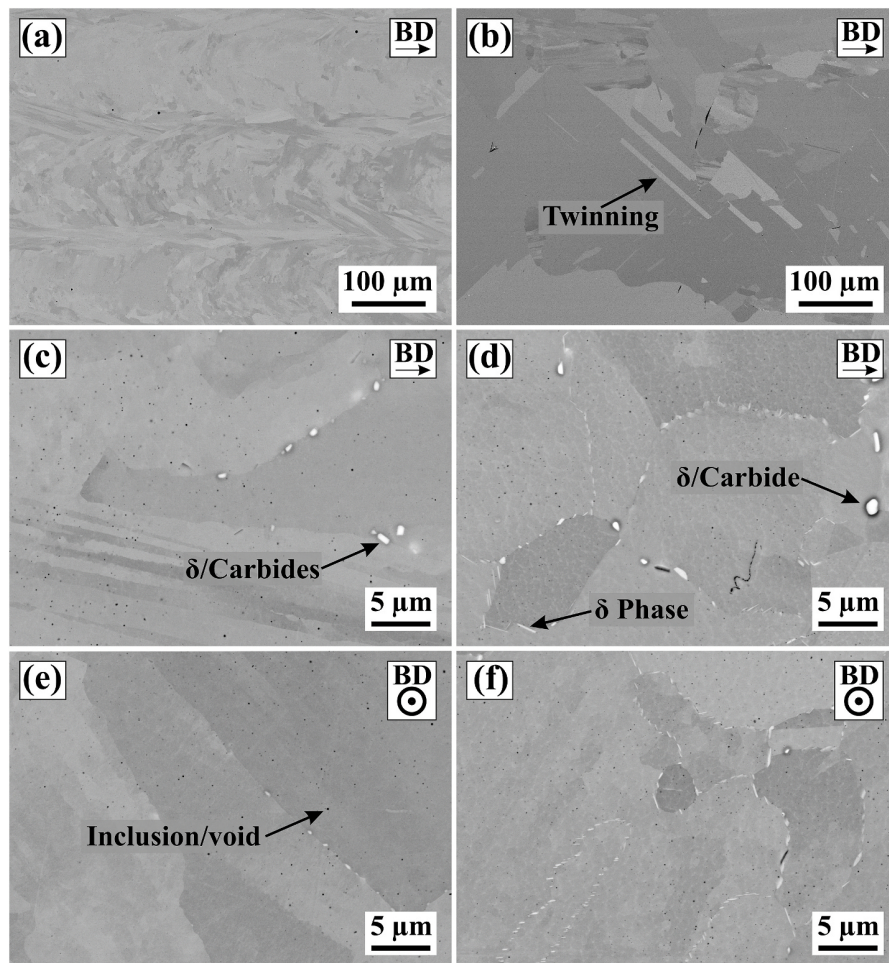


Fig. 4. BSE images of the specimens DA (a, c, e) and FHT (b, d, f) with respect to the building direction showing precipitation (c, d, e, f) and different grain structures (a, b).

the yield strength (σ_{YS}), ultimate tensile strength (σ_{UTS}), strain at rupture (A) and work hardening rate (n) can be observed in Fig. 7b. Representative values for cast and wrought Inconel 718 are included. For the two heat treatment conditions, there are slight differences in the mechanical loading response [43]. The σ_{YS} is noted to be slightly higher and the σ_{UTS} slightly lower for the DA specimens. The differences between the σ_{YS} and σ_{UTS} can be quantified by examining n , the work hardening coefficient. A larger n value, shown in Fig. 7b, indicates a higher work hardening rate for the FHT specimens. The higher work hardening rate correlates with the lower σ_{YS} and higher A for the FHT specimens as compared to the DA specimens.

3.5. In-situ tensile testing

During in-situ tensile testing, the specimens are deformed in incremental steps and held during acquisition of the diffraction patterns. Fig. 8a shows the 3 mm flat tensile specimens in the load frame after in-situ testing to failure at the EDDI beamline. Since the in-situ experiment requires a hold time at each displacement step, the effect of such hold time on the corresponding stress-strain behavior was evaluated. This was done by ex-situ testing a duplicate FHT specimen in the loading rig of the beamline setup. Fig. 8b compares the relative displacement curves of the in-situ and ex-situ tests. In comparing the FHT specimens in Fig. 8b, we observe a small shift in the ex-situ curve stress data relative to the in-situ data. This offset is attributed to stress relaxation occurring during the acquisition hold time at each displacement step during the in-

situ test. It is assumed that this effect is similar for the two specimens. Based upon this assumption, the results of the in-situ tests can then be compared. In fact, as in the case of the ex-situ tests, the DA specimens exhibit a higher σ_{YS} value as compared to the FHT specimens. The lower value of the elongation to failure for the flat 3 mm specimens in Fig. 8b can be attributed to the porosity and surface roughness, which are known to affect the elongation to failure in AM materials [72]. Significant differences in the fractography images for the 3 mm specimens can be observed in Appendix A 2. Both specimens retained the as-built surface roughness and the lack of fusion defects corresponding to the contour layer after their respective heat treatments. While the FHT sample only shows surface related defects from which the failure started, the center of the sample exhibited a classical ductile behavior. In contrast, the bottom part of the image shows a flat fracture surface corresponding to a shear lip. Since internal pores were also present in the DA specimen, there is no defined fracture start but rather multiple initiation sites are observable. This reduces the elongation to failure of the DA specimen compared to FHT. The 6 mm samples, reported in Section 3.4, would only reflect fracture paths associated with the internal defects or voids since the surface was machined. Thus, higher absolute elongations to failure are present for this sample condition while relative differences in the elongation to failure persist. The low ductility of the 3 mm flat specimens did not impact the determination of the elastic and plastic behavior in the specimens, since the changes are most significant at the early stages of yielding. Due to the differences in the testing environments we do not intend for a direct numerical

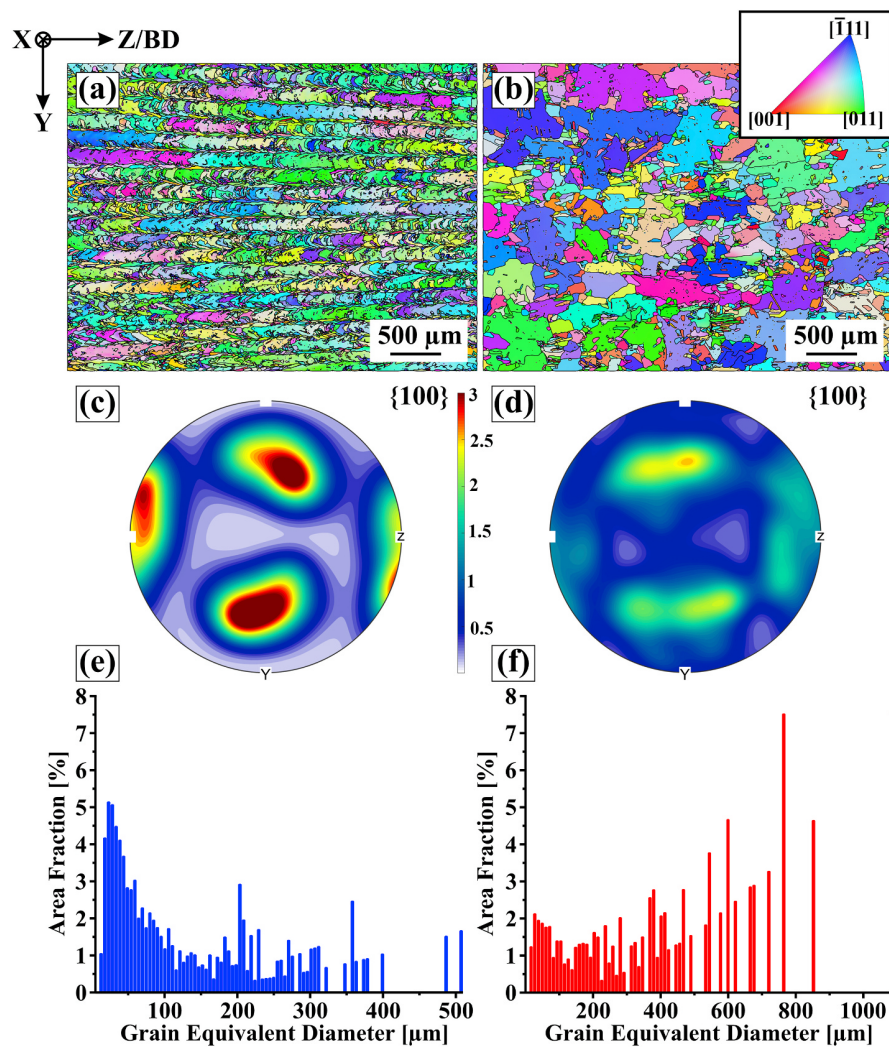


Fig. 5. Orientation maps of the longitudinal sections, their corresponding $\{100\}$ pole figures with respect to the X direction and grain size distributions of the DA (a, c, e) and FHT (b, d, f) specimens. The inset in (b) indicates the color related orientation of each grain. (For interpretation of the references to color in this figure legend, the reader is referred to the Web version of this article.)

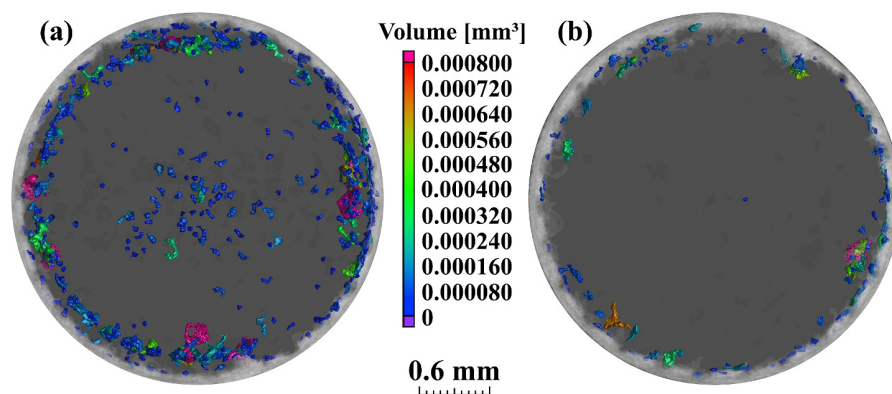


Fig. 6. Projection of the porosity rendering along the 14 mm gauge length in the Z build direction for the 3 mm diameter (a) DA and FHT specimens (b). The material is presented with 95% transparency.

comparison to be made between Figs. 7a and 8 – only to show that the general trends persist for the different load frame capacity.

In Fig. 9a and c, the in-situ XRD patterns are shown for the DA and FHT specimens as a function of the applied displacement. The resulting

positions and intensities of the reflections are observed to change for both samples during loading. Some reflections, such as the 222-peak, are observed to vanish in the DA specimen during the deformation while others appear in the FHT specimen. This must be interpreted with regard

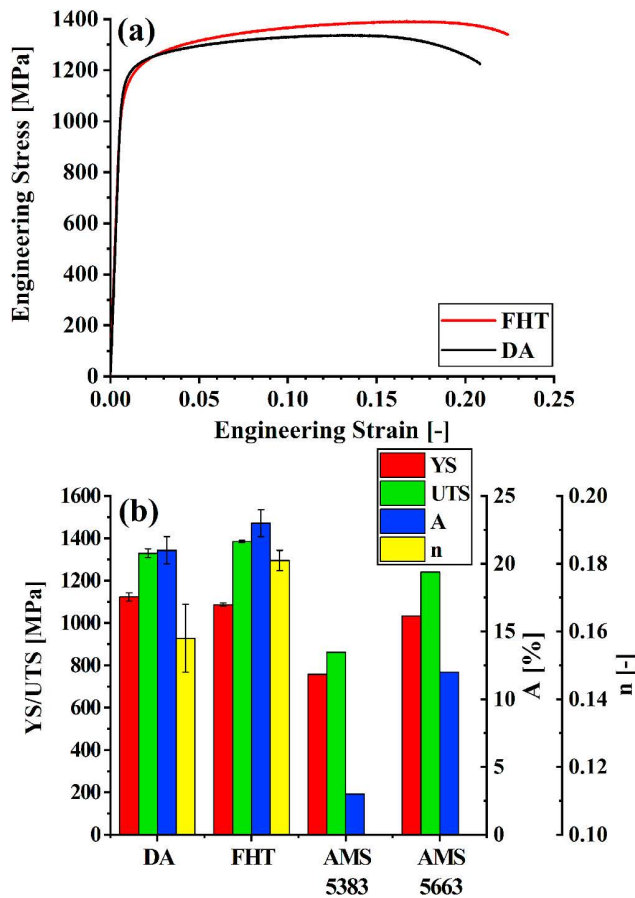


Fig. 7. (a) Exemplary ex situ engineering stress vs strain plots for the DA and FHT specimens of the 6 mm round specimens. (b) Summary of the 6 mm ex-situ tensile data for DA and FHT specimens in comparison with AMS standards [10, 15]. The data were re-evaluated from our previous study [43].

to the small representative gauge volume and the significantly large difference in grain sizes between the two heat treated specimens. As the load frame actuates from one end, it is possible for the larger grains in the FHT sample to move out of the view of the fixed position X-ray beam as the sample elongates.

From the data of Fig. 9a and c, the dependence of the lattice strain evolution from the applied stress for each diffracting lattice plane can be

obtained by evaluating each single peak in the XRD pattern. Fig. 9b and d shows resulting graphs for each heat treatment condition. While the divergence of each plane for the DA specimen in Fig. 9b is evident, the lattice planes for the FHT specimen in Fig. 9d, with the exception of the (400), behave similarly. However, in both cases the (400) elastically deforms the most, since it is the softest plane in FCC materials [73]. The DA specimen in Fig. 9b, reflects more of the typical deformation behavior for polycrystalline FCC materials. The data from Fig. 9b and d for the 400-peak highlights the similarity in the deformation of the (400) lattice plane between the two specimens, although the 400-intensity from the FHT specimen is very small as compared to that of the DA specimen. Indeed, Fig. 9a and c also indicate a lower degree of <100> texture in the FHT specimens as compared to the DA specimen. In addition, for the FHT specimen the (311) shows increased non-linearity and the behavior in the plastic regime above 800 MPa, which is different as compared to the DA specimen (Fig. 9d).

4. Discussion

4.1. Macro mechanical behavior

The macroscopic stress-strain behavior of the two studied heat treatment variants display broadly similar behaviors with key differences arising in the yielding characteristics, the strain hardening behavior, and the ductility. The possible reasons for these differences are explored in the following sections.

4.1.1. Porosity and surface roughness

Increased porosity was observed in both 3 mm samples at the surface corresponding to the contour layer (Fig. 6). The increased scan speed for this outer layer reduces the heat input and can result in insufficient melting of the powders or lack of fusion defects, as reported in other studies on AM materials [34,72]. Due to the high solidification rates, entrapment of the shielding gas can form spherical pores, which is a well-known issue in AM [72]. The HIP processing of the FHT specimen is effective in reducing the closed internal porosity (Fig. 6b). However, since HIP can only reduce internal pores, the open porosity in the outer contour layer is retained. Tillmann et al. [58] reported similar findings and attributed the small amounts of internal spherical porosity to entrapped argon gas.

As Kantzos et al. [74] showed for L-PBF manufactured Inconel 718, absolute values of the yield strength and ultimate tensile strength were not significantly affected by higher amounts of porosity present. In contrast, the average elongation to failure showed a large scatter for large amounts of spherical porosity. Lower values of the elongation to failure are a result of lack-of-fusion defects. The failure initiation sites were in any case found to be surface related. These findings are in

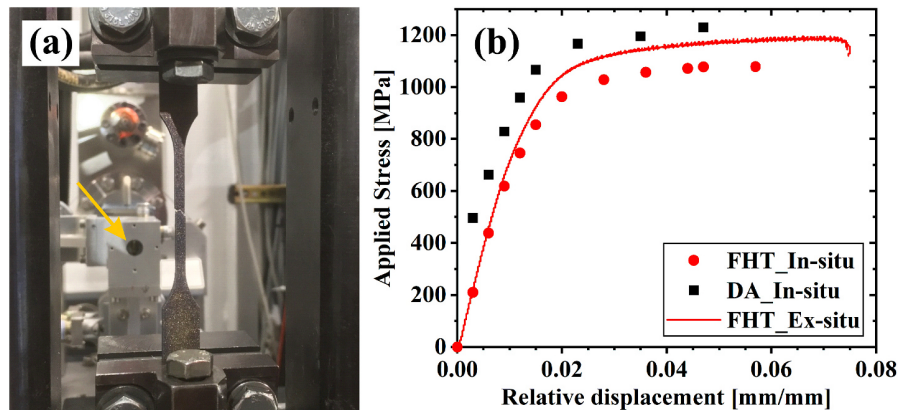


Fig. 8. (a) Image showing a postmortem in-situ specimen at the EDDI beamline. The arrow indicates the position of the primary slits. (b) Applied stress vs. relative displacement curves obtained from in-situ and ex-situ tensile tests at BESSI II.

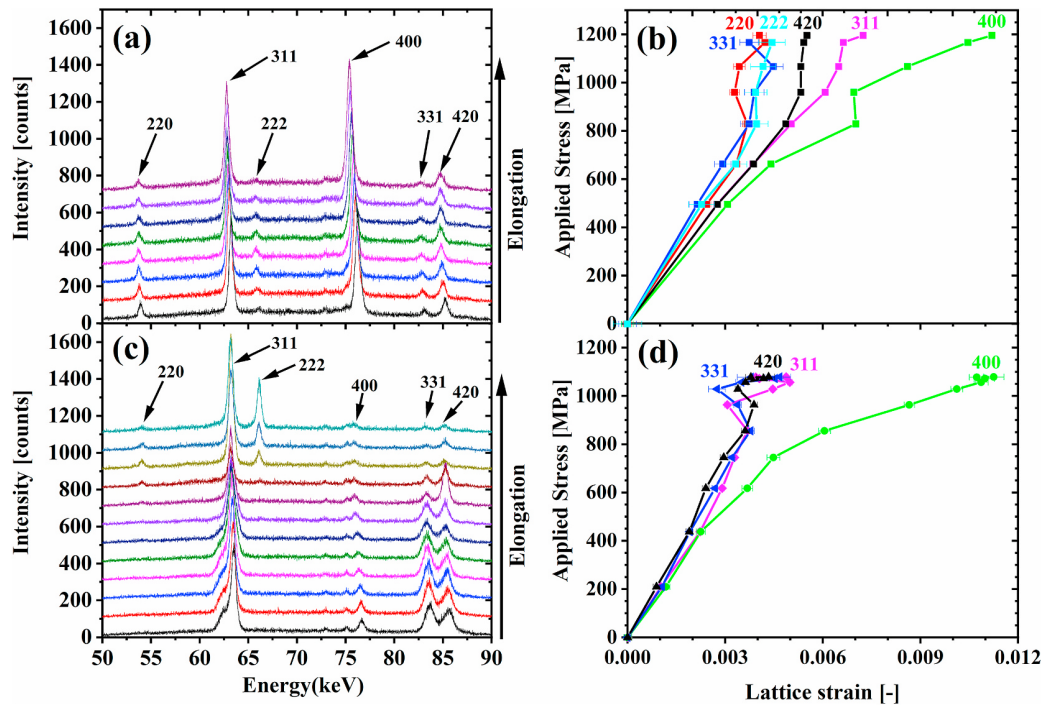


Fig. 9. Changes in the measured XRD-Patterns for the specimen DA (a) and FHT (b) with respect to the applied displacement for an Energy Range of 50–90 keV. In both cases the measurement direction is parallel to the applied load direction (Z build direction). Axial Lattice strain evolution for (c) DA specimen and (d) FHT specimen obtained from in situ tensile tests using energy disperse synchrotron XRD.

accordance to our observations for both, the 3 mm and 6 mm specimens respectively. On the one hand, the lower elongation to failure for the 3 mm specimens can be thus attributed to the presence of the lack of fusion porosity in the outer contour layer (Appendix A2).

On the other hand, Kotzem et al. [75] reported on the surface roughness influence for small scale EBM manufactured Inconel 718 tensile bars. They found that the presence of process induced defects and poor surface quality deteriorated the static mechanical properties, especially the elongation to failure. Besides the different porosity condition being one main difference for the 3 mm and 6 mm specimens the surface condition also is vastly different. Our findings thus also support the conclusion of Kotzem et al. [75], that the surface condition significantly affects the elongation to failure. In contrast, Gallmeyer et al. [52] did not observe a significant difference in the elongation to failure between L-PBF tensile bars tested in the as-built and machined surface condition. Instead, they observed a higher ultimate tensile strength for the as-built surface condition.

4.1.2. Hall-Petch relationship

Pei et al. [76] reported on the grain size dependence of the mechanical properties of AM Ni-based superalloys. Their results showed a good agreement with the Hall-Petch relation for AM and wrought Inconel 718.

$$\sigma_{YS} = \sigma_0 + \frac{k}{\sqrt{d}} \quad (3)$$

where σ_0 is the friction stress, k the Hall-Petch coefficient and d the average grain size. When including the data observed for the 6 mm specimens with the measured grain sizes in this study, a good agreement is obtained with the data reported in Ref. [76] (Fig. 10). Thus, the differences in σ_{YS} for the two heat treatment conditions studied can be attributed to the different grain sizes resulting from the different heat treatments. On the other hand, the data from Sangid et al. [77] do not follow the behavior predicted by Hall-Petch. This can be attributed to the fact that they included twins in their grain size calculation, which

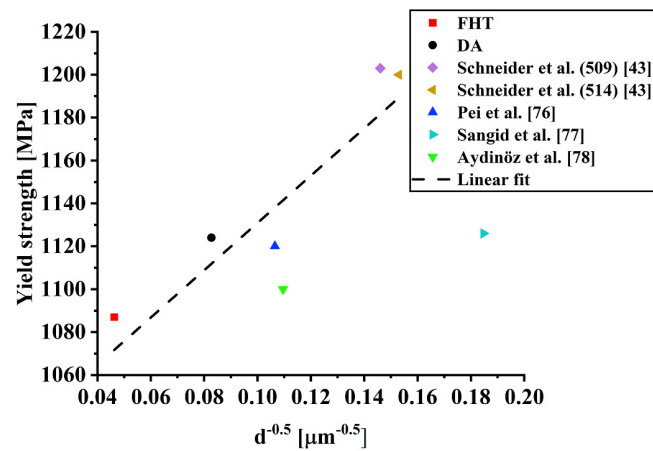


Fig. 10. The Hall-Petch relation (eqn. (3)) for Inconel 718 manufactured by L-PBF tested along their Z build direction [43,76–78]. Adapted from Ref. [76].

results in a significantly smaller grain size. Therefore, that data point is not included in the linear regression shown in Fig. 10.

4.1.3. Strain hardening

Although a SR cycle was applied to all specimens, a heat treatment at the SR temperature alone might not be able to annihilate the initial dislocations in the DA specimen. This is in agreement with the reported literature [39,52]. During subsequent loading, the higher initial dislocation density would be expected to lead to an increase in yield strength. To quantify the hardening contribution of the dislocation cells, the Taylor hardening model has been recently applied by Gallmeyer et al. [52] for as-built L-PBF Inconel 718 and achieved a satisfying prediction of the yield strength. The model adds the term $\alpha M G b \sqrt{\rho}$ to equation (3)

(α is a material constant, G the shear modulus, b the Burgers vector, M the Taylor factor, ρ the dislocation density). The contribution of the strain hardening accounted for an increase in strength by 63%. Since the dislocation density is altered by the SR, the contribution in this study is of smaller magnitude.

In contrast to DA, the HIPing for the FHT specimen is more effective in annihilating the initial dislocation structure as the driving forces (time, temperature, pressure) are higher, thereby driving recrystallization. However, the resulting multi-modal grain size distribution suggests that the dislocation density did not uniformly decrease. This can be attributed to the non-uniform distribution of dislocations in AM materials. A lower dislocation density in the FHT specimen would correspond to the lower yield stress and higher work hardening rate in the respective ex-situ tensile test.

4.1.4. Precipitations

The use of the single step aging heat treatment at 720 °C for the DA specimen would favor the formation of γ'' over that of γ' [5]. Thus, in the DA specimen the precipitation state should mainly consist of γ'' as depicted in Fig. 11c. As γ'' is considered to be the primary strengthening phase in Inconel 718 [32], this may also explain the similar yield stress for the DA specimen as compared to the FHT specimen observed in the 6 mm ex-situ tension tests. The γ' phase would still contribute to the hardening, but only by 10 to 20% [3]. Another study by Hall et al. [79] suggests that the usage of double ageing would lead to an increased strength by 69–138 MPa. In contrast, Gallmeyer et al. [52] observed for a standard heat treatment (980 °C/1 h + 720 °C/8 h + 620 °C/8 h) that the sizes of γ'' and γ' were similar to those in single step DA (1020 °C/0.25 h + 720 °C/24 h), whereas the aging time was 3 times longer than for the DA in this study. The δ phase was not observed in their DA

heat treatment, although it was observed after the standard heat treatment. In our study, we observed little variation in strength between the FHT and DA. Ferreri et al. [80] showed that although samples subjected to a HIP before standard heat treatment precipitate higher amounts of γ'' and γ' , the resulting tensile strength is still lower than that for the sample without a prior HIP. They attributed this difference to the presence of nanometer-size carbides with a higher density in the sample without HIP as well as a finer grain size. The HIP treatment applied to L-PBF material yields a comparison to the FHT in our study, since the respective heat treatments are quite similar. Therefore, the volume fraction of γ'' and γ' for FHT are expected to be similar to that reported by Ferreri et al. [80]. The standard heat treatment in Gallmeyer et al. [52] did not incorporate a HIP process and should reflect lower fraction of γ'' and γ' with higher amounts of carbides and δ phase. Conclusively, the volume fraction and sizes of γ'' and γ' are expected to be smaller for the DA than for the FHT specimen. The combination of higher density of MC carbides, finer grain size and the retention of the dislocation cells in the DA specimen enhances the tensile mechanical strength to exceed those of the FHT specimen.

4.1.5. Texture influence

Although, Ni et al. [81] reported the influence of texture on the resulting mechanical properties due to activation of different slip systems, only the DA heat treatment produced strongly textured specimens in this study. In the literature, the dependence of the as-built microstructure and crystal texture on the applied process parameters such as laser power, scan parameters and strategy are known [48,82]. The alternating 90° scan strategy has been reported to favor a <001> orientation in the scan direction, and a <110> in the Z build direction for as-built Inconel 718 [83]. This agrees well with our findings for the

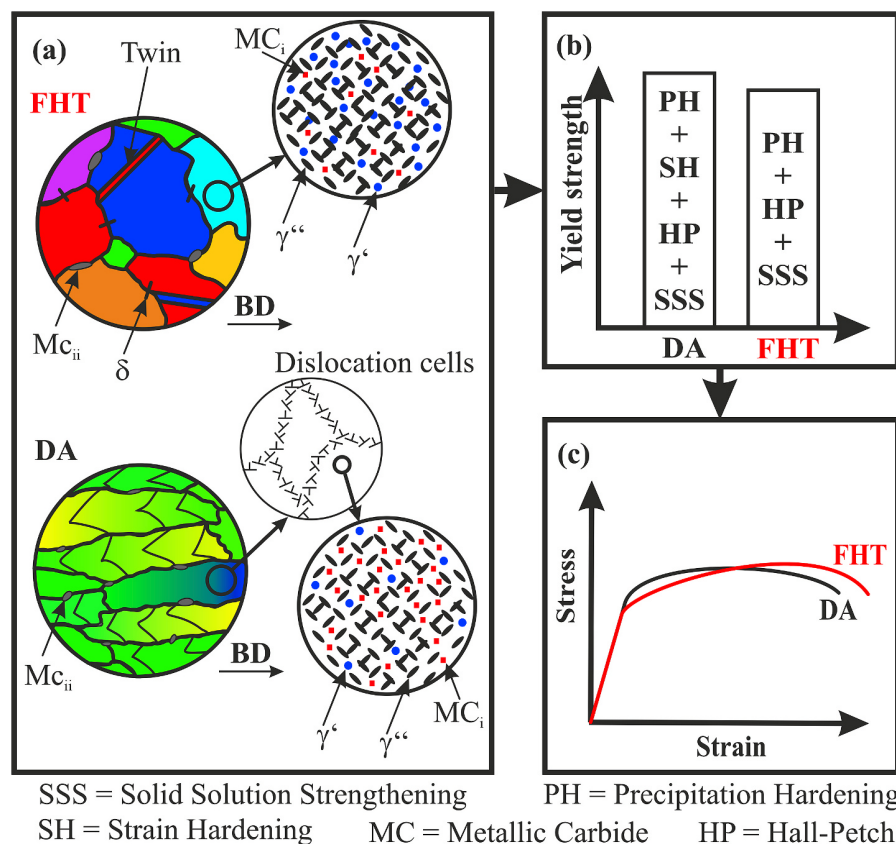


Fig. 11. Qualitative illustration of the hardening contributor factors. Where (a) represents the schematic microstructures under consideration of [52,80], (b) shows a schematic of the different hardening contributor factors for DA and FHT, respectively. In (c) a schematic of the obtained stress-strain curves is given.

DA specimen, except that the respective orientations swapped with $\langle 001 \rangle$ being aligned with the Z build direction in the heat-treated condition.

Based on results of other studies, it can be expected, that the behavior of the FHT specimen with lower texture would be more isotropic than that of the DA specimen [77,82,84]. Bean et al. [82] showed that a higher degree of texture displayed a lower elongation to failure when compared to less textured specimens. This agrees with the observations in our study, as the less textured specimens (FHT) tend to display higher elongations to failure. Besides the lower elongation, the respective Taylor factors also affect the yield strength of the FHT and DA materials. This is reflected in the Taylor strain hardening model and also contributes to a larger degree to the DA specimen as it shows a higher Taylor factor.

It has been shown that the texture can be considerably reduced by using rotation scanning strategies (e.g., 67° interlayer rotation) [85]. Therefore, by combining such strategies with a SR and single DA heat treatment, higher static mechanical properties, particularly at RT, may be achievable with lower costs associated with the reduced number of heat treatment cycles when compared to wrought alloys.

Combining the findings of the present work and of [52,80,82], the sketch in Fig. 11 provides a qualitative description of the factors contributing to the differences in mechanical behavior for DA and FHT variants. Fig. 11a shows a direction comparison of the different microstructural features for both heat treatment variants. The underlying colors indicate the difference in the texture as observed in Fig. 5. The different hardening contributions are summarized in Fig. 11b, having different but unknown magnitudes for each heat treatment variant. Finally, although many factors contributed to the resulting tensile properties of the two heat treated conditions, only slight differences were observed although the grain size and texture were vastly different (Fig. 11c).

4.2. Micro-mechanical properties

The micromechanical testing of the two variants (in-situ loading experiments by synchrotronED-XRD) revealed differences in both the elastic and plastic responses. The key observations are discussed in the following sections.

4.2.1. Lattice strain evolution

From Fig. 9c and d we observe that for the DA specimen, the linear elastic response among the grains is retained up to a stress of 700 MPa compared to 800 MPa for the FHT specimen. After this stress, some grains begin to plastically deform as evidenced by the change of gradient of lattice strain accumulation with applied stress. Common to the DA and FHT specimens is the response of the 400-peak in carrying the load. The {400} is the softest plane in the elastic region, but once plastic deformation starts to occur it carries most of the load. In the case of the DA specimen, it can be observed that the {220} and {222} families appear to cease accumulating elastic strain during plastic deformation and this load is transferred to the {400} families. This is due to the texture, since the load direction is parallel to the Z build direction. The texture is predominant along $\langle 100 \rangle$. The Schmid-factor m is 0 for {100} lattice planes and maximum for {111} $\langle 110 \rangle$ slip system. This means that plastic deformation occurs first along the {111} planes; this results in earlier saturation of the accumulated elastic strain. The gauge volume investigated in the DA specimen contained a statistically significant amount of grains with size less than 100 μm . As the DA specimen deforms, the response of other planes is observed to deviate from linearity, as observed in wrought Inconel 718. Studies on as-built Inconel 718 display the same trends, although the stresses are lower due to the lack of precipitates [77]. The 311 peak for the DA specimen shows the lowest dependence on intergranular stresses as reported in Ref. [86]. This is in contrast to the findings of Wagner et al., who concluded for conventionally manufactured Inconel 718 alloy, that the 220 reflection

is least affected by intergranular strains [73].

The γ'' precipitates can lead to radial streaking on the detector based on load shedding and strain partitioning [77]. As the γ'' precipitates are oriented on the {100} planes of the γ crystal parallel to the plane normal [3] they may alter the response of the {100} planes during loading when compared to as-built material. However, as the response of the {100} planes show similar trends for DA and FHT, the differences in the lattice response of the {331} and {420} can be mainly associated with the different grain shape and texture.

Furthermore, the different in-situ behavior of the FHT specimen could also be attributed to the larger grain size: fewer grains in the sampling volume fulfill the Bragg condition. This is also indicated by the emergence of the 222-peak at higher applied load in Fig. 9c while the 331, 420, 400-peaks vanished. Thus, further measurements utilizing neutron diffraction could aid to clarify the grain size effect on the resulting data.

4.2.2. Splitting of diffraction peaks

Interestingly (and relevant for the strengthening mechanisms of these alloys), the in-situ ED-XRD patterns for the FHT specimen (Fig. 9c) show a shoulder on the 311-peak. This shoulder is shifted to a lower energy position (larger d_{hkl} value) and vanishes for larger displacements. It is not present in the DA specimen (Fig. 9a). Mignaneli et al. [87] observed an asymmetry among the reflections with a pronounced shoulder on the 311 peak for a γ'' hardened Ni-based alloy. They attributed this asymmetry to the presence of γ'' , i.e. to its increased c axis length as compared to γ and γ' . Since the DA and FHT specimens showed similar strengths, one would initially assume that the pronounced shoulder in this study is not caused by the difference in the presence of the γ'' phase. However, it still is possible since the precipitation state is different as discussed in section 4.1.4, with higher volume fractions present for the FHT condition. Considering the multi-modal grain size distribution for the FHT specimen, the shift in the shoulder of the 311-peak could also be due to mosaic sub-structure of the grains. Since residual stress is cited as the driver for recrystallization [44,45], the smaller grains may have retained larger residual stress. This would result in a variation in the d spacing between the finer and larger grains. Since the grain structure of the DA specimen is columnar, a more uniform response would be expected in the Z direction, explaining the absence of a shoulder on the 311-peak.

4.2.3. Diffraction elastic constants

The use of Hooke's law for the calculation of macroscopic stresses from measured lattice strains requires knowledge of the DEC for each diffracting plane [88]. As recently shown, the evaluation of appropriate diffraction elastic constants is even more paramount for AM materials, as in this case the single crystal EC may not be known, and the microstructure of AM materials is particularly complex [89–91]. Several classic models, reported over the past century to calculate the DEC's including Voigt [92], Reuss [93], and Eshelby-Kröner [94], are still widely in use. Fig. 12 summarizes the experimentally determined diffraction elastic constants (DECs) obtained in this study for FHT and DA samples, and compares them with data available in the literature for other Ni-based wrought and AM alloys [73,95–99] together with the model predictions (calculated with the software XEC [100]) of Reuss and Eshelby-Kröner.

All Ni-based alloys presented in Fig. 12 show similar DEC's. It is clearly visible, that the Eshelby-Kröner model accurately predicts those for wrought Ni-based alloys. For this study, the FHT specimen also seems to agree with the Eshelby-Kröner model, since its isotropic microstructure is very close to wrought Inconel 718. In contrast, the Reuss model seems to predict the behavior of the DA specimen with an over-estimation only for the 222 reflection. It should be noted that the 222-reflection of the DA specimen had a low intensity (Fig. 9a) that affects the error bar. For textured materials with elongated grains, it has already been shown that the Reuss model (homogeneous stress) can

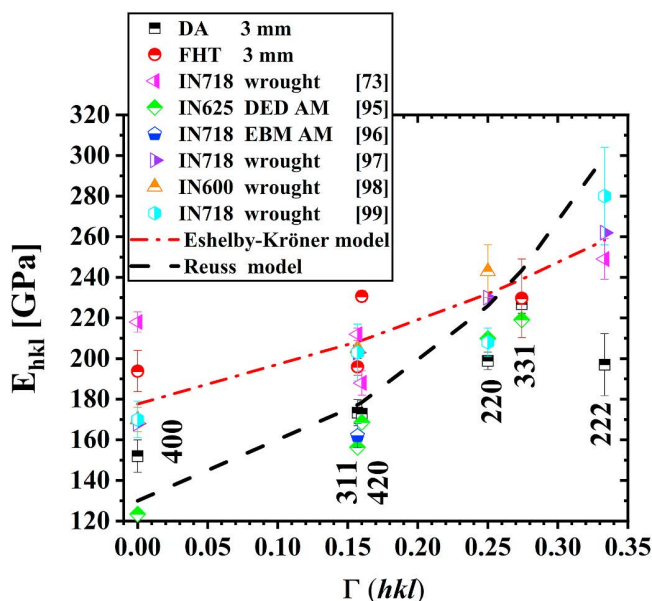


Fig. 12. DECs for various AM and wrought Ni-based alloys as a function of anisotropy factor $\Gamma_{hkl} = (h^2k^2 + k^2l^2 + h^2l^2)/(h^2 + k^2 + l^2)^2$. The Voigt model is a straight line and is not shown for the sake of clarity.

approximate the experimental data well [101].

Thus, it is highly dependent on the microstructure of the sample if the Eshelby-Kröner or Reuss model provides a better fit to the experimental data. From the observations in this study, we can conclude, that the 311 reflection is suitable for residual stress analysis of the DA specimen using monochromatic diffraction methods.

5. Conclusions

While the influence of heat treatments on the overall room-temperature tensile properties was shown not to be major, such heat treatments resulted in a large variation of the final grain morphology and texture. A discussion on the various contributors to strengthening (σ_{YS}) showed that grain size, precipitation state, strain hardening, and crystal texture all impact the yield strength to different extents. The similar tensile properties for different microstructures could therefore be explained by the different importance of the various contributions. The main findings of this study can be summarized as follows:

- The hot isostatic pressing temperature of the Ni-based Inconel 718 fully heat-treated (FHT) specimen produced by laser powder bed fusion resulted in partial recrystallization with equiaxed grains. A subsequent solutionizing heat treatment re-precipitates a fine acicular δ phase at the boundaries of the smaller grains. In contrast, the lower temperatures used in stress relief + direct aging heat-treatment (DA) allowed for the retention of the globular δ phase at grain

boundaries. With the DA, a columnar grain structure is obtained with adjacent regions of finer elongated grains.

- The different contributions of the Hall-Petch effect, the precipitation hardening, the solid solution strengthening, and strain hardening combine such that tensile macroscopic response is broadly similar between the FHT and DA specimens; their different microstructures induce, however, a very different microscopic strain behavior, since the texture is the most important factor influencing the lattice strain evolution during loading.
- The selection of an appropriate model for diffraction elastic constants (DECs) appears to be dependent on the microstructure. It was found that the experimentally determined DECs for the DA condition agreed well with the Reuss model predictions, while the DECs for the FHT condition were closer to the Eshelby-Kröner model and to reported results for conventionally manufactured Inconel 718.

Data availability statement

The raw data required to reproduce these findings cannot be shared at this time due to technical limitations. The processed data required to reproduce these findings cannot be shared at this time due to time limitations but is available on request from the corresponding author.

CRediT authorship contribution statement

Jakob Schröder: Writing - original draft, Writing - review & editing, Visualization, Formal analysis, Conceptualization. **Tatiana Mishurova:** Writing - review & editing, Methodology, Software, Formal analysis, Investigation. **Tobias Fritsch:** Conceptualization, Investigation, Methodology, Formal analysis, Writing - review & editing. **Itziar Serrano-Munoz:** Conceptualization, Methodology, Formal analysis, Investigation, Writing - review & editing. **Alexander Evans:** Supervision, Writing - review & editing, Methodology, Conceptualization. **Maximilian Sprengel:** Writing - review & editing, Investigation, Conceptualization. **Manuela Klaus:** Writing - review & editing, Investigation, Resources. **Christoph Genzel:** Writing - review & editing, Investigation, Resources. **Judith Schneider:** Writing - original draft, Writing - review & editing, Supervision, Project administration, Resources. **Giovanni Bruno:** Writing - review & editing, Supervision, Project administration, Resources.

Declaration of competing interest

The authors declare that they have no known competing financial interests or personal relationships that could have appeared to influence the work reported in this paper.

Acknowledgements

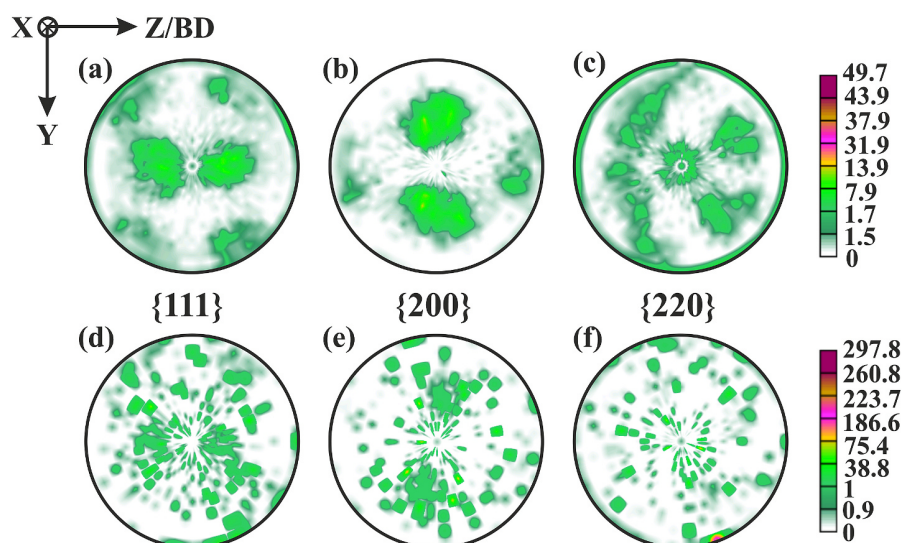
The authors want to acknowledge the support of Mr. Romeo Saliwan-Neumann at the microstructural characterization of the specimens.

Judith Schneider acknowledges funding as a guest scientist at the Bundesanstalt für Materialforschung und -prüfung (BAM).

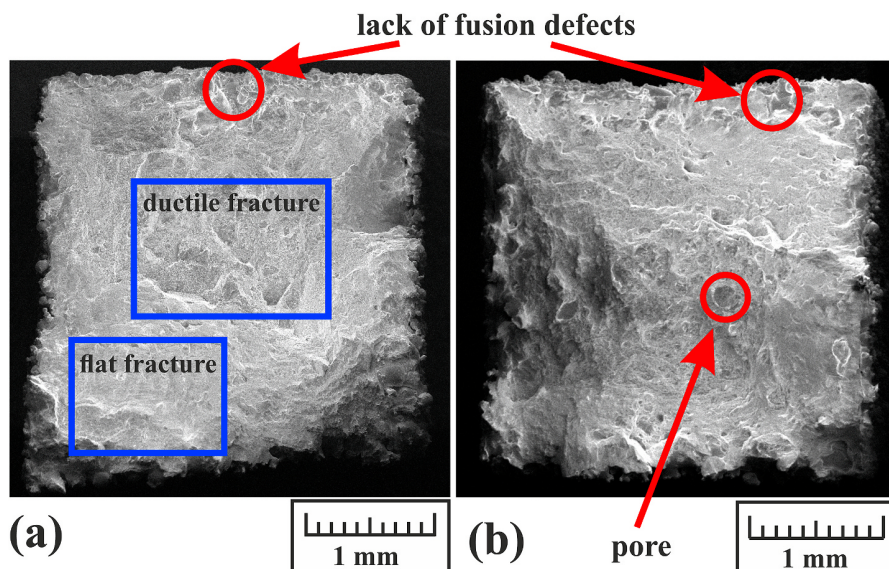
Appendix A. Supplementary data

Supplementary data to this article can be found online at <https://doi.org/10.1016/j.msea.2020.140555>.

Appendix



A 1. Results of the XRD texture measurements: (a-c) DA (d-f) FHT. Note that for the FHT specimen a large {220} might be sampled, thus leading to the high intensity. (colored, 1.5 column fit)



A 2. SEM images of the fracture surfaces of the specimen (a) FHT and (b) DA acquired from the broken in-situ tensile bars. (colored, 1.5 column fit)

References

- [1] I. Gibson, D.W. Rosen, B. Stucker, Additive Manufacturing Technologies: Rapid Prototyping to Direct Digital Manufacturing, Springer, Boston, MA, 2010, <https://doi.org/10.1007/978-1-4419-1120-9>.
- [2] J.F. Radavich, The physical metallurgy of cast and wrought alloy 718, *Superalloy 718, Metall. Appl., Proc. Int. Symp. Metall. Appl. Superalloy 718* (1989) 229–240, https://doi.org/10.7449/1989/Superalloys_1989_229_240.
- [3] D.F. Paulonis, J.M. Oblak, D.S. Duvall, Precipitation in nickel-base alloy 718, *ASM Trans. Q.* 62 (3) (1969) 611–622.
- [4] I. Kirman, D.H. Warrington, Precipitation of Ni₃Nb phases in a Ni-Fe-Cr-Nb alloy, *Metall. Trans.* 1 (10) (1970) 2667–2675, <https://doi.org/10.1007/BF03037800>.
- [5] A. Oradei-Basile, J.F. Radavich, A current T-T-T diagram for wrought alloy 718, in: *Superalloys 718, 625 Var. Deriv., Proc. Int. Symp. Metall. Appl. Superalloys*, vol. 718, 1991, pp. 325–335, https://doi.org/10.7449/1991/Superalloys_1991_325_335, 625 Var. Deriv.
- [6] C. Slama, M. Abdellaoui, Structural characterization of the aged Inconel 718, *J. Alloys Compd.* 306 (1–2) (2000) 277–284, [https://doi.org/10.1016/S0925-8388\(00\)00789-1](https://doi.org/10.1016/S0925-8388(00)00789-1).
- [7] J. Belan, GCP and TCP phases presented in nickel-base superalloys, *Mater. Today-Proc.* 3 (4) (2016) 936–941, <https://doi.org/10.1016/j.matpr.2016.03.024>.
- [8] J.J. Schirra, Development of a improved heat treatment for investment cast Inconel 718 (PWA 649), in: *Superalloys 718, 625, 706 Var. Deriv., Proc. Int. Symp.*, 4th, 1996, pp. 439–446, https://doi.org/10.7449/1997/Superalloys_1997_439_446.
- [9] R.G. Carlson, J.F. Radavich, Microstructural characterization of cast 718, superalloys 718 - metall. Appl, in: *Proc. Int. Symp. Metall. Appl. Superalloy*, vol. 718, 1989, pp. 79–95, https://doi.org/10.7449/1989/Superalloys_1989_79_95.
- [10] AMS5383, Nickel Alloy, Corrosion and Heat-Resistant, Investment Castings, 52.5Ni - 19Cr - 3.0Mo - 5.1Cb(Nb) - 0.90Ti - 0.60Al - 18Fe, Vacuum Melted Homogenization and Solution Heat Treated, SAE International, Warrendale, PA, 2018, <https://doi.org/10.4271/AMS5383>.
- [11] G.A. Rao, M. Kumar, M. Srinivas, D.S. Sarma, Effect of standard heat treatment on the microstructure and mechanical properties of hot isostatically pressed superalloy inconel 718, *Mater. Sci. Eng., A* 355 (1–2) (2003) 114–125, [https://doi.org/10.1016/S0921-5093\(03\)00079-0](https://doi.org/10.1016/S0921-5093(03)00079-0).
- [12] C.L. Qiu, M.M. Attallah, X.H. Wu, P. Andrews, Influence of hot isostatic pressing temperature on microstructure and tensile properties of a nickel-based superalloy powder, *Mater. Sci. Eng., A* 564 (2013) 176–185, <https://doi.org/10.1016/j.msea.2012.11.084>.
- [13] C.L. Qiu, X.H. Wu, J.F. Mei, P. Andrews, W. Voice, Influence of heat treatment on microstructure and tensile behavior of a hot isostatically pressed nickel-based

- superalloy, *J. Alloys Compd.* 578 (2013) 454–464, <https://doi.org/10.1016/j.jallcom.2013.06.045>.
- [14] AMS5662, Nickel Alloy, Corrosion and Heat-Resistant, Bars, Forgings, and Rings 52.5Ni - 19Cr - 3.0Mo - 5.1Cb (Nb) - 0.90Ti - 0.50Al - 18Fe Consumable Electrode or Vacuum Induction Melted 1775 °F (968 °C) Solution Heat Treated, Precipitation Hardenable, SAE International, Warrendale, PA, 2016, <https://doi.org/10.4271/AMS5662>.
- [15] AMS5663, Nickel Alloy, Corrosion and Heat-Resistant, Bars, Forgings, and Rings 52.5Ni - 19Cr - 3.0Mo - 5.1Cb (Nb) - 0.90Ti - 0.50Al - 18Fe Consumable Electrode or Vacuum Induction Melted 1775 °F (968 °C) Solution and Precipitation Heat Treated SAE International, 2016, <https://doi.org/10.4271/AMS5663>.
- [16] AMS5664, Corrosion and Heat-Resistant, Bars, Forgings, and Rings 52.5Ni - 19Cr - 3.0Mo - 5.1Cb (Nb) - 0.90Ti - 0.50Al - 18Fe Consumable Electrode or Vacuum Induction Melted 1950 °F (1066 °C) Solution Heat Treated, Precipitation-Hardenable SAE International, Warrendale, PA, 2017, <https://doi.org/10.4271/AMS5664>.
- [17] ASTM-F3301-18a, Standard for Additive Manufacturing - Post Processing Methods - Standard Specification for Thermal Post-Processing Metal Parts Made via Powder Bed Fusion, ASTM International, West Conshohocken, PA, 2018, <https://doi.org/10.1520/F3301-18A>.
- [18] M. Anderson, A.L. Thielin, F. Bridier, P. Bocher, J. Savoie, Delta Phase precipitation in Inconel 718 and associated mechanical properties, *Mater. Sci. Eng., A* 679 (2017) 48–55, <https://doi.org/10.1016/j.msea.2016.09.114>.
- [19] K.N. Amato, S.M. Gaytan, L.E. Murr, E. Martinez, P.W. Shindo, J. Hernandez, S. Collins, F. Medina, Microstructures and mechanical behavior of Inconel 718 fabricated by selective laser melting, *Acta Mater.* 60 (5) (2012) 2229–2239, <https://doi.org/10.1016/j.actamat.2011.12.032>.
- [20] S. Mahadevan, S. Nalawade, J. Bahadur Singh, A. Verma, B. Paul, K. Ramaswamy, Evolution of δ phase microstructure in alloy 718, in: *Superalloy 718 Deriv.*, Proc. Int. Symp., 7th, 2010, pp. 737–750, https://doi.org/10.7449/2010/Superalloys_2010_737_750.
- [21] Y. Idell, L.E. Levine, A.J. Allen, F. Zhang, C.E. Campbell, G.B. Olson, J. Gong, D. R. Snyder, H.Z. Deutchman, Unexpected delta-phase formation in additive-manufactured Ni-based superalloy, *Jom-Us* 68 (3) (2016) 950–959, <https://doi.org/10.1007/s11837-015-1772-2>.
- [22] R.S. Cremisio, H.M. Butler, J.F. Radavich, Effect of thermomechanical history on stability of alloy 718, *Jom-Us* 21 (11) (1969) 55–61, <https://doi.org/10.1007/Bf03378798>.
- [23] R. Cozar, A. Pineau, Morphology of γ' and γ'' precipitates and thermal-stability of inconel 718 type Alloys, *Metall. Trans. A* 4 (1) (1973) 47–59, <https://doi.org/10.1007/Bf02649604>.
- [24] A. Devaux, L. Naze, R. Molins, A. Pineau, A. Organista, J.Y. Guedou, J.F. Uginet, P. Heritier, Gamma double prime precipitation kinetic in Alloy 718, *Mater. Sci. Eng., A* 486 (1–2) (2008) 117–122, <https://doi.org/10.1016/j.msea.2007.08.046>.
- [25] W.M. Tucho, V. Hansen, Characterization of SLM-fabricated Inconel 718 after solid solution and precipitation hardening heat treatments, *J. Mater. Sci.* 54 (1) (2019) 823–839, <https://doi.org/10.1007/s10853-018-2851-x>.
- [26] W.D. Cao, R. Kennedy, Role of chemistry in 718-type alloys - allvac (R) 718Plus (TM) alloy development, in: *Superalloys 2004*, Proc. Int. Symp., 10th, 2004, pp. 91–99, https://doi.org/10.7449/2004/Superalloys_2004_91_99.
- [27] S. Azadian, L.Y. Wei, R. Warren, Delta phase precipitation in Inconel 718, *Mater. Char.* 53 (1) (2004) 7–16, <https://doi.org/10.1016/j.matchar.2004.07.004>.
- [28] H. Yuan, W.C. Liu, Effect of the delta phase on the hot deformation behavior of Inconel 718, *Mater. Sci. Eng., A* 408 (1–2) (2005) 281–289, <https://doi.org/10.1016/j.msea.2005.08.126>.
- [29] D.Y. Cai, W.H. Zhang, P.L. Nie, W.C. Liu, M. Yao, Dissolution kinetics of delta phase and its influence on the notch sensitivity of Inconel 718, *Mater. Char.* 58 (3) (2007) 220–225, <https://doi.org/10.1016/j.matchar.2006.04.020>.
- [30] P.J.P. Kanetas, L.A.R. Osorio, M.P.G. Mata, M. De La Garza, V.P. Lopez, Influence of the delta phase in the microstructure of the inconel 718 subjected to "Delta-processing" heat treatment and hot deformed, *Procedia Mater. Sci.* 8 (2015) 1160–1165, <https://doi.org/10.1016/j.mspro.2015.04.180>.
- [31] D.D. Krueger, The development of direct age 718 for gas turbine engine disk applications, *Superalloy 718*, Metall. Appl., Proc. Int. Symp. Metall. Appl. Superalloy 718 (1989) 279–296, https://doi.org/10.7449/1989/Superalloys_1989_279_296.
- [32] L.T. Chang, W.R. Sun, Y.Y. Cui, F.Q. Zhang, R. Yang, Effect of heat treatment on microstructure and mechanical properties of the hot-isostatic-pressed Inconel 718 powder compact, *J. Alloys Compd.* 590 (2014) 227–232, <https://doi.org/10.1016/j.jallcom.2013.12.107>.
- [33] H. Qi, M. Azer, A. Ritter, Studies of standard heat treatment effects on microstructure and mechanical properties of laser net shape manufactured INCONEL 718, *Mater. Sci. Eng., A* 40a (10) (2009) 2410–2422, <https://doi.org/10.1007/s11661-009-9949-3>.
- [34] Q.B. Jia, D.D. Gu, Selective laser melting additive manufacturing of Inconel 718 superalloy parts: densification, microstructure and properties, *J. Alloys Compd.* 585 (2014) 713–721, <https://doi.org/10.1016/j.jallcom.2013.09.171>.
- [35] D.Y. Zhang, W. Niu, X.Y. Cao, Z. Liu, Effect of standard heat treatment on the microstructure and mechanical properties of selective laser melting manufactured Inconel 718 superalloy, *Mater. Sci. Eng., A* 644 (2015) 32–40, <https://doi.org/10.1016/j.msea.2015.06.021>.
- [36] T. Trotsch, J. Ströbner, R. Völk, U. Glatzel, Microstructure and mechanical properties of selective laser melted Inconel 718 compared to forging and casting, *Mater. Lett.* 164 (2016) 428–431, <https://doi.org/10.1016/j.matlet.2015.10.136>.
- [37] D.H. Smith, J. Bicknell, L. Jorgensen, B.M. Patterson, N.L. Cordes, I. Tsukrov, M. Knezevic, Microstructure and mechanical behavior of direct metal laser sintered Inconel alloy 718, *Mater. Char.* 113 (2016) 1–9, <https://doi.org/10.1016/j.matchar.2016.01.003>.
- [38] J.P. Choi, G.H. Shin, S. Yang, D.Y. Yang, J.S. Lee, M. Brochu, J.H. Yu, Densification and microstructural investigation of Inconel 718 parts fabricated by selective laser melting, *Powder Technol.* 310 (2017) 60–66, <https://doi.org/10.1016/j.powtec.2017.01.030>.
- [39] W.M. Tucho, P. Cuvillier, A. Sjolyst-Kvemeland, V. Hansen, Microstructure and hardness studies of Inconel 718 manufactured by selective laser melting before and after solution heat treatment, *Mater. Sci. Eng., A* 689 (2017) 220–232, <https://doi.org/10.1016/j.msea.2017.02.062>.
- [40] A. Mostafa, I.P. Rubio, V. Brailovski, M. Jahazi, M. Medraj, Structure, texture and phases in 3D printed IN718 alloy subjected to homogenization and HIP treatments (vol 7, 196, 2017), *Metals-Basel* 7 (8) (2017), <https://doi.org/10.3390/met7060196>.
- [41] S. Kou, *Welding Metallurgy*, 2 ed., John Wiley & Sons, Hoboken, NJ, 2002 <https://doi.org/10.1002/0471434027>.
- [42] T. DebRoy, H.L. Wei, J.S. Zuback, T. Mukherjee, J.W. Elmer, J.O. Milewski, A. M. Beese, A. Wilson-Heid, A. De, W. Zhang, Additive manufacturing of metallic components - process, structure and properties, *Prog. Mater. Sci.* 92 (2018) 112–224, <https://doi.org/10.1016/j.pmatsci.2017.10.001>.
- [43] J. Schneider, B. Lund, M. Fullen, Effect of heat treatment variations on the mechanical properties of Inconel 718 selective laser melted specimens, *Addit. Manuf.* 21 (2018) 248–254, <https://doi.org/10.1016/j.addma.2018.03.005>.
- [44] F.C. Liu, X. Lin, G.L. Yang, M.H. Song, J. Chen, W.D. Huang, Microstructure and residual stress of laser rapid formed Inconel 718 nickel-base superalloy, *Optic Laser. Technol.* 43 (1) (2011) 208–213, <https://doi.org/10.1016/j.optlastec.2010.06.015>.
- [45] J. Cao, F.C. Liu, X. Lin, C.P. Huang, J. Chen, W.D. Huang, Effect of overlap rate on recrystallization behaviors of Laser Solid Formed Inconel 718 superalloy, *Optic Laser. Technol.* 45 (2013) 228–235, <https://doi.org/10.1016/j.optlastec.2012.06.043>.
- [46] E. Chlebus, K. Gruber, B. Kuznicka, J. Kurzac, T. Kurzynowski, Effect of heat treatment on the microstructure and mechanical properties of Inconel 718 processed by selective laser melting, *Mater. Sci. Eng., A* 639 (2015) 647–655, <https://doi.org/10.1016/j.msea.2015.05.035>.
- [47] W.J. Sames, F.A. List, S. Pannala, R.R. Dehoff, S.S. Babu, The metallurgy and processing science of metal additive manufacturing, *Int. Mater. Rev.* 61 (5) (2016) 315–360, <https://doi.org/10.1080/09506608.2015.1116649>.
- [48] H.Y. Wan, Z.J. Zhou, C.P. Li, G.F. Chen, G.P. Zhang, Effect of scanning strategy on mechanical properties of selective laser melted Inconel 718, *Mater. Sci. Eng., A* 753 (2019) 42–48, <https://doi.org/10.1016/j.msea.2019.03.007>.
- [49] D.Y. Deng, R.L. Peng, H. Brodin, J. Moverare, Microstructure and mechanical properties of Inconel 718 produced by selective laser melting: sample orientation dependence and effects of post heat treatments, *Mater. Sci. Eng., A* 713 (2018) 294–306, <https://doi.org/10.1016/j.msea.2017.12.043>.
- [50] M. Calandri, S. Yin, B. Aldwell, F. Calignano, R. Lupoi, D. Ugues, Texture and microstructural features at different length scales in inconel 718 produced by selective laser melting, *Materials* 12 (8) (2019), <https://doi.org/10.3390/ma12081293>.
- [51] L. Zhou, A. Mehta, B. McWilliams, K. Cho, Y. Sohn, Microstructure, precipitates and mechanical properties of powder bed fused inconel 718 before and after heat treatment, *J. Mater. Sci. Technol.* 35 (6) (2019) 1153–1164, <https://doi.org/10.1016/j.jmst.2018.12.006>.
- [52] T.G. Gallmeyer, S. Moorthy, B.B. Kappes, M.J. Mills, B. Amin-Ahmadi, A. P. Stebner, Knowledge of process-structure-property relationships to engineer better heat treatments for laser powder bed fusion additive manufactured Inconel 718, *Addit. Manuf.* 31 (2020), <https://doi.org/10.1016/j.addma.2019.100977>.
- [53] G. Lindwall, C.E. Campbell, E.A. Lass, F. Zhang, M.R. Stoudt, A.J. Allen, L. E. Levine, Simulation of TTT curves for additively manufactured inconel 625, *Metall. Mater. Trans.* 50a (1) (2019) 457–467, <https://doi.org/10.1007/s11661-018-4959-7>.
- [54] C. Kumara, A.R. Balachandramurthi, S. Goel, F. Henning, J. Moverare, Toward a better understanding of phase transformations in additive manufacturing of Alloy 718, *Materialia* 13 (2020), <https://doi.org/10.1016/j.mta.2020.100862>.
- [55] X.M. Zhao, J. Chen, X. Lin, W.D. Huang, Study on microstructure and mechanical properties of laser rapid forming Inconel 718, *Mater. Sci. Eng., A* 478 (1–2) (2008) 119–124, <https://doi.org/10.1016/j.msea.2007.05.079>.
- [56] A.J. Sterling, B. Torries, N. Shamsaei, S.M. Thompson, D.W. Seely, Fatigue behavior and failure mechanisms of direct laser deposited Ti-6Al-4V (vol 655, pg 100, 2016), *Mater. Sci. Eng., A* 655 (2016), <https://doi.org/10.1016/j.msea.2016.01.007>, 425–425.
- [57] A. Yadollahi, N. Shamsaei, S.M. Thompson, A. Elwany, L. Bian, Effects of building orientation and heat treatment on fatigue behavior of selective laser melted 17-4 PH stainless steel, *Int. J. Fatig.* 94 (2017) 218–235, <https://doi.org/10.1016/j.ijfatigue.2016.03.014>.
- [58] W. Tillmann, C. Schaak, J. Nellesen, M. Schaper, M.E. Aydinöz, K.P. Hoyer, Hot isostatic pressing of IN718 components manufactured by selective laser melting, *Addit. Manuf.* 13 (2017) 93–102, <https://doi.org/10.1016/j.addma.2016.11.006>.
- [59] S. Leuders, M. Thöne, A. Riemer, T. Niendorf, T. Tröster, H.A. Richard, H. J. Maier, On the mechanical behavior of titanium alloy TiAl6V4 manufactured by selective laser melting: fatigue resistance and crack growth performance, *Int. J. Fatig.* 48 (2013) 300–307, <https://doi.org/10.1016/j.ijfatigue.2012.11.011>.
- [60] S. Tammam-Williams, P.I. Withers, I. Todd, P.B. Prangnell, Porosity regrowth during heat treatment of hot isostatically pressed additively manufactured

- titanium components, *Scripta Mater.* 122 (2016) 72–76, <https://doi.org/10.1016/j.scriptamat.2016.05.002>.
- [61] F. Brenne, A. Taube, M. Pröbstle, S. Neumeier, D. Schwarze, M. Schaper, T. Niendorf, Microstructural design of Ni-base alloys for high-temperature applications: impact of heat treatment on microstructure and mechanical properties after selective laser melting, *Prog. Addit. Manuf.* 1 (2016) 141–151, <https://doi.org/10.1007/s40964-016-0013-8>.
- [62] I. Kelbassa, E.W. Kreutz, P. Albus, L. Zhu, Mechanical properties of the laser clad alloys Ti-6Al-4V and Inconel 718, in: *International Congress on Applications of Lasers & Electro-Optics*, 2005, pp. 660–665, <https://doi.org/10.2351/1.5060594>.
- [63] K. Kunze, T. Etter, J. Grasslin, V. Shklover, Texture, anisotropy in microstructure and mechanical properties of IN738LC alloy processed by selective laser melting (SLM), *Mater. Sci. Eng., A* 620 (2015) 213–222, <https://doi.org/10.1016/j.msea.2014.10.003>.
- [64] C. Genzel, I.A. Denks, J. Gibmeler, M. Klaus, G. Wagener, The materials science synchrotron beamline EDDI for energy-dispersive diffraction analysis, *Nucl. Instrum. Methods Phys. Res., Sect. A* 578 (1) (2007) 23–33, <https://doi.org/10.1016/j.nima.2007.05.209>.
- [65] F. Bachmann, R. Hielscher, H. Schaeben, Grain detection from 2d and 3d EBSD data-Specification of the MTEX algorithm, *Ultramicroscopy* 111 (12) (2011) 1720–1733, <https://doi.org/10.1016/j.ultramic.2011.08.002>.
- [66] H. Gruber, C. Luchian, E. Hryha, L. Nyborg, Effect of powder recycling on defect formation in electron beam melted alloy 718, *Metall. Mater. Trans.* 51 (5) (2020) 2430–2443, <https://doi.org/10.1007/s11661-020-05674-8>.
- [67] S. Tammas-Williams, H. Zhao, F. Leonard, F. Derguti, I. Todd, P.B. Prangnell, XCT analysis of the influence of melt strategies on defect population in Ti-6Al-4V components manufactured by Selective Electron Beam Melting, *Mater. Char.* 102 (2015) 47–61, <https://doi.org/10.1016/j.matchar.2015.02.008>.
- [68] T. Mishurova, K. Artzt, J. Haubrich, G. Requena, G. Bruno, New aspects about the search for the most relevant parameters optimizing SLM materials, *Addit. Manuf.* 25 (2019) 325–334, <https://doi.org/10.1016/j.addma.2018.11.023>.
- [69] R. Laquai, B.R. Müller, J.A. Schneider, A. Kupsch, G. Bruno, Using SXRR to probe the nature of discontinuities in SLM additive manufactured inconel 718 specimens, *Metall. Mater. Trans.* 51 (8) (2020) 4146–4157, <https://doi.org/10.1007/s11661-020-05847-5>.
- [70] R. Laquai, B.R. Müller, G. Kasperovich, J. Haubrich, G. Requena, G. Bruno, X-ray refraction distinguishes unprocessed powder from empty pores in selective laser melting Ti-6Al-4V, *Mater. Res. Lett.* 6 (2) (2018) 130–135, <https://doi.org/10.1080/21663831.2017.1409288>.
- [71] R. Laquai, B.R. Müller, G. Kasperovich, G. Requena, J. Haubrich, G. Bruno, Classification of defect types in SLM Ti-6Al-V4 by X-ray refraction topography, *Mater. Perform. Char.* 9 (1) (2020), <https://doi.org/10.1520/MPC20190080>.
- [72] B. Zhang, Y.T. Li, Q. Bai, Defect formation mechanisms in selective laser melting: a review chin, *J. Mech. Eng.* 30 (6) (2017), <https://doi.org/10.1007/s10033-017-0184-3>, 1476–1476.
- [73] J.N. Wagner, M. Hofmann, R. Wimpory, C. Kremaszky, M. Stockinger, Microstructure and temperature dependence of intergranular strains on diffractometric macroscopic residual stress analysis, *Mater. Sci. Eng., A* 618 (2014) 271–279, <https://doi.org/10.1016/j.msea.2014.09.033>.
- [74] C. Kantzos, J. Pauza, R. Cunningham, S.P. Narra, J. Beuth, A. Rollett, An investigation of process parameter modifications on additively manufactured inconel 718 parts, *J. Mater. Eng. Perform.* 28 (2) (2019) 620–626, <https://doi.org/10.1007/s11665-018-3612-3>.
- [75] D. Kotzem, P. Dumke, P. Sepehri, J. Tenkamp, F. Walther, Effect of miniaturization and surface roughness on the mechanical properties of the electron beam melted superalloy Inconel 718, *Prog. Addit. Manuf.* 5 (2020) 267–276, <https://doi.org/10.1007/s40964-019-00101-w>.
- [76] C.H. Pei, D. Shi, H. Yuan, H.X. Li, Assessment of mechanical properties and fatigue performance of a selective laser melted nickel-base superalloy Inconel 718, *Mater. Sci. Eng., A* 759 (2019) 278–287, <https://doi.org/10.1016/j.msea.2019.05.007>.
- [77] M.D. Sangid, T.A. Book, D. Naragani, J. Rotella, P. Ravi, A. Finch, P. Kenesei, J. S. Park, H. Sharma, J. Almer, X.H. Xiao, Role of heat treatment and build orientation in the microstructure sensitive deformation characteristics of IN718 produced via SLM additive manufacturing, *Addit. Manuf.* 22 (2018) 479–496, <https://doi.org/10.1016/j.addma.2018.04.032>.
- [78] M.E. Aydinöz, F. Brenne, M. Schaper, C. Schaak, W. Tillmann, J. Nellesen, T. Niendorf, On the microstructural and mechanical properties of post-treated additively manufactured Inconel 718 superalloy under quasi-static and cyclic loading, *Mater. Sci. Eng., A* 669 (2016) 246–258, <https://doi.org/10.1016/j.msea.2016.05.089>.
- [79] R.C. Hall, The metallurgy of alloy 718, *J. Basic Eng.* 89 (3) (1967) 511–516, <https://doi.org/10.1115/1.3609651>.
- [80] N.C. Ferreri, S.C. Vogel, M. Knezevic, Determining volume fractions of γ , γ' , γ'' , δ , and MC-carbide phases in Inconel 718 as a function of its processing history using an advanced neutron diffraction procedure, *Mater. Sci. Eng., A* 781 (2020), <https://doi.org/10.1016/j.msea.2020.139228>.
- [81] M. Ni, C. Chen, X.J. Wang, P.W. Wang, R.D. Li, X.Y. Zhang, K.C. Zhou, Anisotropic tensile behavior of in situ precipitation strengthened Inconel 718 fabricated by additive manufacturing, *Mater. Sci. Eng., A* 701 (2017) 344–351, <https://doi.org/10.1016/j.msea.2017.06.098>.
- [82] G.E. Bean, T.D. McLouth, D.B. Witkin, S.D. Sitzman, P.M. Adams, R.J. Zaldivar, Build orientation effects on texture and mechanical properties of selective laser melting inconel 718, *J. Mater. Eng. Perform.* 28 (4) (2019) 1942–1949, <https://doi.org/10.1007/s11665-019-03980-w>.
- [83] H.Y. Wan, Z.J. Zhou, C.P. Li, G.F. Chen, G.P. Zhang, Effect of scanning strategy on grain structure and crystallographic texture of Inconel 718 processed by selective laser melting, *J. Mater. Sci. Technol.* 34 (10) (2018) 1799–1804, <https://doi.org/10.1016/j.jmst.2018.02.002>.
- [84] R. Jiang, A. Mostafaei, J. Pauza, C. Kantzos, A.D. Rollett, Varied heat treatments and properties of laser powder bed printed Inconel 718, *Mater. Sci. Eng., A* 755 (2019) 170–180, <https://doi.org/10.1016/j.msea.2019.03.103>.
- [85] I. Serrano-Munoz, T. Mishurova, T. Thiede, M. Sprengel, A. Kromm, N. Nadammal, R. Saliwan-Neumann, A. Evans, G. Bruno, The residual stress in as-built Laser Powder Bed Fusion IN718 alloy as a consequence of the scanning strategy induced microstructure, *Sci. Rep.* 10 (2020) 14645, <https://doi.org/10.1038/s41598-020-71112-9>.
- [86] ISO-21432, Non-destructive testing - standard test method for determining residual stresses by neutron diffraction, International Organization for Standardization, Geneva, Switzerland, 2019, <https://doi.org/10.31030/3150883>.
- [87] P.M. Mignaneli, N.G. Jones, M.C. Hardy, H.J. Stone, On the time-temperature transformation behavior of a new dual-supperlattice nickel-based superalloy, *Metall. Mater. Trans.* 49a (3) (2018) 699–707, <https://doi.org/10.1007/s11661-017-4355-8>.
- [88] T. Gnäupel-Herold, A.A. Creuziger, M. Iadicola, A model for calculating diffraction elastic constants, *J. Appl. Crystallogr.* 45 (2012) 197–206, <https://doi.org/10.1107/S0021889812002221>.
- [89] T. Mishurova, K. Artzt, J. Haubrich, S. Evsevlev, A. Evans, M. Meixner, I. S. Munoz, I. Sevostianov, G. Requena, G. Bruno, Connecting diffraction-based strain with macroscopic stresses in laser powder bed fused Ti-6Al-4V, *Metall. Mater. Trans.* 51 (6) (2020) 3194–3204, <https://doi.org/10.1007/s11661-020-05711-6>.
- [90] T. Mishurova, G. Bruno, S. Evsevlev, I. Sevostianov, Determination of macroscopic stress from diffraction experiments: a critical discussion, *J. Appl. Phys.* 128 (2) (2020), <https://doi.org/10.1063/5.0009101>.
- [91] I. Serrano-Munoz, T. Thiede, T. Mishurova, A. Trofimov, D. Apel, A. Ulbricht, A. Kromm, R. Hesse, A. Evans, G. Bruno, On the interplay of microstructure and residual stress in LPBF IN718, *J. Mater. Sci.* (2020), <https://doi.org/10.1007/s10853-020-05553-y> accepted.
- [92] W. Voigt, Ueber die Beziehung zwischen den beiden Elasticitätsconstanten isotroper Körper, *Ann. Phys.* 274 (12) (1889) 573–587, <https://doi.org/10.1002/andp.18892741206>.
- [93] A. Reuss, Account of the liquid limit of mixed crystals on the basis of the plasticity condition for single crystal, *Z. Angew. Math. Mech.* 9 (1929) 49–58, <https://doi.org/10.1002/zamm.19290090104>.
- [94] E. Kröner, Berechnung der elastischen Konstanten des Vielkristalls aus den Konstanten des Einkristalls, *Z. Phys. Atom. Nucl.* 151 (4) (1958) 504–518, <https://doi.org/10.1007/bf01337948>, 1975.
- [95] Z.Q. Wang, A.D. Stoica, D. Ma, A.M. Beese, Diffraction and single-crystal elastic constants of Inconel 625 at room and elevated temperatures determined by neutron diffraction, *Mater. Sci. Eng., A* 674 (2016) 406–412, <https://doi.org/10.1016/j.msea.2016.08.010>.
- [96] E. Cakmak, T.R. Watkins, J.R. Bunn, R.C. Cooper, P.A. Cornwell, Y.L. Wang, L. M. Sochalski-Kolbus, R.R. Dehoff, S.S. Babu, Mechanical characterization of an additively manufactured inconel 718 theta-shaped specimen, *Metall. Mater. Trans.* 47a (2) (2016) 971–980, <https://doi.org/10.1007/s11661-015-3186-8>.
- [97] P.E. Aba-Perea, T. Pilling, P.J. Withers, J. Kelleher, S. Kabra, M. Preuss, Determination of the high temperature elastic properties and diffraction elastic constants of Ni-base superalloys, *Mater. Des.* 89 (2016) 856–863, <https://doi.org/10.1016/j.matdes.2015.09.152>.
- [98] T.M. Holden, R.A. Holt, A.P. Clarke, Intergranular strains in Inconel-600 and the impact on interpreting stress fields in bent steam-generator tubing, *Mater. Sci. Eng., A* 246 (1–2) (1998) 180–198, [https://doi.org/10.1016/S0921-5093\(97\)00732-6](https://doi.org/10.1016/S0921-5093(97)00732-6).
- [99] J. Repper, M. Hofmann, C. Kremaszky, R.C. Wimpory, W. Petry, E. Werner, Microstrain accumulation in multiphase superalloys, *Powder Diffr.* 24 (2) (2009) S65–S67, <https://doi.org/10.1154/1.3134582>.
- [100] H. Wern, R. Johannes, H. Walz, Dependence of the X-ray elastic constants on the diffraction plane, *Phys. Status Solidi B* 206 (2) (1998) 545–557, [https://doi.org/10.1002/\(Sici\)1521-3951\(199804\)206:2<545::Aid-Pssb545>3.0.Co;2-J](https://doi.org/10.1002/(Sici)1521-3951(199804)206:2<545::Aid-Pssb545>3.0.Co;2-J).
- [101] L. Spieß, G. Teichert, R. Schwarzer, H. Behnken, C. Genzel, *Moderne Röntgenbeugung*, 2 ed., Vieweg+Teubner Verlag, Wiesbaden, 2009 <https://doi.org/10.1007/978-3-8349-9434-9>.

Understanding the impact of texture on the micromechanical anisotropy of laser powder bed fused Inconel 718

P3

J. SCHRÖDER, A. EVANS, E. POLATIDIS, J. ČAPEK, G. MOHR,
I. SERRANO-MUNOZ, G. BRUNO

8th August 2022

J Mater Sci (2022) 57:15036-15058
DOI: 10.1007/s10853-022-07499-9

0 Preface

While Publication 2 focused on the impact of heat treatments on the mechanical behavior of PBF-LB/M/IN718, this article focusses on the mechanical behavior in the as-built state. Such studies are motivated from findings of Publication 2, where we observed that the diffraction elastic behavior significantly depends on the underlying microstructure. Therefore, we took a step back to understand the mechanical behavior of as-built material. In fact, most of residual stress measurements are conducted on as-built material. In particular, emphasis is put on understanding the role of crystallographic texture on the macro and micro mechanical scale.

In that regard, specimens with different build orientations, thereby possessing differences crystallographic textures, are manufactured. Once subjected to macroscopic load, the lattice strain responses are monitored during *in situ* neutron diffraction experiments. Besides the determination of the diffraction elastic moduli, the impact of the cellular solidification sub-structure on the deformation behavior is discussed.


Reprinted under the open access CC BY 4.0 license

<https://creativecommons.org/licenses/by/4.0/>





Understanding the impact of texture on the micromechanical anisotropy of laser powder bed fused Inconel 718

Jakob Schröder^{1,*} , Alexander Evans^{1,*}, Efthymios Polatidis², Jan Čapek², Gunther Mohr¹, Itziar Serrano-Munoz¹, and Giovanni Bruno^{1,3}

¹Bundesanstalt für Materialforschung und -prüfung, Unter den Eichen 87, 12205 Berlin, Germany

²Laboratory for Neutron Scattering and Imaging, Paul Scherrer Institut, Forschungsstrasse 111, 5232 Villigen, Switzerland

³Universität Potsdam, Institut für Physik und Astronomie, Karl-Liebknecht-Str. 24-25, 14476 Potsdam, Germany

Received: 11 May 2022

Accepted: 27 June 2022

Published online:

8 August 2022

© The Author(s) 2022

ABSTRACT

The manufacturability of metallic alloys using laser-based additive manufacturing methods such as laser powder bed fusion has substantially improved within the last decade. However, local melting and solidification cause hierarchically structured and crystallographically textured microstructures possessing large residual stress. Such microstructures are not only the origin of mechanical anisotropy but also pose metrological challenges for the diffraction-based residual stress determination. Here we demonstrate the influence of the build orientation and the texture on the microstructure and consequently the mechanical anisotropy of as-built Inconel 718. For this purpose, we manufactured specimens with [001]/[011]-, [001]- and [011]/[$\bar{1}11$]-type textures along their loading direction. In addition to changes in the Young's moduli, the differences in the crystallographic textures result in variations of the yield and ultimate tensile strengths. With this in mind, we studied the anisotropy on the micromechanical scale by subjecting the specimens to tensile loads along the different texture directions during in situ neutron diffraction experiments. In this context, the response of multiple lattice planes up to a tensile strain of 10% displayed differences in the load partitioning and the residual strain accumulation for the specimen with [011]/[$\bar{1}11$]-type texture. However, the relative behavior of the specimens possessing an [001]/[011]- and [001]-type texture remained qualitatively similar. The consequences on the metrology of residual stress determination methods are discussed.

Handling Editor: Sophie Primig.

Address correspondence to E-mail: Jakob.Schroeder@bam.de; Alexander.Evans@bam.de

Introduction

Powder-based additive manufacturing (AM) processes such as laser powder bed fusion (L-PBF) allow the fabrication of complex structures within a single manufacturing step [1, 2]. In the L-PBF process, a laser locally melts powder particles to incrementally form a body layer-wise [1]. However, localized heat inputs induce large local temperature gradients, which result in the formation of large internal stress (IS) during production [2, 3]. Excessive IS buildup may cause delamination or cracking during manufacturing [2–4]. Upon cooling, these IS lead to locked residual stress (RS) in the final part [2, 3]. If not accounted for, these RS can be detrimental to the structural integrity, causing in-service part failure [3, 5–7]. Although these drawbacks exist, AM promises improvements in the design of lightweight structures (*e.g.*, for aerospace applications) [8, 9]. Therefore, it is imperative to fully understand the impact of RS on the performance of AM parts, if we want to exploit these potential improvements.

In particular, AM of nickel (Ni)-based alloys such as Inconel 718 has been widely studied in open research (see *e.g.*, [10–17]). Inconel 718 is a multiphase Ni–Cr–Fe alloy with additions of niobium (Nb) and molybdenum (Mo), as well as low amounts of aluminum (Al) and titanium (Ti) [18]. Among Ni-based alloys, Inconel 718 exhibits an excellent weldability [19, 20]. Furthermore, it retains its high temperature properties up to a temperature of 650 °C, making it suitable for jet engine applications [21]. The desired properties are obtained by inducing the precipitation of two main strengthening phases: γ'' (Ni₃Nb, tetragonal D0₂₂) and γ' (Ni₃(Al,Ti), cubic L1₂). Such precipitates occur when submitting the material to aging heat-treatments after production [18, 22, 23].

The large local thermal gradients occurring in L-PBF manufacturing have a further relevance for Inconel 718: parts typically contain columnar type hierarchical microstructures in conjunction with a distinct crystallographic texture [10, 13, 14, 16, 17, 24, 25]. On a smaller scale, a cellular solidification substructure forms with an inherent microsegregation of Nb, Mo and Ti at the cell walls [10, 14, 17, 25, 26]. This microsegregation is typically accompanied by dislocation entanglement [10, 13, 17, 27, 28]. It is known that the processing parameters such as the laser power, the scanning

velocity, the hatching distance, the layer thickness and the scanning strategy affect the microstructure, the texture and the quality (*e.g.*, in terms of porosity) of the build [13, 25, 29–31]. In the case of face centered cubic (FCC) materials (*e.g.*, Inconel 718), it is known that the <100> directions of the crystal lattice align with the direction of heat dissipation [32]. Thus, the scanning strategy is the main driving factor for the texture formation along the scanning direction [29]. Moreover, the heat flow along the building direction highly depends on the melt pool shape [29, 30].

As a consequence of these microstructural characteristics inherent to the process, an anisotropic mechanical behavior typically prevails with a dependence of the build orientation [10, 15, 25, 30, 33–35]. However, the severity of the mechanical anisotropy depends on the processing conditions, as shown by Liu et al. [34]. In contrast to the macroscopic mechanical behavior, the literature on the micromechanical behavior is primarily limited to data related to a single build orientation [35–38]. The results in literature show that the elastic behavior of additively manufactured Ni-based alloys is affected by the microstructure induced by the particular AM technology used: this leads to apparent changes in the values of the plane-specific Young's moduli (E^{hkl}) [36, 37]. Even though the role of texture and grain morphology on the mechanical anisotropy is well understood at the macroscopic scale, it widely remains an open question at the microscopic scale. This is one of the subjects of this work.

As mentioned previously, large RS are locked in the final as-built parts because of the localized melting. Diffraction-based RS measurements allow the determination of the RS in a non-destructive fashion. However, metrological challenges arise due to the underlying microstructure and texture; such challenges are reviewed in detail elsewhere [39]. In essence, the measured lattice plane spacings require a conversion into microscopic strain by relation to a reference value. Successively, the obtained microscopic strain is converted into a macroscopic stress by applying the (plane)-specific elastic constants as proportionality factors [40]. As both the elastic constants and the reference value have a strong impact on the magnitude of the determined RS, accurate values representative of each relevant microstructure need to be used. A further complication arises by the formation of crystallographic textures in L-PBF manufactured specimens: as they behave elastically

anisotropic at the macroscopic scale [41], the plane-specific elastic constants generally become dependent on the measurement direction within the specimen. The study of the micromechanical behavior needs to take the underlying texture into account [42, 43]. In this regard, the orientation distribution function can be used as a weighting factor (the so-called stress factors) in the calculation of the direction independent elastic constants [44].

There is an additional consequence of the unique anisotropic microstructure of L-PBF alloys for the determination of RS with diffraction-based methods: In the case of monochromatic diffraction-based methods such as laboratory X-ray or steady-source neutron diffraction, a suitable lattice plane family must be selected for the determination of the RS [45]. This lattice plane family should represent the bulk behavior and exhibit a low sensitivity to the accumulation of residual strain (also referred to as intergranular or type II strain) [45]. In the case of conventionally manufactured FCC materials, the lattice plane families {111}, {422} and {311} are considered to fulfill these requirements the best [45–47]. However, it was shown for L-PBF manufactured stainless steel that the {311} lattice plane family may accumulate significant residual strain during tensile loading [48]. An overview of the accumulation of the residual strains and the E^{hkl} for different laser powder-based metal AM is given in [39].

It is apparent that two main aspects need to be addressed to gain a detailed understanding of the micromechanical behavior and its impact on the diffraction-based RS analysis. First, we need to characterize the response of the lattice planes in dependence of the build orientation to understand the elastic anisotropy of the material. Second, we ought to investigate the accumulation of the residual strains for different build orientations. Such strategy is required to understand the influence of the microstructure on the plastic anisotropy of the material and the suitability of specific reflections to represent the bulk behavior.

With this in view, we designed a strategy to investigate how changes in the build orientation and texture affect the micromechanical behavior of L-PBF as-built Inconel 718. Furthermore, we examine the E^{hkl} and compare them to model predictions calculated from single crystal elastic constants (SCEC) using established micromechanical models. Finally,

we evaluate the accumulation of the plane-specific residual strains during plastic deformation.

Materials and methods

Sample fabrication

The specimens used in this study were built by L-PBF using an SLM 280 (SLM Solutions Group AG, Lübeck, Germany). The gas atomized Inconel 718 powder nominal composition (manufacturers certificate) is reported in Table 1. The powder with a particle size distribution between 10–45 μm and a $D_{50} \approx 38 \mu\text{m}$ was provided by SLM Solutions. The processing parameters suggested by the manufacturer were applied, using a layer thickness (t) of 0.06 mm: laser power (P) of 350 W, scanning velocity (v) of 800 mm s^{-1} , spot size diameter of 0.08 mm and hatch spacing (h) of 0.15 mm, while the baseplate was pre-heated to 200 °C. This parameter set corresponds to a volume energy density ($E_{laser} = P/vht$) of $\approx 49 \text{ J mm}^{-3}$. The build chamber was kept under an argon atmosphere with a constant gas flow (to prevent oxidation during manufacturing).

Both horizontal ($110 \times 13 \times 13 \text{ mm}^3$) and vertical ($13 \times 13 \times 110 \text{ mm}^3$) rectangular prisms were manufactured in separate build jobs using a bidirectional scanning strategy with a 90° interlayer rotation. The horizontal prisms have their longest direction parallel to the build plate, whereas the vertical prisms have their longest direction perpendicular to the build plate, as depicted in Fig. 1. The horizontal and vertical prisms were manufactured with an interlayer time (ILT) of 107 s and 81 s. Mohr et al. [49] showed for L-PBF 316L that such longer ILT cause insignificant heat accumulation, with a low dependence on the build height. The scanning tracks were aligned parallel to the edges of specimens for the vertical (V_{0° : Fig. 2a) and horizontal (H_{0° : Fig. 2b) builds, respectively. In addition, a second horizontal variant was built, for which the scanning pattern was rotated by 45° relative to the prism edges, while the rest of the manufacturing parameters were kept constant (H_{45° : Fig. 2c). After completion of the manufacturing process, the prisms were removed from the baseplate and retained in the as-built state (*i.e.*, no heat treatments were applied).

Table 1 Nominal composition of the Inconel 718 powder (manufacturer data)

	Ni	Cr	Fe	Ta + Nb	Mo	Ti	Al	B	C	Co	Cu	Mn	P	S	Si
wt.%	54	17.96	bal.	5.19	3.1	0.94	0.47	< 0.006	0.05	0.08	0.02	0.09	0.011	< 0.010	0.08

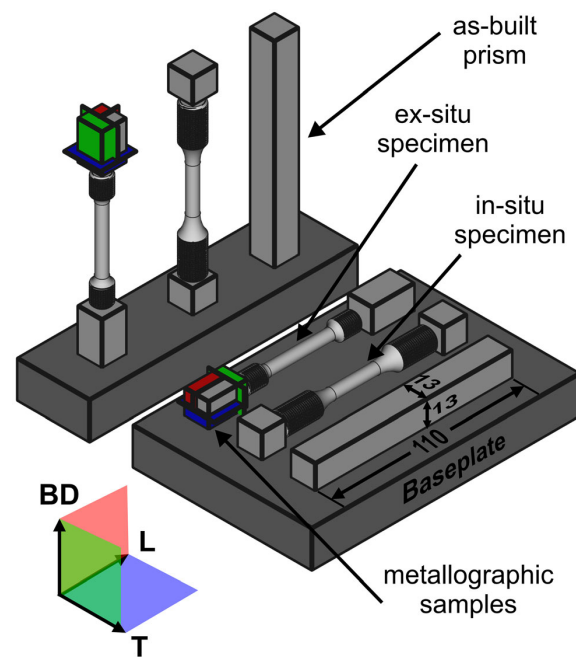


Figure 1 Schematic illustration of the vertically and horizontally built prisms on the baseplate, also showing the extraction of the two tensile specimen geometries after removal from the baseplate. The cuts from which the metallography samples were extracted are highlighted in color. All dimensions are in mm.

Microstructural analysis

For microstructural analysis, three samples were extracted from each prism (V_{0° , H_{0° and H_{45°), as shown in Fig. 1. All nine samples were mounted in conductive epoxy resin (Technotherm 3000, Kulzer GmbH, Hanau, Germany). Thereafter, the samples were prepared as metallographic sections (BD-T, BD-L and L-T) by subsequent grinding down to 1200 SiC Grit, followed by polishing steps of 9, 3 and 1 μm using diamond paste. BD refers to the building direction, while L and T denote the longitudinal and the transversal direction, respectively. A final polishing step using an 0.04 μm Active Oxide Polishing Suspension (OPS, Struers GmbH, Crinitz, Germany) was performed. For the sake of brevity, we focus

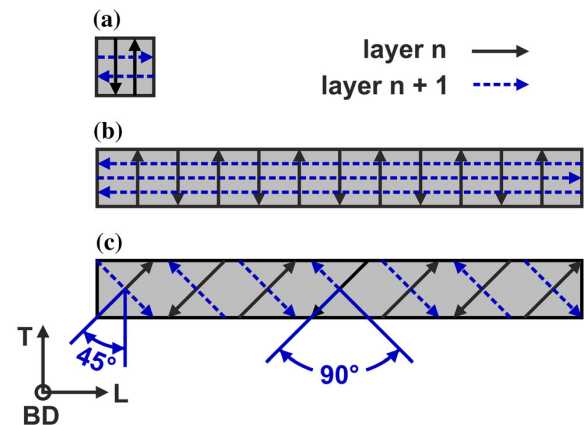


Figure 2 Schematic illustration of the top view of the vertical prism V_{0° (a) and of the horizontal prisms H_{0° (b) and H_{45° (c) showing the different scanning strategies. The hatch spacing is the same for all prisms.

solely on the microstructures along the direction of applied load (V_{0° : BD-T, H_{0° and H_{45° : L-T). For the microstructural characterization of the metallographic sections, a LEO 1530VP (Carl Zeiss Microscopy GmbH, Oberkochen, Germany) scanning electron microscope (SEM) was used, equipped with an electron backscatter (EBSD) Bruker Nano e⁻-Flash HD 5030 detector (Bruker Corporation, Billerica, USA).

For the EBSD analysis, an acceleration voltage of 20 kV was set at an approximate working distance of 18 mm under the standard tilt of 70° . A map with a resolution of 800×600 pixel was defined at a magnification of $75\times$ at the center of each section, thereby defining a pixel size of 5 μm and a probed area of approximately $4 \times 3 \text{ mm}^2$. For data acquisition and pattern indexing, the ESPRIT 1.94 package from Bruker nano was used. For data post-processing, the open-source MTEX toolbox [50] installed within the MATLAB (The MathWorks, Inc., Natick, USA) software was used. For the analysis, grains containing less than 10 pixels were removed and a misorientation angle of 10° was used as a threshold to define high angle grain boundaries. Afterwards, the non-

indexed pixels were filled by their nearest neighbor and denoising was performed using a variational spline filter [51]. Finally, the grain boundaries were smoothed using the default smoothing kernel in MTEX with 25 iterations. The average grain size (d_{area}) was defined as the equivalent spherical diameter of the grain area weighted by the area fraction. The effective grain size (d_{eff}) along the loading direction was determined averaging the results of the line intersection method (as implemented in MTEX) along seven vertical lines. The Taylor factor (M) was calculated in MTEX using the FCC $\{111\}\langle 110\rangle$ slip systems with the deformation tensor

$$\mathbf{E}_{\text{kl}}^s = \begin{bmatrix} -(1-q) & 0 & 0 & 0 \\ 0 & 1 & 0 & 0 \\ 0 & 0 & 0 & -q \end{bmatrix} \quad (\text{see [52]}).$$

The contraction ratios $q = 1/2$ and $q = 1/3$ were estimated from the ex situ tests for the vertical and the horizontal specimens, respectively. The grains cutting the image border were excluded from all calculations.

SEM images in backscattered electron (BSE) mode were acquired under an acceleration voltage of 15 kV and a working distance of 6–7 mm at different magnifications.

X-ray diffraction

X-ray diffraction measurements on the surfaces of the as-built samples (BD-L plane) and of the raw feedstock powder were carried out using the ETA X-ray diffractometer GE XRD 3003 available at the Helmholtz Zentrum Berlin (HZB), Germany. Cu $K\alpha_{1+2}$ radiation at an acceleration voltage of 40 kV under a current of 45 mA was used together with a polycapillary semi lens (2 mm) in the primary beam. In the diffracted beam, an equatorial Soller slit (0.4°) was used in combination with a flat secondary monochromator (001-LiF). The diffraction data were acquired in angular dispersive mode ranging from $2\theta = 5\text{--}155^\circ$ with a step size of 0.1° and a counting time of 20 s per measurement point. The instrument was calibrated using LaB_6 powder.

Ex situ mechanical testing

One tensile specimen for each build condition was manufactured from the prisms according to the geometry specified in DIN 50125:2004-01-B 6×30 (6 mm gauge diameter, 30 mm gauge length) [53].

The ex situ tensile tests were performed at room temperature according to DIN EN ISO 6892-1 [54] using a 100 kN Instron 4505 machine (Instron GmbH, Darmstadt, Germany). The loading direction was parallel to the build direction in the vertical specimen and parallel to the longitudinal direction in the horizontal specimens. The strain was recorded by a 632.12C-21 MTS extensometer (MTS Systems GmbH, Berlin, Germany) with a gauge length of 25 mm calibrated to a strain range of 0% to 50% according to DIN EN ISO 9513 [55]. All tests were run in displacement control at a constant strain rate of $2.5 \times 10^{-4} \text{ s}^{-1}$. The ex situ tests were primarily meant as a benchmark of the tensile behavior of each condition, to define the acquisition points for the in situ tensile tests. In addition, the 0.2% yield strength (σ_y), the ultimate tensile strength (UTS), the macroscopic Young's modulus (E^M) and the strain to failure (A) were determined from the obtained engineering stress–strain curves.

In situ mechanical testing

The presence of crystallographic texture, grain clustering or coarse grains may restrict the presence of certain lattice planes within the gauge volume along the scattering vector. As opposed to synchrotron X-ray diffraction, neutron diffraction allows the usage of a larger gauge volume leading to improving grain sampling statistics and thus being more representative of the bulk behavior [56]. Therefore, in this study, neutron diffraction was preferred over synchrotron X-ray diffraction.

The in situ tensile tests were performed at the pulse overlap time-of-flight (TOF) diffractometer POLDI at the Swiss Spallation Neutron Source (SINQ) at the Paul Scherrer Institut (PSI), Villigen, Switzerland. Threaded round tensile specimens with a gauge diameter of 6 mm were machined from each condition according to the beamline requirements (see [57]). The specimens were mounted in the in-house built load frame available at the beamline, which has a maximum load capacity of 30 kN. The test was performed at a strain rate of $4 \times 10^{-4} \text{ s}^{-1}$; An MTS 634.12F-25 extensometer (MTS Systems GmbH, Berlin, Germany) measured the (macroscopic) strain over the 25 mm gauge length. The test was run up to a total true strain of $\approx 10\%$. In the elastic region the test was run in load control mode, while it was

changed (manually) to displacement control in the plastic region.

The TOF diffraction technique at POLDI uses a multi-slit chopper allowing multiple frame overlap [58]. The arrival time is consequently not unambiguously determined by its TOF, which requires additional information for data evaluation [58]. In fact, the TOF is dependent on the scattering angle, which requires the time and angular information to be recorded with a 2D detector [58]. For data evaluation a specific correlation method is used to obtain the correlated diffraction pattern [58], which can then be fitted within the open source software Mantid [59] to obtain the peak information. More detailed information on the beamline and the evaluation technique can be found in the literature [58, 60, 61].

The scattering vector (\vec{q} with the absolute value Q) was aligned with the tensile direction to monitor the axial response of the lattice plane spacings (d^{hkl}) to the external load (Fig. 3). A second test with the scattering vector \vec{q} aligned to one direction perpendicular to the tensile direction to monitor the transversal response was also performed. However, since for textured materials the lateral contraction becomes direction-dependent (within the specimen itself), a crystal plasticity model would be required to relate the mechanical behavior to the texture. This is beyond the scope of this article and will be addressed in a companion publication. For the acquisition of the diffraction data a gauge volume of $3.8 \times 3.8 \times 3.8 \text{ mm}^3$ was defined under an angular

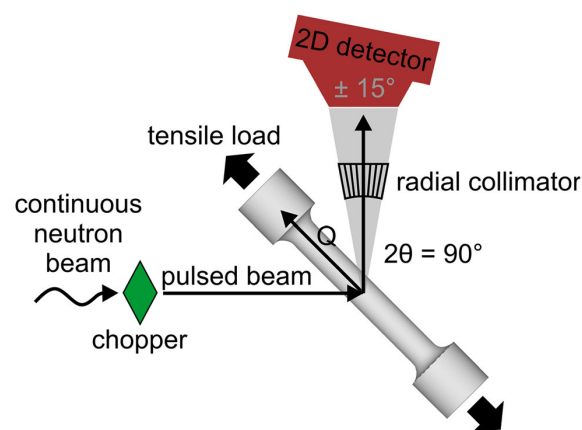


Figure 3 Schematic of the in situ loading setup at POLDI. The grey triangle indicates the $\pm 15^\circ$ angular coverage of the detector. Q denotes the absolute value of the scattering vector ($|\vec{q}|$).

coverage of $2\theta = 75\text{--}105^\circ$. The measurement time per point was approximately 45 min. In the plastic region, a three-minute waiting time was applied to allow for stress relaxation before the acquisition of neutron diffraction data. For single peak analysis of the γ phase, the available Gaussian function within Mantid [59] was used to fit the experimental data. Additionally, the γ -phase lattice parameter was refined using a full pattern Pawley fit [62] (using a Gaussian peak profile).

The lattice strain (ϵ^{hkl}) was calculated from the respective d^{hkl} for each load step using:

$$\epsilon^{hkl} = \frac{d^{hkl} - d_0^{hkl}}{d_0^{hkl}} \quad (1)$$

where d_0^{hkl} is defined as the initial d^{hkl} at a preload of approximately 50 N. The lattice strain is therefore relative to this macroscopically unstrained condition. It must be noted that, by nature of the diffraction technique, only elastic strains can be determined [63].

Results

Microstructure and texture

The as-manufactured microstructures characterized by SEM in backscattered electron mode reveal the typical columnar solidification structure displaying both fine- and coarse-grained regions (Fig. 4a, c). In the interdendritic regions of the build, the typical microsegregation can be observed. Furthermore, small amounts of gas porosity ($< 0.005\%$) are present within the builds, as measured by X-ray computed tomography (see Fig. S1 in supplementary information). Additional observations using energy-dispersive X-ray spectroscopy (see Fig. S2 in supplementary information) reveal the presence of (Ti, Nb)N particles (Fig. 4c). Similar microstructures can be observed irrespective of the build orientation and scanning strategy.

The orientation-maps (Fig. 5a–c) (as measured by EBSD) show the dependence of the grain morphology and texture on the build strategy: Both V_{0° (Fig. 5a) and H_{0° (Fig. 5b) builds qualitatively display a similar texture along their loading directions, BD and L, respectively. However, the grain morphology along these two directions is significantly different. For the sample V_{0° columnar grains oriented along the BD are observed. As the sample H_{0° is observed

perpendicular to the build direction, a chessboard-like pattern can be observed: this morphology is determined by the cross sectional cut through the columnar grains. The alteration of the scanning pattern for the sample H_{45° leads to a 45° rotation of the chessboard-like pattern with respect to the sample geometry (Fig. 5c). Figure 5d–l shows the inverse pole figures of each sample. With respect to the BD, the texture formation is not significantly affected by the scanning strategy, being mixed [001]/[011]-type (Fig. 5d–f). In the case of scanning along the geometrical axes, the texture components along L and T are comparable among the samples (Fig. 5g, h, j, k); this is expressed by the qualitatively equal [001]-type texture components of V_{0° (Fig. 5g, j) and H_{0° (Fig. 5h, k) along their L and T. In line with the rotation of the scanning pattern, H_{45° contrarily developed an [011]/ $[\bar{1}11]$ -type texture along L and T (Fig. 5i, l). In view of the loading directions, V_{0° displays an [001]/[011]-type texture (max. ≈ 2.7 m.r.d.) along BD (Fig. 5d), while H_{0° and H_{45° depict an [001]- (max. ≈ 3.8 m.r.d., Fig. 5h) and an [011]/ $[\bar{1}11]$ -

(max. ≈ 2 m.r.d., Fig. 5i) type texture along L, respectively.

The microstructural characteristics are listed in Table 2. In essence, neither the grain size nor the shape factor of the grains is significantly affected by the build orientation or scanning strategy: An average grain size of $\approx 60 \mu\text{m}$ and a shape factor (perimeter/equivalent perimeter weighted after the area fraction) of ≈ 1.5 are present in all build conditions. The large standard deviation associated to the average grain size is attributed to the wide grain size distribution.

X-ray diffraction

The X-ray diffraction peaks of the first four γ reflections observed in the data measured on the surface of the sample H_{0° compared to data on the feedstock powder are shown in Fig. 6. Firstly, over the complete angular range, no secondary phases could be evidently identified within the measurements' resolution of 0.1° in 2θ (see full diffraction pattern, Fig. S3 in supplementary information). Secondly, all peaks

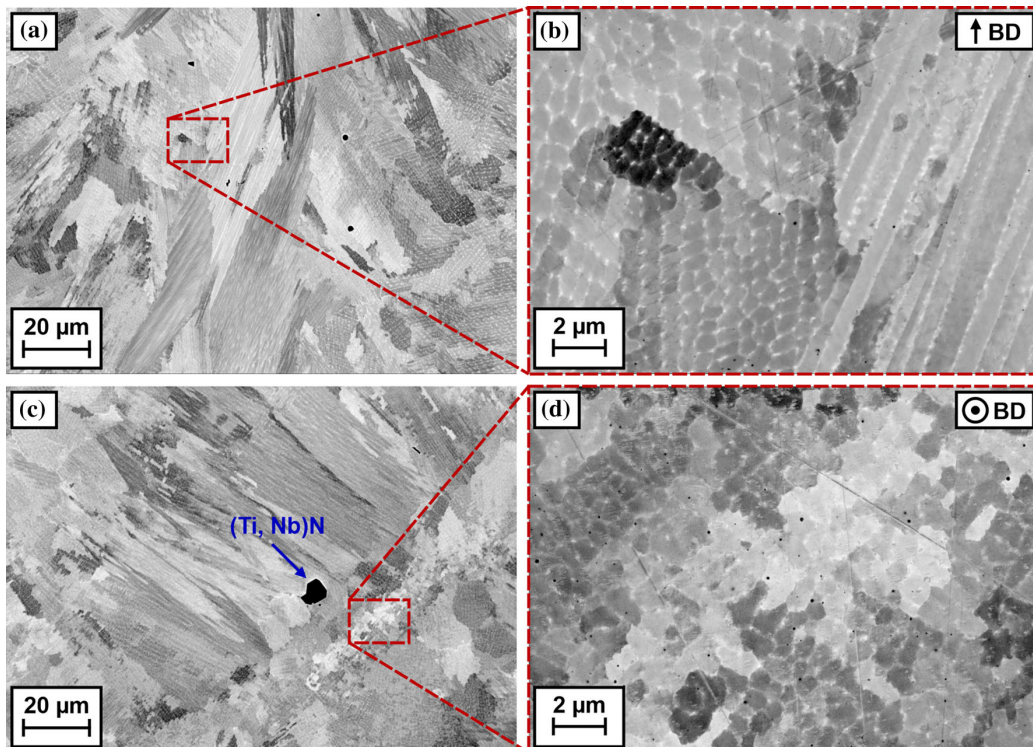


Figure 4 BSE images revealing the microstructures of H_{45° in the build direction (a, b) and perpendicular to it (c, d).

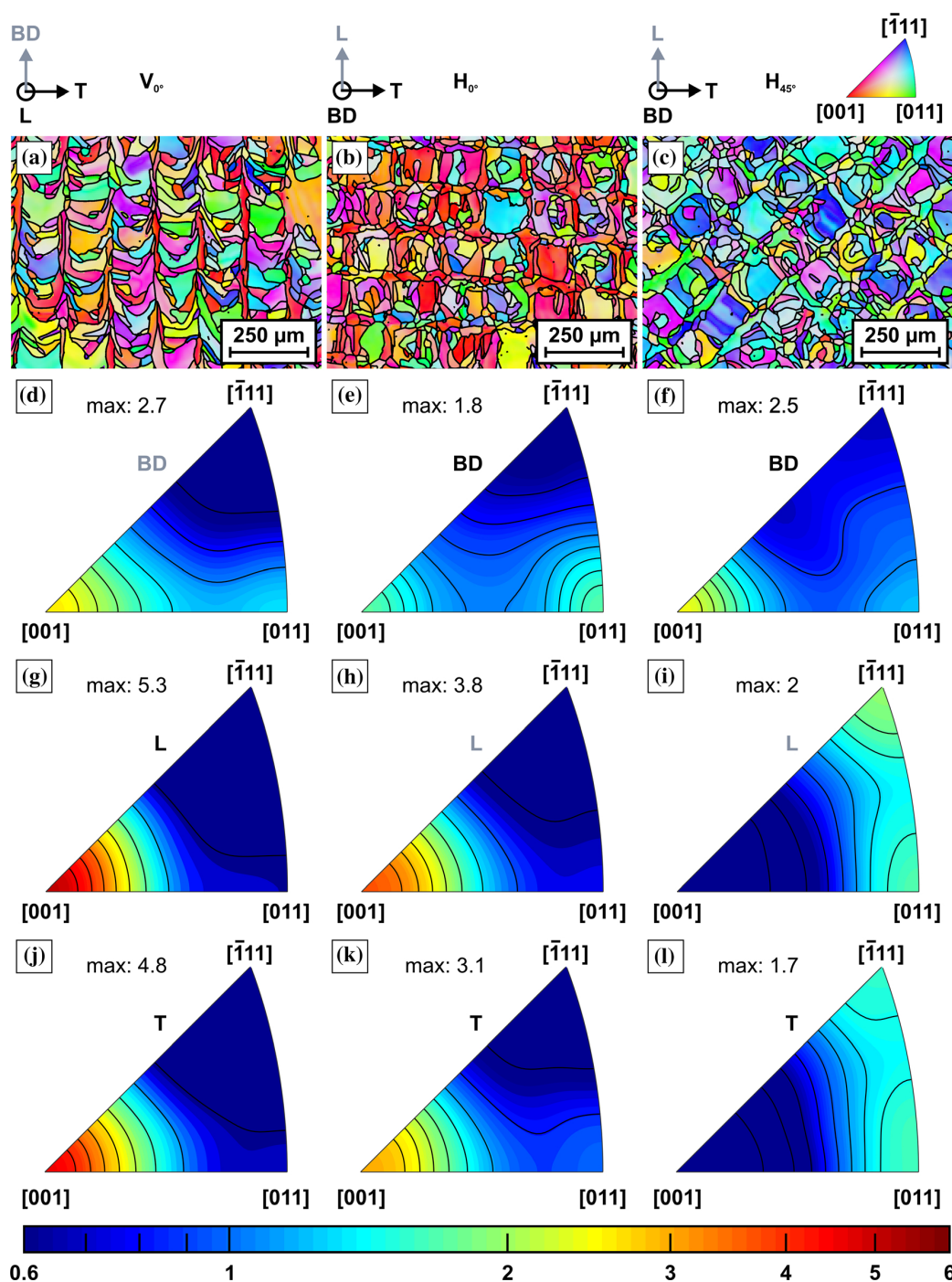


Figure 5 Orientation-maps (a–c) (probed area $1 \times 0.75 \text{ mm}^2$) and the corresponding logarithmically scaled inverse pole figures (d–l) (probed area $4 \times 3 \text{ mm}^2$) for the sections V_{0° BD–T (d, g, j), H_{0° L–T (e, h, k) and H_{45° L–T (f, i, l). The viewing

directions of the orientation-maps (a–c) correspond to the respective loading directions as indicated in grey color. Texture intensity is in m.r.d. (multiples of a random distribution).

Table 2 Microstructural characteristics of the samples obtained from EBSD data. For each value \pm denotes the standard deviation (not the experimental error). Shape factor, average grain size, and Taylor factor are weighted over the area fraction of each grain

ID	Section	$d_{area}/\mu\text{m}$	Nr. of grains	Taylor factor (M)	$d_{eff}/\mu\text{m}^*$	Avg. shape factor
V_{0°	BD-T	75 ± 43	12,283	2.9 ± 0.5	32 ± 8	1.7 ± 0.5
H_{0°	L-T	55 ± 28	20,934	2.6 ± 0.7	26 ± 3	1.4 ± 0.3
H_{45°	L-T	61 ± 32	14,035	3.4 ± 0.6	25 ± 2	1.4 ± 0.3

*Taken as effective grain size along the loading direction

exhibit an asymmetry at smaller diffraction angles (Fig. 6a). When the intensity is normalized to the maximum intensity of each peak, we observe that the peak asymmetry appears independent of the sample tilt angle and the sample condition (bulk/powder). This is exemplarily shown for the 200 reflection in Fig. 6b.

Ex situ tensile testing

The engineering stress–strain curves measured during the ex situ tensile testing of the specimens V_{0° , H_{0° and H_{45° are shown in Fig. 7a. Their respective mechanical properties determined from the curves are shown in Table 3. Clear differences in the mechanical behavior can be observed: The σ_y of the vertical build V_{0° displays the lowest value of 635 MPa, while horizontal builds H_{0° and H_{45° show significantly higher values of 725 MPa and 814 MPa, respectively. The same ascending order can be observed for the UTS, while the strain to failure decreases with the increase of the tensile strength.

In situ tensile testing

In Fig. 7b the true stress–strain curve obtained during the in situ test (blue) is shown together with the ex situ curves (red) for the specimen V_{0° . In addition, the yellow points indicate the average stress and strain values during the acquisition of neutron diffraction data (see inset in Fig. 7b). The ex situ stress–strain curve well matches the mechanical data obtained during the in situ test. Furthermore, we observe a stress relaxation during the acquisition of neutron diffraction data in the displacement-controlled region, which becomes more significant at higher strains. During unloading and reloading, the specimens display some hysteresis, which appears more pronounced at higher strains. This behavior

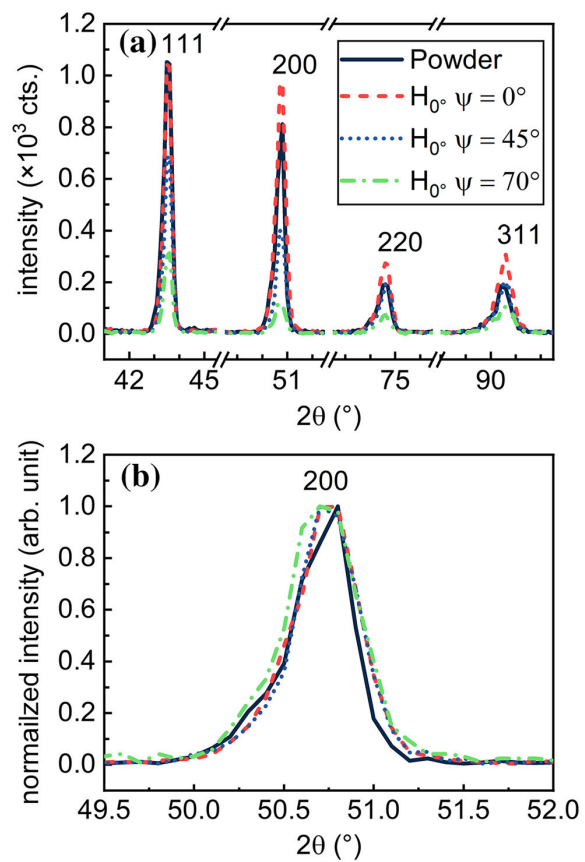


Figure 6 a The first four diffraction peaks acquired on the BD-L surface of H_{0° at different sample (ψ) tilts, compared to feedstock powder. b The 200 peaks of (a), normalized to the respective maximum intensities.

was observed for each condition (see Fig. S4 in supplementary information). Thus, only the V_{0° specimen is exemplarily shown.

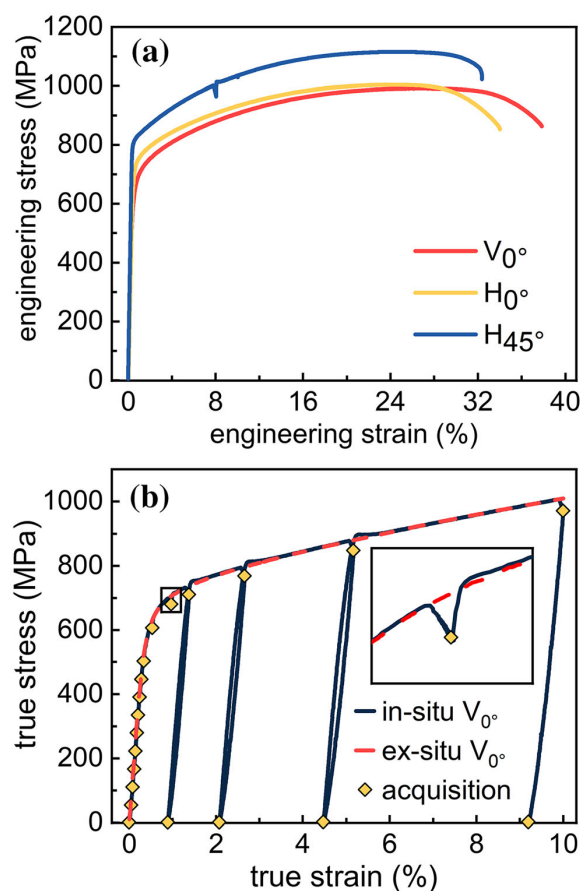


Figure 7 **a** Engineering stress–strain curves of the different specimens. The kink in the ex situ curve of H_{45° corresponds to an interruption during the test, which did not affect the overall behavior. **b** The true stress–strain curve for the specimen V_{0° acquired during the in situ test shown together with the respective ex situ response as well as the average stresses during the acquisition of neutron diffraction data (errors lie within the symbol size). The inset in (b) depicts the stress relaxation during the in situ test.

Diffraction peaks

Figure 8 shows the first four diffraction peaks of the specimen H_{0° during loading; the one-dimensional peak fit is also shown. In response to the macroscopic load, the diffraction peaks shift toward smaller Q values due to the applied tensile strain. In addition, a peak asymmetry similar to that observed by X-ray diffraction can be observed, while the peaks significantly broaden at higher plastic strain ($\epsilon_{true} = 10\%$). Except from an overall peak broadening, the degree of peak asymmetry of H_{0° seems not affected by

Table 3 Mechanical properties of the specimens as determined from the ex situ tensile tests

Specimen	σ_y /MPa	UTS/MPa	A /%
V_{0°	635 ± 8	992 ± 13	37 ± 2
H_{0°	725 ± 9	1005 ± 13	32 ± 2
H_{45°	814 ± 10	1116 ± 13	26 ± 2

plastic deformation, as exemplarily shown for the 200 reflection.

Lattice strain evolution during deformation

The true stress–lattice strain plots are shown in Fig. 9. The strain response of the {111}, {200}, {220} and {311} lattice plane families is compared to the Pawley refinement. The response of the lattice parameter as calculated by the Pawley refinement is a convolution of all lattice planes considered: since, in contrast to a Rietveld refinement, the intensity is a free parameter within the Pawley refinement [62], the texture is empirically considered within the refinement.

In the elastic region, the response of the lattice strain for each reflection to the applied load is close to linear up to 500 MPa, 600 MPa, and 700 MPa for V_{0° , H_{0° and H_{45° respectively (Fig. 9). Therefore, the E^{hkl} can be quantified by performing a linear regression of the first ten points. The values obtained are shown in Table 4. As an aftereffect of the low intensity of the 111 reflection for H_{0° (Fig. 8), the higher error of the peak position causes the increased scatter in the applied stress–lattice strain plot (Fig. 9b). Consequently, this leads to an increased error of the linear regression (Table 4). Beyond that, the {111}, {200}, and {311} families exhibit very different values, but are independent of the build orientation and texture. The only difference exceeding the error limits can be found for the {220} of the specimen H_{0° , which exhibits a significantly lower value than E^{220} for the other two specimens. The E^P obtained by the Pawley refinement reasonably describes the bulk behavior: they broadly agree with those determined from the ex situ mechanical test, which depend on the underlying texture.

In the region where macroscopic plastic deformation occurs, also lattice strains are characterized by a deviation from linearity [64]. The {220}, {111}, {200} lattice plane families and the Pawley refinement show increased nonlinearity for V_{0° and, to a lesser

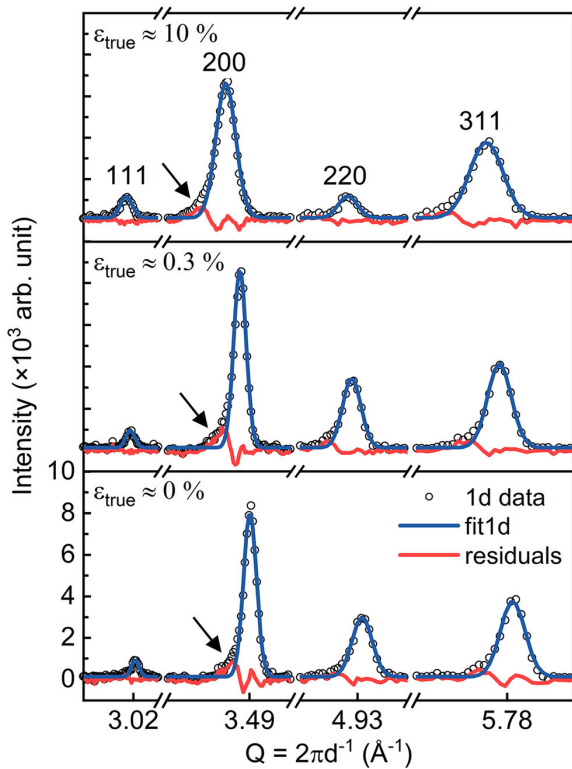


Figure 8 First four neutron diffraction peaks of H_{0° during in situ loading and the respective Gaussian fits of the γ phase. The black arrows depict the peak asymmetry within the acquired neutron diffraction data.

extent, for H_{0° . However, the {311} response remains broadly linear during the whole in situ experiment. This seems not to hold for H_{45° , where the {311} starts to deviate from linearity, while the {111} remains broadly linear. For H_{45° the response of the {200} is not shown because of its low intensity (caused by the texture in the loading direction).

Lattice micro residual strain accumulation

In Fig. 10, the residual lattice strains following unloading are plotted against the true plastic strain for each specimen. For V_{0° (Fig. 10a), the largest tensile residual strains develop for the {200}, while the largest compressive strains develop for the {220}. Lower compressive residual strains are accumulated for the {111} and {311}. The Pawley refinement displays nearly zero residual strain. In comparison, the magnitude of residual strains is lower for H_{0° as shown in Fig. 10b. However, the overall trends of the

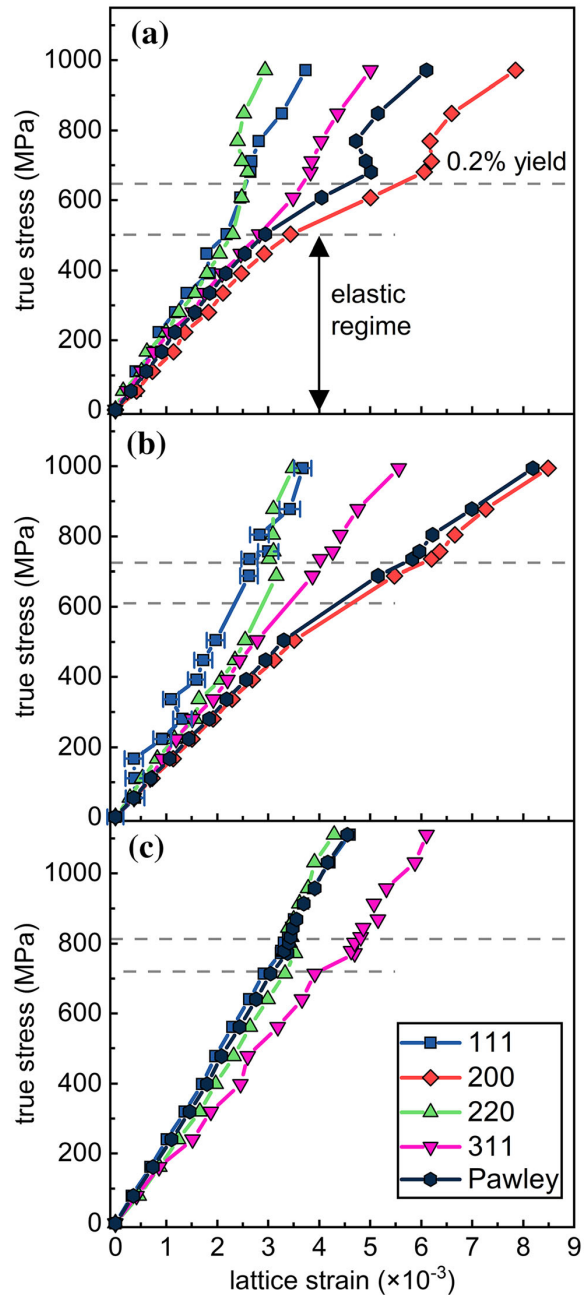


Figure 9 True stress–lattice strain plots showing the response of V_{0° (a), H_{0° (b) and H_{45° (c). The average obtained by a full pattern Pawley refinement is additionally shown for each specimen. Except of 111 in (b), the errors in lattice strain and average true stress lie within the symbol sizes.

lattice planes are similar to V_{0° , except that the Pawley refinement exhibits larger residual strains, slightly lower than the {200}. In contrast, for the H_{45°

Table 4 The plane-specific Young's moduli (E^{hkl}), the average Young's modulus of all lattice planes (E^P) and the macroscopic Young's modulus (E^M) obtained by linear regression. All values in GPa

Specimen	E^{111}	E^{200}	E^{220}	E^{311}	E^P	E^M
V_{0°	233 ± 12	152 ± 4	211 ± 5	176 ± 4	173 ± 3	178 ± 2
H_{0°	244 ± 21	143 ± 1	191 ± 5	182 ± 3	151 ± 1	163 ± 2
H_{45°	245 ± 2	*	218 ± 4	178 ± 5	234 ± 2	223 ± 2

*Not accessible because of texture

build (Fig. 10c) the {311} develops tensile residual strains, while the {111}, {220}, and the Pawley refinement exhibit negligible residual strains. As the residual strains are relative to the d^{hkl} values at pre-load, the initial RS state is not taken into account in this analysis.

Discussion

Microstructure and texture

The grain structure (Fig. 5a) in the building direction corresponds well to the findings of Gokcekaya et al. [30]: for a comparable E_{laser} of 40–47 J mm⁻³ columnar <100> regions are found, separated by <110> oriented “v-shaped” grains (see also [31]). However, the texture formation is different: as opposed to the dominant <110> texture along the build direction reported in [30] and [31], we observe mixed [001]/[011]-type textures (Fig. 5d–f). In fact, at the bottom of the melt pool (depending on the curvature) the solidification occurs mainly along the building direction, which favors the <100> directions to dominate crystal growth [30]. At the melt pool flank, crystal growth is promoted at an approximate angle of 45°, causing primary <100> growth in that direction [30, 31]. Therefore, qualitatively shallower melt pools caused by different processing conditions cause an [001]/[011]-type texture to form along the building direction, as shown in [10, 34]. Thus, the difference in the texture along the building direction could be explained by the dissimilarity in the local solidification conditions associated to the processing parameters. Furthermore, a pre-heating temperature of 200 °C led to a type of microstructure, which is comparable to the microstructure obtained using an E_{laser} of 40 J mm⁻³ and pre-heating at 80 °C [30]. In fact, the processing parameters and their different consequences for the

solidification conditions need to be considered when comparing the various studies.

The texture along the scanning direction is mainly determined by the relative orientation between the specimen edges and the laser tracks: for parts with simple scan strategies, such as no rotation or 90° interlayer rotation, the <100> directions of the crystals align with the laser pass directions [30, 31, 34]. Shorter hatch lengths typically increase the intensity of the texture [31]. This difference can be also found for V_{0° and H_{0° : the hatching along the length and the width of the prism H_{0° (Fig. 5h, k) caused a weaker texture relative to V_{0° (Fig. 5g, j).

Precipitation of primary and secondary phases

Although microsegregation occurs in L-PBF Inconel 718, it has been shown across several studies that only few precipitates exist in the as-built state of L-PBF Inconel 718: such particles are mainly identified as C14 Laves phase, carbides, and oxides [10, 17, 28, 65, 66]. In view of the cellular solidification structure, Rielli et al. [28] found (for $E_{laser} = 62.5$ J mm⁻³) that the size of the cellular solidification structure depends on the scan vector length: a chessboard strategy resulted in slower heat dissipation, which increased the interdendritic arm spacing compared to a meander-type scan strategy. In addition to the increased size of the cellular substructure, twice the volume fraction ($\approx 2\%$) of 80% larger Laves phase has been found within the chessboard sample [28]. However, besides some Al clustering within the chessboard strategy no precipitation of the γ'' or of the γ' phase was observable by atom probe tomography in the dendritic core regardless of the scan strategy [28]. For the meander-type scan strategy, this agrees to diffraction measurements made in the transmission electron microscope (TEM) on the selected area: the superlattice

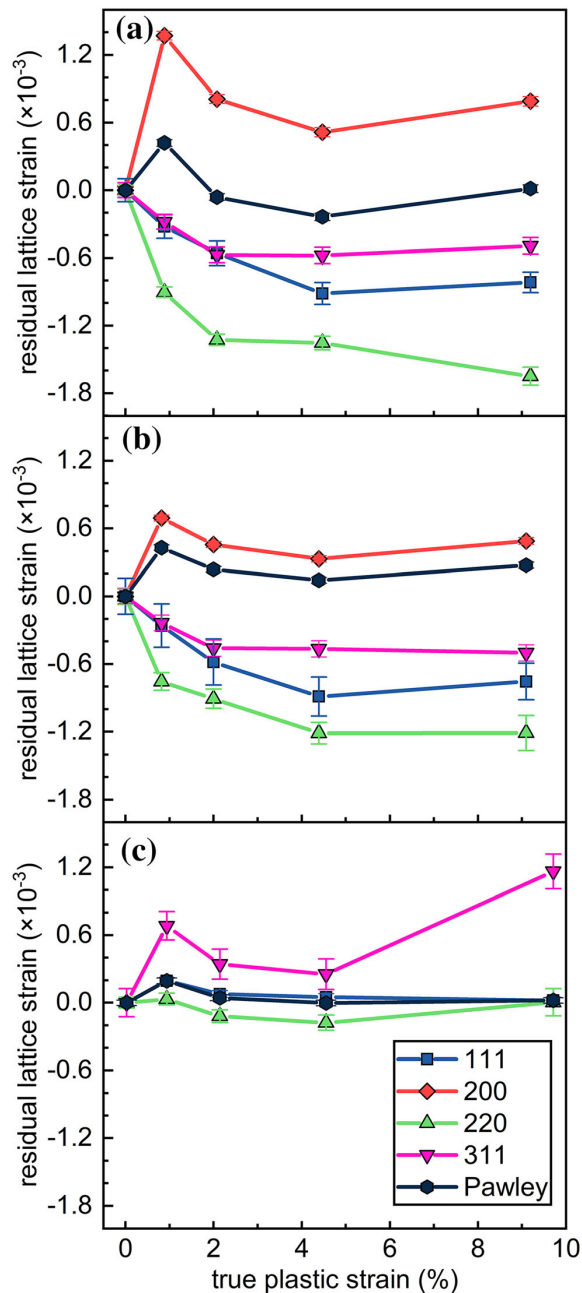


Figure 10 Residual lattice strains after unloading shown in dependence of the true plastic strain for V_{0° (a), H_{0° (b) and H_{45° (c). The average obtained by the Pawley refinement is also shown.

reflections of γ'' and γ' were not observed [28]. Similar findings were obtained by Zhou et al. [65] ($E_{laser} = 62 \text{ J mm}^{-3}$) and Xu et al. [66] ($E_{laser} = 62 \text{ J mm}^{-3}$). Even though Gallmeyer et al.

[10] observed nano-sized precipitates in high-resolution TEM micrographs of as-built L-PBF Inconel 718 ($E_{laser} = 25 \text{ J mm}^{-3}$), their small size and sparsity precluded the determination of their crystallographic structure. In fact, Zhou et al. [65] subjected as-built Inconel 718 to a direct aging procedure and observed an enrichment of γ'' precipitates along the cellular boundaries. The selective precipitation of γ'' at the cellular boundaries during direct aging indicates the presence of a Nb-rich supersaturated FCC solid solution in the as-built condition.

In essence, regardless of the (standard) process parameters reviewed here, precipitation of γ'' nor γ' has not been observed in as-built Inconel 718. This can be attributed to the sluggish precipitation kinetics of the γ'' phase [66] in conjunction to the rapid cooling inherent to the L-PBF process. As a relatively long inter-layer time (ILT) and a pre-heating temperature of 200°C were used alongside an E_{laser} of 49 J mm^{-3} to produce the specimens in this study, the heat accumulation is expected to be insignificant [49]; this would suppress the subsequent precipitation of γ'' and γ' during manufacturing. Thus, although the microstructural characterization by means of TEM was beyond the scope of the article, the specimens in this study can be considered free of γ'' and γ' precipitates. Our specimens likely contain low amounts of C14 Laves phase, (Nb, Ti)C, and (Nb, Ti)N.

Macromechanical behavior

As known from the literature, the classic Hall–Petch equation fails to predict the σ_y of as-built L-PBF Inconel 718 [10]. In particular, to decouple the different causes of the σ_y anisotropy in dependence of the build orientation remains challenging: The columnar microstructure effectively changes the number of grain boundaries present in the loading direction. However, we observe that the change in grain size alone is not capable to explain the change of the σ_y . In that context, the texture has been identified as one of the main driving factors of the mechanical anisotropy, which can be quantified by the Taylor factor [15, 25, 30, 33]. Besides, Zhang et al. [67] showed that the dislocation density is different for their horizontally and vertically built L-PBF Inconel 718 specimens. Thus, the Taylor strain hardening model has been added to the classic σ_y

prediction by Hall–Petch for an additively manufactured high entropy alloy [68]. This has been successfully applied to as-built L-PBF Inconel 718 by Gallmeyer et al. [10], showing good agreement with the experimental data. However, this approach does not consider differences of the other strengthening mechanisms (*i.e.*, solid solution strengthening) as described in [67]. In that context, Zhang et al. [67] quantitatively decoupled the strengthening mechanisms in L-PBF vertical and horizontal as-built Inconel 718. When we apply the approach (and the modeling parameter set) as described in [67] while considering the Taylor factor and the effective grain size listed in Table 2; we obtain the following predictions for the σ_y : 660 MPa, 727 MPa, and 782 MPa for V_{0° , H_{0° and H_{45° , respectively. However, the model does not account for the chemical gradients within the solid solution associated to the local segregation at the cell walls. Therefore, the impact on local solid solution strengthening is not considered within the model and the associated contribution to the overall strength. Instead, the strength increment of the segregated regions is only considered by the Orowan strengthening of the Laves phase. Despite these limitations in the comparability to our material, the agreement to the experimental values (Table 3) remains reasonable. Thus, the σ_y difference between V_{0° and H_{0° can be attributed to the potentially higher dislocation density present in the horizontal build, to the texture, and to the effective grain size. In contrast, the higher σ_y of H_{45° , compared to H_{0° could be explained by the stronger [011]/ $\bar{1}11$ -type texture, as quantified by the Taylor factor.

Micromechanical behavior

Elastic behavior

As a consequence of the single crystal anisotropy of nickel, it is known that the response of the lattice planes to a macroscopic load show large variations (the so-called elastic anisotropy) [69].

Figure 11a shows the comparison of the experimentally determined E^{hkl} with isotropic calculations using the established grain interaction models of Eshelby–Kröner [70] (spherical inclusion in an isotropic material) and Reuss [71] (isostress among grains). In regard of the selected SCEC, this study further supports the observation that the textured microstructures of L-PBF Inconel 718 are better

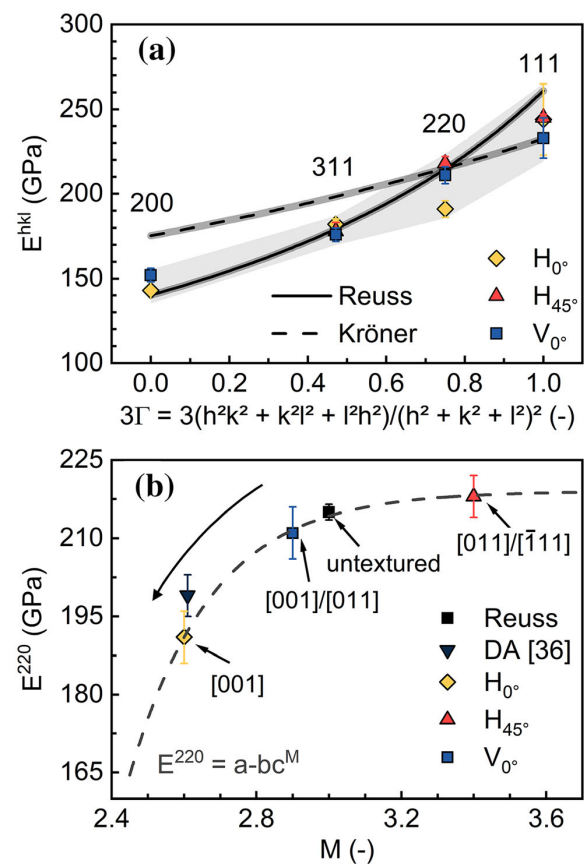


Figure 11 **a** Comparison of the experimentally obtained E^{hkl} with the isotropic model predictions of Reuss and Kröner, calculated with the software ISODEC (see [74]), using the SCEC of GFM-A Inconel 718 ($c_{11} = 242.35 \pm 0.66$ GPa, $c_{12} = 139.73 \pm 0.42$ GPa, and $c_{44} = 104.44 \pm 0.74$ GPa) reported in [75]. The error limits of all experimental and model (error band width ≈ 3 GPa) data, are indicated by the shaded bands. The Voigt model is a horizontal straight line (at ≈ 215 GPa) and is not shown for the sake of clarity. **b** The dependence of the E^{220} on the Taylor factor M (*i.e.* on the texture type).

described by the Reuss than by the Kröner model [36]. Furthermore, we show that the E^{200} , E^{311} , E^{111} are not affected by the texture, since they have similar values for the three specimens. However, some dependence of the E^{220} on the texture (quantified by the Taylor factor M) can be observed (Fig. 11b): As the [001] texture component increases, E^{220} significantly decreases. This dependence on the texture indicates a stronger interaction between {220} and {001} lattice plane families. Other lattice plane families in the vicinity of {220} seem to have less influence

on E^{220} . In fact, the stiffness difference between the {220} and {111} lattice plane families is much smaller than that between {220} and {200}, so that with increasing [011]/ $\bar{1}$ 11 texture components we observe an increasing insensitivity of E^{220} to M .

Overall, a good agreement between experimental data and grain interaction models can be obtained even though SCEC of conventional material are used for the calculations. It is noted that the model predictions largely depend on the choice of the SCEC. In that context, Wang et al. [37] determined the SCEC and the diffraction-elastic constants of conventional Inconel 625 at different temperatures from in situ neutron diffraction measurements on polycrystalline specimens. They obtained a good agreement between the Kröner model and the experimental data for room temperature, 600 °C and 700 °C [37]. Furthermore, they determined the E^{hkl} of direct energy deposited (DED) Inconel 625 at room temperature and 600 °C [37]. In general alignment with this study, their experimental data gave reasonable agreement to the Reuss model when considering the SCEC of the conventional Inconel 625 at room temperature (see [39]). In fact, Aminforoughi et al. [72] conducted an in situ tensile experiment on solution heat-treated L-PBF Inconel 718 using synchrotron X-ray diffraction in transmission geometry. In their experiment they showed that stresses calculated on the base of Reuss model elastic constants gave similar values for different lattice planes in the early stages of deformation. With increasing applied stress, some lattice planes (especially 311) exhibit a deviation of the calculated stress compared to the other lattice planes; we suppose that this splitting might be attributed to the build-up of intergranular strains due to the plastic anisotropy of the material. As the solution heat treatment conceivably precipitated δ -phase at the grain boundaries, an interphase stress may also cause such deviation to the calculated stress [38].

However, to the best of authors' knowledge the SCEC have not been experimentally determined for L-PBF Inconel 718. Although phase-specific SCEC have been reported for direct laser metal sintered Inconel 718 by Ghorbanpour et al. [73], the values are based on homogenized calculations of the SCEC reported in Haldipur et al. [73]. In general, more research (e.g., the combination of the experimental data with a crystal plasticity model) is needed to determine the SCEC from measured diffraction-

elastic constants. In particular, since the required transverse contraction of a lattice plane family {hkl} is not accessible from diffraction experiments of textured specimens (as discussed in [39, 40]), more theoretical and experimental work (using texture based approaches) is needed for AM materials.

Plastic behavior

In the plastic regime the relation between macroscopic stress and microscopic strain becomes highly nonlinear [69]. Dye et al. [69] have described the elastic and plastic anisotropy occurring in FCC metals during tensile deformation. They have shown that the elastically stiffest grains do not need to be the first to yield. Instead, these elastically stiffest grains often take the load from the surrounding softer grains, relieving the load on them. Once the {220} grains start yielding in V_{0° (Fig. 9a) and H_{0° (Fig. 9b), the {220} lattice plane family transfers the load to the {200}. This is reflected by the jump in accumulated lattice strain (Fig. 9a,b). This type of behavior is well known for conventional Inconel 718 [76] and has been reported for L-PBF Inconel 718 [35, 36, 38], DED Inconel 625 [37], as well as L-PBF austenitic (FCC) stainless steel 316L [77]. As opposed to H_{0° and V_{0° , the specimen H_{45° has very few {200} grains oriented along the loading direction (Fig. 5i). In this case the yielding {220} family transfers the load to the {311} (Fig. 9c). Therefore, the texture has a significant impact on the load partitioning around the σ_y . Once all grains have yielded, and hence slip has been initiated in all grains, the strain response (i.e. the slopes of the applied stress vs. lattice strain) is similar to that prior to plastic deformation [69]. As the texture is empirically captured within the Pawley refinement, the behavior of the lattice parameter refined with Pawley's approach displays the same behavior as the dominant texture component upon loading. Even further, the atypical behavior of macroscopically unrepresentative reflections may skew the determined lattice parameters [63].

Accumulation of residual strain

The broad range of plastic anisotropy behaviors observed for the different specimens indicates a variation of the accumulation of residual micro strains during uniaxial deformation. The consequence of this behavior is the development of

compressive micro-strains for the {220} and {111} families. This has been previously observed for conventional Inconel 718 [76] and L-PBF 316L [48]. In contrast, the {311} accumulates compressive residual strain for H_{0° and V_{0° , which does not seem to occur in conventional Inconel 718 [76]. However, in the case of a heat-treated material the load may be transferred to the different phases of Inconel 718 (e.g., δ [38] or γ'' [35]). This may affect how the residual strains accumulate with increasing plastic load [63]. As the load partitioning between the lattice planes changes for the specimen H_{45° , the {311} accumulates tensile residual micro strains. In fact, this is comparable to the {200} lattice plane family of V_{0° and H_{0° .

The texture influences the load partitioning; it also determines the lattice plane that best describes the Pawley behavior. In fact, contrary to the recommendation given for conventional materials [47], the {311} family might not be the best choice for RS determination along L of specimen H_{45° . As discussed in Clausen et al. [45], even weak textures influence the selection of the best suited reflection for RS analysis. However, as the determination of bulk RS is a three-dimensional problem, a suitable lattice plane must contain the best behavior averaged over multiple (specimen) directions. As E^{311} remains unaffected by the texture, the {311} family remains suitable for RS analysis although the degree of accumulation of residual strain changes with the texture. In fact, we must consider that the {220} and {111} families accumulate even larger residual strains in V_{0° and H_{0° .

Origin of the diffraction peak asymmetry

By performing a single peak fit based on a single Gaussian function, we only consider the γ matrix in our analysis. However, the peak asymmetry we observed in both X-ray (Fig. 6) and neutron diffraction (Fig. 8) patterns has been often connected to the precipitation of secondary phases (especially γ'' and γ') in heat-treated Inconel 718 [36, 38, 78, 79]. Given the absence of γ'' and γ' precipitates in as-built Inconel 718 as discussed above, the diffraction peak asymmetry is concluded to arise from a different contribution. In fact, Liu et al. [80] already observed such peak asymmetry in cold rolled Inconel 718 and attributed this to the segregation of Nb rather than solely to the precipitation of γ'' and γ' : as the lattice parameter of the supersaturated solution containing more Nb is larger than γ [81], the contribution of such

segregations to each diffraction peak would be visible at smaller scattering angles.

In addition, we could also observe the same peak asymmetry within the gas atomized feedstock powder (Fig. 6); This was also found by Gruber et al. [82] and Parimi et al. [83], who qualitatively show chemical segregation effects for gas atomized Inconel 718 powder. Recently, Schmeiser et al. [84] observed a similar peak asymmetry for L-PBF Inconel 625 and attributed it mainly to Nb and Mo segregation at the walls of intragranular cells (see Fig. 4). Furthermore, the studies of Tucho et al. [78] on L-PBF Inconel 718 show that the homogenization of the microstructure and the annihilation of dislocations by the high temperature heat-treatment change the 111 peak shape from a broad asymmetric type to a symmetric diffraction peak. Analogously, Levine et al. [85, 86] have shown that the formation of dislocation cells during the deformation of a copper single crystal result in a broad asymmetric diffraction peak.

Based on these observations we propose an explanation for the peak asymmetry in as-built L-PBF Inconel 718: The localized higher content of Nb and Mo in the segregation regions around the cell walls increases the FCC lattice parameter and therefore shifts the peak to smaller scattering angles. In addition to a peak shift, the cell wall regions also impose a peak broadening due to their high dislocation density (tensile type III stresses [87]). Furthermore, small amounts of Laves phases ($\approx 1\text{--}2\%$) [28, 38] present at the cell wall may also contribute to the diffraction signal. However, due to their different crystallographic structure compared to γ , their low volume fraction and the absence of visible peaks in the pattern, they are excluded as the primary cause of the diffraction peak asymmetry. This scenario is sketched in Fig. 12.

Role of cell walls on deformation mechanisms

Based on the discussion above, it is noteworthy that the peak fit should theoretically be performed considering two separate FCC lattices (γ for interior and γ^* for wall) with different lattice parameters. However, as described by Levine et al. [85] the fit of a single asymmetric peak with a certain number of Gaussian functions is not uniquely determined (see also [88]). Therefore, especially for peaks with small intensity (and thus less distinct asymmetry), such an approach may lead to an erroneous determination of

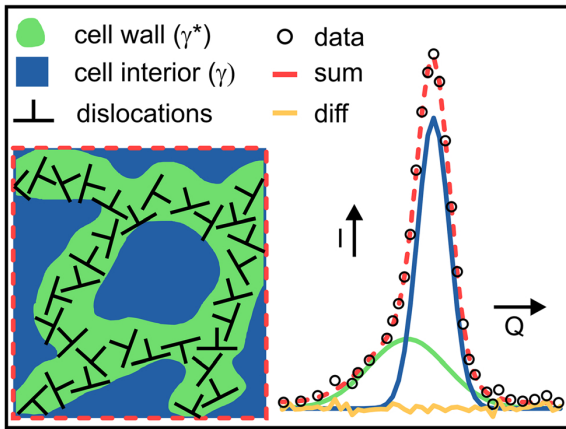


Figure 12 Schematic illustration for the hypothesis of the origin of diffraction peak asymmetry in as-built Inconel 718. The red dotted line depicts the cumulative diffraction signal of γ and γ^* for H_{0° -200 at $\epsilon_{true} \approx 0\%$. The orange line illustrates the residuals between the acquired diffraction data and the cumulative fit.

the peak position. Thus, we consider that the single peak fits performed above reliably describe the micromechanical behavior of the γ phase. In addition, performing a two-phase peak fit (following the approach shown in Fig. 12) using peaks with large diffraction intensities, enables us to further understand how the interior and wall of the cells behave upon external load. Consequently, the two-phase peak fit was performed using the 200-peak of V_{0° and H_{0° (Fig. 13). For V_{0° both regions (cell wall and cell interior) behave similarly in the elastic regime and at the early stages of plasticity, where the $\{220\}$ transfers load to the $\{200\}$. At larger plastic strains, the peak asymmetry increases, *i.e.* the $\gamma - 200$ does not accumulate significant lattice strain, while the $\gamma^* - 200$ continues to build up lattice strain with applied load. This indicates that the cell interior transfers load to the cell wall during deformation and could be explained by the motion of dislocations from the cell interior to the cell wall. This scenario is corroborated by the increase of the full width at half maximum (FWHM) of $\gamma^* - 200$ observed after unloading of V_{0° in the plastic region (Fig. 14). While the $\gamma - 200$ peak, corresponding to the cell interior, exhibits only a minor increase in the FWHM, the increase is much larger for $\gamma^* - 200$ in the plastic region. Rielli et al. [28] have shown the presence of dislocations within the cell interior (referred to as the interdendritic core) in non-deformed as-built L-PBF Inconel 718. In the

deformed case using TEM, Wang et al. [89] have shown that for L-PBF 316L, possessing a similar cellular substructure, dislocation trapping and retention mechanisms occur at the cell wall of material deformed to 3% tensile strain. It is therefore hypothesized that the enhanced relative increase of the FWHM for the cell wall originates from these dislocation mechanisms.

The single $\gamma - 200$ peak fit does not fully capture the interior-to-wall dislocation behavior, as the cell wall is only a minor contributor to the peak shape. The lack of deconvolution may also explain the significant nonlinearity of the Pawley refinement of V_{0° : it indicates that load partitioning from another phase occurs [64]. Interestingly, such a load transfer from cell interior to cell walls is not observed in H_{0° : both peaks behave similarly upon loading (Fig. 13b). In fact, when comparing the FWHM at the unload positions within the deformation sequence for

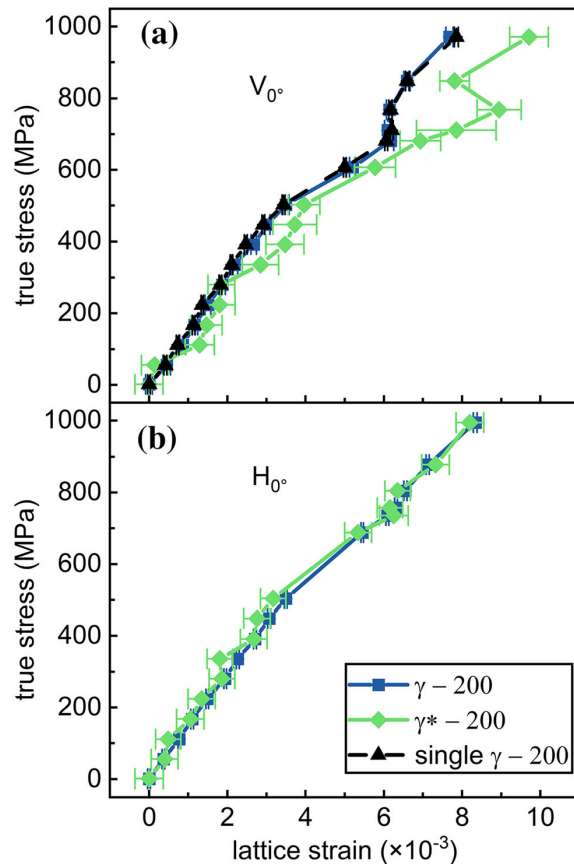


Figure 13 Behavior of the 200-peak for the cell interior (γ) and the cell wall (γ^*) for the specimens V_{0° (a) and H_{0° (b).

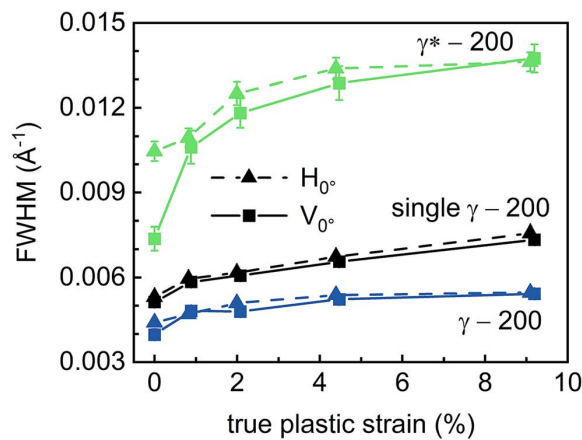


Figure 14 Full width at half maximum (FWHM) at the unloads of the specimen V_{0° and H_{0° for the cell interior (γ), the cell wall (γ^*), and the performed single peak fit (single γ) of the 200-reflection.

$\gamma^* - 200$ of H_{0° (Fig. 14), the relative increase is less pronounced compared to V_{0° . This may be an effect of the cell morphology along the load directions and the texture (pure [001]-type in H_{0°), as both determine the motion of dislocations during plastic deformation. Future work is planned to test this hypothesis for the peak asymmetry and the analysis of intragranular misfit strains associated with the deformation of the cellular microstructure.

Conclusions

This work reports the influence of the texture and build orientation on the mechanical properties and load transfer mechanisms of as-built laser powder bed fused Inconel 718. The scanning strategy was employed to alter the crystallographic texture with respect to the loading direction of the specimens: 0° , and 45° rotation of the scanning vectors to the longitudinal direction were employed. Moreover, specimens within different build jobs were tested (horizontal and vertical variants). The consequences of the different grain morphology and the crystallographic texture were studied at the macroscopic and the microscopic scale.

The following conclusions can be drawn:

- The variation of the scanning strategy leads to a significant change in texture for the horizontal variant: the alignment of the scan vector parallel

to one geometrical axis leads to an [001]-type texture along such axis. Instead, by rotating the scan vectors 45° to the geometrical axes, an [011]/ $[\bar{1}11]$ -type texture is obtained.

- On the macroscopic scale, the different yield strength in the vertical (635 MPa) and horizontal specimen (725 MPa) can be attributed to possible differences in the dislocation density and in the grain structure. The further increase of the yield strength for the rotation of the scanning vectors by 45° (814 MPa) can be explained by the difference in texture.
- On the microscopic scale the elastic behavior is well described by the Reuss grain interaction model (isostress). Furthermore, the plane-specific diffraction elastic moduli are (apart from the {220} lattice plane family) broadly unaffected by the variations of texture with respect to the loading direction.
- Upon yielding, several load partitioning scenarios among the different lattice planes were observed as a consequence of the range of crystallographic texture. For the specimens with an [001]-type texture the load transfers from the {220} to the {200} lattice plane family during deformation, while it is transferred to the {311} in presence of an [011]/ $[\bar{1}11]$ -type texture. In fact, the difference in load partitioning also affects the accumulation of micro residual strains in a comparable manner.
- A possible explanation for the diffraction peak asymmetry observed in both X-ray and neutron diffraction data has been provided. This explanation, corroborated by the existing literature, is based on niobium and molybdenum segregation accompanied by the presence of dislocation entanglement at the cell walls.

Acknowledgements

The authors kindly acknowledge the support of Benjamin Piesker (BAM) with the microstructural preparation of the samples and Romeo Saliwan-Neumann (BAM) for the acquisition of EBSD data. Furthermore, Luis A. Ávila C. (BAM) and Benjamin Piesker are acknowledged for conducting the ex situ tensile tests. We want to also acknowledge Alexander Ulbricht (BAM) for acquisition and analysis of the X-ray computed tomography data. In addition, we

want to thank Matthias Meixner (HZB) who carried out the surface X-ray measurements. We acknowledge the Paul Scherrer Institut, Villigen, Switzerland for the provision of neutron beamtime at the instrument POLDI of the SINQ under the proposal numbers 20202019 and 20202296. This work has been partially funded by the BAM internal project AGIL.

Author contributions

JS, GB, AE and ISM contributed to conceptualization; JS, JC and EP performed data curation; JS carried out formal analysis; JS, JC, EP and GM performed investigation; JS, GM and AE provided methodology; GB and AE performed project administration; GB, JC and EP provided resources; JS, AE and GB performed supervision; JS performed visualization and writing—original draft; JS, ISM and AE performed validation; JS, AE, ISM, JC, EP, GB and GM performed writing—review and editing.

Funding

Open Access funding enabled and organized by Projekt DEAL.

Data availability

The datasets generated during and/or analyzed during the current study are available from the corresponding author on reasonable request.

Declarations

Conflict of interest The authors declare that there are no conflicts of interest.

Supplementary Information: The online version contains supplementary material available at <http://doi.org/10.1007/s10853-022-07499-9>.

Open Access This article is licensed under a Creative Commons Attribution 4.0 International License, which permits use, sharing, adaptation, distribution and reproduction in any medium or format, as long as you give appropriate credit to the original author(s) and the source, provide a link to the Creative Commons licence, and indicate if changes were

made. The images or other third party material in this article are included in the article's Creative Commons licence, unless indicated otherwise in a credit line to the material. If material is not included in the article's Creative Commons licence and your intended use is not permitted by statutory regulation or exceeds the permitted use, you will need to obtain permission directly from the copyright holder. To view a copy of this licence, visit <http://creativecommons.org/licenses/by/4.0/>.

References

- [1] Emmelmann C, Kranz J, Herzog D, Wycisk E (2013) Laser additive manufacturing of metals. *Biol Med Phys Biomed*. https://doi.org/10.1007/978-3-642-41341-4_6
- [2] Kruth JP, Froyen L, Van Vaerenbergh J, Mercelis P, Rombouts M, Lauwers B (2004) Selective laser melting of iron-based powder. *J Mater Process Tech* 149:616–622. <https://doi.org/10.1016/j.jmatprotec.2003.11.051>
- [3] Mercelis P, Kruth JP (2006) Residual stresses in selective laser sintering and selective laser melting. *Rapid Prototyp J* 12:254–265. <https://doi.org/10.1108/13552540610707013>
- [4] Yadroitsev I, Yadroitsava I (2015) Evaluation of residual stress in stainless steel 316L and Ti6Al4V samples produced by selective laser melting this paper investigates the residual stress distribution in SLM-made parts and suggests thermal gradient control strategies. *Virtual Phys Prototy* 10:67–76. <https://doi.org/10.1080/17452759.2015.1026045>
- [5] Lai WJ, Ojha A, Li Z, Engler-Pinto C, Su XM (2021) Effect of residual stress on fatigue strength of 316L stainless steel produced by laser powder bed fusion process. *Prog Addit Manuf* 6:375–383. <https://doi.org/10.1007/s40964-021-00164-8>
- [6] Gorelik M (2017) Additive manufacturing in the context of structural integrity. *Int J Fatigue* 94:168–177. <https://doi.org/10.1016/j.ijfatigue.2016.07.005>
- [7] Yadollahi A, Shamsaei N (2017) Additive manufacturing of fatigue resistant materials: challenges and opportunities. *Int J Fatigue* 98:14–31. <https://doi.org/10.1016/j.ijfatigue.2017.01.001>
- [8] Khorasani M, Ghasemi A, Rolfe B, Gibson I (2021) Additive manufacturing a powerful tool for the aerospace industry. *Rapid Prototyp J* 28(1):87–100. <https://doi.org/10.1108/Rpj-01-2021-0009>
- [9] Emmelmann C, Sander P, Kranz J, Wycisk E (2011) Laser additive manufacturing and bionics: redefining lightweight design. *Physcs Proc* 12:364–368. <https://doi.org/10.1016/j.phpro.2011.03.046>

- [10] Gallmeyer TG, Moorthy S, Kappes BB, Mills MJ, Amin-Ahmadi B, Stebner AP (2020) Knowledge of process-structure-property relationships to engineer better heat treatments for laser powder bed fusion additive manufactured Inconel 718. *Addit Manuf* 31:100977. <https://doi.org/10.1016/j.addma.2019.100977>
- [11] Amato KN, Gaytan SM, Murr LE, Martinez E, Shindo PW, Hernandez J, Collins S, Medina F (2012) Microstructures and mechanical behavior of Inconel 718 fabricated by selective laser melting. *Acta Mater* 60:2229–2239. <https://doi.org/10.1016/j.actamat.2011.12.032>
- [12] Caiazzo F, Alfieri V, Corrado G, Argenio P (2017) Laser powder-bed fusion of inconel 718 to manufacture turbine blades. *Int J Adv Manuf Tech* 93:4023–4031. <https://doi.org/10.1007/s00170-017-0839-3>
- [13] Calandri M, Yin S, Aldwell B, Calignano F, Lupoi R, Ugués D (2019) Texture and microstructural features at different length scales in inconel 718 produced by selective laser melting. *Materials* 12(8):1293. <https://doi.org/10.3390/ma12081293>
- [14] Deng DY, Peng RL, Brodin H, Moverare J (2018) Microstructure and mechanical properties of Inconel 718 produced by selective laser melting: sample orientation dependence and effects of post heat treatments. *Mater Sci Eng, A* 713:294–306. <https://doi.org/10.1016/j.msea.2017.12.043>
- [15] Bean GE, McLouth TD, Witkin DB, Sitzman SD, Adams PM, Zaldivar RJ (2019) Build orientation effects on texture and mechanical properties of selective laser melting inconel 718. *J Mater Eng Perform* 28:1942–1949. <https://doi.org/10.1007/s11665-019-03980-w>
- [16] Brenne F, Taube A, Pröbstle M, Neumeier S, Schwarze D, Schaper M, Niendorf T (2016) Microstructural design of Ni-base alloys for high-temperature applications: impact of heat treatment on microstructure and mechanical properties after selective laser melting. *Prog Addit Manuf* 1:141–151. <https://doi.org/10.1007/s40964-016-0013-8>
- [17] Tucho WM, Cuvillier P, Sjolyst-Kvemeland A, Hansen V (2017) Microstructure and hardness studies of Inconel 718 manufactured by selective laser melting before and after solution heat treatment. *Mater Sci Eng, A* 689:220–232. <https://doi.org/10.1016/j.msea.2017.02.062>
- [18] Cozar R, Pineau A (1973) Morphology of γ' and γ'' precipitates and thermal-stability of inconel 718 type alloys. *Metall Mater Trans A* 4:47–59. <https://doi.org/10.1007/Bf02649604>
- [19] Tharappel JT, Babu J (2018) Welding processes for inconel 718-A brief review. *IOP Conf Ser: Mater Sci Eng* 330:012082. <https://doi.org/10.1088/1757-899x/330/1/012082>
- [20] Lingenfelter A (1989) Welding of Inconel Alloy 718: A Historical Overview. *The Minerals, Metals & Materials Society Superalloy 718 Metallurgy and Applications*: 673–683. https://doi.org/10.7449/1989/Superalloys_1989_673_683
- [21] Collier JP, Song HW, Phillips JC, Tien JK (1988) The effect of varying Al, Ti, and Nb content on the phase-stability of inconel-718. *Metall Trans A* 19:1657–1666. <https://doi.org/10.1007/Bf02645133>
- [22] Paulonis DF, Oblak JM, Duvall DS (1969) Precipitation in nickel-base alloy 718. *ASM Trans Quart* 62:611–622
- [23] Sundararaman M, Mukhopadhyay P, Banerjee S (1992) Some aspects of the precipitation of metastable intermetallic phases in inconel-718. *Metall Mater Trans A* 23:2015–2028. <https://doi.org/10.1007/Bf02647549>
- [24] Wang XQ, Chou K (2017) Electron backscatter diffraction analysis of inconel 718 parts fabricated by selective laser melting additive manufacturing. *Jom-Us* 69:402–408. <https://doi.org/10.1007/s11837-016-2198-1>
- [25] Ni M, Chen C, Wang XJ, Wang PW, Li RD, Zhang XY, Zhou KC (2017) Anisotropic tensile behavior of in situ precipitation strengthened Inconel 718 fabricated by additive manufacturing. *Mater Sci Eng, A* 701:344–351. <https://doi.org/10.1016/j.msea.2017.06.098>
- [26] Serrano-Munoz I, Fritsch T, Mishurova T et al (2021) On the interplay of microstructure and residual stress in LPBF IN718. *J Mater Sci* 56:5845–5867. <https://doi.org/10.1007/s10853-020-05553-y>
- [27] Piglione A, Attard B, Rielli VV, Santos Maldonado C-T, Attallah MM, Primig S, Pham M-S (2021) On the constitutive relationship between solidification cells and the fatigue behaviour of IN718 fabricated by laser powder bed fusion. *Addit Manuf* 47:102347. <https://doi.org/10.1016/j.addma.2021.102347>
- [28] Rielli VV, Piglione A, Pham M-S, Primig S (2022) On the detailed morphological and chemical evolution of phases during laser powder bed fusion and common post-processing heat treatments of IN718. *Addit Manuf* 50:102540. <https://doi.org/10.1016/j.addma.2021.102540>
- [29] Wan HY, Zhou ZJ, Li CP, Chen GF, Zhang GP (2018) Effect of scanning strategy on grain structure and crystallographic texture of Inconel 718 processed by selective laser melting. *J Mater Sci Technol* 34:1799–1804. <https://doi.org/10.1016/j.jmst.2018.02.002>
- [30] Gokcekaya O, Ishimoto T, Hibino S, Yasutomi J, Narushima T, Nakano T (2021) Unique crystallographic texture formation in Inconel 718 by laser powder bed fusion and its effect on mechanical anisotropy. *Acta Mater* 212:116876. <https://doi.org/10.1016/j.actamat.2021.116876>

- [31] Nadammal N, Cabeza S, Mishurova T et al (2017) Effect of hatch length on the development of microstructure, texture and residual stresses in selective laser melted superalloy Inconel 718. *Mater Des* 134:139–150. <https://doi.org/10.1016/j.matdes.2017.08.049>
- [32] Chalmers B (1964) *Principles of solidification*. Wiley, New York
- [33] Du DF, Dong AP, Shu D, Zhu GL, Sun BD, Li X, Lavernia E (2019) Influence of build orientation on microstructure, mechanical and corrosion behavior of Inconel 718 processed by selective laser melting. *Mater Sci Eng, A* 760:469–480. <https://doi.org/10.1016/j.msea.2019.05.013>
- [34] Liu SY, Li HQ, Qin CX, Zong R, Fang XY (2020) The effect of energy density on texture and mechanical anisotropy in selective laser melted Inconel 718. *Mater Des* 191:108642. <https://doi.org/10.1016/j.matdes.2020.108642>
- [35] Sangid MD, Book TA, Naragani D et al (2018) Role of heat treatment and build orientation in the microstructure sensitive deformation characteristics of IN718 produced via SLM additive manufacturing. *Addit Manuf* 22:479–496. <https://doi.org/10.1016/j.addma.2018.04.032>
- [36] Schröder J, Mishurova T, Fritsch T et al (2021) On the influence of heat treatment on microstructure and mechanical behavior of laser powder bed fused Inconel 718. *Mater Sci Eng, A* 805:140555. <https://doi.org/10.1016/j.msea.2020.140555>
- [37] Wang ZQ, Stoica AD, Ma D, Beese AM (2016) Diffraction and single-crystal elastic constants of Inconel 625 at room and elevated temperatures determined by neutron diffraction. *Mater Sci Eng, A* 674:406–412. <https://doi.org/10.1016/j.msea.2016.08.010>
- [38] Capek J, Polatidis E, Knapek M, Lyphout C, Casati N, Pederson R, Strobl M (2021) The effect of γ and δ phase precipitation on the mechanical properties of inconel 718 manufactured by selective laser melting: an in situ neutron diffraction and acoustic emission study. *Jom-U*s 73:223–232. <https://doi.org/10.1007/s11837-020-04463-3>
- [39] Schröder J, Evans A, Mishurova T et al (2021) Diffraction-based residual stress characterization in laser additive manufacturing of metals. *Metals* 11(11):1830. <https://doi.org/10.3390/met11111830>
- [40] Mishurova T, Bruno G, Evsevlev S, Sevostianov I (2020) Determination of macroscopic stress from diffraction experiments: a critical discussion. *J Appl Phys* 128:02510-3. <https://doi.org/10.1063/5.0009101>
- [41] Hollmann A, Meixner M, Klaus M, Genzel C (2021) Concepts for nondestructive and depth-resolved X-ray residual stress analysis in the near-surface region of nearly single crystalline materials with mosaic structure. *J Appl Crystallogr* 54:22–31. <https://doi.org/10.1107/S1600576720014016>
- [42] Dölle H, Hauk V (1978) Influence of mechanical anisotropy of polycrystal (texture) upon stress evaluation by means of X-rays. *Z Metallkd* 69:410–417
- [43] Dölle H, Hauk V (1979) Evaluation of residual-stresses in textured materials by X-rays. *Z Metallkd* 70:682–685
- [44] Behnken H, Hauk V (1991) Calculation of X-ray stress factors of textured materials - comparison with experimental results. *Z Metallkd* 82:151–158
- [45] Clausen B, Leffers T, Lorentzen T (2003) On the proper selection of reflections for the measurement of bulk residual stresses by diffraction methods. *Acta Mater* 51:6181–6188. <https://doi.org/10.1016/j.actamat.2003.07.002>
- [46] DIN-EN-15305 (2019) Non-destructive testing - Test method for residual stress analysis by X-ray diffraction. German Institute for Standardization. Berlin, Germany. doi: <https://doi.org/10.31030/1425472>
- [47] DIN-EN-ISO-21432 (2021) Non-destructive testing - Standard test method for determining residual stresses by neutron diffraction (ISO 21432:2019); German version EN ISO 21432:2020. German Institute for Standardization. Berlin, Germany. <https://doi.org/10.31030/3202037>
- [48] Choo H, Koehler MR, White LP, Ren Y, Morin D, Garlea E (2020) Influence of defect characteristics on tensile deformation of an additively manufactured stainless steel: evolutions of texture and intergranular strain. *Mater Sci Eng, A* 791:139637. <https://doi.org/10.1016/j.msea.2020.139637>
- [49] Mohr G, Sommer K, Knobloch T, Altenburg SJ, Recknagel S, Bettge D, Hilgenberg K (2021) Process induced pre-heating in laser powder bed fusion monitored by thermography and its influence on the microstructure of 316L stainless steel parts. *Metals* 11(7):1063. <https://doi.org/10.3390/met11071063>
- [50] Bachmann F, Hielscher R, Schaeben H (2011) Grain detection from 2d and 3d EBSD data-specification of the MTEX algorithm. *Ultramicroscopy* 111:1720–1733. <https://doi.org/10.1016/j.ultramic.2011.08.002>
- [51] Hielscher R, Silbermann CB, Schmidl E, Ihlemann J (2019) Denoising of crystal orientation maps. *J Appl Crystallogr* 52:984–996. <https://doi.org/10.1107/S16005767190009075>
- [52] Bunge HJ (1970) Some applications of the Taylor theory of polycrystal plasticity. *Krist Tech* 5:145–175. <https://doi.org/10.1002/crat.19700050112>
- [53] DIN-50125 (2004) Testing of metallic materials - Tensile test pieces. German Institute for Standardization. Berlin, Germany.
- [54] DIN-EN-ISO-6892-1 (2019) Metallic materials –Tensile testing –Part 1: Method of test at room temperature (ISO/FDIS 6892-1:2019); German and English version prEN ISO 6892-1:2019. German Institution for Standardization. Berlin, Germany. <https://doi.org/10.31030/3132591>

- [55] DIN-EN-ISO-9513 (2013) Metallic materials - Calibration of extensometer systems used in uniaxial testing (ISO 9513:2012 + Cor. 1:2013); German version EN ISO 9513:2012. German Institution for Standardization. Berlin, Germany. doi: <https://doi.org/10.31030/1912742>
- [56] Heldmann A, Hoelzel M, Hofmann M et al (2019) Diffraction-based determination of single-crystal elastic constants of polycrystalline titanium alloys. *J Appl Crystallogr* 52:1144–1156. <https://doi.org/10.1107/S1600576719010720>
- [57] Paul-Scherrer-Institut (2021) Tensile sample M12. https://www.psi.ch/sites/default/files/styles/primer_full_xl/public/import/sinq/poldi/LoadFrameUniaxialEN/04_tensile_M12.jpg?itok=217Y6anp. Accessed 02 December 2021
- [58] Stuhr U (2005) Time-of-flight diffraction with multiple pulse overlap. part I: the concept. *Nucl Instrum Meth A* 545:319–329. <https://doi.org/10.1016/j.nima.2005.01.320>
- [59] Arnold O, Bilheux JC, Borreguero JM et al (2014) Mantid-Data analysis and visualization package for neutron scattering and mu SR experiments. *Nucl Instrum Meth A* 764:156–166. <https://doi.org/10.1016/j.nima.2014.07.029>
- [60] Stuhr U, Grosse M, Wagner W (2006) The TOF-strain scanner POLDI with multiple frame overlap-concept and performance. *Mater Sci Eng, A* 437:134–138. <https://doi.org/10.1016/j.msea.2006.04.069>
- [61] Stuhr U, Spitzer H, Egger J et al (2005) Time-of-flight diffraction with multiple frame overlap part II: the strain scanner POLDI at PSI. *Nucl Instrum Meth A* 545:330–338. <https://doi.org/10.1016/j.nima.2005.01.321>
- [62] Pawley GS (1981) Unit-cell refinement from powder diffraction scans. *J Appl Crystallogr* 14:357–361. <https://doi.org/10.1107/S0021889881009618>
- [63] Daymond MR, Priesmeyer HG (2002) Elastoplastic deformation of ferritic steel and cementite studied by neutron diffraction and self-consistent modelling. *Acta Mater* 50:1613–1626. [https://doi.org/10.1016/S1359-6454\(02\)00026-5](https://doi.org/10.1016/S1359-6454(02)00026-5)
- [64] Daymond MR, Bourke MAM, VonDreele RB, Clausen B, Lorentzen T (1997) Use of rietveld refinement for elastic macrostrain determination and for evaluation of plastic strain history from diffraction spectra. *J Appl Phys* 82:1554–1562. <https://doi.org/10.1063/1.365956>
- [65] Zhou L, Mehta A, McWilliams B, Cho K, Sohn Y (2019) Microstructure, precipitates and mechanical properties of powder bed fused inconel 718 before and after heat treatment. *J Mater Sci Technol* 35:1153–1164. <https://doi.org/10.1016/j.jmst.2018.12.006>
- [66] Xu JH, Ma TR, Peng RL, Hosseini S (2021) Effect of post-processes on the microstructure and mechanical properties of laser powder bed fused IN718 superalloy. *Addit Manuf*. 48B:102416. <https://doi.org/10.1016/j.addma.2021.102416>
- [67] Zhang S, Lin X, Wang L, Yu X, Hu Y, Yang H, Lei L, Huang W (2021) Strengthening mechanisms in selective laser-melted Inconel718 superalloy. *Mater Sci Eng, A* 812:141145. <https://doi.org/10.1016/j.msea.2021.141145>
- [68] Zhu ZG, Nguyen QB, Ng FL, An XH, Liao XZ, Liaw PK, Nai SML, Wei J (2018) Hierarchical microstructure and strengthening mechanisms of a CoCrFeNiMn high entropy alloy additively manufactured by selective laser melting. *Scr Mater* 154:20–24. <https://doi.org/10.1016/j.scriptamat.2018.05.015>
- [69] Dye D, Stone HJ, Reed RC (2001) Intergranular and inter-phase microstresses. *Curr Opin Solid State Mater Sci* 5:31–37. [https://doi.org/10.1016/S1359-0286\(00\)00019-X](https://doi.org/10.1016/S1359-0286(00)00019-X)
- [70] Kröner E (1958) Berechnung der elastischen konstanten des vielkristalls aus den konstanten des einkristalls. *Z Phys* 151:504–518. <https://doi.org/10.1007/Bf01337948>
- [71] Reuss A (1929) Account of the liquid limit of mixed crystals on the basis of the plasticity condition for single crystal. *Z Angew Math Mech* 9:49–58. <https://doi.org/10.1002/zam.19290090104>
- [72] Aminforoughi B, Degener S, Richter J, Liehr A, Niendorf T (2021) A novel approach to robustly determine residual stress in additively manufactured microstructures using synchrotron radiation. *Adv Eng Mater* 23:2100184. <https://doi.org/10.1002/adem.202100184>
- [73] Ghorbanpour S, Zecevic M, Kumar A, Jahedi M, Bicknell J, Jorgensen L, Beyerlein IJ, Knezevic M (2017) A crystal plasticity model incorporating the effects of precipitates in superalloys: application to tensile, compressive, and cyclic deformation of Inconel 718. *Int J Plasticity* 99:162–185. <https://doi.org/10.1016/j.ijplas.2017.09.006>
- [74] Gnäupel-Herold T (2012) ISODEC: software for calculating diffraction elastic constants. *J Appl Crystallogr* 45:573–574. <https://doi.org/10.1107/S0021889812014252>
- [75] Haldipur P, Margetan FJ, Thompson RB (2004) Estimation of single-crystal elastic constants from ultrasonic measurements on polycrystalline specimens. *Rev Prog Q* 23:1061–1068
- [76] Wagner JN, Hofmann M, Wimpory R, Krempaszky C, Stockinger M (2014) Microstructure and temperature dependence of intergranular strains on diffractometric macroscopic residual stress analysis. *Mater Sci Eng, A* 618:271–279. <https://doi.org/10.1016/j.msea.2014.09.033>
- [77] Chen W, Voisin T, Zhang Y, Forien J-B, Spadaccini CM, McDowell DL, Zhu T, Wang YM (2019) Microscale residual stresses in additively manufactured stainless steel. *Nat Commun* 10:4338. <https://doi.org/10.1038/s41467-019-12265-8>
- [78] Tucho WM, Hansen V (2021) Studies of post-fabrication heat treatment of L-PBF-Inconel 718: effects of hold time on

- microstructure, annealing twins, and hardness. *Metals* 11(2):266. <https://doi.org/10.3390/met11020266>
- [79] Ferreri NC, Vogel SC, Knezevic M (2020) Determining volume fractions of γ , γ' , γ'' , δ , and MC-carbide phases in Inconel 718 as a function of its processing history using an advanced neutron diffraction procedure. *Mater Sci Eng, A* 781:139228. <https://doi.org/10.1016/j.msea.2020.139228>
- [80] Liu WC, Yao M, Chen ZL, Wang SG (1999) Niobium segregation in Inconel 718. *J Mater Sci* 34:2583–2586. <https://doi.org/10.1023/A:1004648615561>
- [81] Dehmas M, Lacaze J, Niang A, Viguier B (2011) TEM study of high-temperature precipitation of delta phase in inconel 718 alloy. *Adv Mater Sci Eng* 2011:940634. <https://doi.org/10.1155/2011/940634>
- [82] Gruber K, Smolina I, Kasprowicz M, Kurzynowski T (2021) Evaluation of inconel 718 metallic powder to optimize the reuse of powder and to improve the performance and sustainability of the laser powder bed fusion (LPBF) process. *Materials* 14(6):1538. <https://doi.org/10.3390/ma14061538>
- [83] Parimi LL, RG A, Clark D, Attallah MM (2014) Microstructural and texture development in direct laser fabricated IN718. *Mater Charact* 89:102–111. <https://doi.org/10.1016/j.matchar.2013.12.012>
- [84] Schmeiser F, Krohmer E, Wagner C, Schell N, Uhlmann E, Reimers W (2021) In situ microstructure analysis of inconel 625 during laser powder bed fusion. *J Mater Sci* 57:9663–9677. <https://doi.org/10.1007/s10853-021-06577-8>
- [85] Levine LE, Geantil P, Larson BC, Tischler JZ, Kassner ME, Liu WJ (2012) Validating classical line profile analyses using microbeam diffraction from individual dislocation cell walls and cell interiors. *J Appl Crystallogr* 45:157–165. <https://doi.org/10.1107/S0021889812001616>
- [86] Levine LE, Larson BC, Yang W, Kassner ME, Tischler JZ, Delos-Reyes MA, Fields RJ, Liu WJ (2006) X-ray microbeam measurements of individual dislocation cell elastic strains in deformed single-crystal copper. *Nat Mater* 5:619–622. <https://doi.org/10.1038/nmat1698>
- [87] Withers PJ, Bhadeshia HKDH (2001) Residual stress. part 2 – nature and origins. *Mater Sci Technol* 17:366–375. <https://doi.org/10.1179/026708301101510087>
- [88] Pinto HC, Bruno G (2003) Formation and relaxation of coherency strain in the nickel-base superalloy SC16. *J Synchrotron Radiat* 10:148–153. <https://doi.org/10.1107/S0909049502019076>
- [89] Wang YM, Voisin T, McKeown JT et al (2018) Additively manufactured hierarchical stainless steels with high strength and ductility. *Nat Mater* 17:63–71. <https://doi.org/10.1038/Nmat5021>

Publisher's Note Springer Nature remains neutral with regard to jurisdictional claims in published maps and institutional affiliations.

Supplementary Information

Understanding the impact of texture on the micromechanical anisotropy of laser powder bed fused Inconel 718

Jakob Schröder^{1*}, Alexander Evans^{1*}, Efthymios Polatidis², Jan Čapek², Gunther Mohr¹, Itziar Serrano-Munoz¹, and Giovanni Bruno^{1,3}

¹Bundesanstalt für Materialforschung und -prüfung, Unter den Eichen 87, 12205 Berlin, Germany

²Paul Scherrer Institut, Forschungsstrasse 111, 5232 Villigen, Switzerland

³Universität Potsdam, Institut für Physik und Astronomie, Karl-Liebknecht-Str. 24-25, 14476 Potsdam, Germany

*Corresponding Authors: Jakob.Schroeder@bam.de, Alexander.Evans@bam.de

X-ray computed tomography

The gauge regions of the ex-situ tensile specimens were inspected by micro-CT using a custom-made industrial 3D micro-CT scanner. The scanner was equipped with a 225 kV micro focus X-ray source (X-ray WorX GmbH, Garbsen, Germany) and a flat panel detector of 2048×2048 pixels. More details about this micro-CT scanner can be found in [1]. Specimen V_{0° was scanned using a voltage of 220 kV and a current of $68 \mu\text{A}$. A silver prefilter of a thickness of 0.25 mm was used. For each of the 2550 projections a five-time average of a 2 s acquisition was calculated.

Due to constraints of the CT scanner the scan parameters were altered marginally for specimens H_{0° and H_{45° : 2400 projections were acquired at a voltage of 210 kV, while the current was adjusted to $72 \mu\text{A}$. The silver prefilter was replaced by 0.5 mm of tin. For all specimen a voxel size of $5 \mu\text{m}$ was achieved, enabling the detection of voids of a diameter of larger than $10 \mu\text{m}$.

The reconstructed data were filtered using the Non-local Means filter plugin [2, 3] of the open-source image analysis software Fiji [4]. The commercial software VG Studio Max 3.4 (Volume Graphics GmbH, Heidelberg, Germany) was used to analyse the filtered CT data. In an 8 mm high cylindrical region of interest around the mid height of the specimens, void analysis was performed. The volumetric porosity in each 3D dataset of the three volumes was calculated using VG studio's porosity analysis module.

[1] Oesch T, Weise F, Meinel D, Gollwitzer C (2019) Quantitative In-situ Analysis of Water Transport in Concrete Completed Using X-ray Computed Tomography. *Transp Porous Med* 127:371-389. doi: 10.1007/s11242-018-1197-9

[2] Buades A, Coll B, Morel J-M (2011) Non-Local Means Denoising, *Image Processing On Line* 1:208–212. doi: 10.5201/ipol.2011.bcm_nlm

[3] Darbon J, Cunha A, Chan TF, Osher S, Jensen GJ, (2008) Fast nonlocal filtering applied to electron cryomicroscopy, *2008 5th IEEE International Symposium on Biomedical Imaging: From Nano to Macro*:1331-1334, doi: 10.1109/ISBI.2008.4541250.

[4] Schindelin J, Arganda-Carreras I, Frise E et al. (2012) Fiji: an open-source platform for biological-image analysis. *Nat Methods* 9:676–682. doi: 10.1038/nmeth.2019

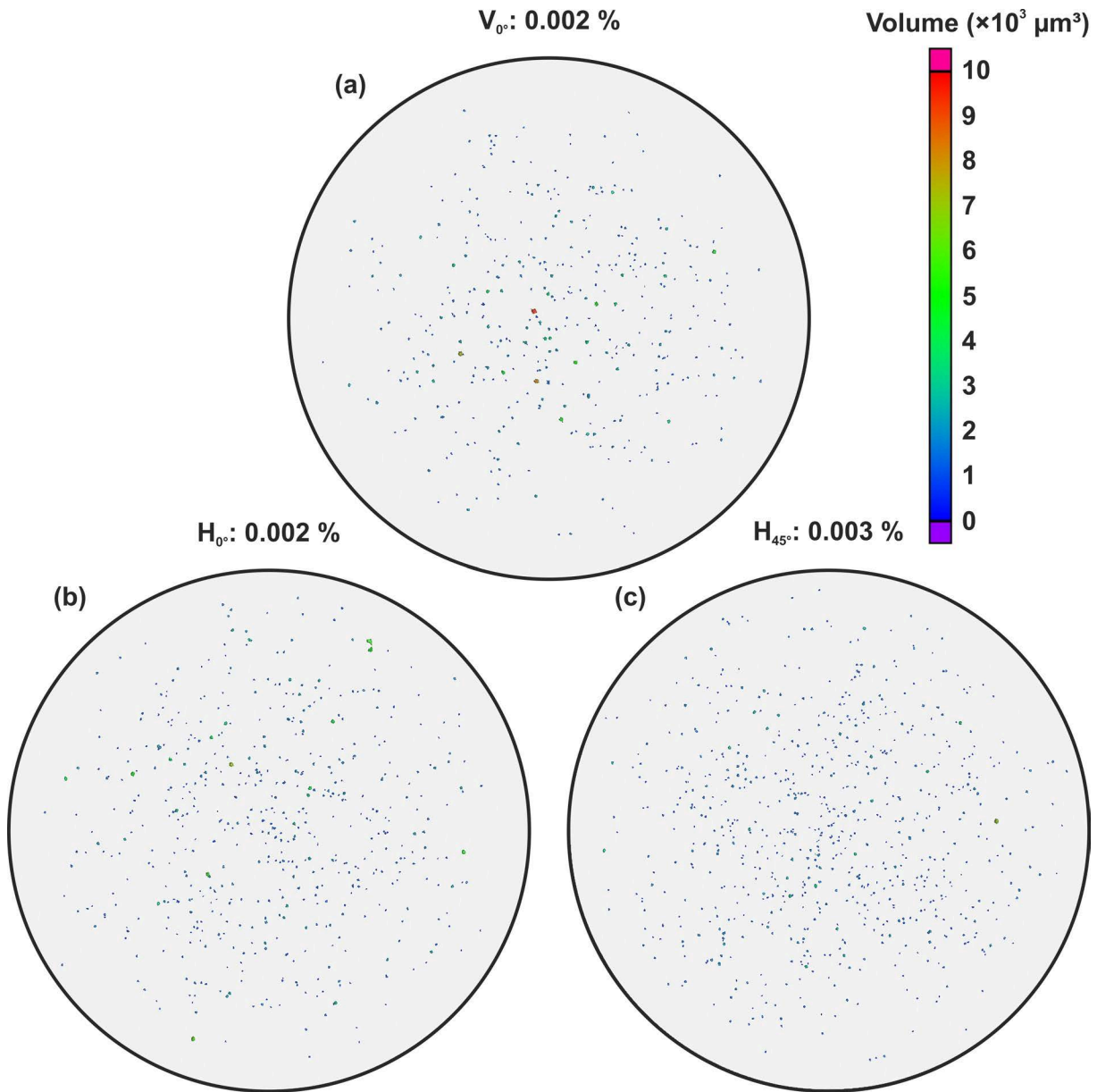


Fig. S1 Projection of the porosity rendering along 8 mm of the gauge length acquired at mid height of the ex-situ tensile specimens V_{0° (a), H_{0° (b) and H_{45° (c).

Energy dispersive X-ray spectroscopy

Atomic percent (%)											
	C	N	O	Al	Si	Ti	Cr	Fe	Ni	Nb	Mo
1	15.17	43.54	-	-	-	37.85	0.31	-	0.49	2.64	-
2	14.76	43.29	-	-	-	39.36	0.35	0.19	0.48	1.58	-
3	14.65	41.47	3.60	0.27	-	37.38	0.38	-	0.38	1.87	-
4	14.87	42.85	2.20	-	-	36.67	0.62	0.36	0.80	1.65	-
5	14.38	42.85	2.13	-	-	39.29	0.21	-	-	1.14	-
6	9.81	2.40	-	0.75	0.18	1.07	19.45	17.05	45.11	2.61	1.57

Fig. S2 X-ray spectroscopy analysis of the sample section H_{45} N-L at different positions. Positions 1-5 reveal the presence of titanium niobium nitride (Ti, Nb)N particles. Besides, a gas pore is also visible within the sample.

X-ray diffraction

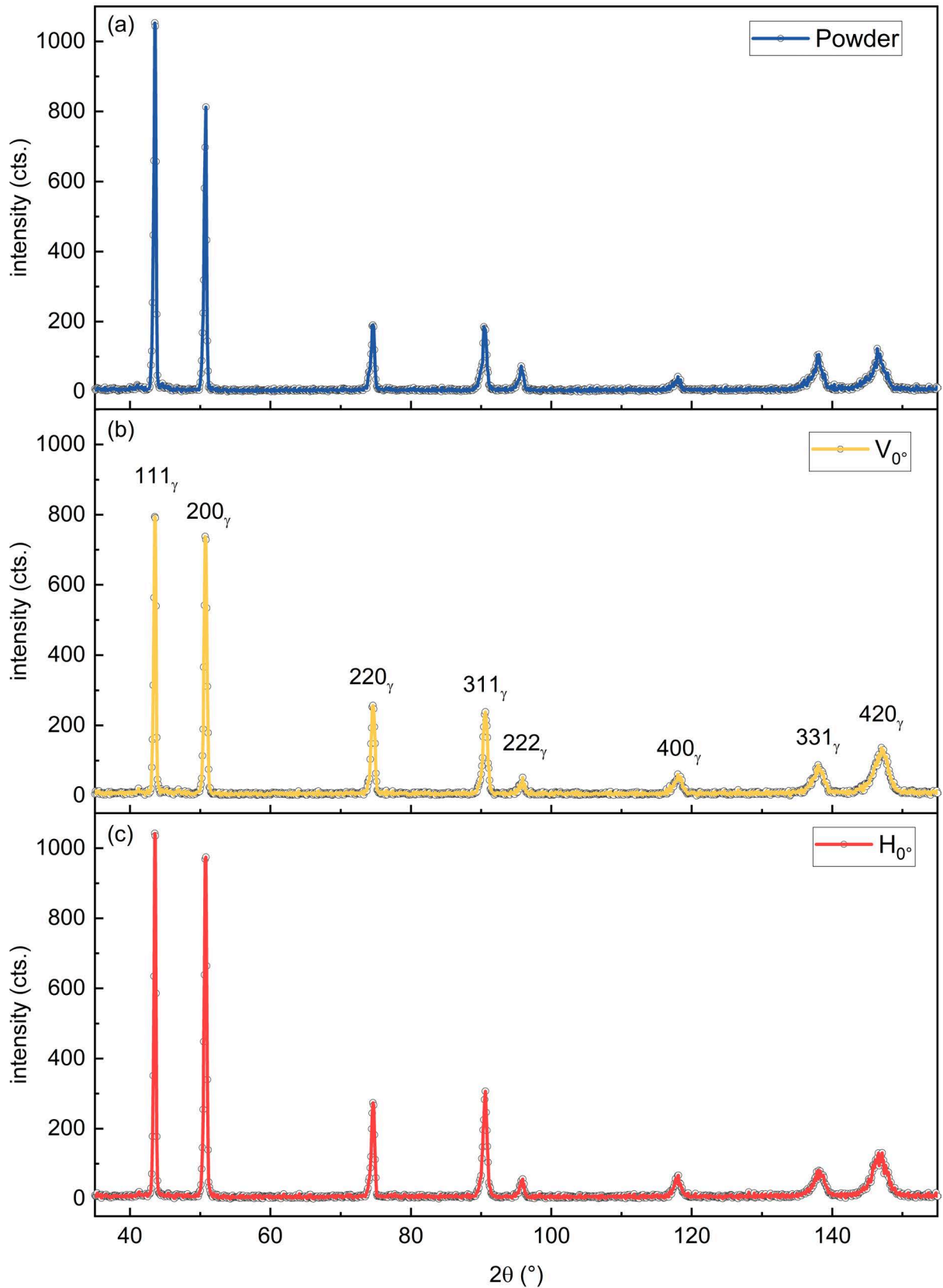


Fig. S3 Complete X-ray diffraction patterns of the feedstock powder (a), the sample V_{0° at $\Psi = 0^\circ$ (b), and the sample H_{0° (c) at $\Psi = 0^\circ$. No secondary peaks could be evidently identified under the given measurement conditions. However, according to the microstructural observations it is likely that secondary peaks of Laves phase, $(Nb,Ti)C$, and $(Nb, Ti)N$ exist.

Mechanical data

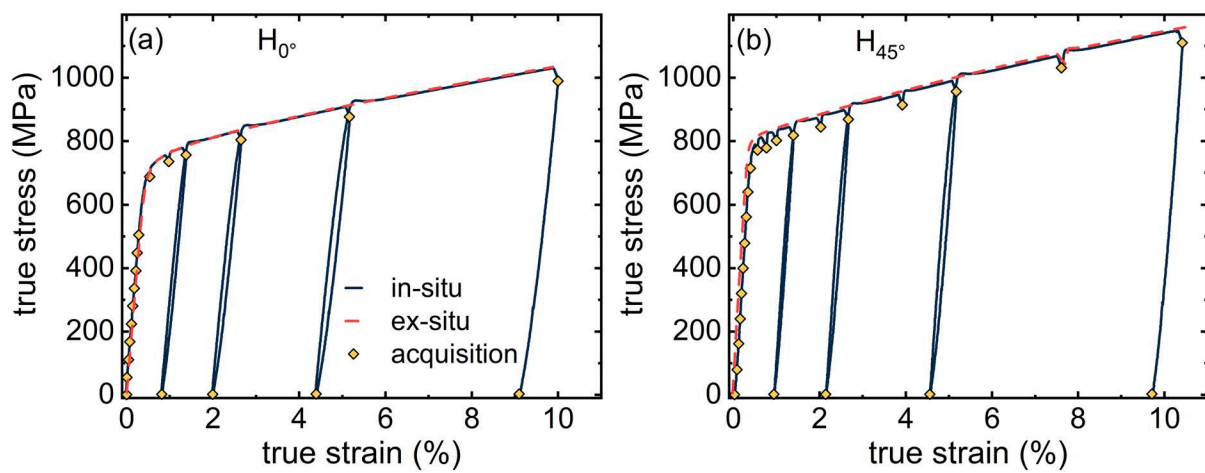


Fig. S4 The true stress-strain curves of H_{0° (a) and H_{45° (b) acquired during in-situ neutron diffraction. The yellow points depict the average of the stress and strain during the acquisition of diffraction data.

Texture-based residual stress analysis of laser powder bed fused Inconel 718 parts

M4

J. SCHRÖDER, A. EVANS, V. LUZIN, G. ABREU FARIA, S. DEGENER,
E. POLATIDIS, J. ČAPEK, A. KROMM, G. DOVZHENKO, G. BRUNO

27th January 2023

Submitted to Journal of Applied Crystallography

0 Preface

With knowledge of the elastic micro mechanical behavior one of the main influencing factors on the determination of residual stress has been clarified. As already mentioned, besides the diffraction elastic constants several other aspects are needed for a reliable diffraction-based assessment of residual stress. Such aspects include the influence of preferred orientation and, dependent on the method, the stress-free reference as well as the selection of an appropriate lattice plane. By the employment of multiple methods using two different crystallographic textures (as introduced by two different scanning strategies) the outstanding challenges of diffraction-based residual stress determination are addressed.

Within this article, the residual stress state within PBF-LB/M/IN718 prisms is characterized by means of laboratory X-ray diffraction, energy dispersive X-ray synchrotron diffraction, and neutron diffraction using texture-based evaluation. For neutron diffraction, the stress-free reference is spatially acquired on small cuboids and compared to results obtained using the stress balance condition. Beyond that, the sub-surface principal stress tensor is acquired using energy dispersive synchrotron X-ray diffraction. Laboratory X-ray diffraction techniques complement such methods, so that the surface and sub-surface residual stress distributions are fully characterized.

Texture-based residual stress analysis of laser powder bed fused Inconel 718 parts

Jakob Schröder¹, Alexander Evans¹, Vladimir Luzin², Guilherme Abreu Faria³, Sebastian Degener³, Efthymios Polatidis⁴, Jan Čapek⁴, Arne Kromm¹, Gleb Dovzhenko³, and Giovanni Bruno^{1,5}

¹Bundesanstalt für Materialforschung und -prüfung, Unter den Eichen 87, 12205 Berlin, Germany

²Australia Nuclear Science and Technology Organisation, New Illawara Rd, Lucas Heights, NSW 2234, Australia

³Helmholtz-Zentrum Hereon, Max-Planck-Str. 1, 21502, Geesthacht, Germany

⁴Laboratory for Neutron Scattering and Imaging, Paul Scherrer Institut, Forschungsstrasse 111, 5232 Villigen, Switzerland

⁵Universität Potsdam, Institut für Physik und Astronomie, Karl-Liebknecht-Str. 24-25, 14476, Potsdam, Germany

Abstract

Although layer-based additive manufacturing (AM) methods such as laser powder bed fusion (PBF-LB) offer an immense geometrical freedom in design, they typically suffer from a buildup of internal stress (i.e., thermal stress) during manufacturing. Consequently, significant residual stress (RS) is retained in the final part as a footprint of these internal stresses. Furthermore, localized melting and solidification inherently induce columnar type grain growth accompanied by crystallographic texture. Inasmuch diffractive methods are used to determine the RS distribution in PBF-LB parts, such features pose metrological challenges in their application. In theory, preferred grain orientation invalidates the hypothesis of isotropic material behavior underlying the common methods to determine RS. In this work, more refined methods are employed to determine RS in PBF-LB/M/IN718 prisms, based on crystallographic texture data. In fact, the employment of direction-dependent elastic constants (i.e., stress factors) for the calculation of RS result in insignificant differences to conventional approaches based on the hypothesis of isotropic mechanical properties. It is concluded that such observation is directly linked to the fact that $\{311\}$ lattice planes typically used for RS analysis in nickel-based alloys have high multiplicity and less strong texture intensities compared to other lattice planes. It is also found that the length of the laser scan vectors determines the surface RS distribution in prisms prior to their removal from the baseplate. In fact, upon removal from baseplate the surface RS considerably relaxes and/or redistributes: a combination of the geometry and the scanning strategy dictates the sub-surface RS distribution.

1. Introduction

Layer-wise additive manufacturing (AM) methods such as laser powder bed fusion (PBF-LB) have attracted major interest of both academics and industry within the past decade (Attaran, 2017). This interest is based on the immense geometrical design flexibility in the manufacturing of dense parts in a single

manufacturing step (Attaran, 2017). In fact, aerospace and gas turbine industry sectors demand complex geometries to increase the efficiency of lightweight construction in high temperature applications. Even further, the geometrical freedom enables the design of sophisticated internal cooling geometries in such parts. Due to its excellent weldability (Lingenfelter, 1989) paired with its potential in high temperature applications up to 650° (Collier *et al.*, 1988), the alloy Inconel 718 (in the following IN718) is an established candidate for PBF-LB processing (Volpato *et al.*, 2022). IN718 is a niobium (Nb), aluminum (Al), and titanium (Ti)-containing precipitation-hardenable Ni-Cr-Fe-Mo based superalloy. Its high strength is achieved by the precipitation of γ'' (Ni₃Nb, tetragonal D0₂₂ crystal structure) and γ' (Ni₃(Al, Ti), cubic L1₂ crystal structure) phases during aging heat treatments (Cozar & Pineau, 1973).

However, the layer-wise nature of the PBF-LB process has certain drawbacks, which undermine the applicability of the technique: Manufactured parts may suffer from defect formation such as porosity, caused by either gas inclusions or lack of fusion (Foster *et al.*, 2018). Another inherent problem of the technique is the significant surface roughness (Foster *et al.*, 2018) of the parts. Although the defect formation can be nowadays strongly reduced by the selection of appropriate process parameters (Foster *et al.*, 2018), the surface finish remains a critical aspect for engineering applications (Kasperovich *et al.*, 2021). Besides, the localized melting and solidification mechanisms of the layer-wise technique inevitably induce large internal stresses during part manufacturing (Kruth *et al.*, 2004, Mercelis & Kruth, 2006). These are based on the so-called temperature gradient mechanism in combination with the thermal contraction (i.e., shrinkage) during cooling of the previous layer, due to mechanical constraint by the substrate plate (Mercelis & Kruth, 2006, Kruth *et al.*, 2004, Ulbricht *et al.*, 2020). In extreme cases, the internal stresses may lead to cracking or delamination during production (Yadroitsev & Yadroitsava, 2015). In most cases residual stress (RS) of high magnitude is retained in as-built parts as a footprint of these internal stresses during manufacturing (Schröder, Evans, *et al.*, 2021).

Diffraction-based methods allow the non-destructive determination of the RS distribution in full parts. In principle, lattice plane spacings d^{hkl} are measured and subsequently used to calculate a lattice strain by comparing them to a stress-free reference value (d_0^{hkl}). In the case of laboratory X-ray diffraction experiments plane stress can be assumed, i.e. the normal stress component vanishes within the penetration depth of the radiation, and a precise knowledge of d_0^{hkl} is not required (Spieß *et al.*, 2009). However, whenever triaxiality of the stress state cannot be excluded, a precise knowledge of such d_0^{hkl} is indispensable (Withers *et al.*, 2007), in particular when using penetrant radiation such as Neutrons (well suited to the determination of 3D stress fields).

With the knowledge of the relationship between elastic lattice strains and macroscopic stress provided by the so-called diffraction-elastic constants (DECs) (Gnäupel-Herold *et al.*, 2012), RS can be determined from measured strains, based on Hooke's law (Hauk, 1997). For anisotropic crystals the DECs depend on the reflection hkl used for the measurement of lattice

spacing (Gnäupel-Herold *et al.*, 2012). The DEC's can be either determined experimentally or, more commonly, calculated from single crystal elastic tensor data of the material of interest (Hauk, 1997). In the past, several grain-interaction models for polycrystalline aggregates have been developed to calculate such DEC's from single crystal data. To name a few, these include the models of isostrain (Voigt, 1889), isostress (Reuss, 1929), the average suggested by Hill (Hill, 1952) or the Kröner model (Kröner, 1958) based on the solution of the Eshelby inclusion problem (Eshelby, 1957). Apart from the Kröner model, preferred grain orientation and grain-to-grain interaction are neglected in these models (Gnäupel-Herold *et al.*, 2012). However, from Eshelby's theory (Eshelby, 1961) it is known, that the strain/stress response of a single grain depends on the elastic properties and shape of the surrounding grains (Gnäupel-Herold *et al.*, 2012). The formulation of Hooke's law in the form of Dölle and Hauk (Dölle & Hauk, 1978, 1979) overcomes the problem and considers the preferred orientation by introducing the so-called stress factors.

If one wants to select an appropriate model for the calculation of the DEC's, it is commonly accepted that the Kröner model provides a reasonable agreement to experimental data for equiaxed polycrystalline IN718 (Schröder, Mishurova, *et al.*, 2021) and IN625 (Wang *et al.*, 2016). However, another consequence of the localized melting and solidification within the PBF-LB process is the columnar grain growth as reviewed in (Volpato *et al.*, 2022). In such cases, it has been experimentally shown that the Reuss model represents the materials behavior for PBF-LB/M/IN718 more accurately (Schröder *et al.*, 2022, Schröder, Mishurova, *et al.*, 2021). In fact, the usage of DEC's based on the Kröner model may lead to RS exceeding the yield strength of as-built PBF-LB/M/IN718 (Pant *et al.*, 2020, Serrano-Munoz, Fritsch, *et al.*, 2021). Additionally, strong crystallographic textures are characteristic for PBF-LB/M/IN718 (Gokcekaya *et al.*, 2021), since the fcc crystals growth along $\langle 100 \rangle$ directions (Chalmers, 1964). On the one hand, this dependence of the texture on the heat flow allows the texture to be tailored by choosing appropriate scanning strategies and beam parameters (Gokcekaya *et al.*, 2021). On the other hand, the presence of texture requires the usage of the stress factor notation for the determination of RS. Yet, in the open literature it is common to neglect crystallographic texture when determining RS in PBF-LB/M/IN718. Beyond that, the validity of the general assumption that the directions of principal strain/stress are governed by the main geometrical axes should be additionally questioned (Mishurova, Serrano-Munoz, *et al.*, 2020).

It becomes clear that several metrological challenges of the RS determination in PBF-LB/M/IN718 need to be reevaluated. In this article the strain and RS distribution in as-built PBF-LB/M/IN718 prisms (manufactured with two different scan strategies) will be determined using a combined approach of laboratory X-ray, high energy synchrotron, and neutron diffraction. These investigations are made on identical material as the in-situ loading studies reported in (Schröder *et al.*, 2022). Hence for the isotropic case, the DEC's are known to be well predicted by Reuss for the 311 reflection, which mitigates one of the key unknowns for the accurate RS determination. The distribution of sub-surface principal strain and stress is

evaluated by strain pole figures and a subsequent eigenvalue decomposition considering texture-based stress factors. Finally, the RS calculations encompassing the crystallographic texture of the two scan strategies are compared to approaches neglecting the presence of texture. Some metrological consequences for RS determination in PBF-LB/M/IN718 prisms are discussed.

2. Material and methods

2.1. Sample manufacturing

Subject of this study are horizontally built PBF-LB/M/IN718 prisms ($110 \times 13 \times 13 \text{ mm}^3$) manufactured using an SLM 280 (SLM Solutions Group AG, Lübeck, Germany). The specimens were manufactured with their longest direction within the build plane but tilted by 12° to the build plate edges (Figure 1). The baseplate was pre-heated to 200°C and processing parameters suggested by SLM Solutions were applied: laser power (P) of 350 W, scanning velocity (v) 800 mm s^{-1} , spot size diameter of 0.08 mm defocused by 4 mm, and hatch spacing (h) of 0.15 mm. Two different scanning strategies with an interlayer rotation of 90° were applied to produce the specimens (Figure 1): in the first variant, the scanning tracks were aligned parallel to the specimen edges (H_{0°), while the scanning pattern was rotated by 45° relative to the prism edges for the second variant (H_{45°). The specimens were all used in the as-built state (*i.e.* no heat treatments were applied).

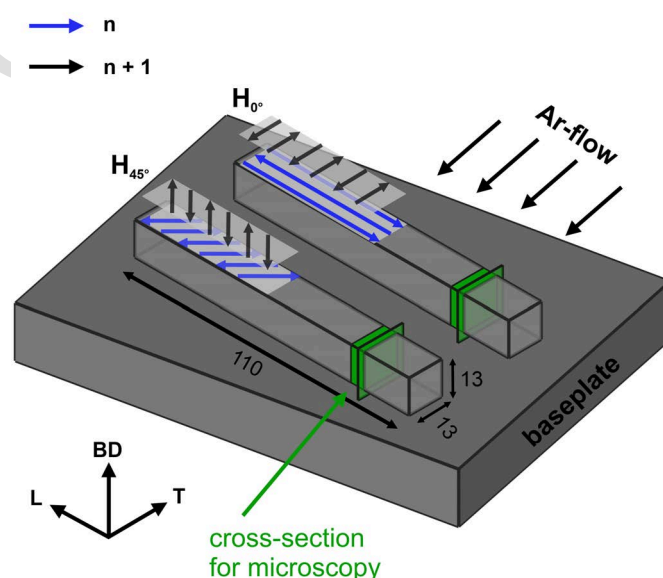


Figure 1: Schematic illustration of the specimens H_{0° and H_{45° with their scanning pattern (for layers n and $n+1$) and the extracted cross-sections used for microstructural analysis.

2.2. Microstructural analysis

2.2.1. Electron backscattered diffraction (EBSD)

As depicted in Figure 1 BD-T (build-transverse directions) cross-sections were extracted from sister specimens for microstructural analysis. These cross sections were ground to 1200 grit with SiC abrasive paper followed by 9, 3 and $1 \mu\text{m}$ polishing steps. The final polishing step was performed using

an 0.04 μm Active Oxide Polishing Suspension (OPS, Struers GmbH, Crinitz, Germany). The samples were then mounted in a LEO 1530VP (Carl Zeiss Microscopy GmbH, Oberkochen, Germany) scanning electron microscope, equipped with an electron backscatter (EBSD) Bruker Nano e-Flash HD 5030 detector (Bruker Corporation, Billerica, USA). For the EBSD analysis, the sample was tilted by 70° and kept at a working distance of approximately 18 mm. The acceleration voltage of the electron beam was 20 kV. In essence, for the bulk microstructure an area of $4 \times 3 \text{ mm}^2$ was probed over an 800×600 Pixel map, i.e. with a pixel size of $5 \mu\text{m}$. In contrast, the near surface maps were acquired at a higher magnification ($250\times$) with a pixel size of $1.5 \mu\text{m}$, i.e. over an approximate probed area of $1.2 \times 0.9 \text{ mm}^2$. For data acquisition and indexing the ESPRIT 1.94 package from Bruker nano was used. For data post-processing, the open-source MTEX toolbox (Bachmann *et al.*, 2011) installed within the MATLAB (The MathWorks, Inc. Natick, USA) software was utilized. A misorientation angle of 10° was used as the threshold to define high angle grain boundaries, whereby grains containing less than 10 pixels were excluded from the analysis.

The grain boundaries were then smoothed using the default kernel (25 iterations). In addition, non-indexed pixels were filled by their nearest neighbor and denoising was performed using a variational spline filter.

2.2.2. Neutron diffraction texture measurements

The bulk texture measurements were performed at the KOWARI strain scanner located at the Australian Nuclear Science and Technology Organisation (ANSTO) in Lucas Heights. For the measurements cylinders with a diameter and a height of 8 mm were extracted from grips of tensile specimens of H_0° and H_{45° see (Schröder *et al.*, 2022). The neutron wavelength of 1.4 \AA was selected from the 400 reflection of the Si-monochromator. With the cylinders fully immersed in the beam, measurements were run with an approximate 3×3 ($^\circ$) mesh (in φ - χ space) over the intervals χ $[0, 90]^\circ$ and φ $[0, 360]^\circ$. Three detector positions of $2\theta = 43^\circ$, $2\theta = 67^\circ$, and $2\theta = 82^\circ$ corresponding to the 111, 200, 220, and 311 reflections were selected with an acquisition time of $\approx 2 \text{ s}$. Data post processing and analysis was performed using MTEX. First, the pole figures were normalized and subsequently orientation distribution functions (ODFs) were calculated using a halfwidth of 5° . These ODFs were exported into ISODEC (Gnäupel-Herold, 2012). From these ODFs $\{200\}$, $\{220\}$, $\{111\}$, and $\{311\}$ pole figures were calculated). Furthermore, the strength of these textures can be quantified by the texture index J_{ODF} (equation 1) as implemented in MTEX (Mainprice *et al.*, 2015). The orientation distribution function can be described as a function $f(g)$. In this context, the texture index J_{ODF} can be defined as the integral of $f(g)^2$ over the rotationally invariant volume element dg . For a uniform distribution, J_{ODF} returns a value of 1. For a single orientation, it becomes an infinitely large value (Mainprice *et al.*, 2015).

$$J_{ODF} = \int |f(g)|^2 dg = \|f\|_{L^2}^2 \quad (1)$$

2.3. Texture-based RS analysis

The general principal of RS analysis by diffraction-based methods rests on Bragg's law (Bragg & Bragg, 1913). Therefore, the lattice interplanar distance d^{hkl} can be effectively used as a strain gauge. From the comparison between the measured d^{hkl} and a reference lattice distance d_0^{hkl} , the strain can be calculated as the relative difference. In that regard, Hooke's law can be written in the special form of Dölle and Hauk (Dölle & Hauk, 1978, 1979) to determine the RS from lattice spacings d^{hkl} (equation 2).

$$\begin{aligned} \langle \varepsilon_{33}^L \rangle &= \langle \varepsilon_{\varphi\psi}^L \rangle = \frac{d^{hkl}(\varphi, \psi, hkl) - d_0^{hkl}(\varphi, \psi, hkl)}{d_0^{hkl}(\varphi, \psi, hkl)} \\ &= \sum_{i,j=1}^3 F_{33ij}(\varphi, \psi, hkl) \langle \sigma_{ij} \rangle \end{aligned} \quad (2)$$

Where $_{33}$ denotes the laboratory direction \vec{L}_3 and $F_{33ij}(\varphi, \psi, hkl)$ are the so-called stress factors introduced by Dölle and Hauk (Dölle & Hauk, 1978, 1979). Dölle and Hauk (Dölle & Hauk, 1978, 1979) called them F_{ij} , thereby formally missing their fourth rank tensor character; deriving from the definition (Mishurova, Bruno, *et al.*, 2020) have shown that the notation is somewhat imprecise, as in fact in the literature ε often replaces ε_{33} , and F_{ij} is effectively taken as a second rank tensor. For a material without preferred orientation, the stress factors are independent of the measurement directions ψ, φ ; thus they become linear combinations of the DEC's s_1 and $1/2s_2$ (Hauk, 1997). However, in presence of a preferred crystallographic orientation, the $F_{33ij}(\varphi, \psi, hkl)$ depend on the measurement directions. Similar to the DEC's, the stress factors can be either directly measured by in-situ tests or calculated from single crystal elastic properties using grain-interaction models (Gnäupel-Herold *et al.*, 2012) - note that Gnäupel-Herold *et al.* also use the misleading notation F_{ij} , while properly defining the stress factors. In the latter case, the ODF is required to account for the crystallographic texture of the studied material (Behnken & Hauk, 1991).

In this study, the texture dependent $F_{33ij}(\varphi, \psi, hkl)$ were calculated with the software ISODEC 3.0 (Gnäupel-Herold, 2012) based on the Reuss model (Reuss, 1929) using the single crystal elastic constants of IN718 ($c_{11} = 242.35 \text{ GPa}$, $c_{12} = 139.73 \text{ GPa}$, $c_{44} = 104.44 \text{ GPa}$) reported in (Haldipur *et al.*, 2004). For the orientation relationships used in this study see Figure 2a.

2.3.1. Laboratory X-ray diffraction

The surface RS measurements were performed with a Xstress G3 diffractometer (StressTech, Vaajakoski, Finland) at BAM. The system operates in modified χ -mode (see standard DIN EN 15305: 2009-01: *Non-destructive testing - Test method for RS analysis by X-ray diffraction*) using two position-sensitive detectors, which are calibrated to $2\theta \approx 156^\circ$ using copper powder. For all measurements a $\varnothing 2 \text{ mm}$ collimator and an acquisition time of 5 s were used. For detailed information on the measurement conditions see Table S1 in the supplementary information. The measurement plane for the surface measurements of the top surface (for H_0° and H_{45°) is

shown in Figure 2e. These measurements were performed prior and post removal of the specimens from the baseplate to determine the redistribution of the surface RS. Data analysis was performed in the software Xtronic using a Pearson VII function to fit the diffraction peaks and determine d^{311} values. As the classic analysis of the $\sin^2\psi$ method data does not allow the incorporation of texture, the calculation of the RS was performed by the matrix method (also referred to as the generalized $\sin^2\psi$ method) reported by Ortner (Ortner, 2009, 2011, 2014). For all measurements, the overdetermined system of linear equations (see equation 2) was solved using the generalized linear model as implemented in the statsmodels.api within Python (Seabold & Perktold, 2010). Since the penetration depth of the Mn- k_α radiation is at maximum $\approx 5 \mu\text{m}$, the out-of-plane stresses were disregarded for the top ($\sigma_{i-BD} = 0$) and side ($\sigma_{i-TD} = 0$) surfaces. Furthermore, the measurements carry the assumptions that the measured directions ($\varphi = 0^\circ, 90^\circ$) are principal, so that the in-plane shear components vanish. As for surface measurements, a precise knowledge of d_o^{hkl} is not required, the tensor equation (1) can be written in d^{hkl} form. This treatment yields an overdetermined set of linear equations with the unknowns d_o^{311} , σ_{TD} , σ_{LD} (top) and d_o^{311} , σ_{LD} , σ_{BD} (side).

2.3.2. Electrolytic layer removal

Incremental electrolytic layer removal was performed (after removal from the baseplate) at the side surfaces of H_{0° and H_{45° , as indicated in Figure 2e. A Kristall 650 electrolytic polishing device (ATM Qness GmbH, Mammelzen, Germany) was used, operated at a voltage of 30 V and a current of 2 A with a circular polishing diameter of 9 mm. The solution used for electropolishing consisted of 550 ml of saturated saline solution, 150 ml of water, 200 ml ethylene glycol, and 100 ml ethanol. The depth after each removal increment was measured using an ID-C series 543-471B dial indicator (Mitutoyo Corporation, Kawasaki, Japan) with an accuracy of $\pm 3 \mu\text{m}$.

2.3.3. Synchrotron X-ray diffraction

The synchrotron X-ray diffraction measurements were performed at the white beam engineering materials science beamline P61A at the Deutsches Elektronen-Synchrotron DESY located in Hamburg, Germany (for details see (Farla *et al.*, 2022)). A largely simplified illustration of the basic instrument principle is depicted in Figure 2b. Prior to the measurements, a diffraction angle of $2\theta \approx 11.946^\circ$ was calibrated using NIST Silicon powder. The specimens, mounted in a Eulerian cradle, were scanned in χ -mode using the energy dispersive detector in the horizontal diffraction plane ($\psi = \chi - 90^\circ$ for the detector in the horizontal diffraction plane). The specimens were measured at the top and side surfaces according to Figure 2e. The acquisition time varied between 10 - 20 s up to $\psi = 60^\circ$ and were increased to 20 - 40 s between $\psi = 60 - 80^\circ$. The incoming beam was narrowed by the vertical and horizontal slits to $0.5 \times 0.5 \text{ mm}$ cross-section. In the diffracted beam, the slits narrowed the beam to $26 \times 26 \mu\text{m}$ (for further details on the measurement conditions see Table S1 in the supplementary information). Peak fitting was performed in the opensource software P61A:Viewer developed at the P61A beamline, using a PseudoVoigt

function. Peaks under 100 counts were excluded from the analysis. The diffraction angle used was approximately 12° giving a penetration depth of the 311 of $\tau_0 \approx 30 \mu\text{m}$. In consequence, stress triaxiality should not be neglected although an influence on the obtained stress values is expected to be low; this represents the appropriate methodological approach.

The overdetermined set of linear equations was solved using the mean value of all measured d^{311} as stress-free reference d_o^{311} . Afterwards an eigenvalue decomposition was performed to determine the principal directions represented by the eigenvectors $\mathbf{v}_1, \mathbf{v}_2, \mathbf{v}_3$, and eigenvalues $\sigma^L, \sigma^T, \sigma^{BD}$.

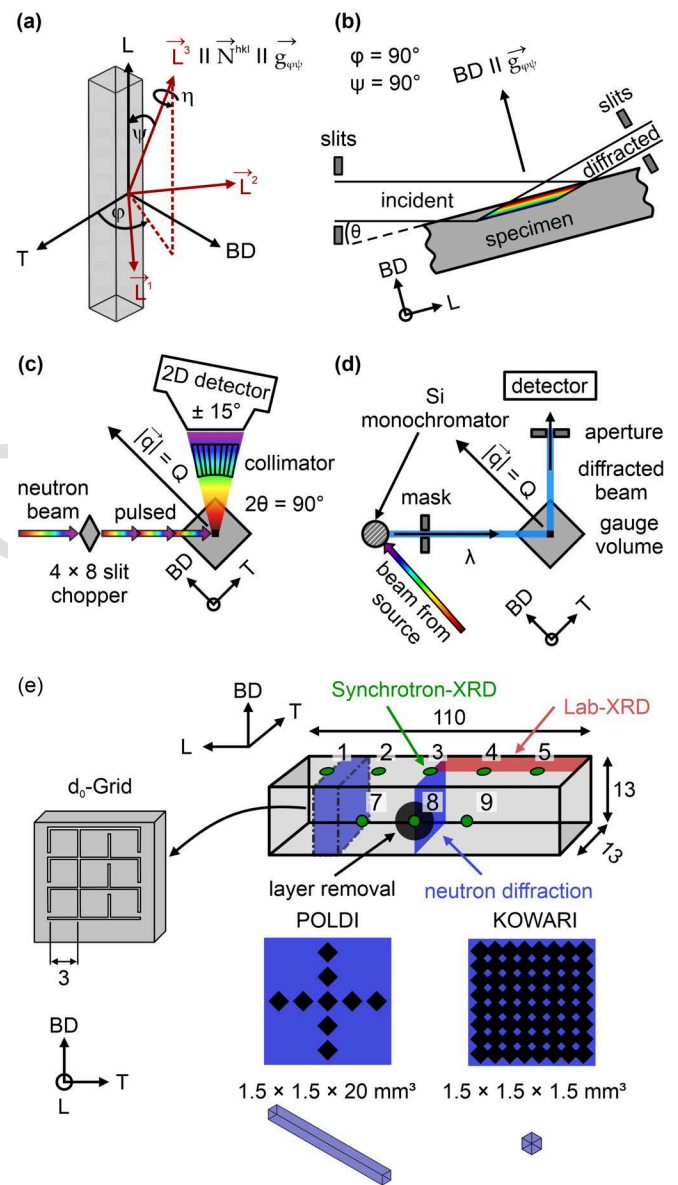


Figure 2: Schematic illustration of the measurement principles: (a) reference coordinate system, (b) energy dispersive synchrotron X-ray diffraction (c) pulse overlap time of flight neutron diffraction at POLDI, (d) monochromatic neutron diffraction at KOWARI, and (e) measurement positions for the characterization of RS with extracted d_0 -grid from sister specimen.

All calculations were repeated 10000 times selecting a random value within the 95 % confidential interval of the least square solution to estimate an error band for the principal stress directions and magnitudes. The procedure is described in more detail in (Fritsch *et al.*, 2021). While the choice of d_o^{311} as the mean value of all measured d^{311} values remains somewhat arbitrary, it may affect the absolute values of the principal stresses but not the principal stress directions.

2.3.4. Time-of-flight neutron diffraction

Bulk d_o^{hkl} and strain measurements were performed at the pulse overlap time-of-flight (TOF) diffractometer POLDI at the Swiss Spallation Neutron source (SINQ) at the Paul Scherrer Institut (PSI), Villigen, Switzerland. A largely simplified sketch of POLDI's measurement principle is depicted in Figure 2c. POLDI uses a pulsed neutron beam with a 1D ^3He chamber detector. The detector is time-of-flight and angular sensitive with an angular coverage of $2\theta = 75\text{--}105^\circ$. The signal is properly integrated over the whole angular range. This implies that the strain component is averaged around $\pm 7.5^\circ$ from the scattering vector. All measurement were made using the $1.5 \times 1.5 \text{ mm}^2$ full width at half maximum (FWHM) collimator to define the diffracted beam. The incident beam shape was defined by the slit optics. A d_o -grid was extracted from a sister specimen by electrical discharge machining as depicted in Figure 2e. The single cubes have dimensions of $3 \times 3 \times 3 \text{ mm}^3$ and are connected in the grid to simplify their alignment. To fully immerse the gauge volume in the cuboids of the d_o -grid, a $2.6 \times 2.6 \times 1.5 \text{ mm}^3$ gauge volume was defined for the measurements of d_o along the three orthogonal directions BD, L, and T. However, to obtain sufficient sampling statistics, a $1.5 \times 1.5 \times 20 \text{ mm}^3$ matchstick shaped gauge volume was used to measure d^{hkl} along BD and T in the prism. For optimization, dependent on the path length, the acquisition time was adjusted between 30 and 45 min.

Data analysis was performed using a Gaussian peak function within Mantid (Arnold *et al.*, 2014). Additional information on the experimental setup and the data evaluation of POLDI can be found in literature (Stuhr, 2005, Stuhr *et al.*, 2006, Stuhr *et al.*, 2005).

2.3.5. Monochromatic neutron diffraction stress analysis

Bulk residual stress determination was conducted using the KOWARI strain scanner located at the Australian Nuclear Science and Technology Organisation (ANSTO) in Lucas Heights. The principle of the technique is depicted in Figure 2d. In contrast to the pulsed white beam at POLDI, a specific wavelength (in our case 1.53 \AA) is selected by a silicon monochromator. Using a diffraction angle of $2\theta \approx 90^\circ$, a $1.5 \times 1.5 \times 1.5 \text{ mm}^3$ gauge volume was defined by slits in the incoming and diffracted beam. The positional accuracy was better than 0.1 mm . The detailed measurement conditions are listed in Table S1 in the supplementary information. Measurements of d_o^{311} were performed along the L direction of the central cube in the d_o -grids of both H_0° and H_{45° . To assess the RS distribution, an equally distributed 8×8 -point grid was defined in the BD-T cross section of H_0° and H_{45° at specimen

mid-length ($L = 55 \text{ mm}$, Figure 2e). In addition to measurements of d_o^{311} , the stress balance conditions to the T and BD components were applied based on these measured d^{311} values using an in-house developed python script.

The obtained diffraction peaks were fitted using a Gaussian profile and the texture-based analysis of the RS was performed directly in the software ISODEC (Gnäupel-Herold, 2012). The set of linear equations is not overdetermined since we only measured the three orthogonal strain components ϵ_{BD} , ϵ_{LD} , ϵ_{TD} . Thus, the error on the stress is estimated propagating the errors in d^{311} and d_o^{311} . Since for neutron diffraction knowledge of d_o^{311} is required, the linear equation system must be expressed in the $\langle \epsilon_{\phi\psi}^L \rangle$ form (see equation 2).

3. Results

3.1. Microstructure & texture

The orientation-maps viewed along L acquired by EBSD of the specimens H_0° and H_{45° are shown in Figure 3a-c and Figure 3e-g. In addition, the calculated $\{200\}$ pole figures (for the maps acquired on the cross-section) are shown in Figure 3c.1 and Figure 3g.1. The near surface maps reveal that qualitatively no texture gradient towards the surface exists. However, they also shown that the lateral and top surfaces of both H_0° (Figure 3a, b) and H_{45° (Figure 3e, f) exhibit a degree of surface roughness, as no contouring was performed during manufacturing. The highest peak to valley measure of the surface roughness based on the localized region (i.e., statistically very limited) of the EBSD maps in Figure 3 are of the order of $70 \mu\text{m}$. The neutron (Figure 3d, h) and EBSD texture measurements (Figure 3c.1, g.1) of the bulk yield similar $\{200\}$ pole figures. In essence, a cube-type texture can be observed in both H_0° (Figure 3d) and H_{45° (Figure 3h) specimens. Since the scanning vectors are aligned with the geometry in H_0° , the $\langle 100 \rangle$ directions (i.e. the faces of the crystal) are aligned with the L, T, and BD directions. The texture strength of H_0° is characterized by the texture index $J_{ODF}(\text{H}_0^\circ) \approx 1.8$. While the texture intensities in the $\{200\}$ pole figure are equal along L and T, the $\{220\}$ pole figure shows that a mixed $\langle 100 \rangle / \langle 110 \rangle$ -type texture is present along BD. Even though the $\langle 100 \rangle / \langle 110 \rangle$ -type texture is preserved along BD in H_{45° , the change of the scan pattern causes a 45° rotation of the cube-type texture around BD (i.e. $\langle 110 \rangle / \langle 111 \rangle$ -type texture along L and T). Such a texture is characterized by a texture index $J_{ODF}(\text{H}_{45^\circ}) \approx 2.1$. EBSD as a surface-specific technique provides spatial resolution to characterize grain morphology and texture. However, the calculation of a representative ODF is limited by the sampling statistics. In this context, the neutron diffraction texture measurements probed the entire volume of the cylinders ($\approx 402 \text{ mm}^3$), rather than the $4 \times 3 \text{ mm}^2$ area probed by EBSD (the penetration depth of the electron beam is only a few nm). Thus, although the textures determined by EBSD and neutron diffraction agree, all subsequent texture-based RS determinations (i.e. bulk and surface) use calculated ODFs from neutron texture measurements, because the probed volume is millions of times larger. Such data show the strongest texture and thereby represent the worst-case scenario of the influence of crystal orientation on the RS determination.

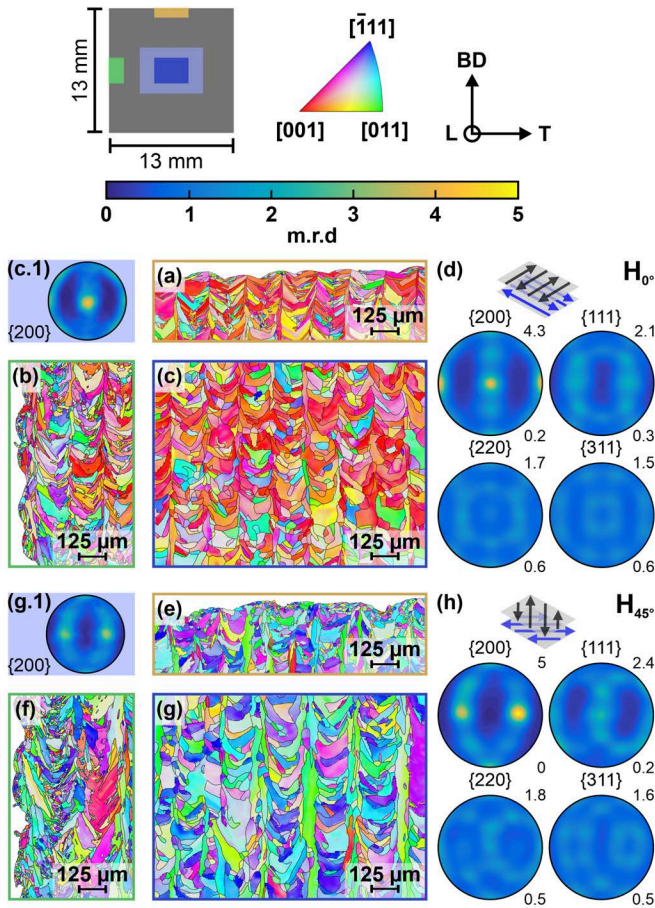


Figure 3: Orientation-maps of the samples H_{0° (a-c) and H_{45° (e-g) acquired near the top surface (a, e), the side surface (b, f), and at the center of the cross section (probed area $1.2 \times 0.9 \text{ mm}^2$) (c, g). Viewing direction corresponds to the L direction. The $\{200\}$ -pole figures (probed area $4 \times 3 \text{ mm}^2$) corresponding to (c) and (g) are shown in (c.1) and (g.1). The $\{200\}$, $\{111\}$, $\{220\}$, and $\{311\}$ pole figures acquired via neutron diffraction are shown in (d) and (h) for H_{0° and H_{45° , respectively.

3.2. Stress factors

Taking into account the calculated $\{311\}$ pole figures shown in Figure 3d and h, the results of the calculated stress factors $F_{33ij}(\varphi, \psi, 311)$ of H_{0° and H_{45° are shown in Figure 4a and b in dependence of ψ and φ respectively. As previously mentioned, the calculations based on the hypothesis of isotropic elasticity are linear combinations of the DEC's s_1 and $1/2s_2$ and show a linear dependence of F_{33ij} on $\sin^2\psi$ in the plane containing the load axis. The calculated F_{33ij} according to the texture based Reuss model deviate considerably for both specimens H_{0° and H_{45° . As an effect of the difference in texture (Figure 3), F_{33ij} is larger for H_{0° up to $\sin^2\psi \approx 0.5$ but smaller above $\sin^2\psi \approx 0.5$ (Figure 4a). It must be noted that the point symmetry of the stress factors in Figure 4a arises from the cube-type texture (see Figure 3): the intensity in the $\{311\}$ pole figures at $\varphi = 0^\circ$ and $\psi = 45^\circ$ is identical for H_{0° (Figure 3d) and H_{45° (Figure 3h). In principle, the textures of H_{0° and H_{45° are akin, just rotated by 45° around the build axis. Therefore, the stress factors are also offset by such angle as they are weighted according to their orientation distribution function. In the plane perpendicular to the applied load, F_{33ij} is independent of φ for an isotropic

material ($= s_1$), while becoming dependent on φ in presence of crystallographic texture (Figure 4b).

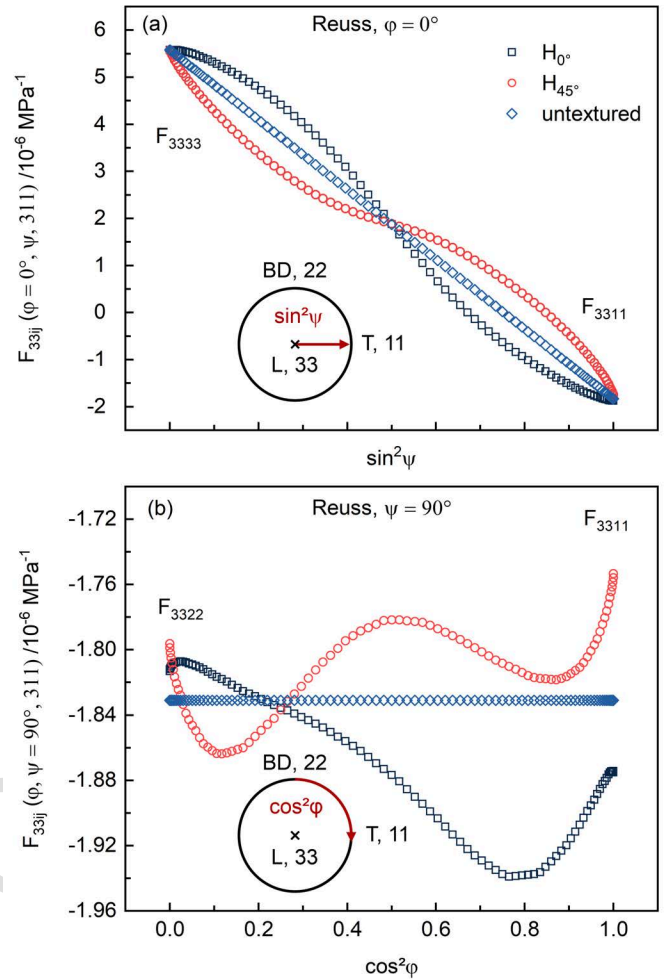


Figure 4: Exemplary comparison of the calculated stress factors F_{33ij} showcased for a uniaxial stress acting along the L direction for H_{0° , H_{45° , and a hypothetically untextured sample: (a) response in the 33-11 plane (i.e., F_{3333}^{-1} akin to E^{hkl}), and (b) response in the 22-11 plane (perpendicular to load axis).

3.3. X-ray diffraction: surface and sub-surface RS

3.3.1. Prior to removal from the baseplate

The surface RS maps (L and T directions) for a quarter of the sample surface of the prisms H_{0° and H_{45° are depicted in Figure 5. The drop in RS close to the specimen edges (width = 6 mm, length = 54 mm) is associated with misalignment. If we ignore these points near the edges, an average maximum stress of $383 \pm 28 \text{ MPa}$ is present in H_{0° along L prior to removal from the baseplate. In contrast, a minimum average stress of $255 \pm 25 \text{ MPa}$ is present in the T direction. For H_{45° the surface stress appears broadly isotropic, as the average stresses have similar magnitude when considering the error: $355 \pm 33 \text{ MPa}$ along L and $305 \pm 34 \text{ MPa}$ along T.

3.3.2. Post removal from the baseplate

Once the specimens are removed from the baseplate, stress redistribution and relaxation occur, due to distortion in the L

direction: the surface longitudinal stress relaxes (from the edge up to $L = 42$ mm) to an average magnitude of 121 ± 17 MPa ($\approx 68\%$ relaxation) and 88 ± 54 MPa ($\approx 75\%$ relaxation) for H_0° and H_{45° , respectively. However, close to the edges a higher magnitude tensile RS of about 240 MPa is present, which introduces a comparable bending moment in the two specimens. Along the T directions, stress redistribution is negligible and only small relaxations of about 55 MPa ($\approx 21\%$) in H_0° and 40 MPa ($\approx 13\%$) in H_{45° are observable.

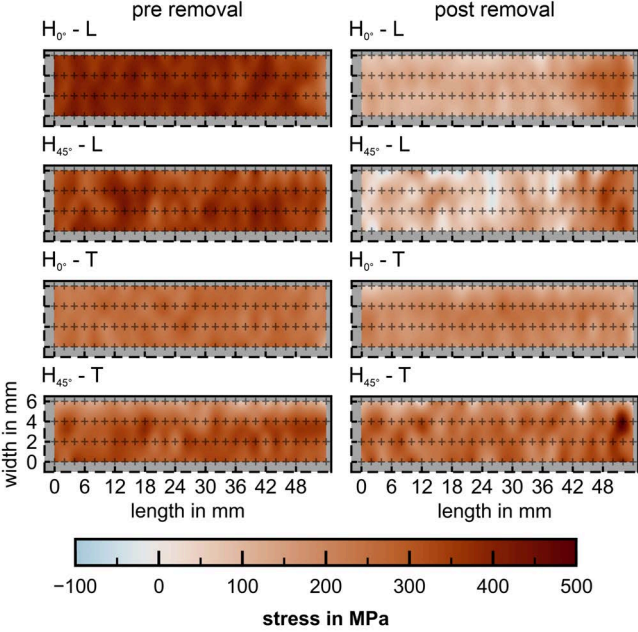


Figure 5: Linearly interpolated contour plots of the laboratory X-ray diffraction RS measurements on the top surface of the specimens H_0° and H_{45° along their L and T directions. The measurements were performed prior (average measurement error $H_0^\circ \approx 27$ MPa, $H_{45^\circ} \approx 34$ MPa) and post removal from the build plate (average measurement error $H_0^\circ \approx 29$ MPa, $H_{45^\circ} \approx 32$ MPa). Measurement positions are highlighted by the crosses and were distributed as depicted in Figure 2e. 0,0 is the center of the specimen top surface.

3.3.3. Determination of sub-surface principal stress

The strain pole figures acquired at the synchrotron beamline P61A are shown in Figure 6 and Figure 7 for the top (points 3 – 5) and side surface (points 8, 9), respectively. From these sub-surface strain pole figures the in-plane principal strain can be directly determined in a qualitative fashion. In all strain pole figures acquired close to the center (i.e., points 3, 4, 8, 9), a strain plateau at $\pm 30^\circ$ in φ is observable around the direction of maximum and minimum strain. This plateau begins to transform into a uniform “ring” of large strain at about 10 mm from the edges (i.e., stress state becomes transversely isotropic) of the top surface point 5. Such observation is in line to the post-removal X-ray diffraction measurements (Figure 5). Even further, the strain pole figures show that the direction of largest sub-surface strain in H_0° coincides with the transversal direction T for measurements in the L-T plane (Figure 6); the smallest strain (i.e. average slope of the ε vs. $\sin^2\psi$ curve) is found along the longitudinal direction L. On the contrary, the strain pole figures of H_{45° in the L-T plane reveal a rotation of the in-plane sub-surface principal axes around BD towards the geometrical axes (Figure 6).

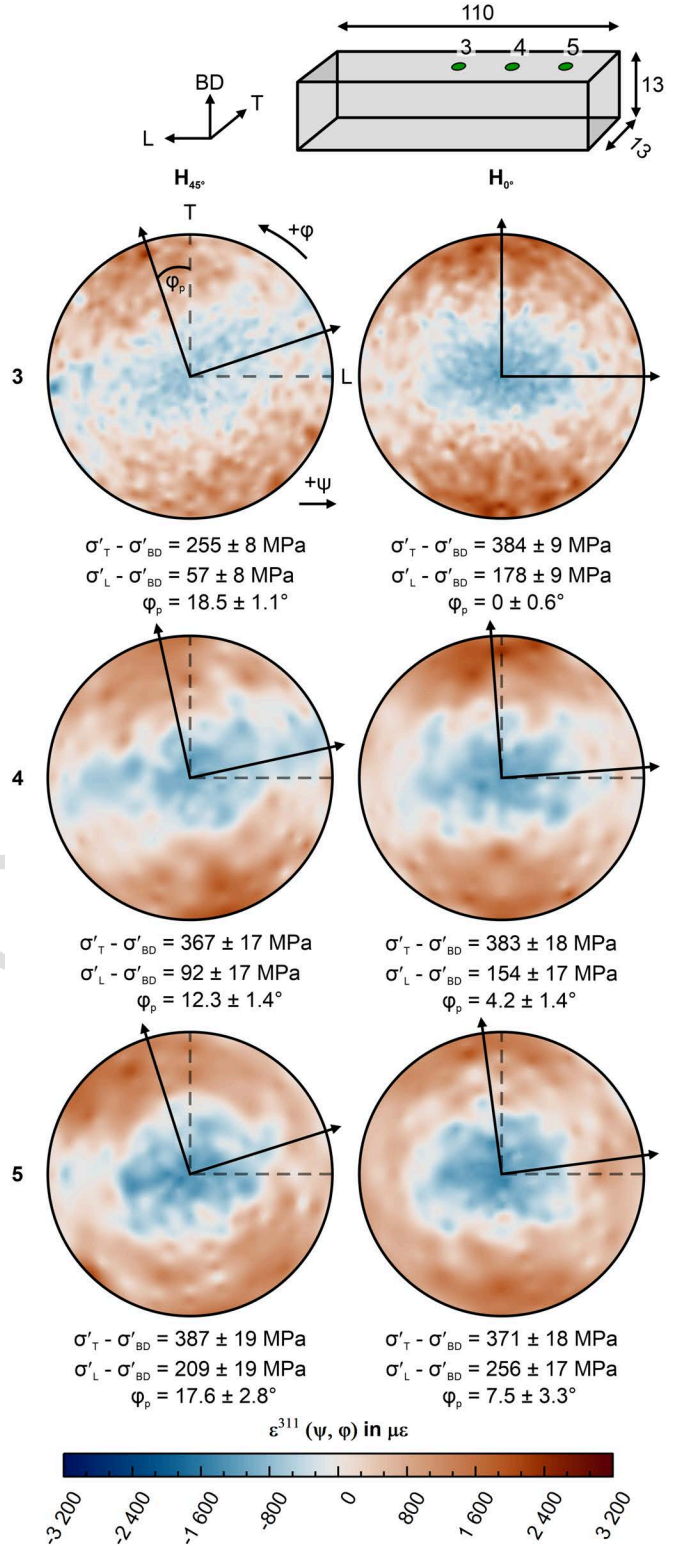


Figure 6: Top surface strain pole figures of measurement points 3 – 5 calculated for the 311 reflection, where d_0^{311} is defined as the average value of all $d^{311}(\psi, \varphi)$ as the d_0^{311} . The arrows mark the in-plane principal directions according to the eigenvalue decomposition.

Such qualitative observations are confirmed quantitatively by the eigenvalue decomposition results as shown in Figure 6. The smaller magnitude of the sub-surface principal stress at measurement point 3 in H_{45° corresponds to local stress relaxation induced by the layer removal performed on the side

surface. In the case of the side surface measurements (7 - 9), the strain pole figures (Figure 7) reveal the alignment of the maximum sub-surface principal strain with BD irrespective of the scanning strategy used. The subsequent eigenvalue decomposition reveals a ≈ 120 MPa larger sub-surface deviatoric principal stress difference $\sigma'_{BD} - \sigma'_T$ in the H_{0° specimen than in H_{45° . Also in this case, the stress state is transverse isotropic with respect to BD (*i.e.* the stress difference $\sigma'_L - \sigma'_T \approx 0$). The resulting sub-surface principal stress values of all measured points 1-9 can be found in the supplementary information (Table S1).

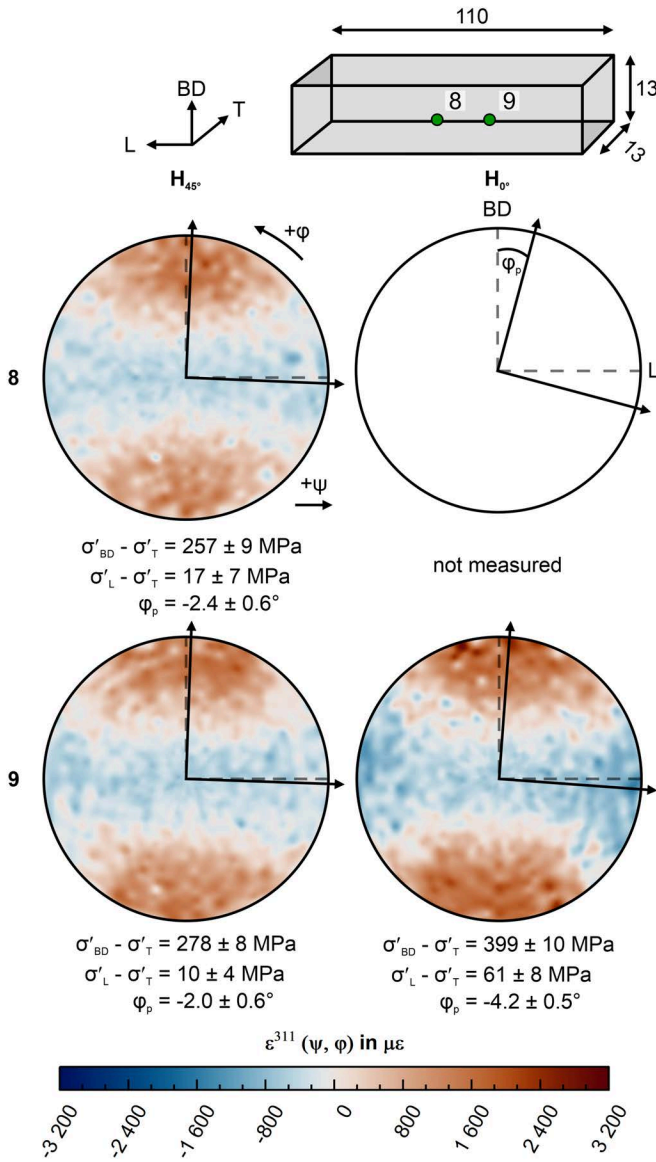


Figure 7: Side surface strain pole figures of measurement points 8 and 9 calculated for the 311 reflection defining the average value of all $d_o^{311}(\psi, \varphi)$ as the d_o^{311} . The arrows mark the in-plane principal directions according to the eigenvalue decomposition.

3.3.4. Layer removal

For relatively shallow removal depths it is known that the differences of residual stress between the measured and corrected values are negligible (Moore & Evans, 1958). Therefore, Figure 8 shows the uncorrected results of the layer

removal method measurements up to a depth of 700 μm ($\approx 5\%$ of the total thickness). For both specimens H_{0° (Figure 8a) and H_{45° (Figure 8b) the RS state at the surface is characterized by tensile stresses of small magnitude along BD, and around 0 MPa along L. At shallow depths (first 100 μm), an increase of the stress is observed, until a stress plateau of $\sigma_{BD} = 350$ MPa and $\sigma_L = 100$ MPa is reached. This observation is believed to be connected to the inherent surface roughness of the specimens, as the penetration depth of Mn- k_α radiation in IN718 is small. Even though the scanning strategy was different, the average stress at the plateau appears to be similar in the two specimens. Yet, at shallower depths (e.g. 125 μm) the maximum stress is larger in H_{0° (≈ 410 MPa) than in H_{45° (≈ 330 MPa).

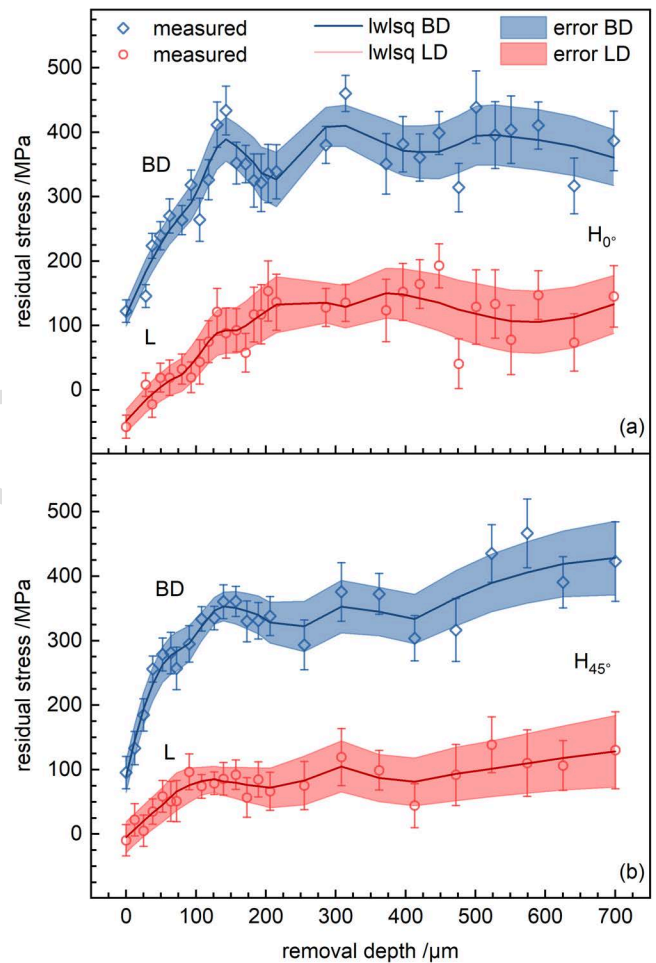


Figure 8: Through thickness (T) RS profiles obtained by incremental electrolytic layer removal at the center of the side surface ($L \approx 55$ mm, $BD \approx 6.5$ mm) (see Figure 2e) for the specimens H_{0° (a) and H_{45° (b). No stress relaxation corrections were applied. To guide the readers eye, data smoothing has been performed in OriginLab by the locally weighted least squares (lwlsq) method.

3.4. Neutron diffraction: Bulk RS

3.4.1. The stress-free reference d_o^{311}

Spatially resolved measurements of d_o^{311} were performed on the d_o -grid (see above) at the POLDI beamline. The results are shown in Figure 9a. No clear variation in dependence of the build height or transversal direction can be observed for H_{0°

(Figure 9a). Even though the $2.6 \times 2.6 \times 1.5 \text{ mm}^3$ gauge volume used for the POLDI measurements is close to full immersion, different $d_{0^{311}}$ values were measured in the three directions (Figure 9a). However, a pointwise average for the three directions corresponds well to the L direction of the measured $3 \times 3 \times 3 \text{ mm}^3$ cuboids. The overall average (dashed line in a) corresponds to the L-direction at positional index 5. This average was used for the calculation of lattice strain from POLDI data for H_{0° .

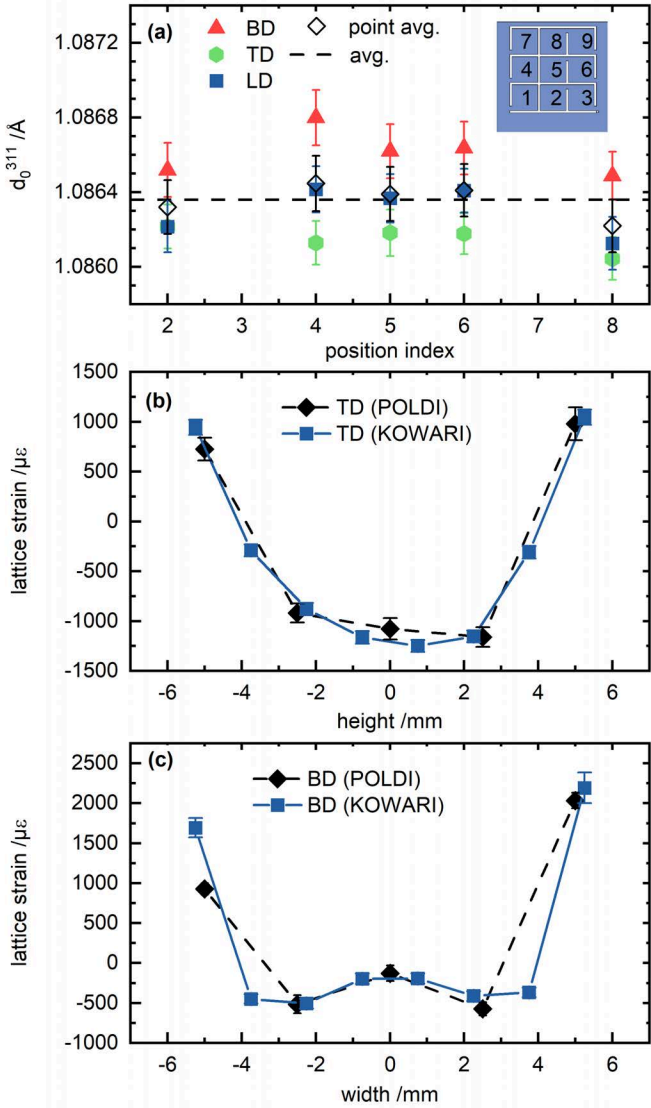


Figure 9: (a) $d_{0^{311}}$ measurements performed at the POLDI beamline in the d_o -Grid of specimen H_{0° according to the coordinate system in Figure 2e. Calculated lattice strains for TD (b) and BD (c), measured along the height and the width in the H_{0° prism. The strain calculation for the POLDI data is based on a position independent average of $d_{0^{311}}$ (see dashed line in (a)), while the strain calculation for the KOWARI data is based on the value obtained from measuring along L at the positional index 5.

In fact, such strain, agrees with the strain determined by KOWARI using the related $d_{0^{311}}$ measured along L at positional index 5 (Figure 9b, c). As opposed to H_{0° , the directional spread of $d_{0^{311}}$ is much smaller in H_{45° , yet the overall average correlates slightly worse (although still within the error bar) to the L-direction in the center of the d_o -grid (i.e. at positional index 5, see Appendix A). For the determination of all

subsequent bulk RS values (for H_{0° and H_{45°) from measurements at KOWARI, $d_{0^{311}}$ along L at positional index 5 is used.

3.4.2. Stress mapping

The RS maps acquired at the strain scanner KOWARI in the cross-sections displayed in Figure 2e are shown in Figure 10. It is evident from these measurements, that the tensile RS close to the surface are balanced by compressive stress in the bulk. Furthermore, a slight asymmetry in the stress maps from left to right can be observed. The stress relaxation upon removal from the baseplate results in a low stress (about 50 MPa) along L close to the sample surface (center of gauge volume 1.25 mm below the surface) in both specimens. Overall, the RS distribution look alike, except for a larger compressive stress preserved in the H_{0° specimen.

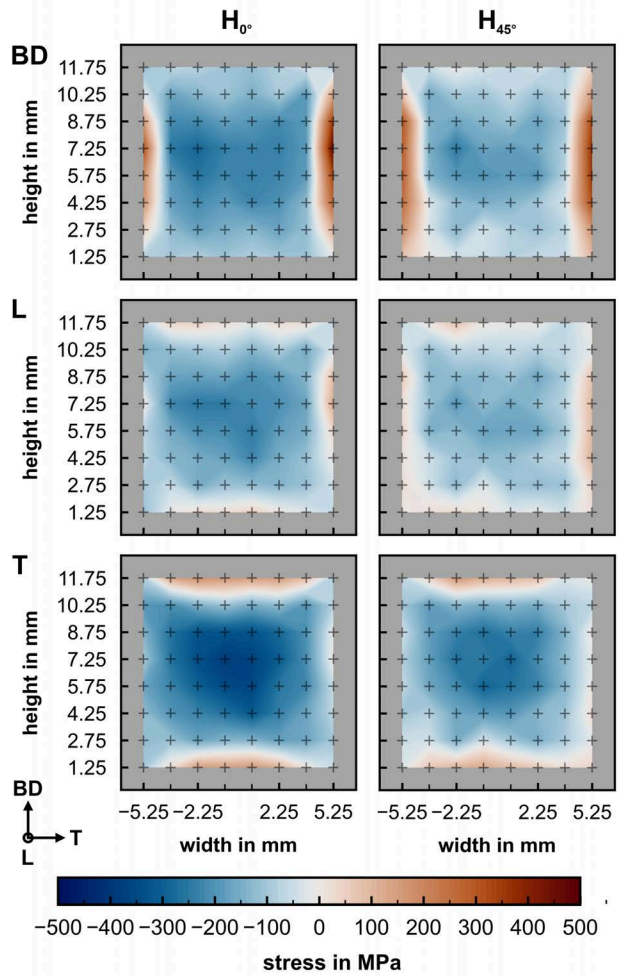


Figure 10: Comparison of the bulk RS maps acquired in the cross-section at mid-length on the KOWARI strain scanner at ANSTO using the measured $d_{0^{311}}$ -L of the respective specimen H_{0° and H_{45° . The average measurement error is 27 MPa for H_{0° and 32 MPa for H_{45° .

4. Discussion

4.1. Influence of preferred grain orientation

In theory, the presence of crystallographic textures invalidates the use of methods based on the hypothesis of isotropic elastic behavior. Yet, in most cases the hypothesis of isotropic elastic constants is used. This holds true even though it is known that crystallographic texture is present in PBF-LB/M/IN718 manufactured specimens (Volpato *et al.*, 2022). Figure 11 exemplary shows the d^{311} - $\sin^2\psi$ curves and their relative intensities at $\varphi = 90^\circ$ in the BD-L plane for H_{0° and H_{45° . In a case without preferred orientation such distribution should exhibit linearity (Vanhoutte & Debuyser, 1993). In addition, the relative intensity should be nearly independent of ψ (Spieß *et al.*, 2009), yet gradually decrease at higher ψ angles due to the grazing incidence. Instead, both d^{311} - $\sin^2\psi$ curves are non-linear (especially for H_{45°), i.e. show clear evidence of crystallographic texture. Such a non-linearity has been recently observed for the $\{311\}$ lattice planes in PBF-LB/M/IN718 (Mishurova *et al.*, 2018, Serrano-Munoz, Fritsch, *et al.*, 2021), although the $\{311\}$ lattice planes are supposed to behave in an isotropic manner. In fact, in (Mishurova *et al.*, 2018, Serrano-Munoz, Fritsch, *et al.*, 2021) the RS was determined using a linear fit. While in the case of (Mishurova *et al.*, 2018, Serrano-Munoz, Fritsch, *et al.*, 2021) this proved to be a fair approximation, such an approach may lead to significant errors in the calculation of the RS, when compared to approaches fitting non-linear functions (i.e. those considering texture) to d - $\sin^2\psi$ curves (Vanhoutte & Debuyser, 1993).

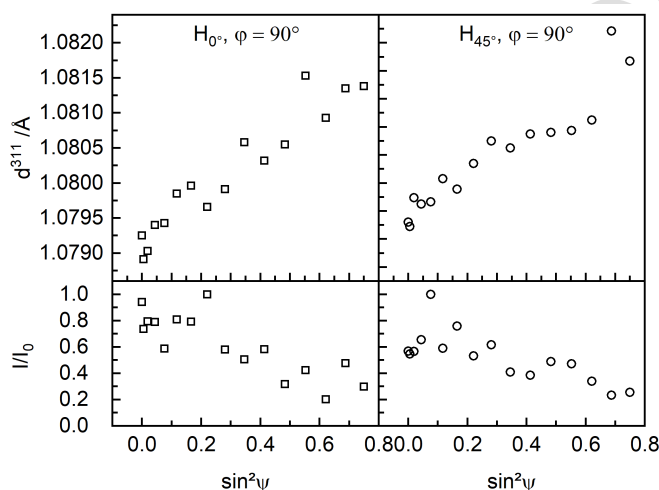


Figure 11: d^{311} - $\sin^2\psi$ distributions and respective relative intensities of H_{0° and H_{45° measured in the BD-L plane at $\varphi = 90^\circ$ (ψ tilting towards BD) at measurement position 9 (see Figure 2e) showing evidence of crystallographic texture.

To quantify the difference between texture-based and isotropic calculations, we used both, isotropic and texture-based calculations within ISODEC. The results are outlined in Table 1. The differences in the obtained RS are small and well within the error bar of the measurements. This corroborates the assumption made in (Mishurova *et al.*, 2018, Serrano-Munoz, Fritsch, *et al.*, 2021, Thiede *et al.*, 2018). Most probably, the mild texture of the 311 reflection (\approx max. 1.6 m.r.d.) has a rather minor effect on the calculated RS and one could still use

the hypothesis of isotropic elastic constants. In fact, the difference between isotropic and texture-based calculations of the neutron diffraction and the energy dispersive RS data is comparable for H_{0° . However, when stronger cube-type textures are modeled in MTEX and accounted for in the texture-based analysis of H_{0° , the absolute stress difference between isotropic and texture-based calculations increases up to 80 MPa (Figure 12). Such a difference is well beyond the error bar of the determination and is above 15 % of the actual stress value. Especially since in high power laser powder bed fusion (1000 W) strong cube-type textures ($t \approx 20$) are realized (Zhong *et al.*, 2023), texture-based methods should be employed in such a case. However, for texture indices $J_{ODF} < 3$, the effect of texture on the RS values seems to rapidly decrease (Figure 12). It must be emphasized that such observation is based on modeled textures applied to experimental data possessing much lower crystallographic texture. However, in reality, it is practically impossible to produce material with different textures, yet the exact same residual stress field using laser powder bed fusion.

Therefore, the general assumptions used for a diffraction-based analysis of RS must be checked on a case-by-case basis (low texture factor, columnar grain shape). Whenever the ODF is known, the use of texture-based methods for the determination of RS is recommended.

Table 1: maximum and average values of the RS difference between calculations neglecting ($\sigma_{isotropic}$) and considering ($\sigma_{textured}$) crystallographic texture for the measurements at KOWARI. Errors represent the standard deviation of all measurements.

specimen	H_{0°	H_{45°
$\max(\sigma_{isotropic} - \sigma_{textured})$	5 MPa	11 MPa
$\text{average}(\sigma_{isotropic} - \sigma_{textured})$	1 ± 1 MPa	2 ± 3 MPa

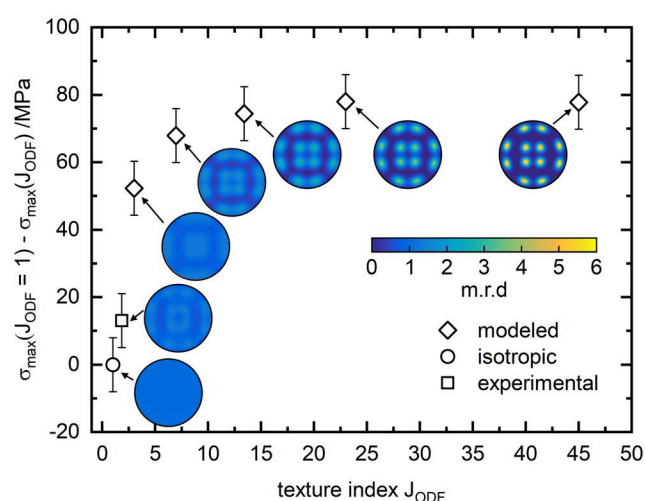


Figure 12: The influence of experimental and modeled $\{311\}$ pole figures on the calculated residual stress difference compared to the isotropic case of H_{0° as determined by energy dispersive diffraction at measurement position 3 (see Figure 2 and Figure 6).

Once different reflections are used for RS analysis (e.g. energy dispersive methods), texture-based approaches become decisive.

4.2. The scanning strategy determines the RS distribution

Several works reporting surface RS distributions have shown that longer scan vectors lead to higher tensile RS in Ti6Al4V (Kruth *et al.*, 2012, Ali *et al.*, 2018) and IN718 (Serrano-Munoz, Ulbricht, *et al.*, 2021). Furthermore, it is known, that the larger principal residual stress is always parallel to the track of the scan direction in the final deposited layer while the specimen is attached to the baseplate for PBF-LB/M/Ti64 (Levkulich *et al.*, 2019). In contrast, Bayerlein *et al.* (Bayerlein *et al.*, 2018) showed (for an unspecified scanning strategy), that the principal directions are approximately aligned in the direction of the sample edges for as-built PBF-LB/M/IN718 cuboids. Similar findings have been observed in PBF-LB/M/IN625 lattice structures, whereby the principal direction coincides with the main geometrical axis of the strut (Fritsch *et al.*, 2021). However, (Fritsch *et al.*, 2021) showed that, rigorously, the determination of the principal stress is only independent of the choice of the measurement directions if one uses *nine* directions.

These observations seem to be transferrable to PBF-LB/M/IN718: In H_0° the scanning vector was oriented along the length (110 mm) and width (13 mm) of the rectangular prism for alternate layers. The largest stress along the L direction in H_0° (Figure 5) can thus be explained by the larger thermal gradient when scanning along such direction: in fact, the aspect ratio between the scan length of alternated layers is about 7. If the scan vectors become of equal length, as in the case of a 45° rotation to the geometrical axis in H_{45° , the surface RS magnitudes along T and L become similar. Even further, the scanning strategy influences the orientation of the surface principal stress axes relative to the geometrical axis: It is hypothesized that prior to removal from the baseplate the scanning direction dictates the sub-surface principal stress direction ($\approx 45^\circ$ to L and T in H_{45°). This would explain the equality of the surface RS along the directions L and T prior to removal: both L and T directions lay at 45° from the principal axis.

4.3. RS redistribution upon removal from baseplate

In agreement to the present work, Thiede *et al.* (Thiede *et al.*, 2018) found a similar relaxation pattern of the surface RS in horizontally manufactured IN718 prisms (with a rounded tip): Prior to removal from the baseplate, the surface RS had high tensile magnitude with insignificant changes across the specimen surface. Upon removal from the baseplate an overall relaxation with a steep increase of the surface RS in the longitudinal direction towards the tip was found, irrespective of the scanning strategy applied (see also (Serrano-Munoz, Ulbricht, *et al.*, 2021)). In contrast to our work, (Thiede *et al.*, 2018) observed, the surface RS in the transversal direction to be the largest prior to removal and additionally showed significant relaxation. However, both the specimen cross-

section ($20 \times 20 \text{ mm}^2$) and the stripe wise scanning strategy were substantially different compared to this study. Therefore, the disagreement to the present study outlines the influence of such aspects on the surface RS distribution.

Additionally, the surface RS values reported in (Thiede *et al.*, 2018) were significantly higher than those observed in our study. On the one hand this is connected to the choice of a Kröner type grain-interaction model (see also (Pant *et al.*, 2020)). In fact, in (Serrano-Munoz, Ulbricht, *et al.*, 2021) it was shown that the use of the Reuss model for similar specimens yields more sensible magnitude of surface and sub-surface RS. On the other hand, this is to a degree also dependent on the geometry and the process parameters (i.e. the scanning strategy) (Nadammal *et al.*, 2021). Distortion measurements of this kind of sample geometry show that the sample tends to deform towards the tip (Thiede *et al.*, 2018, Mishurova *et al.*, 2018, Serrano-Munoz, Fritsch, *et al.*, 2021). In addition, the distortion tends to be somewhat dependent on the scanning strategy (Serrano-Munoz, Ulbricht, *et al.*, 2021).

Our synchrotron experiments reveal that the sub-surface principal axes are aligned with the geometry if the scanning vectors are alternatingly parallel to L and T. On the contrary, the principal directions in the L-T plane are rotated by $\approx 13^\circ$ from the main geometrical axes if the scanning vectors are oriented 45° to the geometry. This indicates that a 'back rotation' of the sub-surface principal components around BD occurs, due to the distortion upon removal from the baseplate. This last finding would explain the similarity of the surface RS for H_0° and H_{45° after removal from the baseplate (Figure 5). The inherent distortion causes the geometry to influence the sub-surface principal direction. In consequence, the slight rotation, in conjunction with the strain plateau of $\pm 30^\circ$, results in similar determined RS values along the geometrical axes. This is emphasized by the negligible difference between the sub-surface deviatoric stress along T ($\sigma_T - \sigma_{BD} = 373 \pm 13 \text{ MPa}$) and the maximum principal components for H_{45° ($\sigma'_T - \sigma'_{BD} = 381 \pm 18 \text{ MPa}$) measured at point 2. In neutron diffraction measurements, the detectors typically average over a range of $\pm 15^\circ$ ($\pm 7.5^\circ$ from the diffraction vector). This average implies that any small difference between geometrical and stress axes would not influence the RS values.

On the other hand, one of the sub-surface principal stress axes always remains aligned with BD irrespective of the scanning strategy. In fact, the laser beam parameters dominate the RS distribution along BD, rather than the scanning strategy. This results in similar distortion along BD for different scanning strategies.

4.4. On the choice of the stress-free reference

A critical point of uncertainty for the determination of the bulk RS by neutron diffraction techniques may arise from inaccuracy of the stress (or strain)-free reference (Withers *et al.*, 2007). It has thus been proposed to utilize different methods to cross-check d_0^{hkl} values (Withers *et al.*, 2007). In fact, the cross-check between mechanically relaxed cubes and the application of theoretical boundary conditions such as the stress balance

yields a suitable sanity check for the measured d_o^{hkl} values. However, for the applicability of the stress balance method it must be ensured that no spatial variation of d_o^{hkl} exists within the cross-section of interest (Withers *et al.*, 2007). In the case of PBF-LB it has been shown that no large variations of d_o^{hkl} across the specimen occur (Serrano-Munoz *et al.*, 2022, Bayerlein *et al.*, 2018); at least when significant heat concentrations are avoided (Capek *et al.*, 2022). This fact is also observed for the specimens being subject of this work (Figure 9). The d_o^{311} calculated from the application of the stress balance condition to bulk data are listed in Table 2. The use of the stress balance-based d_o^{311} (instead of the one based on measurements of the coupons) would shift the calculated stress by about 70 MPa for H_0° and 30 MPa and H_{45° . This may be since the surface RS were not included in the stress balance. In fact, if the surface RS (accounting for the surface roughness) is not included in the stress balance, a deviation between experimentally measured and theoretical d_o^{311} occurs (Serrano-Munoz *et al.*, 2022). The use of the post-removal RS values of the relaxed surface (Figure 5) should shift the stress balance-based d_o^{311} to smaller values. Although no spatial gradient of the experimentally determined d_o^{311} exists, a directional dependence is evident (Figure 9). Such directional dependence has been reported by other researchers for PBF-LB/M/IN718 (Bayerlein *et al.*, 2018, Thiede *et al.*, 2018) and PBF-LB/M/316L (Ulbricht *et al.*, 2020). This direction dependence might arise from possible retention of macroscopic (if the gauge volume is not fully immersed in the cuboid), or intergranular stress (Withers *et al.*, 2007). As we lack evidence of the cause of this directional dependence, we considered the global average of all d_o^{311} as an appropriate value. Yet, the fact that the gauge volume was close to full immersion implies the containment of intergranular rather than macro stress. If one accounts for the directional dependence of d_o^{311} (Figure 9a), the RS values would shift in H_0 but not in H_{45° (the directional variation is much smaller, see Appendix A). Finally, the similarity between the XRD-based (where no precise d_o^{311} is required) and neutron diffraction-based RS strongly indicates that the direction independent d_o^{311} of the L component (being alike the overall average) is appropriate in this special case.

Table 2: Comparison of measured and calculated (boundary condition of BD, T) d_o^{311} values of the L component of the specimens H_0° and H_{45° .

KOWARI	H_0°	H_{45°
d_o^{311} measured /Å	1.08089 $\pm 3 \times 10^{-5}$	1.08068 $\pm 4 \times 10^{-5}$
d_o^{311} calculated /Å	1.08074	1.08061
$\Delta\varepsilon^{311}$ / $\mu\varepsilon$	-136	-62
$\Delta\sigma^{311}$ /MPa	-71	-32

4.5. Through thickness stress distribution

A critical point of the stress profile within PBF-LB manufactured alloys is their distribution close to the surface. Overall, the initial increase of the RS magnitudes can be linked to the surface roughness of the parts, since the roughness contributes to a stress relaxation in the vicinity of the surface (Serrano-Munoz *et al.*, 2022). In fact, the mean roughness of PBF-LB specimens manufactured without a contouring parameter set is reported to be in the range of 10-25 μm (Fritsch *et al.*, 2022, Mishurova *et al.*, 2019, Sprengel *et al.*, 2022). It is further known that high tensile stresses are usually present in the sub-surface region (Bayerlein *et al.*, 2018, Serrano-Munoz *et al.*, 2022, Serrano-Munoz, Fritsch, *et al.*, 2021, Serrano-Munoz, Ulbricht, *et al.*, 2021, Busi *et al.*, 2021). The layer removal + XRD experiments we performed revealed a sub-surface stress plateau rather than a peak stress. Interestingly, such behavior has been also found by Serrano-Munoz (Serrano-Munoz *et al.*, 2022) using neutron diffraction. Therefore, additional sample preparation (e.g., electro polishing) or use of high energy X-ray diffraction techniques is recommended to overcome such surface roughness effects (Mishurova *et al.*, 2019).

Figure 13 shows the through-thickness stress profiles for the BD and L components of the specimens H_0° and H_{45° , combining surface XRD (layer removal) and bulk ND data. The full profiles are drawn assuming symmetry of the surface and sub-surface RS with respect to the sample center point. It becomes apparent, that a strong RS gradient must be present at depths 0.7-2.75 mm. In this context, Serrano-Munoz *et al.* (Serrano-Munoz *et al.*, 2022) recently showed that such plateau decreased at 1.4 mm depth from the lateral surfaces in a $20 \times 20 \text{ mm}^2$ cross-section prism produced with a 67° -rotation scan strategy. However, in (Serrano-Munoz *et al.*, 2022) the plateau displayed higher RS compared to our study. First and foremost, the build-up of RS in PBF-LB/M/IN718 is known to depend on the build height (much larger for (Serrano-Munoz *et al.*, 2022) than in the present study): the addition of new layers produces tensile stress in the material directly below (Bayerlein *et al.*, 2018). In fact, Pant *et al.* (Pant *et al.*, 2020) reported that the magnitude of RS depends on the build orientation of L-shaped specimens produced with a 13° interlayer rotation. While the horizontally built specimen (10 mm build height) showed the lowest magnitudes of residual stress, the largest magnitudes were found for the vertical build orientation (build height 55 mm). Secondly, the use of up-skin (also referred as contouring) processing is known to cause higher RS magnitudes in Ti6Al4V (Artzt *et al.*, 2020). While the rotation scanning strategy used in (Serrano-Munoz, Ulbricht, *et al.*, 2021) would lead to lower RS values compared to other scanning strategies, the effect of the contour and by the addition of layers prevails in the present case. Interestingly, the RS profiles observed by Pant *et al.* (Pant *et al.*, 2020) show a similar distribution in their horizontally built specimen: tensile stress is present at the side surfaces along BD, while it is observed along the short direction at the top surface of the structure. It should be emphasized that the RS values reported by Pant *et al.* are not metrologically comparable to our study, because the diffraction elastic constants were calculated using the Kröner model.

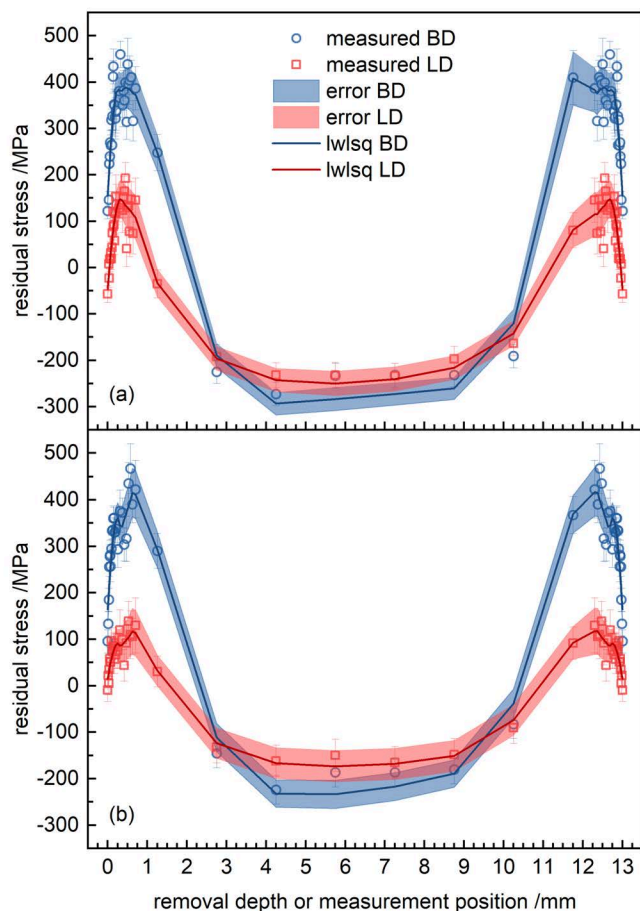


Figure 13: Through-thickness stress profiles of the specimen H_{0° (a) and H_{45° (b) of the uncorrected layer removal data combined with neutron diffraction assuming symmetry of the layer removal depth profiles.

5. Conclusions

This work discusses the texture-based determination of residual stress in as-built laser powder bed fused Inconel 718 prisms. Different crystallographic textures were obtained by employing different scanning strategies. The scan vectors aligned with the specimen geometrical axes, resulted in $\langle 100 \rangle$ in plane texture. In contrast, the ones rotated by 45° to such axes, while maintaining the 90° interlayer rotation, resulted in $\langle 111 \rangle / \langle 110 \rangle$ in plane texture. Residual stress determination was performed utilizing laboratory X-ray diffraction methods employing stress factors to account for the specimen texture. Additional laboratory X-ray (layer removal) and neutron diffraction measurements provided further insight into the residual stress distribution after removal from the baseplate. Furthermore, sub-surface principal stress was assessed by energy-dispersive synchrotron diffraction. The consequences of the presence of crystallographic texture on the residual stress determination were studied for both surface and bulk related measurements.

The following conclusions can be drawn:

- In the condition used in this study (texture indices smaller than 3), the preferred grain orientation (i.e. the crystallographic texture) has a negligible influence on the

determined residual stress values. It is identified that the high multiplicity of the 311 reflection, its propensity to exhibit mild texture intensities when compared to other reflections (e.g. 200), and its quasi-isotropic elastic behavior result in such behavior.

- Significant redistribution and relaxation of the residual stress (both bulk and surface) occurs after the removal from the baseplate. Prior to removal, the longitudinal residual stress is the highest if scan vectors are aligned with the sample geometrical axes, but longitudinal and transverse stress components become similar when the scan vectors are rotated by 45° . After removal, the residual stress redistributes in such a way, that the longitudinal stress relaxes, and a bending moment is induced in the specimens. On the other hand, the transversal component barely shows any signs of relaxation or redistribution.
- Post-removal synchrotron X-ray diffraction measurements in the plane perpendicular to the build direction revealed an alignment of the sub-surface stress tensor's principal axes with the geometrical axes if the scan vectors are aligned with such. In contrast, the sub-surface stress tensor's principal axes rotate around the building direction when the scan vectors are aligned by 45° to the geometry. This rotation seems to be influenced the residual stress redistribution upon removal from the baseplate. Furthermore, the sub-surface strain does not vary as a function of angle around the principal axes; therefore, determining bulk residual stress using measurements along the geometrical axes does not induce large errors.
- The combination of laboratory X-ray and neutron diffraction allowed further insight in the residual stress formation and spatial distribution: irrespective of the scanning strategy, similar residual stress distributions after removal from the baseplate were found. By combination of X-ray electrolytic layer removal and neutron diffraction data, the through thickness stress profile was successfully determined, revealing a sub-surface tensile plateau balanced by compressive stress in the bulk.

Acknowledgements

The authors want to express their gratitude to Gunther Mohr (BAM) for specimen production. In addition, we want to thank Romeo Saliwan-Neumann (BAM) and Benjamin Piesker (BAM) for their help in preparation and conduction of electron backscatter analysis. Furthermore, Alexander Ulbricht (BAM) is acknowledged for the provision and help with the stress balance script. We must also thank Thomas Gnäupel-Herold (NIST) for the personal support in working with ISODEC. For the provision of neutron beamtime at the instrument KOWARI we acknowledge the Australian Nuclear Science and Technology Organisation. The Paul Scherrer Institut is acknowledged for provision of neutron beamtime at the POLDI beamline under the proposal number 20211090. JC gratefully acknowledges financial support from the Strategic Focus Area Advanced Manufacturing (SFA-AM) initiative of the ETH Board. Finally, the Deutsches Elektronen-Synchrotron DESY is

acknowledged for the provision of beamtime at the white beam engineering materials beamline P61A under the proposal number 20200890.

Author contributions

The conceptualization was done by JS. VL prepared and performed the neutron diffraction measurements with the associated data curation at ANSTO. JS and AK performed the laboratory XRD measurements. JS, AE, EP, JC performed the neutron diffraction experiments at POLDI. JS, AE, GAF, SD, GD performed the energy dispersive synchrotron diffraction measurements. JS evaluated, interpreted, and visualized the data. The main manuscript was written by JS, while all reviewed the manuscript. Project administration was done by GB and AE.

Data availability statement

The data sets generated and/or analyzed during the current study are available from the corresponding author on reasonable request.

Appendix A

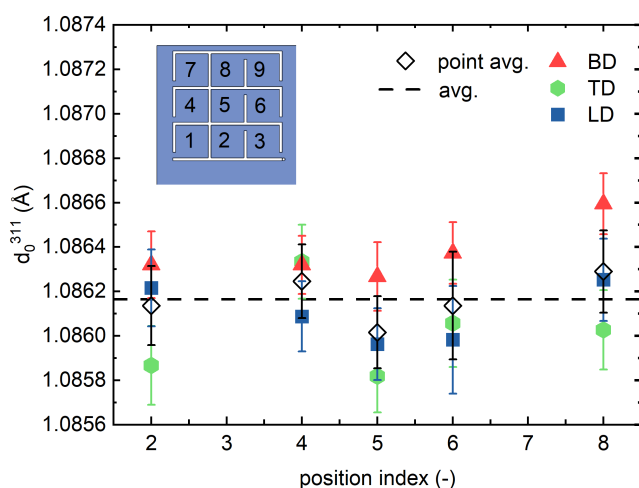


Figure 14: d_0^{311} measurements performed in the d0-Grid of specimen H45° according to the coordinate system in Figure 2e at the POLDI beamline

6. References

- Ali, H., Ghadbeigi, H. & Mumtaz, K. (2018). *Mat Sci Eng A-Struct* **712**, 175-187.
- Arnold, O., Bilheux, J. C., Borreguero, J. M., Buts, A., Campbell, S. I., Chapon, L., Doucet, M., Draper, N., Leal, R. F., Gigg, M. A., Lynch, V. E., Markvardsen, A., Mikkelsen, D. J., Mikkelsen, R. L., Miller, R., Palmen, K., Parker, P., Passos, G., Perring, T. G., Peterson, P. F., Ren, S., Reuter, M. A., Savici, A. T., Taylor, J. W., Taylor, R. J., Tolchenoy, R., Zhou, W. & Zikovsky, J. (2014). *Nucl Instrum Meth A* **764**, 156-166.
- Artzt, K., Mishurova, T., Bauer, P. P., Gussone, J., Barriobero-Vila, P., Evsevlev, S., Bruno, G., Requena, G. & Haubrich, J. (2020). *Materials* **13**.

- Attaran, M. (2017). *Bus Horizons* **60**, 677-688.
- Bachmann, F., Hielscher, R. & Schaeben, H. (2011). *Ultramicroscopy* **111**, 1720-1733.
- Bayerlein, F., Bodensteiner, F., Zeller, C., Hofmann, M. & Zaeh, M. F. (2018). *Addit. Manuf.* **24**, 587-594.
- Behnken, H. & Hauk, V. (1991). *Z Metallkd* **82**, 151-158.
- Bragg, W. H. & Bragg, W. L. (1913). *P R Soc Lond a-Conta* **88**, 428-438.
- Busi, M., Kalentics, N., Morgano, M., Griffiths, S., Tremsin, A. S., Shinohara, T., Loge, R., Leinenbach, C. & Strobl, M. (2021). *Addit Manuf* **39**.
- Capek, J., Polatidis, E., Casati, N., Pederson, R., Lyphout, C. & Strobl, M. (2022). *Mater Design* **221**.
- Chalmers, B. (1964). *Principles of solidification*. New York: Wiley.
- Collier, J. P., Song, H. W., Phillips, J. C. & Tien, J. K. (1988). *Metall Trans A* **19**, 1657-1666.
- Cozar, R. & Pineau, A. (1973). *Metall Trans* **4**, 47-59.
- Dölle, H. & Hauk, V. (1978). *Z Metallkd* **69**, 410-417.
- Dölle, H. & Hauk, V. (1979). *Z Metallkd* **70**, 682-685.
- Eshelby, J. D. (1957). *Proc R Soc Lon Ser-A* **241**, 376-396.
- Eshelby, J. D. (1961). *Progress in Solid Mechanics II*, 88-140.
- Farla, R., Bhat, S., Sonntag, S., Chanyshev, A., Ma, S. L., Ishii, T., Liu, Z. D., Neri, A., Nishiyama, N., Faria, G. A., Wroblewski, T., Schulte-Schrepping, H., Drube, W., Seeck, O. & Katsura, T. (2022). *J Synchrotron Radiat* **29**, 409-423.
- Foster, S. J., Carver, K., Dinwiddie, R. B., List, F., Unocic, K. A., Chaudhary, A. & Babu, S. S. (2018). *Metall Trans* **49a**, 5775-5798.
- Fritsch, T., Farahbod-Sternahl, L., Serrano-Munoz, I., Leonard, F., Haberland, C. & Bruno, G. (2022). *Adv Eng Mater* **24**.
- Fritsch, T., Sprengel, M., Evans, A., Farahbod-Sternahl, L., Saliwan-Neumann, R., Hofmann, M. & Bruno, G. (2021). *J Appl Crystallogr* **54**, 228-236.
- Gnäupel-Herold, T. (2012). *J Appl Crystallogr* **45**, 573-574.
- Gnäupel-Herold, T., Creuziger, A. A. & Iadicola, M. (2012). *J Appl Crystallogr* **45**, 197-206.
- Gokcekaya, O., Ishimoto, T., Hibino, S., Yasutomi, J., Narushima, T. & Nakano, T. (2021). *Acta Materialia* **212**, 116876.
- Haldipur, P., Margetan, F. J. & Thompson, R. B. (2004). *Rev Prog Q* **23**, 1061-1068.
- Hauk, V. (1997). *Structural and Residual Stress Analysis by Nondestructive Methods*. Amsterdam: Elsevier Science.
- Hill, R. (1952). *P Phys Soc Lond A* **65**, 349-355.
- Kasperovich, G., Becker, R., Artzt, K., Barriobero-Vila, P., Requena, G. & Haubrich, J. (2021). *Mater Design* **207**.
- Kröner, E. (1958). *Z Phys* **151**, 504-518.

- Kruth, J. P., Deckers, J., Yasa, E. & Wauthle, R. (2012). *P / Mech Eng B-J Eng* **226**, 980-991.
- Kruth, J. P., Froyen, L., Van Vaerenbergh, J., Mercelis, P., Rombouts, M. & Lauwers, B. (2004). *J Mater Process Tech* **149**, 616-622.
- Levkulich, N. C., Semiatin, S. L., Gockel, J. E., Middendorf, J. R., DeWald, A. T. & Klingbeil, N. W. (2019). *Addit Manuf* **28**, 475-484.
- Lingenfelter, A. (1989). *Superalloy 718 Metallurgy and Applications*, pp. 673-683. The Minerals, Metals & Materials Society (TMS).
- Mainprice, D., Bachmann, F., Hielscher, R. & Schaeben, H. (2015). *Geol Soc Spec Publ* **409**, 251-271.
- Mercelis, P. & Kruth, J. P. (2006). *Rapid Prototyping J* **12**, 254-265.
- Mishurova, T., Artzt, K., Haubrich, J., Requena, G. & Bruno, G. (2019). *Metals-Basel* **9**.
- Mishurova, T., Bruno, G., Evsevlev, S. & Sevostianov, I. (2020). *J Appl Phys* **128**.
- Mishurova, T., Cabeza, S., Thiede, T., Nadammal, N., Kromm, A., Klaus, M., Genzel, C., Haberland, C. & Bruno, G. (2018). *Metall Trans* **49a**, 3038-3046.
- Mishurova, T., Serrano-Munoz, I., Fritsch, T., Ulbricht, A., Sprengel, M., Evans, A., Kromm, A., Madia, M. & Bruno, G. (2020). *Structural Integrity of Additive Manufactured Materials and Parts*, edited by N. Shamsaei & M. Seifi, pp. 122-138. West Conshohocken: ASTM International.
- Moore, M. G. & Evans, W. P. (1958). *SAE Transactions* **66**, 340-345.
- Nadammal, N., Mishurova, T., Fritsch, T., Serrano-Munoz, I., Kromm, A., Haberland, C., Portella, P. D. & Bruno, G. (2021). *Addit Manuf* **38**.
- Ortner, B. (2009). *Powder Diffr* **24**, S16-S21.
- Ortner, B. (2011). *Mater Sci Forum* **681**, 7-12.
- Ortner, B. (2014). *Adv Mater Res-Switz* **996**, 215-220.
- Pant, P., Proper, S., Luzin, V., Sjostrom, S., Simonsson, K., Moverare, J., Hosseini, S., Pacheco, V. & Peng, R. L. (2020). *Addit Manuf* **36**.
- Reuss, A. (1929). *Z Angew Math Mech* **9**, 49-58.
- Schröder, J., Evans, A., Mishurova, T., Ulbricht, A., Sprengel, M., Serrano-Munoz, I., Fritsch, T., Kromm, A., Kannengießner, T. & Bruno, G. (2021). *Metals-Basel* **11**.
- Schröder, J., Evans, A., Polatidis, E., Mohr, G., Serrano-Munoz, I., Bruno, G. & Čapek, J. (2022). *J Mater Sci* **57**, 15036-15058.
- Schröder, J., Mishurova, T., Fritsch, T., Serrano-Munoz, I., Evans, A., Sprengel, M., Klaus, M., Genzel, C., Schneider, J. & Bruno, G. (2021). *Mat Sci Eng a-Struct* **805**.
- Seabold, S. & Perktold, J. (2010). In 9th Python in Science Conference.
- Serrano-Munoz, I., Evans, A., Mishurova, T., Sprengel, M., Pirling, T., Kromm, A. & Bruno, G. (2022). *Adv Eng Mater* **24**.
- Serrano-Munoz, I., Fritsch, T., Mishurova, T., Trofimov, A., Apel, D., Ulbricht, A., Kromm, A., Hesse, R., Evans, A. & Bruno, G. (2021). *J Mater Sci* **56**, 5845-5867.
- Serrano-Munoz, I., Ulbricht, A., Fritsch, T., Mishurova, T., Kromm, A., Hofmann, M., Wimpory, R. C., Evans, A. & Bruno, G. (2021). *Adv Eng Mater* **23**.
- Spieß, L., Teichert, G., Schwarzer, R., Behnken, H. & Genzel, C. (2009). *Moderne Röntgenbeugung*, 2 ed. Wiesbaden, Germany: Vieweg+Teubner Verlag.
- Sprengel, M., Mohr, G., Altenburg, S. J., Evans, A., Serrano-Munoz, I., Kromm, A., Pirling, T., Bruno, G. & Kannengießner, T. (2022). *Adv Eng Mater* **24**.
- Stuhr, U. (2005). *Nucl Instrum Meth A* **545**, 319-329.
- Stuhr, U., Grosse, M. & Wagner, W. (2006). *Mat Sci Eng a-Struct* **437**, 134-138.
- Stuhr, U., Spitzer, H., Egger, J., Hofer, A., Rasmussen, P., Graf, D., Bollhalder, A., Schild, M., Bauer, G. & Wagner, W. (2005). *Nucl Instrum Meth A* **545**, 330-338.
- Thiede, T., Cabeza, S., Mishurova, T., Nadammal, N., Kromm, A., Bode, J., Haberland, C. & Bruno, G. (2018). *Mater Perform Charac* **7**, 717-735.
- Ulbricht, A., Altenburg, S. J., Sprengel, M., Sommer, K., Mohr, G., Fritsch, T., Mishurova, T., Serrano-Munoz, I., Evans, A., Hofmann, M. & Bruno, G. (2020). *Metals-Basel* **10**.
- Vanhoutte, P. & Debuyser, L. (1993). *Acta Metall Mater* **41**, 323-336.
- Voigt, W. (1889). *Ann. Phys. (Berlin, Ger.)* **274**, 573-587.
- Volpato, G. M., Tetzlaff, U. & Fredel, M. C. (2022). *Addit Manuf* **55**.
- Wang, Z. Q., Stoica, A. D., Ma, D. & Beese, A. M. (2016). *Mat Sci Eng a-Struct* **674**, 406-412.
- Withers, P. J., Preuss, M., Steuwer, A. & Pang, J. W. L. (2007). *J Appl Crystallogr* **40**, 891-904.
- Yadroitsev, I. & Yadroitsava, I. (2015). *Virtual Phys Prototy* **10**, 67-76.
- Zhong, Q., Wei, K. W., Lu, Z., Yue, X. Z., Ouyang, T. Y. & Zeng, X. Y. (2023). *J Mater Process Tech* **311**.

Supplementary Information

Texture-based residual stress analysis of laser powder bed fused Inconel 718 parts

Jakob Schröder^{1*}, Alexander Evans^{1*}, Vladimir Luzin², Guilherme Abreu Faria³, Sebastian Degener³, Efthymios Polatidis⁴, Jan Čapek⁴, Arne Kromm¹, Gleb Dovzhenko³, and Giovanni Bruno^{1,5}

¹Bundesanstalt für Materialforschung und -prüfung, Unter den Eichen 87, 12205 Berlin, Germany

²Australia Nuclear Science and Technology Organisation, New Illawara Rd, Lucas Heights, NSW 2234, Australia

³Helmholtz-Zentrum Hereon, Max-Planck-Str. 1, 21502, Geesthacht, Germany

⁴Laboratory for Neutron Scattering and Imaging, Paul Scherrer Institut, Forschungsstrasse 111, 5232 Villigen, Switzerland

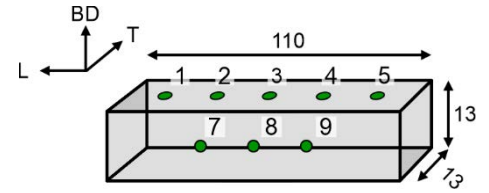
⁵Universität Potsdam, Institut für Physik und Astronomie, Karl-Liebknecht-Str. 24-25, 14476, Potsdam, Germany

*Corresponding Authors: Jakob.Schroeder@bam.de, Alexander Evans@bam.de

Table S1: Overview of the measurement conditions for the different diffraction techniques.

Technique	radiation	reflection Diffraction angle	ψ/χ - tilting (steps)	ϕ -tilting (steps)	assumptions
Laboratory XRD Xstress G3	Monochromatic, $Mn\kappa_\alpha$	Ni-311 $2\theta \approx 156^\circ$	-45° to 45° (19)	$0^\circ, 90^\circ$	Top: $\sigma_{i3} = 0$ $\sigma_{12} = 0$ Side: $\sigma_{i1} = 0$ $\sigma_{23} = 0$
Synchrotron XRD P61A	Energy dispersive, 30 - 200 keV	Ni - 311 $E \approx 55$ keV $2\theta \approx 11.946^\circ$	0 to 80° (20)	0 - 360° 3, 7, 8, 9 (5°) 1, 2, 4, 5 (15°)	-
Neutron diffraction POLDI	Time of flight, $Q \approx 1-8$ $2\pi d^{-1}$	$2\theta \approx 90^\circ \pm$ 15°	2 orthogonal directions (BD, T)		-
Neutron diffraction KOWARI	Monochromatic, $\lambda = 1.53$ Å	Ni-311 $2\theta \approx 90^\circ$	3 orthogonal directions (BD, T, L)		

Table S2: Obtained eigenvalues for the top surfaces of the specimen H_{0° and H_{45° according to the measurement positions 1-9 acquired by energy dispersive synchrotron diffraction.



H_{45°	#d ³¹¹	$\sigma'_T - \sigma'_{BD}$ /MPa	$\sigma'_L - \sigma'_{BD}$ /MPa	φ_p /°	H_{0°	#d ³¹¹	$\sigma'_T - \sigma'_{BD}$ /MPa	$\sigma'_L - \sigma'_{BD}$ /MPa	φ_p /°
1	381	414 ± 18	265 ± 18	21.9 ± 3.6	1	384	392 ± 20	300 ± 20	8.3 ± 7
2	382	381 ± 18	46 ± 17	8.8 ± 1.1	2	384	393 ± 19	172 ± 19	-1.0 ± 0.8
3	1863	255 ± 8	57 ± 8	18.5 ± 1.1	3	1833	384 ± 9	178 ± 9	0 ± 0.6
4	382	367 ± 17	92 ± 17	12.3 ± 1.4	4	384	383 ± 18	154 ± 17	4.2 ± 1.4
5	377	387 ± 19	209 ± 19	17.6 ± 2.8	5	383	371 ± 18	256 ± 17	7.5 ± 3.3
H_{45°	#d ³¹¹	$\sigma'_{BD} - \sigma'_T$ /MPa	$\sigma'_L - \sigma'_T$ /MPa	φ_p /°	H_{0°	#d ³¹¹	$\sigma'_{BD} - \sigma'_T$ /MPa	$\sigma'_L - \sigma'_T$ /MPa	φ_p /°
7	1511	265 ± 9	12 ± 7	-0.5 ± 0.7	7	1512	391 ± 10	96 ± 9	-1.3 ± 0.5
8	1512	257 ± 9	17 ± 7	-2.4 ± 0.6	8	-	-	-	-
9	1512	278 ± 8	10 ± 4	-2.0 ± 0.6	9	1512	399 ± 10	61 ± 8	-4.2 ± 0.5

IV Discussion

1 Deformation Behavior

The room temperature deformation behavior of both, heat-treated (see **P2**) and as-built (see **P3**) PBF-LB/M/IN718, has been studied within this work. The following section compares their behavior at both the macroscopic and microscopic scale.

1.1 Macroscopic Behavior

A comparison of the heat-treated and as-built macroscopic behavior is shown in Figure 8a. In this figure, the tested material reported in **P2** (i.e. FHT, DA) are compared to their as-built counterpart (specimen 554) [49]. In addition, the tensile data of the similarly manufactured as-built specimen V_{0° of publication **P3** is shown. In general, agreement between both as-built specimens is observed, although they were built on two different PBF-LB machines (**P2**: Concept Laser M2, **P3**: SLM 280). However, the two as-built specimens experience differences in their elongation to failure: specimen 554 $\approx 33 \pm 1 \%$ [49], specimen $V_{0^\circ} \approx 37 \pm 2 \%$ [50]. Such difference is likely attributed to the defect population. As reported in **P3** supplementary information, specimen V_{0° is nearly fully dense, with a porosity of only 0.002 vol.% (measured by means of X-ray computed tomography). In contrast, the as-built specimen 554 is reported to have a higher porosity of $\approx 0.2 \%$ (as determined by optical microscopy) [51].

To recall, direct aging (DA) and full heat treatment (FHT) routines were performed to establish different microstructures with two different contents of the strengthening phases γ'' and γ' :

FHT ($^\circ\text{C}/\text{h}/\text{MPa}$): 1066/1.5 + 1150/3/105 + 954/1 + 720/8 + 620/10

DA ($^\circ\text{C}/\text{h}$): 1066/1.5 + 720/8

With the introduction of precipitation phases, the strength significantly increases compared to the as-built variant. Simultaneously the elongation to failure decreases. A comprehensive discussion on the differences of the macroscopic mechanical behavior between FHT and DA is available within **P2**.

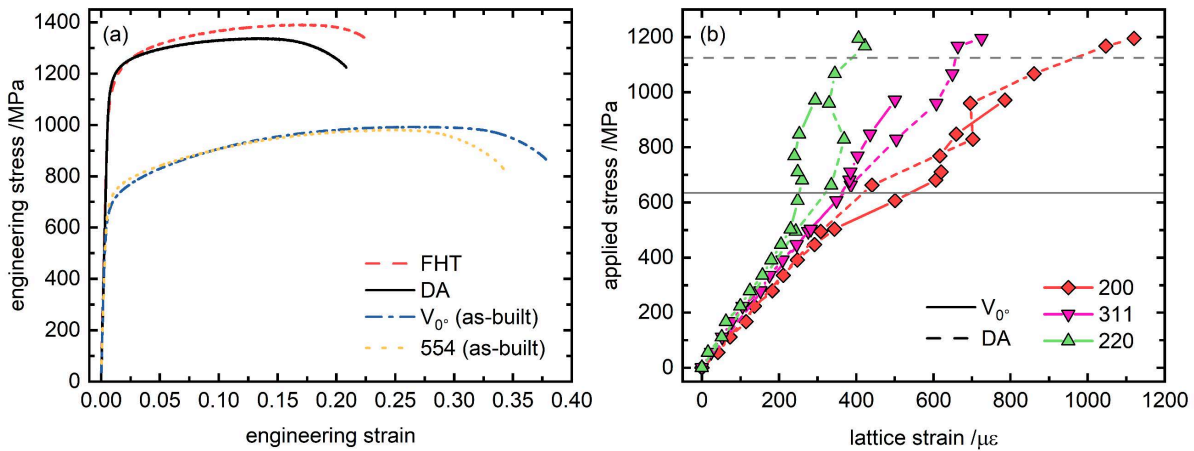


Figure 8: The macroscopic tensile behavior of specimens FHT and DA (**P2**) with its as-built variant 554 [49], compared to the as-built vertical specimen V_{0° (**P3**) (a). The lattice response of $\{200\}$, $\{311\}$, and $\{220\}$ lattice planes to a macroscopic load of DA (**P2**) and V_{0° (**P3**). The solid horizontal line in (b) depicts the macroscopic yield strength of specimen V_{0° , while the horizontal dashed line represents the macroscopic yield strength of the specimen DA.

IV Discussion

1.2 Microscopic Behavior

Figure 8b shows a comparison of the micromechanical response of $\{200\}$, $\{311\}$, and $\{220\}$ lattice planes to macroscopic load of DA (**P2**) and V_{0° (**P3**). It must be noted that the tests have been conducted on two different beamlines using two different techniques and different specimen geometries:

- Specimen DA (**P2**): EDDI beamline, energy dispersive synchrotron diffraction
 $3 \times 3 \text{ mm}^2$ flat tensile specimen, heat-treated
- Specimen V_{0° (**P3**): POLDI beamline, time-of-flight neutron diffraction
6 mm cylindrical tensile specimen, as-built

Although strengthening phases have been introduced in DA (i.e. V_{0° does not contain γ' or γ''), the overall micromechanical response is alike: upon application of external load the $\{220\}$ lattice plane transfers load to $\{200\}$ in both cases after the onset of macroscopic plastic deformation. However, dictated by the macroscopic yield strength, such behavior occurs at larger applied stresses in DA when compared to V_{0° . Throughout the deformation cycle, the $\{311\}$ grains behave linearly in both specimens. Even further, in **P3** it has been shown for V_{0° that the $\{311\}$ has the lowest propensity to accommodate intergranular strain upon plastic deformation.

The lattice plane behavior indicates that load is shed to a different phase upon tensile deformation. The indication is born from the fact that lattice planes cease to accumulate elastic lattice strain at a specific applied stress in both DA and V_{0° (Figure 8b). Within **P3** such behavior has been hypothesized to originate from the presence of the cellular solidification sub-structures of the as-built V_{0° specimen: The cell walls, characterized by Nb segregation and dislocation entanglement, appear to accommodate lattice strain. For the as-built specimen condition V_{0° such behavior becomes apparent straight after the macroscopic 0.2 % yield strength is reached. Thus, the mechanism is explained to originate from the motion of dislocations from the cell interior to the cell wall.

In contrast, in **P2** it is reported that such behavior is appearing in specimen DA before the macroscopic 0.2 % yield strength is reached. In fact, the stress relieving heat treatment removed the local chemical segregation of Nb, while maintaining the columnar grain structure and, at least partly, the dislocation arrangement. According to the literature, the subsequent aging heat treatment precipitated finely dispersed high strength intermetallic γ'' and γ' precipitates. Therefore, it is hypothesized that load transfer associated to the incoherency of γ to γ'' and γ' appears before reaching the macroscopic 0.2 % yield strength [52]. Furthermore, strain partitioning arises from shearing the γ'' precipitates during plastic deformation [53]. Such behavior is pronounced for the 200 reflection as the γ'' platelets are orientated parallel to the $\{100\}$ planes of the γ crystal [18]. Sangid et al. [52] reported similar results while studying the load sharing mechanisms between γ matrix and γ'' precipitates in fully heat-treated PBF-LB/M/IN718 specimens using *in situ* high energy X-ray diffraction. Akin to specimen FHT, the high-temperature heat treatment in Sangid et al. [52] led to recrystallization and grain growth.

These findings outline the importance of the specimen microstructure for the micro-mechanical responses at the onset of plasticity. In particular, the cellular solidification sub-structures in as-built PBF-LB/M/IN718 result in unique elastic and plastic anisotropies once subjected to external load.

IV Discussion

Further, **P3** indicates that such response is even direction dependent and appears to be connected to the orientation of the cells with respect to the load axis. Using different heat treatments, deformation mechanisms significantly change, as strengthening precipitates are introduced.

2 Towards a Reliable Assessment of Residual Stress

2.1 Selection of a Suitable Lattice Plane

From the results of the literature review in **P1** it becomes apparent that for FCC materials the $\{311\}$ lattice planes are the common choice of the lattice plane for RS analysis. However, the propensity of lattice planes $\{hkl\}$ towards the accumulation of intergranular strain (i.e. type II) in presence of crystallographic texture remains unanswered for PBF-LB/M/IN718.

This aspect has been fully elucidated in **P3**. It was concluded that, selecting an appropriate lattice plane in case of monochromatic radiation becomes a “least bad” rather than a “best” selection [46]. Clausen et al. [46] have shown, by elastic/plastic self-consistent calculations of texture-free stainless steel, that the $\{311\}$ lattice planes lose their status as a particularly suited reflection. Instead, they recommend using the 422 and 111 reflections, since they seem to possess zero macroscopic RS. However, in textured material the use of the 111 reflection is hampered by its unavailability in all directions, as only eight equivalent $\{111\}$ lattice planes exist. In addition, our *in situ* experiments in **P3** have shown, that the $\{111\}$ lattice planes accommodate comparable intergranular strain as $\{311\}$. Further, in **M4** the insensitivity of the $\{311\}$ lattice planes towards the presence of crystallographic texture has been reported. This aspect aids the simplification of the determination of RS. Such insensitivity is mainly associated to their multiplicity of 24 within the fcc crystal. In fact, the $\{422\}$ lattice planes might be similarly suited, as the multiplicity is the same as for $\{311\}$. However, as high order reflection, the relative intensity of $\{422\}$ is lower compared to $\{311\}$. Yet, the linearity of the measured stress factors $F_{33ij}(0, \Psi, 422)$ as shown in **Appendix A** further supports the suitability of $\{422\}$ for the determination of type I RS in PBF-LB/M/IN718. In fact, the errors of the $\{422\}$ isotropic diffraction elastic constants s_1 and $1/2s_2$ are almost identical to these of $\{311\}$. This indicates agreement to an isotropic material behavior (see **Appendix A**).

Therefore, the $\{311\}$ lattice planes appear to be a robust selection for the assessment of RS in PBF-LB/M/IN718. However, if available with sufficient intensity, the $\{422\}$ lattice planes are equally suited, as they also appear insensitive towards the presence of crystallographic texture. In that regard, experiments akin to these reported in **P3**, performed using high energy monochromatic X-ray diffraction (see **Appendix A**) could facilitate an assessment of intergranular strain accumulation in $\{422\}$ grains. Given the use of 2D detectors, such experiments would yield the significant advantage of taking into account the Ψ dependence without the need of sample rotation. Beyond that, an additional rotation of φ (i.e. rotation around the load axis) allows the study of the accumulation of intergranular strain for several angles. This would provide greater knowledge on the propensity of reflections to accumulate intergranular strain upon plastic loading.

2.2 Stress-Free Reference

The variety of diffraction methods available for RS determination requires either the validity of the assumption of a biaxial stress state or knowledge of a representative stress-free reference. The latter presents a significant source of error, as errors in the stress-free reference directly translate to the magnitude of the RS [47]. Within **P1** the available methods to obtain a stress-free reference were

IV Discussion

comprehensively reviewed in regard to laser-based additive manufacturing techniques. Such methods include raw powder, mechanical filings, macroscopically relaxed samples, and stress and moment balance. Several advantages and disadvantages were identified. While the use of powder as a stress-free reference appears as a convenient and truly non-destructive solution, such approach rarely yields appropriate values; the feedstock powder does not represent the thermal history of the manufacturing process [54]. Mechanical filings on the other hand represent the thermal history of the material but are destructive and further plastically deformed. In that regard, mechanically relaxed samples yield the best compromise: Although their use suffers from the need of a sister specimen or destruction of the actual specimen, spatial variations of the stress-free reference within the specimen can be accounted for. However, this technique suffers from possible retention of type I or II stress and the necessity of a precise alignment [47]. The use of sister specimens in combination with a stress balance approach increases the confidence on the obtained stress-free reference results [47, 55]. For the heterogeneous microstructures of as-built PBF-LB a directional dependence of the stress-free reference is often found, which is indicative for the retention of type I or II stress.

Consequently, in **M4** stress-free references have been experimentally obtained from measurements of small cuboids. Such measurements were complemented by stress-free references obtained by a stress balance approach. In fact, the directional dependence of the stress-free reference value could be observed to be independent of the measured cuboid. Values obtained by stress balance deviate from experimental values, if one does not take into account near-surface stress [55].

2.3 Diffraction Elastic Constants

One of the key aspects in a reliable assessment of RS is to get an accurate measure of the diffraction elastic constants. Such constants connect lattice strain to macroscopic stress. As mentioned previously, diffraction elastic constants can either be directly measured for the material of interest or calculated from knowledge of the single-crystal elastic constants. The latter approach additionally requires a model of the grain interaction in the polycrystalline aggregate. In that regard, in **P1** the following challenges for a reliable assessment of the diffraction elastic constants were identified:

First, it remains unanswered whether single-crystal constants obtained for conventional materials are representative of the hierarchical structure of their additively manufactured counterpart.

Second, the selection of the assumed grain interaction for the calculation of the diffraction elastic constants from single-crystal elastic constants appears to be both material and grain structure dependent.

Third, literature on the experimental determination of the diffraction elastic constants of PBF-LB materials (e.g. Inconel 718) is still limited.

Fourth, the diffraction elastic constants are only independent of the measurement direction in the case of quasi-isotropic material behavior (i.e. low crystallographic texture) [26]. The validity of such assumption is questionable for the specific microstructure present in additively manufactured materials.

IV Discussion

Several experiments have been undertaken in this study to fill these gaps for PBF-LB/M/IN718. In **P2** it has been shown that the lattice plane specific elastic stiffnesses E^{hkl} tend to depend on the underlying microstructure of heat treated PBF-LB/M/IN718. It was found that for the recrystallized microstructure of specimen FHT, the Kröner model yields a reasonable approximation. In contrast, the columnar microstructure retained for the specimen DA yields a Reuss type behavior of the γ matrix instead. Such observation has been later confirmed in **P3** by means of *in situ* neutron diffraction measurements of as-built PBF-LB/M/IN718. In both cases, the model predictions were based on single-crystal elastic constants of the conventional material taken from literature. In that regard, the work shown in **Appendix A** refined a set of single-crystal elastic constants by inverse calculations based on experimental diffraction elastic constants. Figure 9a compares the experimentally obtained E^{hkl} to Reuss model predictions calculated from single-crystal elastic constants of the conventional material reported by Haldipur et al. [56] to those refined by inverse calculations using the Reuss model. In such representation it appears that conventional single-crystal elastic constants yield a good prediction of E^{hkl} for $3\Gamma < 0.75$, while the ones refined from experimental data for PBF-LB/M/IN718 provide a better agreement for $3\Gamma > 0.75$.

However, the single-crystal elastic constants as determined in **Appendix A**, evidently yield a much better Reuss model prediction of the experimental diffraction elastic constants (Figure 9b). In fact, the diffraction elastic constants are a combination of the elastic stiffness E^{hkl} and Poisson ratio ν^{hkl} (Figure 9b) and are thus more representative of the material behavior. Therefore, the Reuss model refined single-crystal elastic constants from **Appendix A** are considered to appropriately represent the PBF-LB/M/IN718 material behavior. In fact, in **Appendix A** the validity of an isotropic material behavior for lattice planes possessing high multiplicity (e.g. $\{311\}$, $\{422\}$) is outlined. Such observation is in line with the findings in **M4** as the use of isotropic diffraction elastic constants only results in insignificant changes of the RS obtained by using $\{311\}$. In essence, the impact on the resulting RS is much lower than the measurement error for high multiplicity (e.g. $\{311\}$) lattice planes. The lattice planes with lower multiplicity (e.g. $\{200\}$) represent an exception; the non-linearity of $F_{33ij}(0, \Psi, hkl)$ in dependence of $\cos^2\Psi$ is increasing (see **Appendix A**).

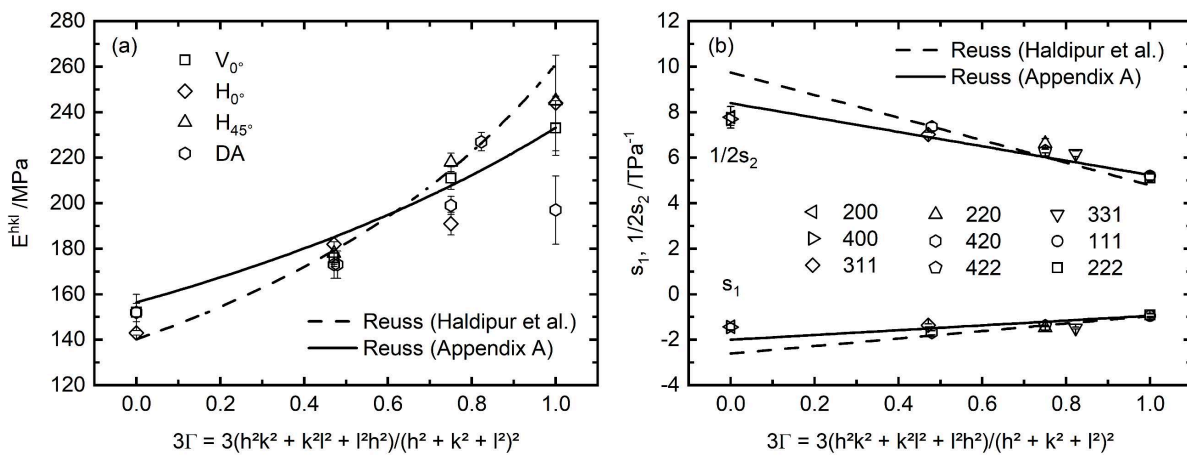


Figure 9: Lattice plane specific young's moduli E^{hkl} of DA (**P2**), V_{0° , H_{0° , H_{45° (**P3**), and Reuss model predictions (a). The experimental diffraction elastic constants s_1 and $1/2s_2$ (**Appendix A**) compared to Reuss model predictions (b). Reuss model calculations were performed using the single-crystal elastic constants from Haldipur et al. ($c_{11} = 242.3$ GPa, $c_{12} = 139.7$ GPa, and $c_{44} = 104.4$ GPa) [56] and those determined in **Appendix A**.

2.4 Unique Aspects of RS Distribution

In conventional processes (i.e. rolling, forging), one can safely assume that the principal stress axes coincide with the geometry ones. For additively manufactured specimens it has been shown that the largest stress direction is usually parallel to the scan vector of the final manufactured layer [57]. However, the scan vectors alternate among the layers with a typical rotation of 67° or 90° applied after each layer. Therefore, for surface related measurements the laser path of the last melted layer provides important information on the stress state. As far as bulk measurements are concerned, the situation complicates: the gauge volume contains multiple manufactured layers and thus a range of different thermal histories. The situation is further complicated by the superposition of the inherent part distortion upon removal from the baseplate. These factors have been analyzed in depth within **M4**. In fact, after the distortion following part removal from baseplate, the geometry dictates the distribution of surface principal stress rather than the scan strategy.

One aspect of the near surface RS distribution in PBF-LB parts is the inherent surface roughness introduced by the process. As discussed in **M4**, the surface roughness leads to an underestimation of the maximum surface RS. More specifically, partially molten powder particles attached at the surface may lead to erroneous results as they are disconnected and do not transmit long range RS [55, 58]. Therefore, the differences in surface roughness may limit the comparability of surface RS measurements among parts manufactured with or without contour parameters. In Figure 10, the obtained RS depth profiles from electrolytic layer removal paired with laboratory X-ray diffraction are overlapped to the atypical near surface microstructures. Such representation shows the increase of the sub-surface RS within the first $100\ \mu\text{m}$. This increase can be attributed to the surface roughness. In addition, equiaxed small grains can be identified at the lateral surface. The microstructure only shows the characteristic columnar grain morphology at depths $\approx 200\ \mu\text{m}$ from the lateral surfaces, at which point the stress plateau is formed. Thus, the surface and sub-surface RS distributions are directly linked to the surface roughness, microstructure, and texture.

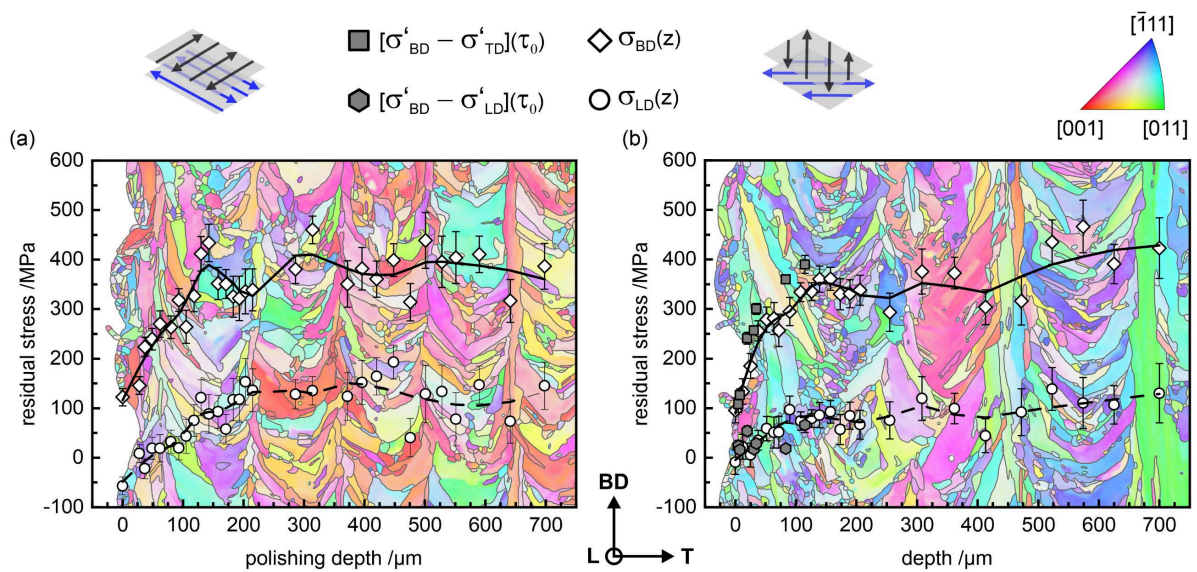


Figure 10: Texture dependent sub-surface RS distribution acquired by means of electrolytic layer removal using the 311 reflection (see **M4**) and energy dispersive synchrotron X-ray diffraction for two different scanning strategies: (a) scanning along the specimen geometry with 90° interlayer rotation, (b) scanning 45° to the specimen geometry with 90° interlayer rotation. The orientation maps acquired by electron backscatter diffraction viewed along L are additionally shown.

IV Discussion

It must be emphasized that when the maximum RS at the lateral surface is of interest, methods should be employed that characterize the sub-surface RS. For example, energy dispersive methods provide depth resolution in a purely non-destructive fashion. However, such methods suffer from the use of different reflections hkl for the determination of the RS profile. Therefore, an accurate measure of diffraction elastic constants is required for many reflections. In addition, the depth profiles obtained by the multi-wavelength method in reflection geometry are in Laplace space as the depth resolution originates from the exponential decay of the sample absorption [59]. Therefore, in theory such stress profiles need to be translated into real space by an inverse Laplace transformation; each depth related measurement in Laplace space covers a depth range [59]. In that regard, the differences between Laplace space and real space RS profiles are dependent on the RS gradient [59]. Therefore, for the relatively small surface stress gradients within PBF-LB/M/IN718 the Laplace and real space profiles become nearly equal (i.e., $\sigma(\tau) \approx \sigma(z)$). The validity of the latter assumption and of the diffraction elastic constants used in **M4** are proven by the agreement of $\sigma(\tau_0)$ and $\sigma(z)$ stress profiles (Figure 10b). It must be noted, that the $\sigma(\tau_0)$ stress profiles represent the deviatoric principal stress (stress tensor is aligned with the geometry at the lateral surfaces, see **M4**), as no precise stress-free reference was measured. However, the subtle deviation from the profile acquired by layer removal is indicative for a negligible out-of-plane stress up to $\approx 125 \mu\text{m}$ depth. In fact, Serrano-Munoz et al. [55] have shown by neutron diffraction measurements for a similar specimen geometry, that the out-of-plane stress component is nearly zero close to the lateral surfaces (0.4 mm from the surface).

V Summary & Outlook

1 Summary

The work presented in this thesis describes the microstructure, texture, and deformation behavior of the nickel-based superalloy Inconel 718 produced by laser powder bed fusion. In fact, the microstructure, the texture, and the lattice plane specific elastic properties of the material of interest are directly linked to the magnitude of the determined residual stress. Therefore, various *ex situ* and *in situ* material characterization techniques were employed to study the relationship between the microstructure, the texture, and the deformation behavior of laser powder bed fused Inconel 718 parts. Using this knowledge, a toolbox for a reliable assessment of residual stress by means of diffraction-based methods was realized.

The main findings of this work can be summarized as follows:

With regard to the *first aim* – Identification of challenges and gaps – **P1** provides a comprehensive overview of diffraction-based residual stress analysis in laser-based additive manufactured materials. In short, several inconsistencies and hindrances prevent a reliable diffraction-based assessment of residual stress. These include the definition of a stress-free reference, a set of diffraction elastic constants, an identification of the stress principal directions, and a suitable lattice plane. Overall, such challenges were identified to arise from the peculiar microstructure and crystallographic texture present in parts manufactured by means of laser-based additive manufacturing processes. More specifically, the localized melting and solidification cause columnar grain growth accompanied by a cellular solidification sub-structure characterized by local segregation. Therefore, the stress-free reference might become position and/or direction dependent under certain manufacturing conditions. In that regard, it is advised to determine the stress-free reference by measurements on mechanically relaxed samples to check for chemically imposed gradients; paired with the validation by imposing stress balance. Furthermore, the diffraction elastic constants depend on the underlying grain structure (i.e. columnar or equiaxed) and crystallographic texture. In particular, the validity of single-crystal elastic constants of conventional material for the model-based prediction of diffraction elastic constants of laser powder bed fused alloys remains an open question. Beyond that, knowledge of the alignment of the stress tensor with respect to the geometry prior to measurements are often not known for additively manufactured material. Therefore, it is advised to characterize the full stress tensor when the maximum magnitude of residual stress is of interest. Lastly, the selection of a single lattice plane representative of the bulk behavior remains a critical aspect for residual stress analysis using monochromatic instruments; more research is needed to understand the accumulation of intergranular strain for hierarchical structures present in laser powder bed fusion.

The *Second aim* – understanding of the deformation behavior – was addressed in **P2** and **P3**. *In situ* energy dispersive synchrotron X-ray and neutron diffraction techniques were employed to study the deformation behavior of both, heat treated and as-built laser powder bed fused Inconel 718. The elastic deformation behavior is mainly controlled by the underlying grain structure (i.e. columnar or equiaxed) and texture. On the one hand, the plastic behavior is controlled by load sharing mechanisms between the matrix and the intermetallic precipitates for the heat-treated specimens. On the other hand, such behavior is dictated by the underlying cellular solidification sub-structure in as-built material. In addition, the phenomenon appears direction dependent owing to the competitive cell growth during manufacturing. Beyond that, an anisotropy of the macro mechanical properties of as-built laser powder bed fused Inconel 718 was observed, which is

V Summary & Outlook

connected to differences in grain morphology and crystallographic texture. Furthermore, the elastic lattice strain responses were unaffected by the underlying texture apart from {220} grain family, which showed grain-to-grain interaction effects to related to neighboring {200} grains. Lastly, the load partitioning and accumulation of intergranular strain among various lattice planes of as-built Inconel 718 was studied for the differently textured specimens. It was found that the load partitioning mechanisms and the propensity of intergranular strain accumulation depend on the underlying crystallographic texture with respect to the applied load.

The *third aim* – study of the microstructure & texture – is inherently linked to all publications. While **P2** showed that different heat treatments result in significant changes in the microstructure and texture, the effect of build orientation and scanning strategy is reported in **P3**. In both cases, the link between microstructure and macro/micro mechanical properties yields interesting findings. If the columnar grain morphology and texture is retained after heat treatment, the iso stress assumption of Reuss represents the elastic anisotropy. In addition, such observation is demonstrated for as-built material. Furthermore, a range of different crystallographic textures resulted in insignificant changes of the elastic anisotropy. Beyond that, in **Appendix A** the diffraction elastic constants are experimentally determined, and the single-crystal elastic constants are refined from inverse calculations. Such calculations confirm the validity of the iso-stress assumption for the polycrystalline microstructure of laser powder bed fused Inconel 718 for the use of single-crystal elastic constants of conventional material. In contrast, the equiaxed microstructure, formed by recrystallization during hot isostatic pressing, led to a better description of the polycrystal by the Kröner model. The influence of the hierarchical microstructures on the stress-free reference was addressed within **M4**. No clear positional variation of the stress-free reference across the cross-section could be observed, irrespective of the scanning strategy. However, a directional dependence indicated the retention of macro stress or the presence of type II intergranular stress within the cuboids.

M4 tackles the *fourth aim* – a reliable assessment of residual stress. This was achieved by studying the residual stress within laser powder bed fused Inconel 718 by means of various diffraction-based techniques. In a texture-based approach, surface, sub-surface and bulk residual stress was determined. It was found, that for the determination of residual stress using the 311 reflection, the crystallographic textures present in the specimens were insignificant thanks to the high multiplicity of the 311 reflection and its quasi-isotropic behavior. Significant residual stress relaxation and redistribution occurred due to part distortion upon removal from the baseplate. Post removal, only a small dependence of the principal stress direction on the scanning strategy was found. Furthermore, the inherent surface roughness results in an underestimation of maximum surface residual stress. When combining depth profiles obtained by means of laboratory X-ray diffraction with incremental layer removal and by neutron diffraction, further insight into the residual stress distribution was gained. Irrespective of the scanning strategy, similar residual stress distributions from the lateral surfaces were found after part removal from the baseplate, revealing a sub-surface tensile plateau balanced by compressive bulk stress.

V Summary & Outlook

2 Outlook

The overarching aims were systematically addressed throughout this thesis. A toolbox for a reliable diffraction-based assessment of residual stress in laser powder bed fused Inconel 718 was developed. Such a toolbox was tested for various diffraction-based techniques to characterize residual stress within laser powder bed fused Inconel 718, where comparable values were obtained. However, due to the wide range of both, manufacturing techniques and alloys available, further research is needed to extend such knowledge.

First, this case study was limited to laser powder bed fused Inconel 718. Extrapolation to other nickel-based alloys produced by laser powder bed fusion would provide a general validation of the results of this thesis. In addition, it is known that the variety of additive manufacturing techniques results in significant differences in microstructure and texture formation during manufacturing. Therefore, it would be necessary to extend the analysis of both the diffraction elastic constants and the stress-free reference to other additive manufacturing methods such as laser-based direct energy deposition, and wire arc additive manufacturing.

Second, the inherent cellular solidification sub-structure, which is caused by the micro-segregation of heavier elements (e.g., niobium) in laser powder bed fused Inconel 718, leads to a diffraction peak asymmetry. This observation is accompanied by dislocation entanglement at cell boundaries. In this context, conventional diffraction techniques cannot reliably separate the contributions from the cell interior and the cell boundary. In fact, synchrotron X-ray micro-diffraction techniques could help to further investigate the role of the interaction between the cell wall and the interior during loading.

Third, the accumulation of intergranular strains during loading is direction dependent. Therefore, its evaluation in three-dimensional space by performing *in situ* loading experiments attributes to the fundamental understanding of the deformation behavior of laser powder bed fused Inconel 718. In this regard, high energy monochromatic synchrotron or neutron diffraction using a 2D detector could facilitate their evaluation by acquiring full Debye-Scherrer rings. Multiple reflections and sample directions would be obtained without the need for sample rotation.

Fourth, the research should be extended to different alloys, since the microstructure and texture formation, as well as the elastic anisotropy, are characteristic for each alloy. In particular, materials with lower crystal symmetry (e.g., hexagonal) are prone to the formation of strong crystallographic textures. In such cases, the influence of crystallographic texture on the determination of residual stress may be more significant compared to cubic materials.

At last, the position dependent surface, sub-surface, and bulk principal stress tensor should be determined before and after removal from the baseplate. Such a task should be performed for different scanning strategies, as they are strongly impact the principal stress tensor orientation. Knowledge of the principal axes prior to residual stress measurements can greatly reduce the experimental effort required to determine the maximum magnitude of residual stress.

Of course, the aspects mentioned here are just a taste of what could be done to further advance the fundamental understanding of the mechanical properties and performance of additively manufactured materials.

VI Appendix

A Determination of Single-Crystal Elastic Constants From Diffraction Experiments

J. SCHRÖDER¹, A. HELDMANN², M. HOFMANN², A. EVANS¹, G. BRUNO¹

¹Bundesanstalt für Materialforschung und -prüfung, Unter den Eichen 87, 12205 Berlin

²Heinz Maier-Leibnitz Zentrum (MLZ), Technische Universität München, 85478 Garching

³Universität Potsdam, Institut für Physik und Astronomie, Karl-Liebknecht-Straße 24-25, 14476 Potsdam

Important Information

This section in its current form shall describe the experimental details and highlight the results from *in situ* loading experiments performed at the HEMS beamline at PETRA III. However, the results shown here are part of a first analysis and are subjected to changes. It is planned to publish this section as a separate article.

Material

Subject of this study is a round tensile specimen (6 mm diameter, 30 mm gauge length) extracted from a vertically manufactured Inconel 718 prism (see Publication 3 [50]). Such specimen was extracted the $13 \times 13 \times 110 \text{ mm}^3$ prisms manufactured with standard set of laser beam parameters using an SLM 280. The alternating scanning vectors followed the geometry of the prisms with an interlayer rotation of 90° . The resulting microstructure and texture were determined by means of electron backscattered diffraction and are shown in Figure 12. In essence, columnar grains with a cube type-texture, characterized by dominant $\langle 100 \rangle$ crystal orientation ($\approx 5.3 \text{ m.r.d.}$), was found perpendicular to the build direction [50]. In contrast, along the build direction a less distinct $\langle 100 \rangle / \langle 110 \rangle$ texture of ($\approx 2.7 \text{ m.r.d.}$) was observed [50]. Further details on the specimen and data analysis can be found in Schröder et al. [50] (i.e. **P3**).

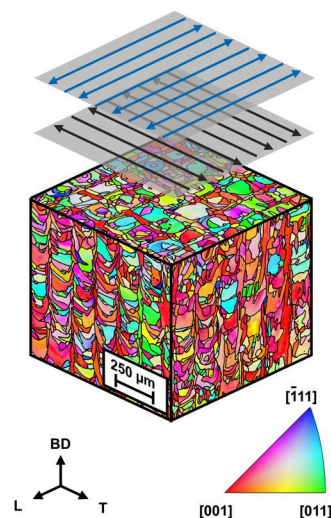


Figure 11: Orientation-maps acquired by electron backscatter diffraction. Viewing directions are out of plane for each image.

VI Appendix

In this previous article (see **P3**), the anisotropy of the lattice plane specific Young's moduli (E^{hkl}) was assessed for different texture components by *in situ* neutron diffraction. In that regard, the Reuss grain-interaction model based on single-crystal elastic constants of conventional Inconel 718 showed reasonable agreement to the experimental values.

Within this experiment the quasi-isotropic diffraction elastic constants s_1 and $1/2s_2$ were experimentally derived from the stress factors by *in situ* loading during high-energy X-ray synchrotron diffraction at the HEMS beamline at PETRA III [60]. Subsequently, the single-crystal elastic constants of the polycrystalline material were obtained by an inversion of the usual calculations applied in the residual stress analysis and fitting by a χ^2 -minimization technique [61].

Experimental Setup

A schematic view of the experimental setup is depicted in Figure 12. The rotary multifunctional uniaxial load frame designed at the research reactor FRM II in Munich (for details see [62]) was integrated in the beamline environment. An energy of 100 keV (corresponding to a wavelength of 0.124 Å) was used. Diffraction data were acquired under a continuous linear load increase from 2.2 kN (≈ 81 MPa) up to 8.45 kN (≈ 299 MPa) using a Perkin Elmer XRD 1621 flat Panel detector. Since full Debye-Scherrer diffraction rings were recorded, no load rig rotation was necessary to obtain the Ψ dependence of the lattice strain. In addition, the φ angle (i.e., rotation around the load axis of the specimen) was kept during the experiment.

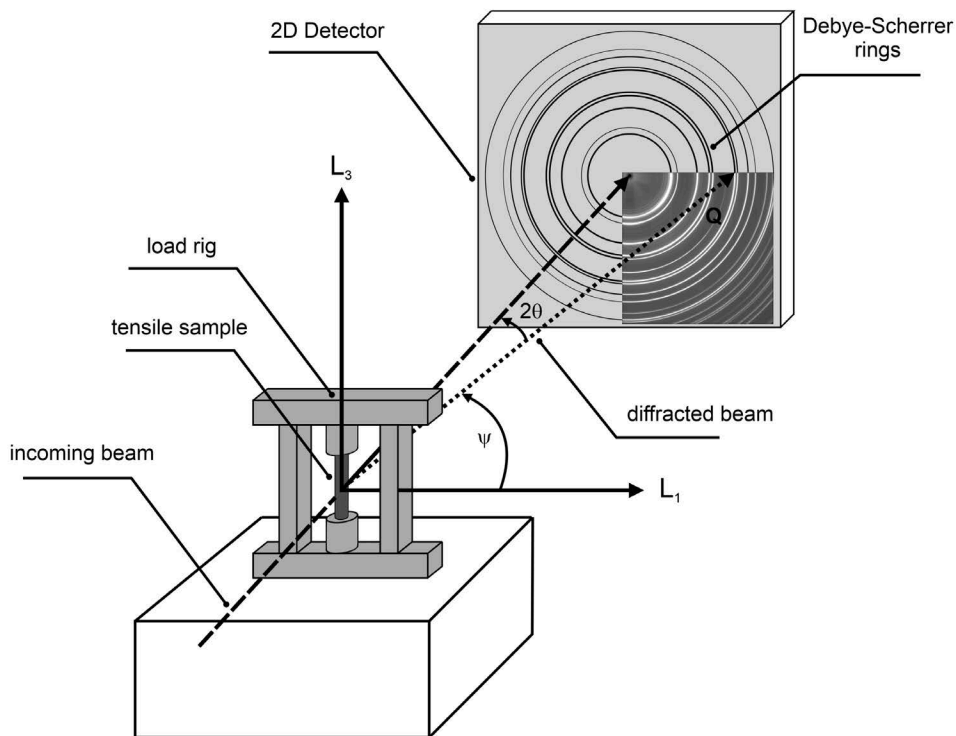


Figure 12: Schematic of the setup for the *in situ* loading experiment at the High Energy Material Science beamline at PETRA III.

VI Appendix

Data Evaluation

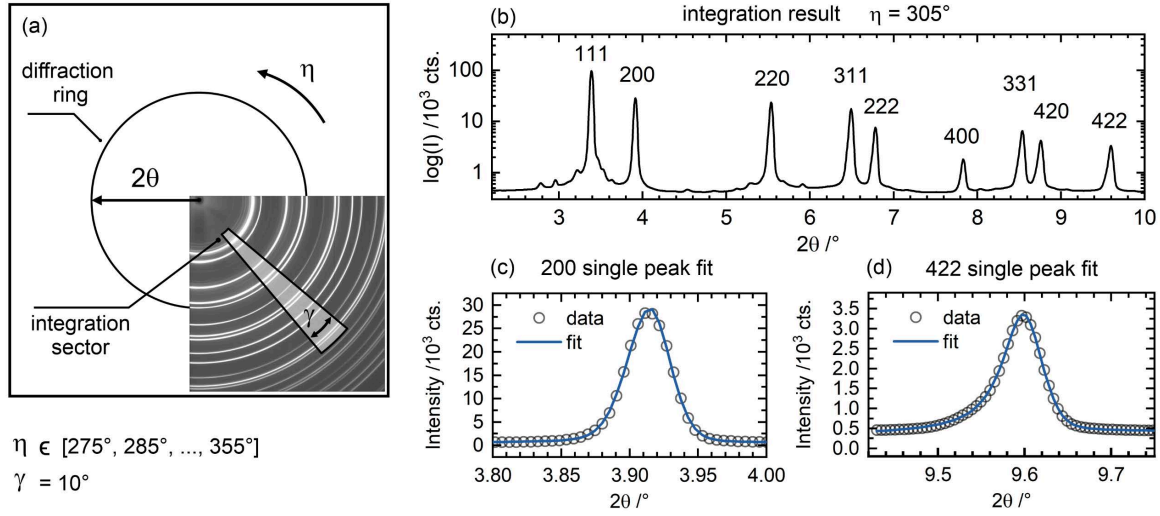


Figure 13: Schematic of the data reduction of the 2D diffraction data (a) to a 1D pattern (b). Single peak fits of the 200 (c) and 422 (d) reflections by an asymmetric PseudoVoigt function performed in the software *fityk* [63].

Peak fitting

A schematic of the data evaluation of the Debye Scherrer rings is shown in Figure 13: The 2D detector data were reduced to 1D diffraction patterns by sector integration using FIT2D [64] (Figure 13a). The 1D diffraction patterns (Figure 13b) were imported into Fytik [63] for single peak analysis as shown for the 200 (Figure 13c) and the 422 (Figure 13d) reflections. The diffraction peaks show an asymmetry at lower 2θ angles. Thus, the single peak fits were performed using an asymmetric PseudoVoigt function. Such peak asymmetry is due to the cellular solidification sub-structure of as-built PBF-LB Inconel 718, see Schröder et al. [50]. The minor peaks observed in the 2D and 1D patterns are associated to Laves and Carbide phases [32]. The overall volume fraction of such phases is around 1-2 %, so that they do not influence the micro mechanical behavior [32].

Determination of diffraction elastic constants

Diffraction elastic constants provide a relationship between elastic lattice strains and macroscopic stress [65]. For anisotropic crystals such constants depend on the lattice plane $\{hkl\}$. In general, these diffraction elastic constants further depend on the measurement directions (φ , Ψ) and are referred to as stress factors (equation 1) [66, 67].

$$\begin{aligned} \overline{\epsilon}_{33}^I(\varphi, \Psi, hkl) &= \frac{d(\varphi, \Psi, hkl) - d_0(\varphi, \Psi, hkl)}{d_0(\varphi, \Psi, hkl)} \\ &= \frac{\partial \overline{\epsilon}_{33}^I(\varphi, \Psi, hkl)}{\partial \overline{\sigma}_{ij}} \overline{\sigma}_{ij} = F_{33ij}(\varphi, \Psi, hkl) \overline{\sigma}_{ij} \end{aligned} \quad (1)$$

In the case of an applied uniaxial stress $\overline{\sigma}_{33}^I$, the actual determination of the stress factors becomes reduces to the application of Hooke's law through a linear regression of lattice strain of reflection $\{hkl\}$ as a function of applied stress for each pair of measurement directions φ and Ψ [65].

VI Appendix

Intergranular residual strain can be removed by choosing the lattice spacing at zero applied load as the reference for the calculation of the lattice strain during application of the load [65]. In the case of isotropic material behavior (i.e. no preferred orientation in the polycrystal) the stress factors become linear combinations of the isotropic diffraction elastic constants s_1 and $1/2s_2$, $F_{33ij}(\varphi, \Psi, hkl) = s_1 + 1/2s_2\cos^2\Psi$ for an applied uniaxial stress $\overline{\sigma}_{33}^I$ [26].

The analysis of the stress factors is exemplarily shown for the 422 reflection in Figure 14a for two Ψ values: 6° and 85° . While the stress was applied along $\Psi = 0^\circ$ (i.e., F_{3333}^{-1} equals E^{hkl}), $\Psi = 90^\circ$ reflects the Poisson response (i.e., the slope is negative). In fact, the stress factors $F_{33ij}(\varphi, \Psi, 422)$ are approximately linear as a function of $\cos^2\Psi$ (Figure 14b). Therefore, although the specimen possesses some crystallographic texture (Figure 12a), such texture only leads to subtle deviations from linearity. Such linear function intersects the ordinate at s_1 and has a slope of $1/2s_2$. Performing such task for all reflections hkl yields the experimental values shown in Table 1. The error on the fit was obtained from the linear regression over $\cos^2\Psi$. Thus, larger errors indicate poorer agreement to an isotropic material behavior. Overall, equivalent reflections (e.g. 200 and 400) yield similar values of s_1 and $1/2s_2$, which outlines the robustness of the approach.

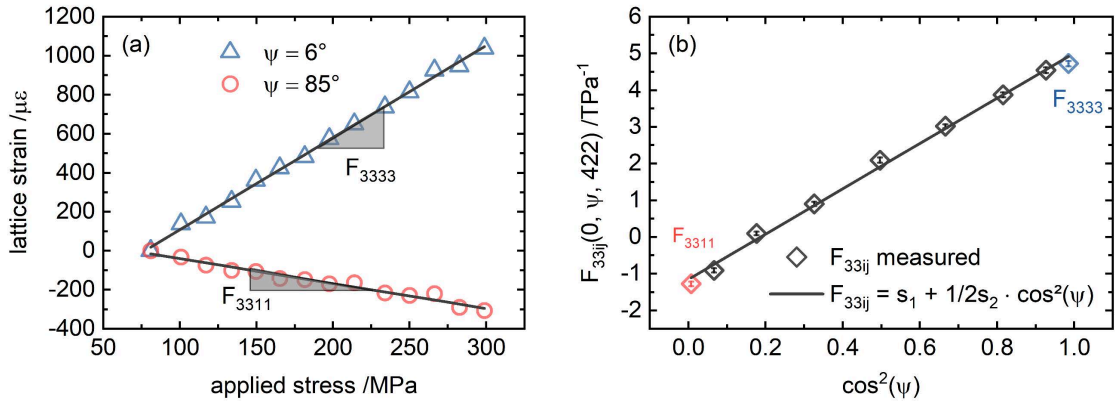


Figure 14: Determination of the experimental stress factors F_{3333} and F_{3311} on the example of the 422 reflection (a). The obtained stress factors plotted over $\cos^2(\Psi)$ with the corresponding linear fit assuming isotropic material behavior (b).

Table 1: Experimentally obtained diffraction elastic constants s_1 and $1/2s_2$ for various lattice planes $\{hkl\}$ obtained by the procedure as shown in Figure 4. The error denotes the standard deviations (1σ) of the linear regressions.

Reflection	$s_1 \pm 1\sigma$ /TPa ⁻¹	$1/2s_2 \pm 1\sigma$ /TPa ⁻¹	Reflection	$s_1 \pm 1\sigma$ /TPa ⁻¹	$1/2s_2 \pm 1\sigma$ /TPa ⁻¹
200	-1.69 ± 0.28	7.96 ± 0.47	400	-1.36 ± 0.24	7.56 ± 0.29
311	-1.37 ± 0.06	7.02 ± 0.10	420	-1.61 ± 0.11	7.22 ± 0.17
422	-1.16 ± 0.08	6.17 ± 0.15	220	-1.72 ± 0.13	6.64 ± 0.21
331	-1.68 ± 0.03	6.68 ± 0.06			
111	-1.07 ± 0.26	5.12 ± 0.47	222	-1.07 ± 0.20	4.94 ± 0.35

VI Appendix

Determination of single-crystal elastic constants

The diffraction elastic constants can be calculated from the single-crystal elastic properties of the material of interest using micromechanical models of the polycrystalline aggregate. Different approaches exist: the Voigt (iso-strain) [68], the Reuss (iso-stress) [69], the Hill (Reuss-Voigt average) [70], the Kröner [71], and the inverse Kröner [65] schemes. One can invert the calculations of these micromechanical models and relate a set of single-crystal elastic constants to the measured diffraction elastic constants. Within ISODEC [72], such approach is implemented as a χ^2 -minimization technique. In such procedure, the single crystal values are refined in a least-squares approach, weighted after the standard deviation 1σ (equation 2) [72].

$$\chi^2 = \sum_{k=1}^n 1\sigma_k^{-2} (F_{33ij}^{meas} - F_{33ij}^{calc})^2 \quad (2)$$

The feasibility of this approach was demonstrated by Hauk & Kockelmann [73] and Gnäupel-Herold et al. [74]. For the sake of comparison, the reduced χ^2 (i.e. the weighted sum of squared differences divided by the degrees of freedom) is used as a quality measure of the fit results. The results of the inverse calculations are exemplarily shown for the 200 reflection in Figure 15a.

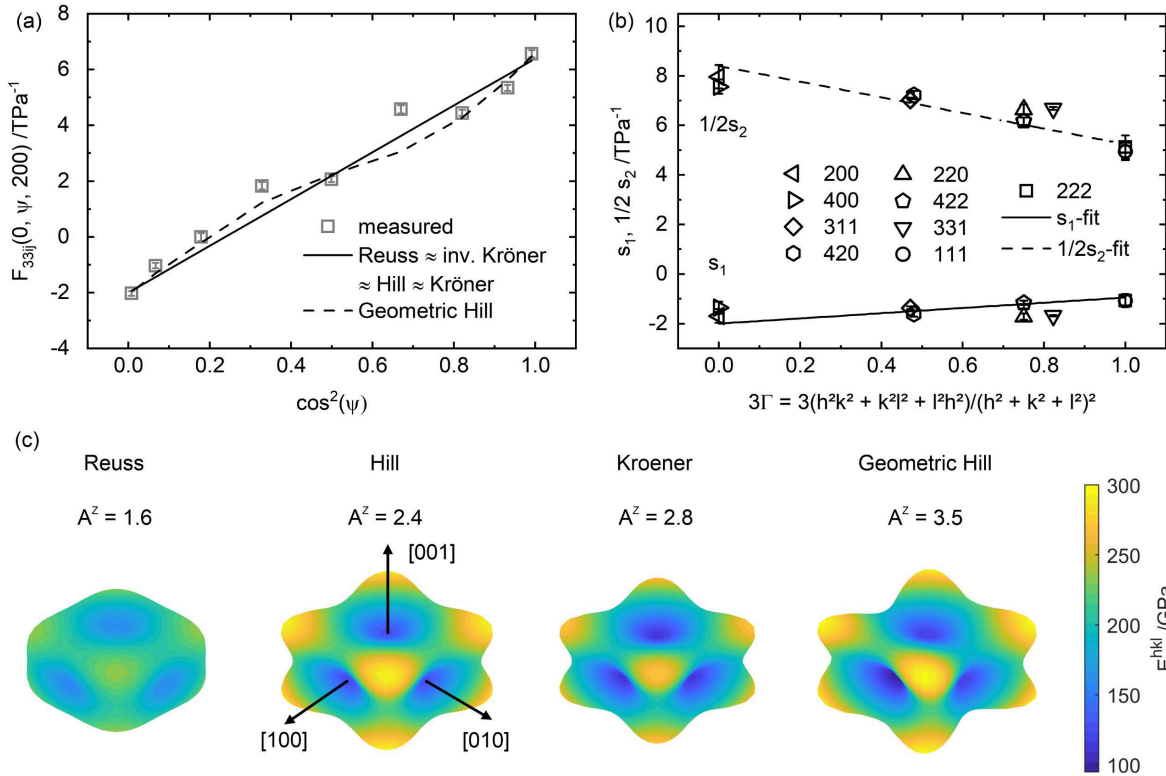


Figure 15: (a) Comparison between the measured and calculated stress factors of the 200 reflection. (b) The experimentally determined isotropic diffraction elastic constants s_1 and s_2 (markers) compared to their model-based fits (lines). (c) Surface plots of the determined single-crystal elastic properties by means of Reuss, Hill, Kröner, and Geometric Hill. For visualization, the MATLAB based script from [48] was used.

As an effect of texture, the measured stress factors of the 200 reflection become non-linear over $\cos^2\Psi$. While the refinement by the geometric Hill model somewhat captures this non-linearity, the Reuss, the inverse Kröner, the Hill, and the Kröner models predict a linear dependence on $\cos^2\Psi$.

VI Appendix

The results of all inverse calculations are shown in Table 2. In Figure 15b, the experimental values of the isotropic diffraction elastic constants s_1 and $1/2s_2$ are compared to the model predictions (using the refined single-crystal elastic constants of Table 2). First, different single-crystal elastic constants are obtained according to different models. This is visualized by the surface plots of the elastic stiffnesses in Figure 15c. Second, regardless of the model, the fit of the experimental data over 3Γ remains similar. Therefore, reliable isotropic diffraction elastic constants can be obtained by the use of the Reuss, the Hill, the geometric Hill, the Kröner, and the inverse Kröner models.

In fact, the Zener factor of the single-crystal elastic constants refined from the Reuss model (1.6) and those reported in Haldipur et al. [56] (2) are close. This proves our previous observation that the iso-stress assumption better reflects the elastic behavior of as-built laser powder bed fused Inconel 718 if one uses conventional single-crystal elastic constants [50].

Table 2: SCEC values of V_0° refined from the $\{111\}$, $\{220\}$, $\{200\}$, $\{400\}$, $\{311\}$, $\{222\}$, $\{331\}$, $\{420\}$, and $\{422\}$ lattice planes for different grain-interaction models. The anisotropy A^Z is calculated after Zener [75].

Model	C_{11} /GPa	C_{12} /GPa	C_{44} /GPa	A^Z	χ^2
Reuss	218.7 ± 1.6	99.6 ± 1.7	95.5 ± 0.8	1.6	10.9
Hill	200.6 ± 1.7	108.6 ± 1.7	110 ± 1.1	2.4	10.9
Geometric Hill	201.7 ± 1.8	129.3 ± 2.1	127.1 ± 1.8	3.5	14.3
Kröner	194.0 ± 1.8	111.9 ± 1.7	115.3 ± 1.3	2.8	10.9
Inverse Kröner	202.6 ± 1.7	107.6 ± 1.6	114.9 ± 1.4	2.4	10.9

VII References

- [1] Attaran M (2017) The rise of 3-D printing: The advantages of additive manufacturing over traditional manufacturing. *Bus Horizons* 60:677-688. <https://doi.org/10.1016/j.bushor.2017.05.011>
- [2] Wohlers T, Gornet T (2016) History of Additive Manufacturing. Wohlers associates, <https://www.wohlersassociates.com/wp-content/uploads/2022/08/history2016.pdf>.
- [3] Bogue R (2013) 3D printing: the dawn of a new era in manufacturing? *Assembly Automation* 33:307-311. <https://doi.org/10.1108/aa-06-2013-055>
- [4] Wang X, Jiang M, Zhou Z, Gou J, Hui D (2017) 3D printing of polymer matrix composites: A review and prospective. *Composites Part B: Engineering* 110:442-458. <https://doi.org/10.1016/j.compositesb.2016.11.034>
- [5] King WE, Anderson AT, Ferencz RM, Hodge NE, Kamath C, Khairallah SA, Rubenchik AM (2015) Laser powder bed fusion additive manufacturing of metals; physics, computational, and materials challenges. *Appl Phys Rev* 2. <https://doi.org/10.1063/1.4937809>
- [6] Ladewig A, Schlick G, Fisser M, Schulze V, Glatzel U (2016) Influence of the shielding gas flow on the removal of process by-products in the selective laser melting process. *Addit Manuf* 10:1-9. <https://doi.org/10.1016/j.addma.2016.01.004>
- [7] Foster SJ, Carver K, Dinwiddie RB, List F, Unocic KA, Chaudhary A, Babu SS (2018) Process-Defect-Structure-Property Correlations During Laser Powder Bed Fusion of Alloy 718: Role of In Situ and Ex Situ Characterizations. *Metall Mater Trans A* 49a:5775-5798. <https://doi.org/10.1007/s11661-018-4870-2>
- [8] Kruth JP, Froyen L, Van Vaerenbergh J, Mercelis P, Rombouts M, Lauwers B (2004) Selective laser melting of iron-based powder. *J Mater Process Tech* 149:616-622. <https://doi.org/10.1016/j.jmatprotec.2003.11.051>
- [9] Mercelis P, Kruth JP (2006) Residual stresses in selective laser sintering and selective laser melting. *Rapid Prototyping J* 12:254-265. <https://doi.org/10.1108/13552540610707013>
- [10] Brenne F, Taube A, Pröbstle M, Neumeier S, Schwarze D, Schaper M, Niendorf T (2016) Microstructural design of Ni-base alloys for high-temperature applications: impact of heat treatment on microstructure and mechanical properties after selective laser melting. *Progress in Additive Manufacturing* 1:141-151. <https://doi.org/10.1007/s40964-016-0013-8>
- [11] Mishurova T, Serrano-Muñoz I, Fritsch T, Ulbricht A, Sprengel M, Evans A, Kromm A, Madia M, Bruno G (2020) A Critical Discussion on the Diffraction-Based Experimental Determination of Residual Stress in AM Parts in Shamsaei N, Seifi M *Structural Integrity of Additive Manufactured Materials & Parts* ASTM International, West Conshohocken. <https://doi.org/10.1520/stp163120190148>
- [12] Donachie MJ, Donachie SJ (2002) *Superalloys: a technical guide*. ASM International, Materials Park, OH
- [13] Henderson MB, Arrell D, Larsson R, Heobel M, Marchant G (2004) Nickel based superalloy welding practices for industrial gas turbine applications. *Sci Technol Weld Joi* 9:13-21. <https://doi.org/10.1179/136217104225017099>
- [14] Haafkens MH, Matthey JHG (1982) A New Approach to the Weldability of Nickel-Base as-Cast and Powder-Metallurgy Super-Alloys. *Weld J* 61:25-30.

VII References

- [15] Lingenfelter A (1989) Welding of Inconel Alloy 718: A Historical Overview. *Superalloy 718 Metallurgy and Applications*:673-683. https://doi.org/10.7449/1989/Superalloys_1989_673_683
- [16] Paulonis DF, Schirra JJ (2001) Alloy 718 at Pratt & Whitney - Historical perspective and future challenges. *Superalloys 718, 625, 706 and Various Derivatives*:13-23. https://doi.org/10.7449/2001/Superalloys_2001_13_23
- [17] Basak A, Das S (2017) Additive Manufacturing of Nickel-Base Superalloy Rene N5 through Scanning Laser Epitaxy (SLE) - Material Processing, Microstructures, and Microhardness Properties. *Adv Eng Mater* 19. <https://doi.org/10.1002/adem.201600690>
- [18] Paulonis DF, Oblak JM, Duvall DS (1969) Precipitation in Nickel-Base Alloy 718. *Asm Trans Q* 62:611-622.
- [19] Xiao L, Chen DL, Chaturvedi MC (2005) Effect of boron and carbon on the fracture toughness of IN 718 superalloy at room temperature and 650 degrees C. *J Mater Eng Perform* 14:528-538. <https://doi.org/10.1361/105994905x56106>
- [20] Zimina LN, Burova NN, Makushok OV (1986) Effect of Hafnium on the Structure and Properties of Wrought Nickel-Base Alloys. *Met Sci Heat Treat+* 28:130-135. <https://doi.org/10.1007/Bf00717535>
- [21] Huang X, Chaturvedi MC, Richards NL, Jackman J (1997) The effect of grain boundary segregation of boron in cast alloy 718 on HAZ microfissuring - A SIMS analysis. *Acta Mater* 45:3095-3107. [https://doi.org/10.1016/S1359-6454\(97\)00017-7](https://doi.org/10.1016/S1359-6454(97)00017-7)
- [22] Xu JH, Kontis P, Peng RL, Moverare J (2022) Modelling of additive manufacturability of nickel-based superalloys for laser powder bed fusion. *Acta Mater* 240. <https://doi.org/10.1016/j.actamat.2022.118307>
- [23] Volpato GM, Tetzlaff U, Fredel MC (2022) A comprehensive literature review on laser powder bed fusion of Inconel superalloys. *Addit Manuf* 55. <https://doi.org/10.1016/j.addma.2022.102871>
- [24] Oliveira JP, LaLonde AD, Ma J (2020) Processing parameters in laser powder bed fusion metal additive manufacturing. *Mater Design* 193. <https://doi.org/10.1016/j.matdes.2020.108762>
- [25] Mohr G, Altenburg SJ, Hilgenberg K (2020) Effects of inter layer time and build height on resulting properties of 316L stainless steel processed by laser powder bed fusion. *Addit Manuf* 32. <https://doi.org/10.1016/j.addma.2020.101080>
- [26] Hauk V (1997) *Structural and Residual Stress Analysis by Nondestructive Methods*. Elsevier Science, Amsterdam
- [27] Noyan IC, Cohen JB (1987) *Residual stress : measurement by diffraction and interpretation*. Springer-Verlag, New York
- [28] Ulbricht A, Altenburg SJ, Sprengel M, Sommer K, Mohr G, Fritsch T, Mishurova T, Serrano-Munoz I, Evans A, Hofmann M, Bruno G (2020) Separation of the Formation Mechanisms of Residual Stresses in LPBF 316L. *Metals* 10. <https://doi.org/10.3390/met10091234>
- [29] Sprengel M, Mohr G, Altenburg SJ, Evans A, Serrano-Munoz I, Kromm A, Pirling T, Bruno G, Kannengiesser T (2022) Triaxial Residual Stress in Laser Powder Bed Fused 316L: Effects of Interlayer Time and Scanning Velocity. *Adv Eng Mater* 24. <https://doi.org/10.1002/adem.202101330>

VII References

- [30] Schröder J, Evans A, Mishurova T, Ulbricht A, Sprengel M, Serrano-Munoz I, Fritsch T, Kromm A, Kannengießer T, Bruno G (2021) Diffraction-Based Residual Stress Characterization in Laser Additive Manufacturing of Metals. *Metals* 11. <https://doi.org/10.3390/met11111830>
- [31] Gallmeyer TG, Moorthy S, Kappes BB, Mills MJ, Amin-Ahmadi B, Stebner AP (2020) Knowledge of process-structure-property relationships to engineer better heat treatments for laser powder bed fusion additive manufactured Inconel 718. *Addit Manuf* 31. <https://doi.org/10.1016/j.addma.2019.100977>
- [32] Rielli VV, Piglione A, Pham M-S, Primig S (2022) On the detailed morphological and chemical evolution of phases during laser powder bed fusion and common post-processing heat treatments of IN718. *Addit Manuf* 50:102540. <https://doi.org/10.1016/j.addma.2021.102540>
- [33] Amato KN, Gaytan SM, Murr LE, Martinez E, Shindo PW, Hernandez J, Collins S, Medina F (2012) Microstructures and mechanical behavior of Inconel 718 fabricated by selective laser melting. *Acta Mater* 60:2229-2239. <https://doi.org/10.1016/j.actamat.2011.12.032>
- [34] Chalmers B (1964) *Principles of solidification*. Wiley, New York
- [35] Gokcekaya O, Ishimoto T, Hibino S, Yasutomi J, Narushima T, Nakano T (2021) Unique crystallographic texture formation in Inconel 718 by laser powder bed fusion and its effect on mechanical anisotropy. *Acta Mater* 212. <https://doi.org/10.1016/j.actamat.2021.116876>
- [36] Hosford WF (2010) *Mechanical Behavior of Materials*. Cambridge University Press, New York
- [37] Ishimoto T, Hagihara K, Hisamoto K, Sun SH, Nakano T (2017) Crystallographic texture control of beta-type Ti-15Mo-5Zr-3Al alloy by selective laser melting for the development of novel implants with a biocompatible low Young's modulus. *Scripta Mater* 132:34-38. <https://doi.org/10.1016/j.scriptamat.2016.12.038>
- [38] Nye JF (1985) *Physical properties of crystals, their representation by tensors and matrices*. Clarendon Press, Oxford,
- [39] Schmid E (1924) *Proc. Internat. Cong. Appl. Mech., Delft*
- [40] Bean GE, McLouth TD, Witkin DB, Sitzman SD, Adams PM, Zaldivar RJ (2019) Build Orientation Effects on Texture and Mechanical Properties of Selective Laser Melting Inconel 718. *J Mater Eng Perform* 28:1942-1949. <https://doi.org/10.1007/s11665-019-03980-w>
- [41] Ni M, Chen C, Wang XJ, Wang PW, Li RD, Zhang XY, Zhou KC (2017) Anisotropic tensile behavior of in situ precipitation strengthened Inconel 718 fabricated by additive manufacturing. *Mat Sci Eng a-Struct* 701:344-351. <https://doi.org/10.1016/j.msea.2017.06.098>
- [42] Zhou L, Mehta A, McWilliams B, Cho K, Sohn Y (2019) Microstructure, precipitates and mechanical properties of powder bed fused inconel 718 before and after heat treatment. *J Mater Sci Technol* 35:1153-1164. <https://doi.org/10.1016/j.jmst.2018.12.006>
- [43] Tucho WM, Cuvillier P, Sjolyst-Kvemeland A, Hansen V (2017) Microstructure and hardness studies of Inconel 718 manufactured by selective laser melting before and after solution heat treatment. *Mat Sci Eng a-Struct* 689:220-232. <https://doi.org/10.1016/j.msea.2017.02.062>

VII References

- [44] Yang G, Park SJ (2019) Deformation of Single Crystals, Polycrystalline Materials, and Thin Films: A Review. *Materials* 12. <https://doi.org/10.3390/ma12122003>
- [45] Bragg WH, Bragg WL (1913) The reflection of X-rays by crystals. *P R Soc Lond a-Conta* 88:428-438. <https://doi.org/10.1098/rspa.1913.0040>
- [46] Clausen B, Leffers T, Lorentzen T (2003) On the proper selection of reflections for the measurement of bulk residual stresses by diffraction methods. *Acta Mater* 51:6181-6188. <https://doi.org/10.1016/j.actamat.2003.07.002>
- [47] Withers PJ, Preuss M, Steuwer A, Pang JWL (2007) Methods for obtaining the strain-free lattice parameter when using diffraction to determine residual stress. *J Appl Crystallogr* 40:891-904. <https://doi.org/10.1107/S0021889807030269>
- [48] Nordmann J, Assmus M, Altenbach H (2018) Visualising elastic anisotropy: theoretical background and computational implementation. *Continuum Mech Therm* 30:689-708. <https://doi.org/10.1007/s00161-018-0635-9>
- [49] Schneider J, Lund B, Fullen M (2018) Effect of heat treatment variations on the mechanical properties of Inconel 718 selective laser melted specimens. *Addit Manuf* 21:248-254. <https://doi.org/10.1016/j.addma.2018.03.005>
- [50] Schröder J, Evans A, Polatidis E, Mohr G, Serrano-Munoz I, Bruno G, Čapek J (2022) Understanding the impact of texture on the micromechanical anisotropy of laser powder bed fused Inconel 718. *J Mater Sci* 57:15036-15058. <https://doi.org/10.1007/s10853-022-07499-9>
- [51] Laquai R, Müller BR, Schneider JA, Kupsch A, Bruno G (2020) Using SXRR to Probe the Nature of Discontinuities in SLM Additive Manufactured Inconel 718 Specimens. *Metall Mater Trans A* 51:4146-4157. <https://doi.org/10.1007/s11661-020-05847-5>
- [52] Sangid MD, Book TA, Naragani D, Rotella J, Ravi P, Finch A, Kenesei P, Park JS, Sharma H, Almer J, Xiao XH (2018) Role of heat treatment and build orientation in the microstructure sensitive deformation characteristics of IN718 produced via SLM additive manufacturing. *Addit Manuf* 22:479-496. <https://doi.org/10.1016/j.addma.2018.04.032>
- [53] Xiao L, Chen DL, Chaturvedi MC (2005) Shearing of gamma " precipitates and formation of planar slip bands in Inconel 718 during cyclic deformation. *Scripta Mater* 52:603-607. <https://doi.org/10.1016/j.scriptamat.2004.11.023>
- [54] Sochalski-Kolbus LM, Payzant EA, Cornwell PA, Watkins TR, Babu SS, Dehoff RR, Lorenz M, Ovchinnikova O, Duty C (2015) Comparison of Residual Stresses in Inconel 718 Simple Parts Made by Electron Beam Melting and Direct Laser Metal Sintering. *Metall Mater Trans A* 46a:1419-1432. <https://doi.org/10.1007/s11661-014-2722-2>
- [55] Serrano-Munoz I, Evans A, Mishurova T, Sprengel M, Pirling T, Kromm A, Bruno G (2022) The Importance of Subsurface Residual Stress in Laser Powder Bed Fusion IN718. *Adv Eng Mater* 24. <https://doi.org/10.1002/adem.202100895>
- [56] Haldipur P, Margetan FJ, Thompson RB (2004) Estimation of single-crystal elastic constants from ultrasonic measurements on polycrystalline specimens. *AIP Conference Proceedings* 700:1061-1068. <https://doi.org/10.1063/1.1711735>
- [57] Levkulich NC, Semiatin SL, Gockel JE, Middendorf JR, DeWald AT, Klingbeil NW (2019) The effect of process parameters on residual stress evolution and distortion in the laser powder bed fusion of Ti-6Al-4V. *Addit Manuf* 28:475-484. <https://doi.org/10.1016/j.addma.2019.05.015>

VII References

- [58] Mishurova T, Artzt K, Haubrich J, Requena G, Bruno G (2019) Exploring the Correlation between Subsurface Residual Stresses and Manufacturing Parameters in Laser Powder Bed Fused Ti-6Al-4V. *Metals-Basel* 9. <https://doi.org/10.3390/met9020261>
- [59] Apel D (2013) Tiefenaufgelöste Analyse randschichtnaher Struktur- und Eigenschaftsgradienten in vielkristallinen Werkstoffen mittels energiedispersiver Röntgenbeugung Dissertation. Technische Universität Berlin. Berlin. <https://doi.org/10.14279/depositonce-3543>
- [60] Schell N, King A, Beckmann F, Fischer T, Müller M, Schreyer A (2014) The High Energy Materials Science Beamline (HEMS) at PETRA III. *Mater Sci Forum* 772:57-61. <https://doi.org/10.4028/www.scientific.net/MSF.772.57>
- [61] Heldmann A, Hoelzel M, Hofmann M, Gan WM, Schmahl WW, Griesshaber E, Hansen T, Schell N, Petry W (2019) Diffraction-based determination of single-crystal elastic constants of polycrystalline titanium alloys. *J Appl Crystallogr* 52:1144-1156. <https://doi.org/10.1107/S1600576719010720>
- [62] Hoelzel M, Gan WM, Hofmann M, Randau C, Seidl G, Juttner P, Schmahl WW (2013) Rotatable multifunctional load frames for neutron diffractometers at FRM II-design, specifications and applications. *Nucl Instrum Meth A* 711:101-105. <https://doi.org/10.1016/j.nima.2013.01.049>
- [63] Wojdyr M (2010) Fityk: a general-purpose peak fitting program. *J Appl Crystallogr* 43:1126-1128. <https://doi.org/10.1107/S0021889810030499>
- [64] Hammersley AP (2016) FIT2D: a multi-purpose data reduction, analysis and visualization program. *J Appl Crystallogr* 49:646-652. <https://doi.org/10.1107/S1600576716000455>
- [65] Gnäupel-Herold T, Creuziger AA, Iadicola M (2012) A model for calculating diffraction elastic constants. *J. Appl. Crystallogr.* 45:197-206. <https://doi.org/10.1107/S0021889812002221>
- [66] Dölle H, Hauk V (1978) Influence of Mechanical Anisotropy of Polycrystal (Texture) Upon Stress Evaluation by Means of X-Rays. *Z Metallkd* 69:410-417.
- [67] Dölle H, Hauk V (1979) Evaluation of Residual-Stresses in Textured Materials by X-Rays. *Z Metallkd* 70:682-685.
- [68] Voigt W (1889) Ueber die Beziehung zwischen den beiden Elasticitätsconstanten isotroper Körper. *Ann. Phys.* (Berlin, Ger.) 274:573-587. <https://doi.org/10.1002/andp.18892741206>
- [69] Reuss A (1929) Account of the liquid limit of mixed crystals on the basis of the plasticity condition for single crystal. *Z Angew Math Mech* 9:49-58. <https://doi.org/10.1002/zamm.19290090104>
- [70] Hill R (1952) The Elastic Behaviour of a Crystalline Aggregate. *P Phys Soc Lond A* 65:349-355. <https://doi.org/10.1088/0370-1298/65/5/307>
- [71] Kröner E (1958) Berechnung Der Elastischen Konstanten Des Vielkristalls Aus Den Konstanten Des Einkristalls. *Z Phys* 151:504-518. <https://doi.org/10.1007/Bf01337948>
- [72] Gnäupel-Herold T (2012) ISODEC: software for calculating diffraction elastic constants. *J Appl Crystallogr* 45:573-574. <https://doi.org/10.1107/S0021889812014252>
- [73] Hauk V, Kockelmann H (1979) Evaluation of Single-Crystal Elastic-Constants from Mechanical and X-Ray Elastic-Constants of the Polycrystal. *Z Metallkd* 70:500-502.

VII References

- [74] Gnäupel-Herold T, Brand PC, Prask HJ (1998) Calculation of single-crystal elastic constants for cubic crystal symmetry from powder diffraction data. *J Appl Crystallogr* 31:929-935. <https://doi.org/10.1107/S002188989800898x>
- [75] Zener CM, Siegel S (1949) Elasticity and Anelasticity of Metals. *The Journal of Physical and Colloid Chemistry* 53:1468-1468. <https://doi.org/10.1021/j150474a017>